



HAL
open science

Pyrolysis and gasification of a solid recovered fuel (SRF) and its model materials

Oscar Sosa Sabogal

► **To cite this version:**

Oscar Sosa Sabogal. Pyrolysis and gasification of a solid recovered fuel (SRF) and its model materials. Chemical and Process Engineering. Ecole des Mines d'Albi-Carmaux, 2022. English. NNT : 2022EMAC0007 . tel-03771696

HAL Id: tel-03771696

<https://theses.hal.science/tel-03771696>

Submitted on 7 Sep 2022

HAL is a multi-disciplinary open access archive for the deposit and dissemination of scientific research documents, whether they are published or not. The documents may come from teaching and research institutions in France or abroad, or from public or private research centers.

L'archive ouverte pluridisciplinaire **HAL**, est destinée au dépôt et à la diffusion de documents scientifiques de niveau recherche, publiés ou non, émanant des établissements d'enseignement et de recherche français ou étrangers, des laboratoires publics ou privés.



THÈSE

En vue de l'obtention du

DOCTORAT DE L'UNIVERSITÉ DE TOULOUSE

délivré par

IMT – École Nationale Supérieure des Mines d'Albi-Carmaux

présentée et soutenue par

Oscar SOSA SABOGAL

le 8 juin 2022

Titre :

**Pyrolysis and gasification of a solid recovered fuel
(SRF) and its model materials**

École doctorale et discipline ou spécialité :

MEGEP : Génie des Procédés et de l'Environnement

Unités de recherche :

Centre RAPSODEE, UMR CNRS 5302, IMT Mines Albi

LITEN/DTCH/SCPC/Laboratoire Réacteurs et Procédés, CEA Grenoble

Directeur et Directrice de thèse :

Sylvain SALVADOR, Professeur, IMT Mines Albi

Sylvie VALIN, Ingénieure de Recherche, CEA Grenoble

Autres membres du jury :

Guillain MAUVIEL, Professeur, Université de Lorraine, Rapporteur

Laurent VAN DE STEENE, Ingénieur de Recherche, Université de Montpellier, Rapporteur

Yann ROGAUME, Professeur, Université de Lorraine, Président

Maxime HERVY, Ingénieur de Recherche, ENGIE Lab CRIGEN, Examineur

PYROLYSIS AND GASIFICATION OF A SOLID RECOVERED FUEL (SRF) AND ITS MODEL MATERIALS

PYROLYSE ET GAZEIFICATION D'UN COMBUSTIBLE SOLIDE DE RECUPERATION
(CSR) ET DE SES MATERIAUX MODELES

Oscar SOSA SABOGAL

Doctoral school : MEGEP - Mécanique, Energétique, Génie civil, Procédés

Speciality : Génie des Procédés et de l'Environnement

June 2022

Directed by:

Sylvain SALVADOR et Sylvie VALIN

*“Ever tried.
Ever failed.
No matter.
Try again.
Fail again.
Fail better.”*

Samuel Beckett

Acknowledgements

First, I would like to thank the members of the jury who took the time to read and evaluate this thesis work. To Guillaïn Mauviel and Laurent Van de Steene, thank you for your annotations, which were very pertinent and useful for the preparation of the defense. To Maxime Hervy, and Yann Rogaume, thank you for your views and constructive discussion.

To my thesis director, Sylvain, thank you for your kindness and helpful advice during this time. For teaching me that the small details are just as important, and that they make us become better researchers.

To Sylvie, co-director and thesis supervisor, my deepest gratitude. Thank you for your constant guidance and immeasurable support (and of course, your patience!). You made me grow not only as a scientist, but also as a person.

I would also like to thank all my colleagues in the LRP at CEA, with whom I had the pleasure to share and work during all these years. Special thanks to Sebastian, Snoop and Serge, without you the new PYRATES reactor would not have been possible. To Gilles and Christian, thanks for taking the time to share some of your expertise with me. To Marine, thanks for believing in me from the beginning. Thank you for being a mentor, counselor, and a friend. To Muriel, Maria, Hary, Nicolas, Michael, Laurent BEDEL and the rest of the biomass team, thank you for your help and good energy.

I would like to thank my fellow PhD colleagues, who also decided to adventure themselves in the research world. My office mate Florent, Tilia, Clément, Morgane, Emile, Hala, Victor, Lucie, and Elie. I am fortunate to have shared many moments, conversations, coffees and beers with all of you. To my friends, who encouraged me and comforted me in the good and not so good times, Aleja, Cata, Darling, Laura, Marie, Sebastian, Fabrice, Robinson, Walter, thanks so much. To Carolina, big thanks for your friendship and help during all this time. Further, I would like to thank Arnaud. Thank you for your patience and your unconditional support, and for showing me that it is possible to go beyond our own limits.

Finally, a heartfelt thank you to my family. To my parents, Gloria y Pedro, who have always supported me and who are the reason for all my achievements. Gracias infinitas. To my sister Sandra, who has always been a great example of resilience. And to my little niece Luciana too! Despite the distance, you were always close.

And to all those who want to help make this planet a better place, Thank you and good luck!

Contents

INTRODUCTION	1
1. LITERATURE REVIEW.....	7
1.1 SOLID WASTE AND ITS DERIVED FUELS	8
1.1.1 Solid waste	8
1.1.2 Waste derived fuels	9
1.1.3 Material content of solid recovered fuels	11
1.1.4 Energy valorization of SRF	20
1.2 PHENOMENOLOGICAL AND TECHNICAL DESCRIPTION OF THE GASIFICATION PROCESS	23
1.2.1 Thermochemical phenomena of gasification.....	23
1.2.2 Gasification reactors.....	26
1.2.3 Process parameters and performance indicators	29
1.2.4 Gas applications and cleaning methods	30
1.3 STATE OF THE ART ON PYROLYSIS AND GASIFICATION OF SOLID WASTE.....	31
1.3.1 Thermogravimetric analysis for thermal decomposition investigation	32
1.3.2 Pyrolysis and gasification studies in laboratory scale fixed bed reactors.....	37
1.3.3 Pyrolysis and gasification studies in fluidized bed reactors	39
1.3.4 Solid waste pyrolysis and gasification modelling	41
1.4 SUMMARY.....	44
1.5 OBJECTIVES AND METHODOLOGY OF THE THESIS	45
2. EXPERIMENTAL SETUP.....	47
2.1 DESIGN OF THE LAB SCALE INDUCTION REACTOR.....	48
2.1.1 Design objectives	48
2.1.2 Previous works: The PYRATES setup	49
2.1.3 Modifications to the PYRATES setup.....	51
2.2 DESCRIPTION OF THE NEW PYRATES SETUP.....	53
2.2.1 Reactor tube	53
2.2.2 Induction system	54
2.2.3 Heat exchanger.....	55
2.2.4 Sample crucible	56
2.2.5 Condensation section.....	56

2.2.6 Gas analysis section	58
2.3 THERMAL CHARACTERIZATION OF THE REACTOR	58
2.3.1 Transient temperature response of the reactor	59
2.3.2 Temperature profile of the sample	60
2.3.3 Steady state temperature profiles	62
2.3.4 CFD modeling of the reactor	63
2.4 CONCLUSIONS	67
3. FEEDSTOCK AND METHODS	70
3.1 FEEDSTOCK MATERIALS	71
3.1.1 Solid Recovered Fuel	71
3.1.2 Model materials	72
3.1.3 Feedstock characterization	76
3.2 EXPERIMENTAL PROCEDURE AND CONDITIONS OF THE TESTS	79
3.2.1 Pyrolysis tests procedure and conditions	79
3.2.2 Procedure and method for the determination of the produced gas flowrate	80
3.2.3 Gasification tests procedure and conditions	83
3.3 PRODUCT COLLECTION, QUANTIFICATION AND ANALYSIS	85
3.3.1 Quantification and analysis of the solid residue	85
3.3.2 Quantification and analysis of the permanent gas	85
3.3.3 Collection, quantification and analysis of the condensable species	86
4. RESULTS AND DISCUSSION	90
4.1 EVOLUTION OF TEMPERATURE AND GAS FLOWRATE DURING PYROLYSIS	91
4.1.1 Time evolution of sample temperature	91
4.1.2 Time evolution of produced volatiles flowrate	93
4.2 PYROLYSIS OF SOLID RECOVERED FUEL AND ITS MODEL MATERIALS	95
4.2.1 Pyrolysis products distribution	95
4.2.2 Distribution of initial C, H and O in pyrolysis products	96
4.2.3 Pyrolysis gas products yields	98
4.2.4 Tar species yields after pyrolysis	100
4.2.5 Pyrolysis solid residue	104
4.2.6 Distribution of the energy content of the initial feedstock	106

4.3 INTERACTIONS BETWEEN OF BIOMASS AND PLASTIC MATERIALS DURING PYROLYSIS	107
4.3.1 Product yields from mixtures pyrolysis	108
4.3.2 Gas products yields from mixtures pyrolysis	110
4.3.3 Tar species yields from mixtures pyrolysis	111
4.4 INFLUENCE OF OXYGEN ADDITION ON SRF CONVERSION: TOWARDS GASIFICATION.....	113
4.4.1 Influence of ER on beech wood gasification at 800 °C	113
4.4.2 Influence of oxygen addition on the conversion of SRF and of model materials	117
4.5 DEVELOPMENT OF A CORRELATION FOR THE PREDICTION OF PYROLYSIS YIELDS.....	126
4.5.1 Feedstock representation	126
4.5.2 Pyrolysis products representation	127
4.5.3 Methodology	129
4.5.4 Results	132
4.5.5 Conclusions.....	137
CONCLUSION AND PERSPECTIVES.....	141
APPENDICES	147
A. APPENDIX A. SRF CLASSIFICATION BY THE EN15359 STANDARD.....	162
B. APPENDIX B. THE NEW PYRATES SETUP	163
C. APPENDIX C. GEOMETRY OF THE CFD MODEL OF THE NEW PYRATES REACTOR	164
D. APPENDIX D. CHARACTERIZATION OF THE SRF SAMPLE	166
E. APPENDIX E. CONDENSABLE AND GAS ANALYSIS INSTRUMENTS	168
RESUME ETENDU EN FRANÇAIS.....	172

List of Tables

Table 1-1. Classification of solid waste based on their source	8
Table 1-2. LHV, ultimate and proximate analyses of different types of wood and wood waste	14
Table 1-3. LHV, ultimate and proximate analysis of different types of paper	15
Table 1-4. LHV, ultimate and proximate analysis of other biogenic materials	15
Table 1-5. LHV, ultimate and proximate analysis of most common plastics	18
Table 1-6. LHV, ultimate and proximate analysis of other fossil derived materials	19
Table 1-7. Main characteristics of thermochemical processes for solid waste thermal treatment	21
Table 1-8. Influence of materials on solid waste fuels properties and impact on thermochemical conversion.	22
Table 1-9. Main reactions during gasification process.	25
Table 1-10. Characteristics of different gasification reactor technologies	26
Table 1-11. Target levels of pollutants in relation with principal gas applications	31
Table 1-12. Summary of the main characteristics of pyrolysis/gasification models for SRF.	43
Table 2-1. Properties of the ceramic material considered in the CFD calculations.	64
Table 3-1. Chemical composition and characteristics of the SRF and of the model materials.	77
Table 3-2. Experimental conditions of pyrolysis tests.	79
Table 3-3. Experimental conditions for gasification tests.	84
Table 3-4. Tar classification according to ECN.	88
Table 4-1. Yields of principal tar species from pyrolysis at 800°C of SRF and model materials.	102
Table 4-2. Chemical composition of the solid residues after pyrolysis at 800°C, and char yields.	104
Table 4-3. Comparison between the calculated and the experimental pyrolysis tar species yields of biomass/plastic mixtures at 800° C.	112
Table 4-4. Effect of ER on tar species yields(in mg.g _{daf} ⁻¹) for wood at 800°C	116

Table 4-5. Mass yields for pyrolysis and gasification tests at 800°C, for SRF, for the five model materials and for the Wood/PE mixture.....	118
Table 4-6. Tar yields from the gasification of SRF, of model materials and of the Wood/PE mixture at 800°C	123
Table 4-7. Chemical composition of the solid residues after gasification at 800°C.	124
Table 4-8. Normalized CHO mass composition, molecular formula and weight of the five model materials.	127
Table 4-9. CHO normalized composition, molecular formula and weight of the char produced by pyrolysis at 800°C for the five model materials.	128
Table 4-10. CHO normalized composition, molecular formula and weight of the tar produced by pyrolysis at 800°C for the five model materials.	129
Table 4-11. Coefficients for the linear equations obtained by MLR, and results of the ANOVA analysis.	131
Table 4-12. Equations for the calculation of the unknown parameters.	132
Table 4-13. CHO normalized composition, molecular formula and weight for the feedstock, char and tar products of SRF and the two mixtures.	135
Table A-1. SRF Classification system according to EN15359.....	162
Table D-1. Fractional composition (wt %) of the SRF fluff.....	167
Table E-1. Gas chromatograph used for the analysis of non-condensable species.....	168
Table D-2. Detected and calibrated species in the GC-FID analysis.....	169
Table E-3. Gas detector used for the online analysis of permanent gases.....	170
Table E-4. Characteristics of the micro-GC chromatograph and its columns.....	171

List of Figures

Figure 1. EU waste management hierarchy scheme.....	2
Figure 1-1. Terminology used for waste sources and waste derived fuels	10
Figure 1-2. Bases used to represent solid waste fuels composition	11
Figure 1-3. Mean material composition of SRF	12
Figure 1-4. Typical content of biopolymers in lignocellulosic fractions of SRF.....	13
Figure 1-5. Most prevalent plastic polymers in solid recovered fuel.....	16
Figure 1-6. Thermochemical phenomena involved in gasification	23
Figure 1-7. Pyrolysis conditions and their effect on product distribution	24
Figure 1-8. Schematic representation of fixed bed reactor technologies	27
Figure 1-9. Schematic representation of fluidized reactor technologies.....	28
Figure 1-10. Schematic representation of an entrained flow reactor	28
Figure 1-11. TG and DTG curves for an RDF sample	32
Figure 1-12. Intervals and maxima of thermal decomposition of biomass components and biogenic materials and their char yield after pyrolysis.....	33
Figure 1-13. Intervals and maximums of thermal decomposition of fossil derived polymers and materials and their char yield after pyrolysis.....	34
Figure 1-14. Effect of plastic content in the feed on gas yields, hydrogen production and tar content in the co-gasification of plastics with biomass	40
Figure 2-1. Picture of the heated zone of the PYRATES device	50
Figure 2-2. Temperature profile along the Inconel pipe	50
Figure 2-3. Schematic overview of the experimental setup.....	53
Figure 2-4. Detailed diagram of the induction coil and reactor tube.	54
Figure 2-5. Detailed diagram of the middle section of the reactor.....	56

Figure 2-6. Schematic representation of an impinger and layout of the impingers in the condensation zone.....	57
Figure 2-7. Schematic of the reactor tube and middle section outlining the position of the thermocouples.....	59
Figure 2-8. Temperature evolution at different locations along the reactor outer wall.	60
Figure 2-9. Temperature evolution in the empty crucible and in the crucible filled with ceramic material.....	60
Figure 2-10. Temperature along the reactor wall at steady state for a setpoint of 800 °C.	63
Figure 2-11. Contour plots of temperature distribution in the gas phase for different gas flowrates.	66
Figure 2-12. Contour plot of temperature at the middle section of the reactor	67
Figure 3-1. SRF pellets used for this study.	71
Figure 3-2. Material composition of the SRF fluff.....	72
Figure 3-3. Selected model materials	74
Figure 3-4. Model materials samples used in the experiments	75
Figure 3-5. Picture of pressed pellets of wood and polyethylene	76
Figure 3-6. Temperature profile for the determination of ash content at 815 °C.....	77
Figure 3-7. Van Krevelen diagram for the different samples used in this study and other common waste materials.	78
Figure 3-8. Calibration runs for the differential pressure transmitter.	81
Figure 3-9. Time response of the setup at 800 °C.....	82
Figure 3-10. Pressure transmitter response in the first seconds after start-up of heating.	83
Figure 4-1. Time evolution of temperature during pyrolysis at 800 °C for wood, PE, and the wood/PE mixture	91
Figure 4-2. Time evolution of the produced gas flowrate during pyrolysis at 800 °C for SRF and model materials	93
Figure 4-3. Distribution of pyrolysis products at 800 °C for SRF and model materials.....	95

Figure 4-4. Carbon distribution in the pyrolysis products at 800 °C for SRF and model materials.	96
Figure 4-5. Tar deposits found in the connection between the reactor outlet and the condensation section.....	97
Figure 4-6. Hydrogen and oxygen distribution in the pyrolysis products at 800 °C for SRF and model materials.....	98
Figure 4-7. Gas yields from the pyrolysis at 800 °C of SRF and of model materials	99
Figure 4-8. Picture of the tar impingers after a pyrolysis test.	100
Figure 4-9. Yield of tar species after pyrolysis at 800 °C.	101
Figure 4-10. Evolution of PE and PP to tar species during pyrolysis.....	103
Figure 4-11. A proposed mechanism for PET pyrolysis.....	104
Figure 4-12. Char after pyrolysis at 800 °C.	105
Figure 4-13. Molar composition of char after pyrolysis at 800 °C and of raw feedstock	105
Figure 4-14. Ratios of the EC of the product to the EC of the feedstock after pyrolysis.....	106
Figure 4-15. Experimental and calculated yields of pyrolysis products for biomass/plastic mixtures at 800 °C.....	108
Figure 4-16. Experimental and calculated distributions of initial carbon for the pyrolysis of biomass/plastic mixtures at 800°C.....	109
Figure 4-17. Char of the wood/PE mixture after pyrolysis at 800°C.	110
Figure 4-18. Comparison between the calculated and the experimental pyrolysis gas yields of biomass/plastic mixtures at 800 °C.....	111
Figure 4-19. Mass yields of gas, char and tar products and carbon distribution for the pyrolysis and gasification tests with beech wood at 800 °C.....	113
Figure 4-20. Effect of ER on gas species yields for wood at 800 °C.....	114
Figure 4-21. Effect of ER on gas yield and on cold gas efficiency for wood at 800 °C.....	115
Figure 4-22. Conversion of the initial carbon to different products in pyrolysis and gasification of SRF, of model materials and of the wood/PE mixture at 800 °C.....	117

Figure 4-23. Yields of gas species obtained from pyrolysis and gasification of SRF, from model materials and from the Wood/PE mixture at 800 °C	119
Figure 4-24. Tar yields from the pyrolysis and gasification for SRF, model materials and the Wood/PE mixture at 800 °C.....	122
Figure 4-25. Molar composition of the char produced in pyrolysis and gasification at 800 °C	125
Figure 4-26. Ratios of the EC of the product to the EC of the feedstock after pyrolysis and gasification.	125
Figure 4-27. Experimental and predicted pyrolysis yields for the five model materials	133
Figure 4-28. Experimental and predicted pyrolysis mass yields for SRF, the Wood/PE mixture and the Wood/PP mixture, with their corresponding relative error values	136
Figure B-1. Photo of the experimental setup.....	163
Figure C-1. Simulated system geometry.....	164
Figure C-2. Close up of the exchanger and sample crucible.....	165
Figure D-1. Photograph of the supplied SRF fluff.....	166
Figure D-2. Manually sorted fractions from the SRF fluff sample.....	167

List of Abbreviations and Acronyms

Artificial Neural Network	ANN
Automotive Shredder Residue	ASR
Bubbling Fluidized Bed	BFB
Carbon Conversion Efficiency	CCE
Cold Gas Efficiency	CGE
Combustibles Solides de Recuperation	CSR
Commercial and Industrial Activities	C&IW
Computational Fluid Dynamics	CFD
Construction and Demolition Waste	C&DW
Dried Sewage Sludge	DSS
Dry Ash Free Basis	DAF
Equivalent Ratio	ER
Fixed Carbon	FC
Flame Ionization Detector	FID
Gas Chromatography	GC
High Density Polyethylene	HDPE
Low Density Polyethylene	LDPE
Low Heating Value	LHV
Mechanical and Biological Treatment	MBT
Mechanical Treatment	MT
Multilinear Regression	MLR
Municipal Solid Waste	MSW
Nitrile Butadiene Rubber	NBR
Polycyclic Aromatic Hydrocarbons	PAH
Polyethylene Terephthalate	PET
Polypropylene	PP
Polystyrene	PS
Polyurethane	PU
Polyvinyl Chloride	PVC
Refuse Derived Fuels	RDF
Solid Recovered Fuels	SRF
Styrene Butadiene Rubber	SBR
Thermogravimetric Analysis	TGA
Volatile Matter	VM
Waste Derived Fuels	WDF

INTRODUCTION

With a rising population and constant evolution of manufacturing and living standards, energy and goods consumption have increased considerably in the last centuries. The fast pace of this economic and social development has caused a depletion of fossil resources, as well as an alarming increase in greenhouse gas emissions, both with negative consequences for the climate and the environment. It is then crucial to find alternative energy sources to meet the demands in a more sustainable manner.

Another consequence of elevated consumption is the constant generation of all kinds of waste, derived from daily human activities. According to the World Bank, the global generation of waste is expected to increase from 2.01 billion tons in 2016 to 3.40 billion tons in 2050 (Kaza et al., 2018). Today, more than 30% of waste ends in landfills. Several government initiatives at the local and regional levels have been launched to address this issue. The European directive (Directive 2008/98/EC), established a hierarchy for the handling of waste (**Figure 1**). This directive dictates that the most desirable action is to reduce the amount of waste generated, followed by material recovery (re-use and recycling), other forms of recovery such as energy valorization, and disposal.

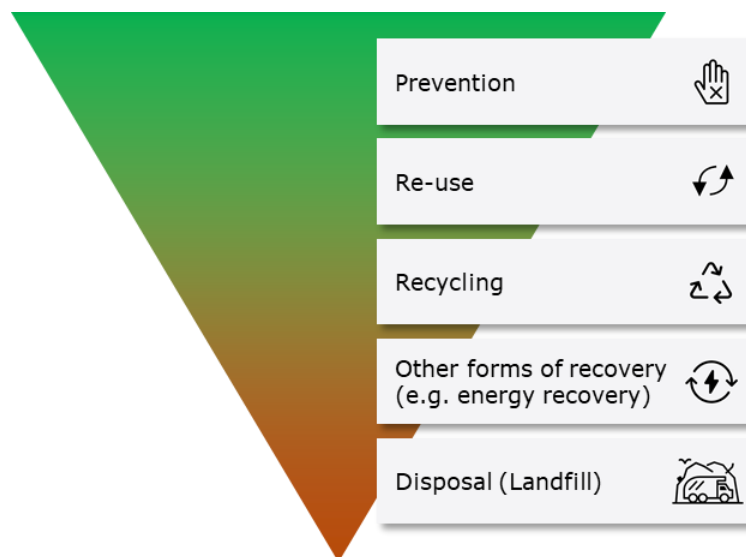


Figure 1. EU waste management hierarchy scheme.

In this context, the French law on the energy transition for green growth “*Loi de transition énergétique pour la croissance verte (LTECV)*” voted in 2015, has set its particular targets towards a circular economy. One of them, which concerns waste management, is the reduction of 50% of the amount of non-hazardous waste in landfills between 2010 and 2025. One pathway for diverting non-hazardous waste from landfills consists of its sorting and preparation for re-use, recycling or other recovery paths as described before (**Figure 1**). Waste is then processed in specialized mechanical or mechanical-

biological treatment centers. The recyclable and non-combustible fractions are removed by sorting operations like shredding, crushing and screening, while the organic fraction is separated for a biological treatment such as digestion or composting. The remaining waste fraction ends up in a “Solid Recovered Fuel” fraction, intended for energy recovery.

Solid Recovered Fuel (SRF) is produced from sorted non-hazardous solid waste fractions (paper, cardboard, plastics, wood, textiles, among others), which cannot be recycled and would otherwise be landfilled. In France, the production and use of SRF is subject to a precise legal framework. SRF have a high calorific value ($>12 \text{ MJ.kg}^{-1}$) and characteristics that allow them to be used as an energy source (to produce heat and/or electricity). Approximately 60% of the SRF content is of biogenic origin (ADEME, FEDEREC, 2019). Therefore, it can partially contribute to the substitution of fossil fuels.

The French Agency for Environment and Energy Management (ADEME) estimates that regulatory targets will lead to the production of about 5 MT per year of SRF in the country by 2050. Currently, SRF is used almost exclusively as a fuel by cement industries. The consumption target by cement manufacturers is estimated at 1.7 MT in 2050 (ADEME, 2021). Consequently, there is still large room for SRF to be used in dedicated energy production units, other than the cement industry.

Currently, most of the projects for energy recovery from SRF rely on combustion facilities such as grate furnaces or rotary kilns. In the last years, alternative processes like gasification have seen a strong development in Europe with fairly advanced technologies for the treatment of biomass and wood waste. Some industrial developers are now looking to extend their technologies to the treatment of SRF. Compared to combustion, gasification is an interesting alternative in terms of high efficiency, small pollutant emissions, and feedstock flexibility (Ribeiro et al., 2017).

Gasification is a thermochemical process in which a carbonaceous feedstock reacts above $700 \text{ }^\circ\text{C}$, in presence of an oxidizing agent. The whole gasification transformation involves several steps and mechanisms. Pyrolysis is defined as the thermal decomposition of the feedstock in the absence of oxygen and is one of the first and key steps in the gasification process. The pyrolysis products consist in light permanent gases, condensable volatiles and char. The distribution and product yields are highly influenced by the nature of the feedstock, by temperature, heating rate and residence time of the volatiles, features that are directly related to the reactor technology. Pyrolysis products participate then in secondary reactions. These transformations occur mainly by homogeneous reactions in the gas phase, and partly by heterogeneous reactions between the oxidant agents and the char.

The major gasification product is a gas, composed mainly by carbon monoxide, dihydrogen, carbon dioxide, methane and other light hydrocarbons. Its significant calorific value and composition allow the produced gas to be used in the generation of heat, electricity or value-added chemicals. Among the reactor technologies used in gasification, three main families are found: fixed beds (co-current or counter-current), fluidized beds and entrained flow reactors. They differ mainly in the way the resource is fed into the reactor vessel, the particle size range they can accept and the energy production capacity of the unit. Particular interest is given to the fluidized bed technology, as it is one of the most mature and most adapted to the characteristics of variable inputs such as SRF. Other advantages include good temperature control, good gas-solid contact and high reaction rates, due to its high internal heat and mass transfer coefficients. However, technical, economic and environmental issues must still be overcome for a large-scale industrial application of SRF gasification. Most of these challenges are linked with the heterogeneity and variability of the fuel composition, which influences the yield and quality of the produced gas (ANCRE, 2018).

The heterogeneity of shapes and low density of SRF poses a problem of flow and segregation of the load within a fluidized bed. Consequently, it is preferable to work with pellets, which induces additional costs. Previous studies (Arena & Di Gregorio, 2014b) have shown that SRF rich in plastic materials, results in a gas with high calorific value, but with a high concentration of organic pollutants (tar) and also deposits of carbonaceous material on the reactor walls. Inorganic pollutant gases (H_2S , COS , HCl , HCN , and NH_3) are formed if the fuel contains significant concentrations of S, Cl and N, which can be linked to the presence of some polymers (for example PVC for chlorine).

This work aims to elucidate the relation between SRF characteristics and its reaction products, and thus to have a better comprehension of its thermal conversion. The approach chosen to tackle the SRF heterogeneity is to investigate the behavior of its components. Model materials that represent the most common waste fractions used in the production of SRF have been selected. Then, mixtures of biomass and plastics have been studied in order to explore their interactions. The selected resources were studied under controlled pyrolysis and gasification conditions. For this purpose, we have developed a laboratory setup adapted to collect and analyze the reaction products. Special attention has been given to the distribution and concentration of the main gaseous products, char and condensable organic pollutants (tar). The experimental data have been used for the development of an empiric correlation to predict the main pyrolysis products of SRF by only using its initial chemical composition.

This present manuscript is organized into 4 chapters, completed by the introduction and conclusion:

Chapter one provides a review of the literature to understand the topics covered in this thesis. First, an overview of solid waste and its derived fuels is presented. Then, the research status on pyrolysis and gasification of waste derived fuels and their main components is discussed. Finally, the detailed objectives and the methodology of the thesis are presented.

Chapter two describes the experimental setup. First, the induction-heated reactor specially designed for this thesis research is introduced. Then, the components of the experimental setup are described in detail. The thermal characterization of the reactor is presented in the third section of this chapter.

Chapter three presents the rationale behind the choice of the model materials to represent SRF, along with their characterization. The experimental procedures and the operating conditions used for the pyrolysis and gasification tests are explained. The methods used to quantify and characterize the reaction products are also described.

Chapter four, presents and discuss the experimental results obtained in the laboratory scale setup. First, an analysis of the evolution of the sample temperature and the flow of volatilized matter produced during pyrolysis is presented. The distribution and analysis of the products generated in the pyrolysis of the SRF and model materials at 800 °C is presented next. Experimental results for biomass and plastics mixtures are compared with the linear sum of each individual materials, to assess their interaction during its co-pyrolysis. Then, the influence of the addition of an oxidant agent (air) as in gasification conditions is studied. Finally, the empirical correlation developed to predict the pyrolysis yields of SRF from its initial composition is described. The accuracy of the predicted results is discussed.

Conclusion and perspectives: The conclusions deriving from the results obtained in this work are discussed, and perspectives regarding future work on the pyrolysis and gasification of SRF are proposed. Some improvements to the laboratory-scale facility that was developed in this study are also proposed.

1. LITERATURE REVIEW

The valorization of solid waste by thermochemical processes is a promising alternative to landfilling. It also has the potential to replace some fossil fuels in industrial applications. In the first section of this chapter, an overview of solid waste, its derived fuels and their main components is made, emphasizing their chemical composition and thermal behavior. The second section makes a global presentation of the gasification process, from the phenomena taking place in gasification to the gasification reactors, so as the process main parameters. The state of the current research on pyrolysis/gasification of SRF and its components is discussed, especially at the laboratory scale. Finally, a brief assessment on modeling approaches for the prediction of reaction products and their yields is discussed. The conclusions of this review serve to establish the methodology to be followed in this study, especially the design of the experimental device, the experimental protocol and the analysis of our results.

1.1 Solid waste and its derived fuels

1.1.1 Solid waste

Solid waste is defined as any unwanted or discarded material arising from human or animal activities. Waste streams can come from households and communities, commercial and industrial activities, construction and demolition, but also many other sources (Saghir et al., 2018). Solid waste streams and their sources are summarized in Table 1-1.

Waste stream	Origin	Production (kg per capita and per day)
Commercial & industrial waste (C&IW)	Commerce and industries, rejects of manufacturing, paper mill sludges, end of life vehicles	12.73
Construction and demolition waste (C&DW)	Civil and road infrastructure	1.68
Municipal Solid Waste (MSW)	Residual household waste, small businesses waste	0.7
Agricultural waste	Farming, cultivation, livestock production, aquaculture residues	3.35
Hazardous waste	Mining; chemical industries, military bases, nuclear and power plants, medical waste, electronic waste	0.59

Table 1-1. Classification of solid waste based on its source (Kaza et al., 2018; Ramos et al., 2018).

Raw waste streams can be treated in mechanical, or mechanical and biological treatment facilities (MT/MBT). The aim of this pretreatment is to separate the waste into fractions according to their type of valorization. For example, recyclable materials are sorted out to be used in the manufacture of new products. Wet putrescible fractions like food or garden waste are usually separated to be used in composting or digestion processes due to its high moisture content and biodegradability.

Concrete, glass, or minerals are not desired in energy recovery since they have no calorific value. Food and kitchen waste are also undesirable because of their high moisture content as well as their high content of minerals. Difficulties associated with the use of these fractions for energy production are low thermal output, high ash clinker formation, and high pollutant emissions (Zaini et al., 2019). This represents high costs, since sub products and pollutants can represent an environmental risk if they are not correctly disposed. In this work, we are interested in combustible solid waste materials

with high calorific content ($>10\text{MJ}\cdot\text{kg}^{-1}$), which are usually used in the production of refuse-derived fuels. Special waste streams (nuclear, medical or electronic waste) are excluded from the scope of interest because of their different processing needs or specific risks, requiring dedicated collection and handling protocols.

1.1.2 Waste derived fuels

Waste can be used directly in thermal valorization or pretreated to improve its homogeneity and heating value. Waste derived fuels (WDF) are produced from residual fractions from MT/MBT facilities and from other high calorific materials coming from industry, which do not require most of the steps followed in municipal waste treatment. Some examples are packaging, furniture, and textile waste, dried sewage sludge (DSS) coming from wastewater treatment plants, plastic and paper waste coming from industry rejects, automotive shredder residue (ASR) and tires coming from end-of-life vehicles.

Pretreatment operations are diverse and can include size reduction, magnetic and optical sorting, among others (Nasrullah et al., 2017). Additional processing steps like screening or pelletization can be implemented to produce a fuel with more consistent physical and chemical characteristics (Luque & Speight, 2015). An ideal solid waste fuel can be handled, transported or stored safely, which facilitates its use in an industrial process. In comparison with raw unsorted waste, WDF are expected to have higher heating values and a lower content of pollutants.

The very heterogeneous nature of solid waste and the lack of regulation during production results in fuels of very different qualities and characteristics. Along the years, waste derived fuels have received many denominations, usually confusing and misused in literature. The most common terms and standards are listed below:

- Refuse Derived Fuel (RDF) is a solid fuel produced from mechanical and biological treatment facilities (MBT) of non-hazardous waste sources such as MSW, or commercial and industrial waste. Its lower heating value (LHV) lies between 8 and 14 $\text{MJ}\cdot\text{kg}^{-1}$ (AMEC, 2013). Regulatory efforts have resulted in local standards, principally for the incineration and cement industry in the USA (ASTM E856-83) and Italy (UNI 9903-12004).
- Solid Recovered Fuel (SRF) is a solid fuel prepared from non-hazardous waste to be utilized for energy recovery in incineration or co-incineration plants. It must meet the classification

and the specification requirements laid down by the European Committee for Standardization (CEN) in the EN 15359 standard (*Solid Recovered Fuels*, 2006). Depending on its composition, SRF usually has a lower heating value (LHV) between 10 and 25 MJ.kg⁻¹ (Iacovidou et al., 2018). The EN15359 standard makes a quality classification of SRF according to their LHV, Cl and Hg contents (**Appendix A**). A new regularization effort is being undertaken by an international committee (*ISO/TC 300 - Solid Recovered Materials*), and is expected to be completed in 2022. The scope of this new standard includes the characterization of chemical and physical characteristics, sampling methods, as well as storage and safety recommendations.

- The term << *Combustibles Solides de Recuperation (CSR)*>> is geographically limited to France, and usually describes SRF and derived fuel that respect specifications and quality requirements of the ministerial decree 630 of May 23 -2016: *fuels for heat/energy production in classified installations* (ICPE 2971, AIDA). Compared to the European standard, the specifications are stricter regarding the calorific value (LHV > 12MJ.kg⁻¹), and the maximum permitted levels of halogens. Concentration limits concern of Hg (3 mg.kg⁻¹), Cl (15 000 mg.kg⁻¹) and Br (15 000 mg.kg⁻¹); sum of the three shall not be greater than 20 000 mg.kg⁻¹.

The different terms related to waste and waste derived fuels are summarized in **Figure 1-1**.

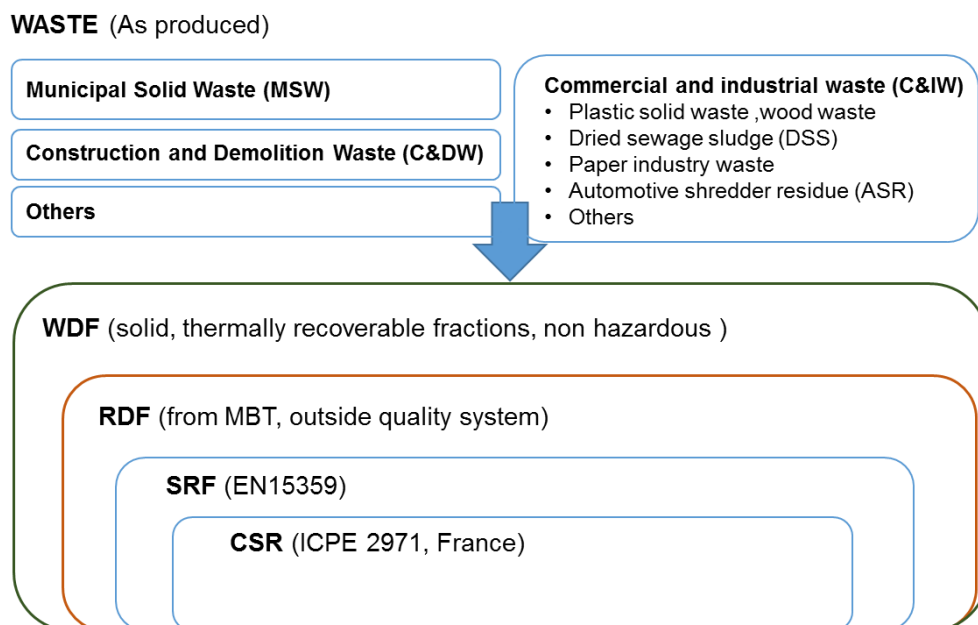


Figure 1-1. Terminology used for waste sources and waste derived fuels.

SRF is characterized and classified according to current European standards of CEN. The material content can be obtained by manual sorting, following the EN15413 standard. Proximate analysis refers to the measurement of moisture content (EN 15414), ash content (EN 15403), and fixed carbon (FC) and volatile matter (VM) contents (EN 15402). The elemental analysis (known as ultimate analysis) gives in particular the content of carbon, hydrogen, nitrogen and sulfur (EN 15407). Composition can be expressed on as-received, dry, or dry ash free (daf) basis. These representations are shown in Figure 1-2.

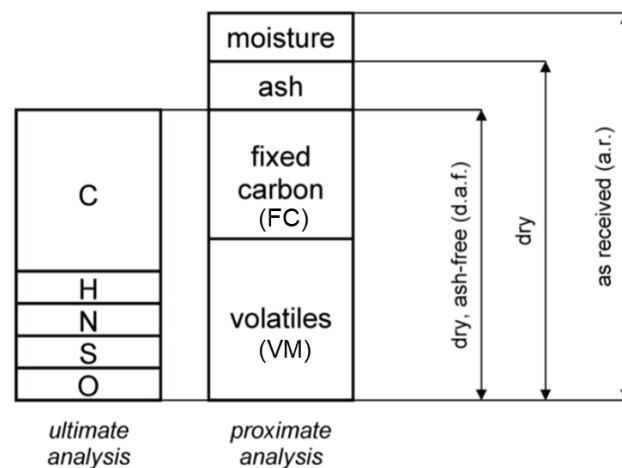


Figure 1-2. Bases used to represent solid waste fuels composition (Siedlecki et al., 2011)

The properties and chemical analysis of diverse SRFs produced from diverse sources are presented in more detail in several publications such as (Nasrullah et al., 2017; Ramos Casado et al., 2016). SRF is partly composed of fossil origin materials, and of biogenic origin ones representing approximately 50 to 70 wt.% (ADEME, FEDEREC, 2019). The physical and chemical characteristics of SRF can vary significantly depending on its origin. For this reason, it is important to identify the material content of the fuel, so as to be able to evaluate the impact of each of its individual components on its properties.

1.1.3 Material content of solid recovered fuels

The material content of SRF depends on the nature of the waste sources, which are heavily influenced by local climate, lifestyle, and economic level (Zhou, 2017). The nature of the consumed goods, the collection and recycling practices as well as the waste management solutions are different between developed and low income countries (US EPA, 2017). Another parameter that influence the content of the SRF is the choice and order of pretreatment operations used during its production (Velis et al., 2013).

Materials in waste derived fuels can be easily classified into biogenic materials (paper, cardboard, wood) and fossil derived materials (plastics, elastomers). Textiles and composite objects are made from raw materials that can come from biogenic or fossil sources. (Porshnov, 2022) identified the most prevalent fractions in waste derived fuels after the identification of the material composition of SRF from several studies around the world. These results are shown in **Figure 1-3**.

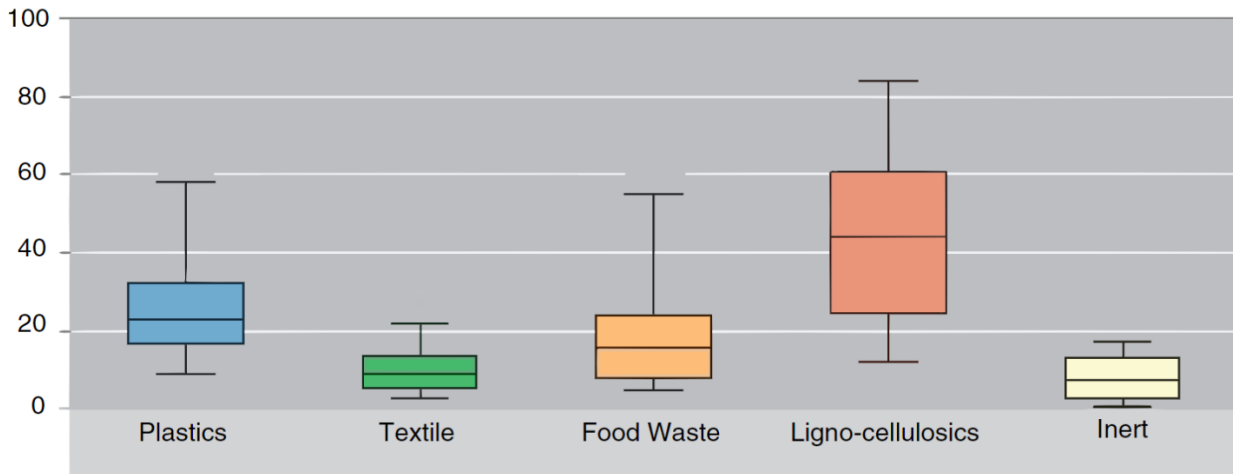
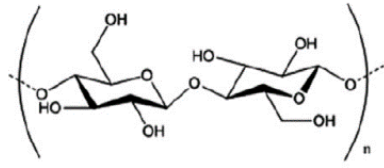


Figure 1-3. Mean material composition of SRF (Porshnov, 2022).

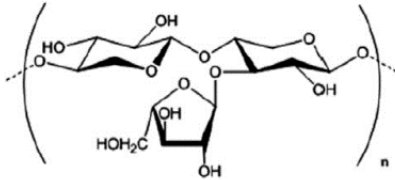
The most prevalent part in SRF gathers lignocellulosic materials like paper and wood (between 30 and 60 wt.%), followed by plastics (20-30 wt.%), and textiles (10-15 wt.%). The high variation of the mass fraction for each category in **Figure 1-3** is evidence of the heterogeneity of fuel composition between producers. In addition to the differences between the main fractions found in solid recovered fuels, the characteristics of the different materials within these categories can also vary. For example, the “plastic” fraction gathers different polymers with distinct properties and chemical structures. In the following sections, data on the proximate analysis, ultimate analysis and calorific value of the most popular materials in each of the fractions recovered in SRF is presented.

1.1.3.1 Biogenic materials

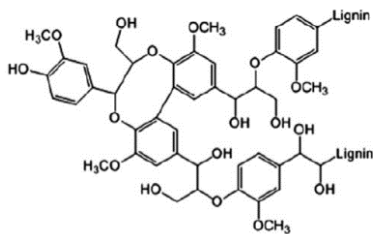
Wood, agricultural residues, paper, cardboard, and textiles made of some natural fibers such as wool and cotton are mainly composed of biopolymers: cellulose, hemicellulose, and lignin. These materials come from renewable sources and represent the biogenic fraction in derived fuels.



Cellulose ($C_6H_{10}O_5$)_n is a linear homopolymer consisting of β -glucose units linked together by 1-4 bonds. It presents a high degree of polymerization ($n=500-4000$). Is the structural basis of plant cells, and the major component of lignocellulosic materials.



Hemicellulose is a second structural polymer, consisting in a mixture of hexose and pentose sugars, forming shorter chains ($n = 50 -200$) and with a branched structure.



Lignin is a set of complex three-dimensional polymers constituted from aromatic phenol derivatives. It acts as a binder compound and provides stability and hydrophobicity to the plant membranes.

These biopolymers can be present in different proportions as shown in **Figure 1-4** (on dry basis).

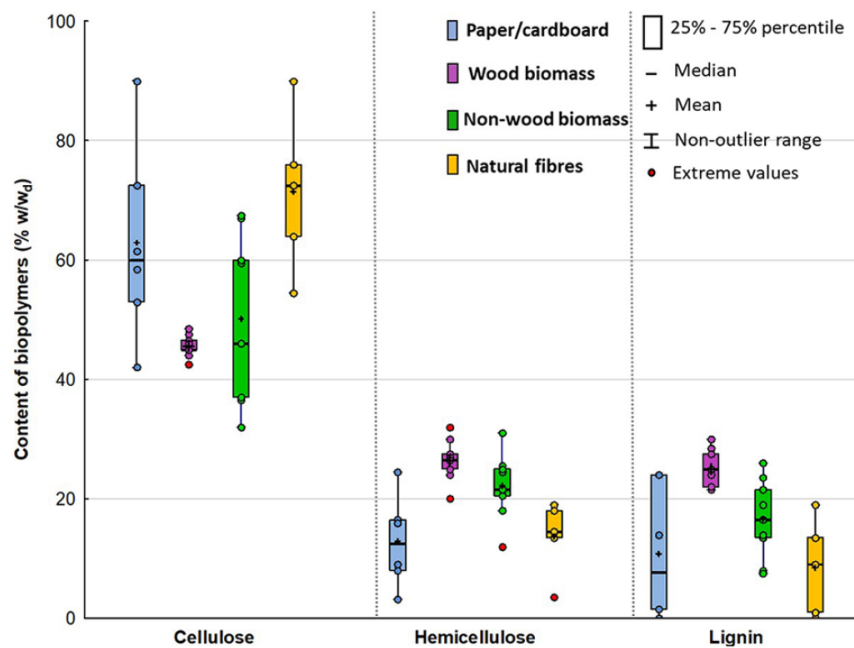


Figure 1-4. Typical content of biopolymers in lignocellulosic fractions of SRF (Gerassimidou et al., 2020).

1.1.3.1.1 Woody biomass

Wood fraction in waste can come from various sources. These include leftovers from forestry and commercial timber exploitation (stumps, crowns, branches, leaves, sawdust, and bark), end of life products and packaging (households and urban construction/demolition streams). Woody biomasses can be classified into hardwood (oak, beech, poplar) and softwood (pine, spruce). Softwood generally has a higher lignin content (26–34 wt.%) than hardwood (23–30 wt.%). Besides cellulose, hemicellulose and lignin, biomasses can also include small quantities of other organic and inorganic compounds.

The chemical composition of different types of wood and wood waste can be found in Table 1-2. Wood waste differs from raw wood especially because of the higher concentration of nitrogen, usually coming from paint, adhesives, and additives like formaldehyde-based resins, used in construction and furniture wood (Czajczyńska et al., 2017).

Type	LHV MJ.kg ⁻¹	Proximate analysis (wt.% dry)			Ultimate analysis (wt.% dry)					
		Ash	V	FC	C	H	O	N	S	Cl
Hard wood	16.6	0.5	82.5	17.0	49.5	6.2	41.2	0.4	-	-
Soft wood	16.3	1.7	80.2	18.1	51.9	6.1	40.9	0.3	-	-
Construction wood	16	13.96	72.17	11.03	37.95	4.43	55.62	1.45	0.55	-
Furniture wood	15.8	1.8	77.3	20.9	47.9	6	41.4	2.9	0.05	0.06

Table 1-2. LHV, ultimate and proximate analyses of different types of wood and wood waste (Demirbas, 2004; Kim et al., 2014; Moreno & Font, 2015; Zhou, Long, et al., 2015).

1.1.3.1.2 Paper and cardboard

This type of materials is widely used in packaging (cardboard, wrapping, paper cups), printing industry (advertising, office paper, newspaper, magazines) and many other sectors. Paper and cardboard present higher cellulose and lower lignin content when compared with woody biomass (Figure 1-4). They present also a lower fixed carbon content.

In addition to the main three components, paper and cardboard contain some extractives and inorganic fillers, which come from pigments, binders and chemical additives used in the production process. CaCO₃ is commonly used during office white paper manufacturing, while clay is used as a coating agent in glossy paper production. Tissue paper can present high contents of nutrients and

halogens (K, Na, Cl, F, Si) from contamination with wet organic material like food residues (Götze et al., 2016). Some examples of papers found in waste and their chemical composition are listed in Table 1-3.

		Proximate analysis (wt.% dry)			Ultimate analysis (wt.% dry)					
Type	LHV MJ.kg ⁻¹	Ash	V	FC	C	H	O	N	S	Cl
Office	11.83	10.69	79.33	9.98	45.12	5.31	48.91	0.09	0.28	0.17
Newspaper	15.67	5.42	82.35	12.24	46.70	6.28	46.37	0.17	0.18	0.15
Glossy	10.4	28.0	67.3	4.7	45.6	4.8	49.41	0.14	0.05	-
Tissue	16.8	0.04	95.36	4.60	44.31	6.06	49.43	0.13	0.06	-
Cardboard	16.9	8.4	84.7	6.9	48.6	6.2	44.96	0.11	0.03	0.15

Table 1-3. LHV, ultimate and proximate analysis of different types of paper (Sørum et al., 2001; Zhou et al., 2014a).

1.1.3.1.3 Other biogenic materials

Clothing and textiles found in waste can be composed of fibers coming from plants (cotton, hemp) mainly composed by cellulose (80-90%). Protein fibers produced from animals (wool, silk, leather) are less common, and they present higher N and S contents compared to cellulosic fibers.

Natural rubber (latex) is an elastomer obtained from the milky white fluid latex, which is an emulsion of cis-1, 4-polyisoprene and water. It is widely used in the manufacture of footwear, latex and many other products, which benefit from its high elongation, flexibility, and elasticity. The composition for some of these other biogenic materials is listed in Table 1-4.

		Proximate analysis (wt.% dry)			Ultimate analysis (wt.% dry)					
Type	LHV MJ.kg ⁻¹	Ash	V	FC	C	H	O	N	S	Cl
Cotton	17.1	1.05	87.93	11.01	47.5	6.3	45.1	0.82	0.13	0.65
Wool	22.76	1.24	84.76	14.0	59.3	5.36	24.8	8.89	1.60	-
Natural Rubber	42.01	0.08	98.17	0.5	87.9	10.8	0.41	0.75	0.01	-

Table 1-4. LHV, ultimate and proximate analysis of other biogenic materials (Wei et al., 2019; Zhou et al., 2014a).

1.1.3.2 Fossil based materials

Fossil waste materials include light and dense plastics, foams and elastomers composed by one or various polymers derived from the petrochemical industry. High carbon and low moisture content make plastics highly energy dense materials. Main differences between these polymers are in their chain structures and dissociation energy of bonds, which defines their thermal stability (Al-Salem et al., 2017).

1.1.3.2.1 Plastics

(Gerassimidou et al., 2020) established an indicative content of the most common plastics in RDF/SRF by comparing data of incoming from the industry and waste streams. Their results are displayed in Figure 1-5. Most common polymers are PE and PP, followed by PET, PVC and others like polystyrene and polycarbonate.

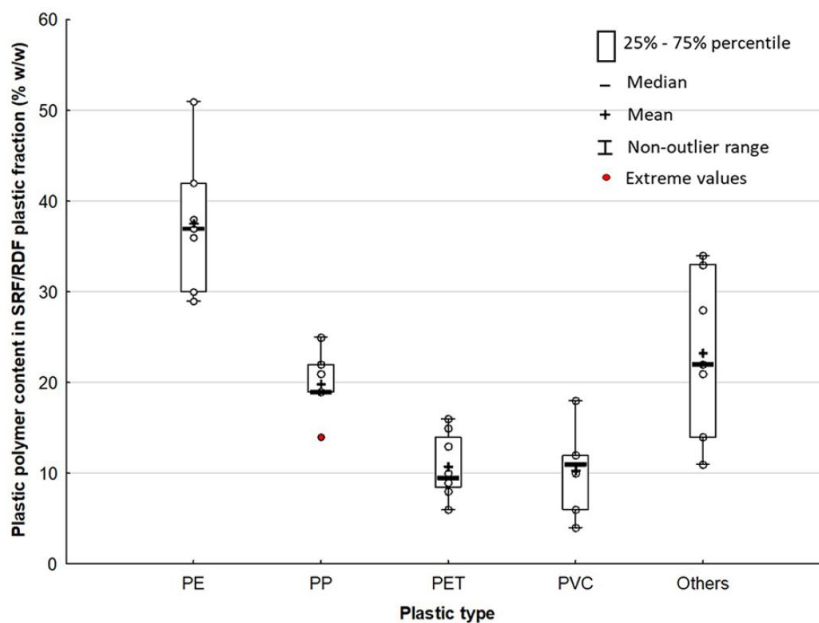
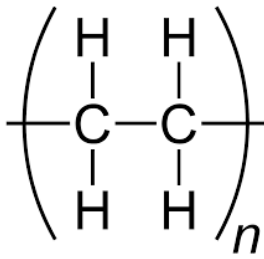


Figure 1-5. Most prevalent plastic polymers in solid recovered fuel (Gerassimidou et al., 2020).

The term “soft plastics” refers to flexible materials commonly found in packaging bags, wraps, and include polymers like low density polyethylene (LDPE) or polypropylene (PP). “Hard plastics” refers to rigid materials such as high-density polyethylene (HDPE) polyethylene terephthalate (PET), polyvinyl chloride (PVC). All these polymers are thermoplastics, which means, plastic resins whose form and viscosity can be modified under the influence of heat. They represent 80% of the total production of plastics and in most cases can be recycled after grinding and washing (Lopez et al., 2018a).

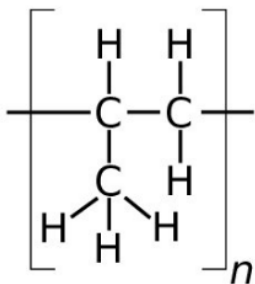
In the “hard plastics” category are also included thermoset plastics, known because they are irreversibly cross-linked during manufacture and cannot be melted or reformed. Examples of thermoset plastics are epoxy resins, silicones, vinyl esters and rigid polyurethanes. They are commonly used in automotive, engineering and electronic sectors. The elevated contents of flame retardants and other fillers leads to the formation of more char than with thermoplastic materials. They contain a high fraction of oxygen or nitrogen, and in some cases halogens (Cl, F, Br) which can lead to the formation of toxic byproducts (King, S. et al., 2021). The most common plastic polymers in SRF are described next.

Polyethylene (PE)



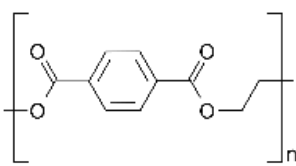
Produced from ethylene, its structure consists essentially in a long chain of aliphatic hydrocarbons. HDPE (high density) has no side chains, allowing to pack more molecules into the same amount of space. It is found in bottles, containers, toys, etc. LDPE (low density) has more branching that results in weaker intermolecular force, making it more flexible. It is used in the production of plastic bags or wrapping foils.

Polypropylene (PP)



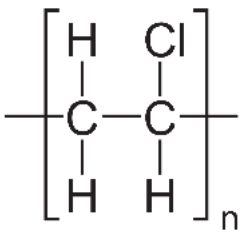
Polypropylene is an aliphatic saturated polymer coming from propene, with a methyl group (CH₃) in the repeating unit. It is known for its chemical and heat resistance (melting temperature above 160 °C). It is used in carpet fibers, medical and kitchen appliances.

Polyethylene terephthalate (PET)



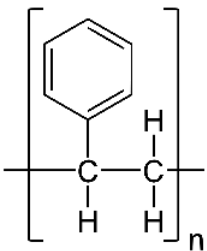
PET is a linear polymer synthesized from ethylene glycol, with oxygen-containing functional groups that make it polar. Its particular characteristics (light weight, pressure resistance) have made it the main choice for beverage packing. It is also used in the production of clothes, films and electronic components.

Polyvinyl chloride (PVC)



In PVC the methyl group of PP is substituted with chlorine (Cl). The chlorine (above 50% in mass) gives to PVC an excellent fire resistance, which is thus very suitable for electrical insulation. The supple form is used in coated textiles, insulation, cables and adhesive tapes. The rigid form is widely used in construction (sanitation pipes, windows).

Polystyrene (PS)



PS is made from the styrene monomer, which repeating unit contains a benzene ring. PS can be found in crystal form (being particularly rigid and fragile, in high-impact PS form, and expanded PS one (usually used in food packaging and insulation).

The ultimate and proximate analyses of the most common plastics are listed in Table 1-5.

Type	LHV MJ.kg ⁻¹	Proximate analysis (wt.% dry)			Ultimate analysis (wt.% dry)					
		Ash	V	FC	C	H	O	N	S	Cl
HDPE	41.24	0.60	99.40	0.00	85.50	14.20	0.00	0.00	0.30	0.00
LDPE	41.81	0.30	99.70	0.00	85.50	14.30	0.00	0.00	0.20	0.00
PP	42.42	0.44	99.54	0.03	85.02	13.93	0.96	0.08	0.01	0.00
PET	21.28	0.20	92.27	7.53	62.30	4.43	33.13	0.09	0.05	0.26
PVC	20.85	5.86	83.47	10.67	39.56	4.85	0.02	0.11	0.28	55.18
PS	39.52	0.19	99.48	0.33	90.37	8.64	0.90	0.00	0.09	0.00

Table 1-5. LHV, ultimate and proximate analysis of most common plastics (Götze et al., 2016; Zhou et al., 2014a).

1.1.3.2.2 Other fossil derived materials

Polyester (PET fibers) accounts for more than 80% of the total production of synthetic fibers used in textiles (Kwon et al., 2021). Other fossil derived materials in textile waste include acrylic and nylon.

Foams found in waste consist in rigid and flexible materials mostly made from polyurethane (PU).

The main difference between polyurethanes and other polymers consists in its nitrogen content, which

is about 6 wt.%, while for other plastics it is usually under 0.1 wt.% (Table 1-6). The high N content in foams is due to the fact that different amino-based catalysts are used during its production.

Synthetic rubbers are produced by polymerization of fossil-based monomers. Vulcanization allows to convert the polymer chains into a network structure by the formation of cross links: This is possible using simultaneous pressing and heating, with the help of a vulcanization agent (usually sulfur). This modification gives increased strength, elasticity, and resistance to temperature, chemicals and abrasion (S. Liu et al., 2018). Most common examples of synthetic rubbers are styrene-butadiene-rubber (SBR), nitrile butadiene-rubber (NBR) and butadiene rubbers (BR). They are principally used in the manufacture of tires, tubes, among other elastomers. The composition of some of this fossil derived materials is listed in Table 1-6.

Type	LHV MJ.kg ⁻¹	Proximate analysis (wt.% dry)			Ultimate analysis (wt.% dry)					
		Ash	VM	FC	C	H	O	N	S	Cl
Nylon waste	35.54	1.1	96.5	2.5	68.0	10.7	16.6	4.7	0	-
Acrylic waste	29.77	0.3	80.9	18.6	66.2	6.0	4.9	22.9	-	-
PU waste	29.06	5.11	82.78	10.28	67.96	6.75	16.18	7.01	-	0.15
Butadiene Rubber	-	0.2	99.7	0	89.3	10.3	0.1	0.1	3.7	-
Styrene Butadiene Rubber	39.5	0,13	98.81	0.67	89.14	10.5	0.09	0.08	0.17	-

Table 1-6. LHV, ultimate and proximate analysis of other fossil derived materials (Nahil & Williams, 2010; Stančin et al., 2019; Q. Yang et al., 2021; Zhou et al., 2014a).

1.1.4 Energy valorization of SRF

1.1.4.1 Thermochemical conversion routes for SRF energy valorization

Since SRF is made from materials with high calorific value, thermochemical conversion processes are the preferred routes for energy recovery. Initially, SRF used to be burnt in incineration facilities. The sole purpose of this type of installations was to burn waste and reduce its volume. In recent years, this trend has changed, and SRF is now used in combustion processes with an objective of energy recovery. Industrial sectors with high energy demands (e.g. the cement industry and thermal power plants) are the actual main users of secondary fuels, as a full or partial substitute for coal or other fossil fuels (RECORD, 2018).

Alternative thermochemical routes like pyrolysis and gasification are receiving interest, since they present various advantages when compared to combustion, such as lower harmful gaseous emissions, and high energy recovery efficiency (You et al., 2018). Products from pyrolysis and gasification can be used in several applications as opposed to hot combustion gases from incineration (Saghir et al., 2018). These processes differ by their operating conditions, and by their end products. Torrefaction involves heating the solid fuel in an inert or oxygen-poor environment in the temperature range of 200–300°C. The result is a coal-like material, which has better fuel characteristics than the original. **Table 1-7** compares the main characteristics of these transformations.

In combustion, the aim is to fully transform the chemical energy present in the fuel into sensible heat by obtaining a gas at high temperature. To achieve this, the oxygen is fed in excess in relation to the stoichiometric amount. Pyrolysis, on the other hand, is a thermal decomposition process in the absence of oxygen. It can be used as a stand-alone process for the production of intermediate products that can then be transformed into fuels and/or chemicals. It is also present in the initial stages of a gasification or combustion process. In gasification, the carbonaceous feedstock is transformed at high temperature (above 700 °C) in the presence of an oxidizing agent (air, oxygen, carbon dioxide, steam or a combination of these), fed at levels below the stoichiometric amount required for total oxidation. The result is a gas composed mainly of carbon monoxide, dihydrogen, carbon dioxide and some light hydrocarbons. The produced gas can be used in the generation of heat, electricity or value-added chemicals, but its tar content makes these applications difficult.

Process	Aim	Temperature	Atmosphere /Medium	Pressure	Gas Products	Byproducts
Pyrolysis	Conversion of the fuel into several products (char, tar, gas)	300 – 800 °C	Inert	Vacuum /1 bar	H ₂ , CO, CO ₂ , CH ₄ and other hydrocarbons	H ₂ S, HCl, NH ₃ , HCN, tar, and particulate
Gasification	Partial oxidation of the fuel to high heating value gas (CO, H ₂ , and CH ₄)	700 – 1500 °C	Partially oxidizing	1 to 45 bar	H ₂ , CO, CO ₂ , H ₂ O, CH ₄ and other hydrocarbons	H ₂ S, HCl, NH ₃ , HCN, COS, tar, particulate
Combustion	Complete oxidation of the fuel to high-temperature flue gas, mainly CO ₂ and H ₂ O	850 – 1200 °C	Oxidizing (in excess of oxidant agent)	1 bar	CO ₂ and H ₂ O	CO, SO _x , NO _x , HCl, PAHs, PCDD/Fs, particulate
Torrefaction	Conversion of the fuel into coal-like material	200 – 300 °C	Inert	1 bar	CO, CO ₂ , CH ₄	H ₂ S, NH ₃ , COS, HCN, CS ₂
Hydrothermal (HT) processing	Converting wet fuel into hydrochar (HT Carbonization) crude-like oil (HT Liquefaction) gas (HT Gasification)	HT Carbonization: 180 – 250 °C HT Liquefaction: 250 – 374 C HT Gasification: >375 °C	Aqueous medium	50 to 250 bar	H ₂ , CO, CO ₂ , CH ₄ and other hydrocarbons	Inorganic salts, Coke, tar

Table 1-7. Main characteristics of thermochemical processes for solid waste thermal treatment (Arena, 2012; Zhou, 2017).

Hydrothermal processes (Carbonization, liquefaction, and gasification) are preferred for treating fuels with high moisture content. They make use of high-pressure conditions to obtain a fuel with a high energy density.

1.1.4.2 Influence of material content of SRF on its energy valorisation

By analyzing the chemical composition and the material content of each SRF, some authors have established qualitative relationships with the behaviour of the SRF during its thermochemical conversion, principally in combustion. This can help producers to adjust the formulation of their fuels, to meet the required limits and avoid technical problems during its conversion (FEDEREC, COMPTE-R, 2015b; Götze et al., 2016b; Nasrullah et al., 2017b; C. Velis et al., 2012; C. A. Velis et al., 2013b). However, these observations can also be applied to emerging technologies such as pyrolysis and gasification. The common findings of these studies have been summarized in Table 1-8.

Properties	Materials in waste	Impact on thermochemical conversion
Heating value	Favored by the presence of plastic films, packaging plastic, rubber or tires. Affected by the presence of inert materials.	Increase of heating value of the fuel its beneficial for the economics of the process
Ash content	Fillers from paper and cardboard, glossy paper Soil and minerals from construction waste Fine fractions	Particulate matter, fouling deposits, agglomeration, deposition
Moisture	Moisture content may increase due to the presence of foams, textiles and papers, which can absorb liquids if in contact with food waste or oils. Undried sewage sludge.	Reduction of final heating value, producer gas quality and fuel conversion
N content	Food waste, Polyurethane foams, acrylic fibers, wool, waste wood additives	Mainly transformed into NH ₃ , HCN: influence in the sizing of gas cleaning sections
S content	Rubber and waste tires	Mainly transformed into H ₂ S, COS: Interaction with alkali metals: emissions, deposits, corrosion Deactivation of downstream catalysts
Cl content	PVC hard plastics, certain kinds of paper, vinyl rubber, shoes, Kitchen waste	Mainly transformed into HCl, Cl ₂ : Dioxides and furans emissions, corrosion, ash sintering
Other halogens content (Br, F)	Brome from flame retardants Fluor for halogenated polymers	Production of undesired pollutants like HBr and HF
Si and P content	Paperboard, rubber	Inhibitory effect Agglomeration issues, erosion of equipment
K, Na content	Food residues	Catalytic effect, agglomeration issues, lowering of ash melting temperatures
Ca,	Paper, cotton	Catalytic effect, increase of ash melting temperature
Hg content	Synthetic textiles, soft plastic, foam, electronic waste	Undesired emissions
Other heavy metals content	Tissue and plastic pigments, electronic waste, wires	Undesired emissions, ash disposal costs
Tar content	Favored by the presence of lignin, and plastics	Production of aromatics, and polycyclic aromatic hydrocarbons (PAHs) which result in equipment blockage, lower efficiency and increased maintenance

Table 1-8. Influence of materials on solid waste fuels properties and impact on thermochemical conversion.

1.2 Phenomenological and technical description of the gasification process

In this work, we are mostly interested in gasification as a promising route for energy valorization of SRF. High temperature pyrolysis is also of interest since it plays an important role as a preliminary step in the gasification process. The generalities of the gasification process are given in the following sections.

1.2.1 Thermochemical phenomena of gasification

The transformation of a solid fuel through gasification involves several steps and mechanisms. In practice, there is no clear boundary between these different stages; so they can occur simultaneously. Each of the steps is shown in Figure 1-6 and described below:

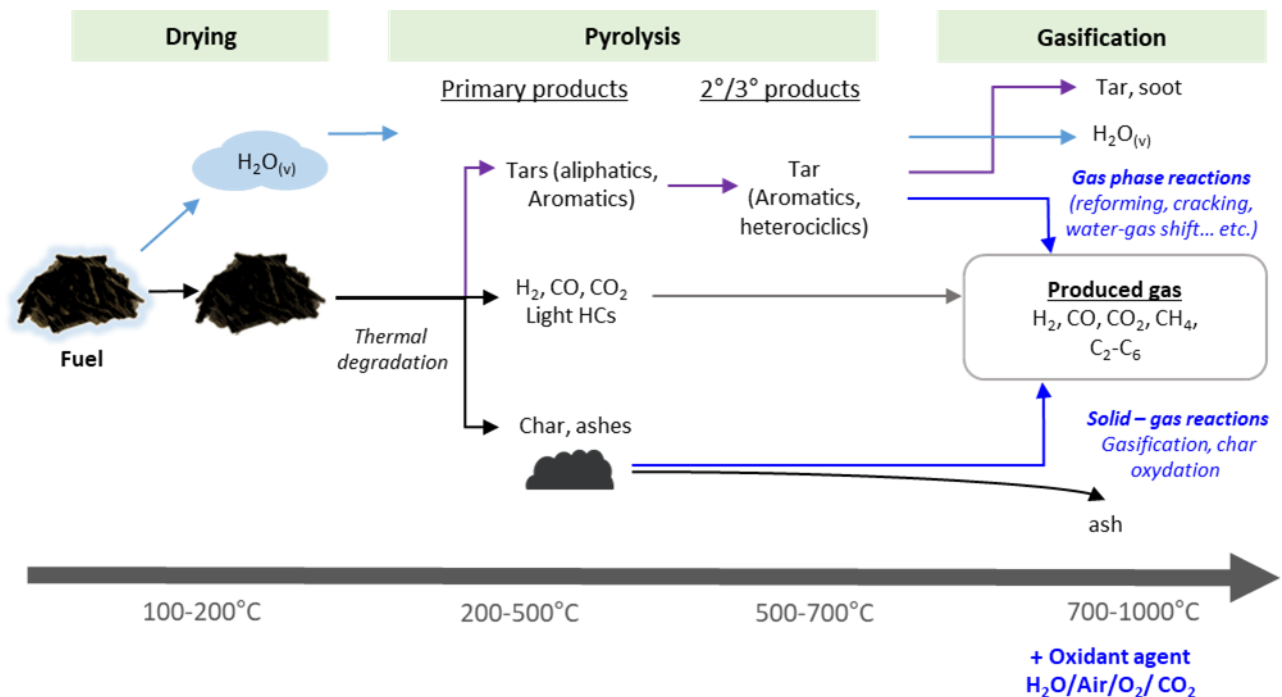


Figure 1-6. Thermochemical phenomena involved in gasification.

Drying: The moisture contained in the feedstock is converted into steam at temperatures between 100-200 °C. At this step, no chemical reactions take place.

Pyrolysis: is the thermal decomposition of the carbonaceous materials in the absence of oxygen. The devolatilization is an endothermic process and occurs in the temperature range of 200 to 700 °C. As a result, three phases are produced: a solid fraction mainly composed of carbon (char), a gaseous fraction formed by non-condensable light gases, and a liquid fraction consisting of a mixture of water and

heavy hydrocarbons (known as tar and defined as organic compounds with a molecular weight higher than that of toluene).

The repartition between three phases depends on the feedstock and on the main operating conditions, in particular the temperature, the residence time and the heating rate (Souza-Santos, 2010). Depending on the temperature and gas residence time, the primary volatile products participate in secondary reactions in the gas phase. Tar species are highly reactive and they usually evolve in more complex molecules, so called secondary and tertiary tars (Wilk & Hofbauer, 2013). The distribution of products as a function of the pyrolysis conditions is shown in **Figure 1-7**.

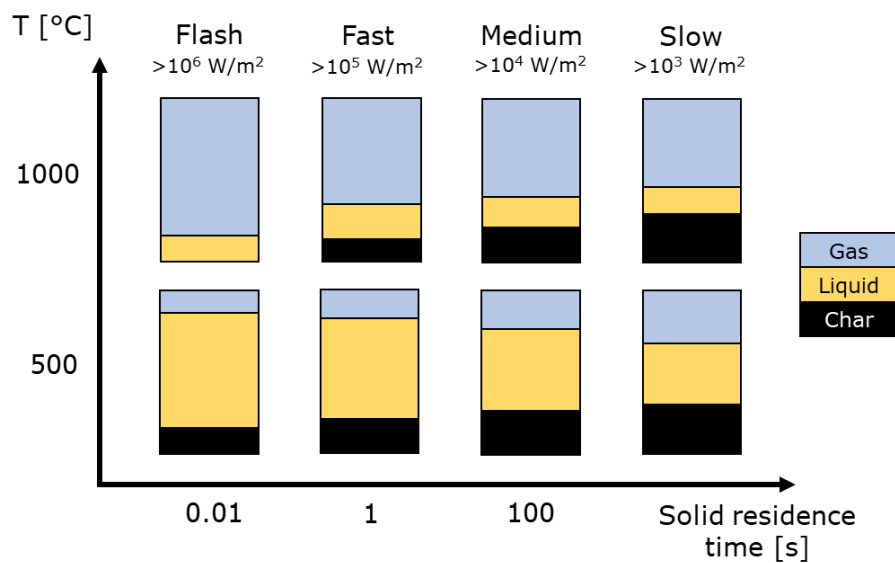


Figure 1-7. Pyrolysis conditions and their effect on product distribution. Adapted from (Deglise and Donnot, 2004).

In slow pyrolysis, low temperatures, slow heating rates (between 0.01 and 2 °C/s) favor the production of a carbonaceous solid. However, this solid still contains most of the pollutants initially present in the waste. In fast pyrolysis, high heating rates (>100 °C/s) and moderate temperatures (400-650 °C) generate large amounts of liquid. Flash pyrolysis, involves higher temperatures and heating rates (100 – 10000 °C/s), which results in a higher amount of gas due to the more intense cracking of the volatiles (Runchal et al., 2018).

Gasification: Above 700 °C and in presence of the gasifying agent, the pyrolysis products participate in several oxidation and reduction reactions, which can take place in the same reactor or in a subsequent one (Block et al., 2019). The main reactions which take place during gasification are listed in **Table 1-9**, in which C represents the char. For the drying and pyrolysis stages as well as for the

endothermic reactions, the heat required can be supplied by partial combustion of the entering fuel (autothermal gasification, common when air or oxygen are used as gasifying agent) or by an external source (allothermal gasification).

Oxidation reactions		Enthalpy*	
1	$C + \frac{1}{2}O_2 \rightarrow CO$	-111 kJ/mol	Carbon partial oxidation
2	$CO + \frac{1}{2}O_2 \rightarrow CO_2$	-283 kJ/mol	Carbon monoxide oxidation
3	$C + O_2 \rightarrow CO_2$	-394 kJ/mol	Carbon oxidation
4	$H_2 + \frac{1}{2}O_2 \rightarrow H_2O$	-242 kJ/mol	Hydrogen oxidation
5	$C_nH_m + \frac{n}{2}O_2 \leftrightarrow n CO + m H_2$	Exothermic	C_nH_m Partial oxidation
Gasification reactions involving steam			
6	$C + H_2O \leftrightarrow CO + H_2$	+131 kJ/mol	Water-gas reaction
7	$CO + H_2O \leftrightarrow CO_2 + H_2$	-41 kJ/mol	Water-gas shift reaction
8	$CH_4 + H_2O \leftrightarrow CO_2 + 3 H_2$	+206 kJ/mol	Steam methane reforming
9	$C_nH_m + n H_2O \rightarrow n CO + (n + \frac{m}{2}) H_2$	Endothermic	Steam reforming
Gasification reactions involving hydrogen			
10	$C + H_2 \leftrightarrow CH_4$	-75 kJ/mol	Hydrogasification
11	$CO + 3 H_2 \leftrightarrow CH_4 + H_2O$	-227 kJ/mol	Methanation
Gasification reactions involving carbon dioxide			
12	$C + CO_2 \leftrightarrow 2 CO$	+172 kJ/mol	Boudouard reaction
13	$C_nH_m + n CO_2 \rightarrow 2n CO + \frac{m}{2} H_2$	Endothermic	Dry reforming
Cracking reactions of tars and hydrocarbons			
14	$p C_xH_y \rightarrow q C_nH_m + H_2$	Endothermic	Dehydrogenation
15	$C_nH_m \rightarrow nC + \frac{m}{2} H_2$	Endothermic	Carbonization
* $T=298 K, P=1.013kPa$, carbon as solid and water in vapour form			

Table 1-9. Main reactions during gasification process.

Oxidation: Part of the combustible gases, tars and char undergo partial oxidation reactions (R1 to R5).

These are exothermic and provide the necessary heat for all the endothermic steps.

Gasification/reduction: Is an endothermic step in which the carbonaceous residue reacts with CO_2 in the Boudouard reaction (R12) and H_2O (R6) to form CO and H_2 . Other important reduction

reactions are the water gas shift reaction (R7), and methanation (R11). The predominance of any of the above reactions depends on the operation conditions of the reactor, the presence of a bed material or catalysts, and the gasifying agent.

The resulting products of gasification are:

- The product gas, composed mainly of H₂, CO, CO₂, CH₄, light hydrocarbons, and in a lower extent inorganic pollutants (HCl, H₂S, HCN, NH₃).
- The solid residue (char), composed principally of unreacted carbon and ash.
- Condensable species like water and tar.

1.2.2 Gasification reactors

The gasification process has been used at first for the transformation of coal. Since the end of the 20th century, a growing interest in substitutes for fossil fuels (particularly biomass and much more recently waste derived fuels) has favored the development of different gasification technologies. At the industrial scale, three main types of reactors can be identified: fixed bed reactors (updraft and downdraft), fluidized bed reactors and entrained flow reactors. They differ by their scale, but also by the way in which the solid is fed into the reactor, the operation conditions, and the way heat is supplied. The three main reactor technologies for gasification are compared in Table 1-10.

	Fixed bed	Fluidized bed	Entrained Flow
Scale	10 kW-10 MWth	5 – 100 MWth	>50 MWth
Particle size	up to 100mm	up to 100mm	smaller than 1mm
Temperature	from 700 to 1200 °C	700 to 900 °C	1200 to 1500 °C
Heating rate	<10 °C.s ⁻¹	Near 10 ³ °C.s ⁻¹	10 ³ -10 ⁴ °C.s ⁻¹
Pressure(bar)	1-100	1-20	2-80
Solid residence time	Particles stay in bed until discharge	Minutes to hours	1-5 s
Gas residence time		1 – 10 s	0.1-2 s
Heating value of produced gas	~5 MJ.Nm ⁻³ (air)	~5 MJ.Nm ⁻³ (air) ~12 MJ.Nm ⁻³ (steam)	~10-12 MJ.Nm ⁻³ (Rich in H ₂ /CO)

Table 1-10. Characteristics of different gasification reactor technologies. Adapted from (Materazzi et al., 2013a).

1.2.2.1 Fixed bed reactors

In this kind of reactors, the fuel is retained on a grate and the oxidation medium flows through the bed. Two configurations exist depending on the flow direction (Figure 1-8). In updraft fixed bed processes, the solid fuel is usually introduced from the top while the gasification agent is introduced from the bottom. A grate is used to retain the bed and to evacuate the ashes. The obtained gas contains high concentrations of tars ($\sim 100 \text{ g.m}^{-3}$) since their oxidation reactions within the reactor are limited. In the downdraft process, the gasification agent and solid are introduced upstream of the reactor. The tar concentration is usually lower (0.1 to 1 g.m^{-3}) since they undergo partial oxidation reactions at the level of the air injection.

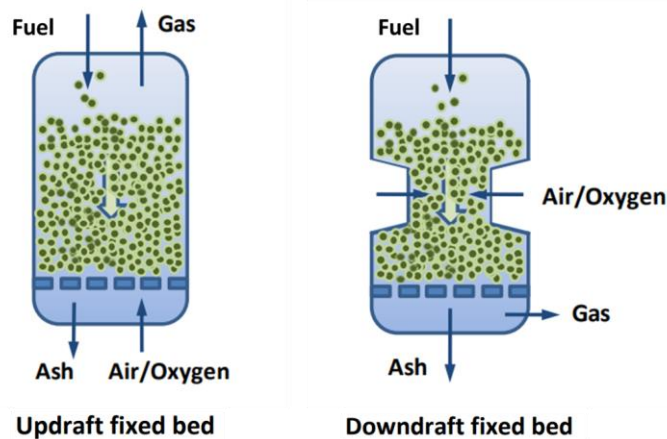


Figure 1-8. Schematic representation of fixed bed reactor technologies (E4tech, NNFCC, 2009).

Fixed beds can handle solid fuels relatively uniform in size and with low content of fines (Bridgwater, 2003). They are not very suitable for treatment of SRF with high ash content, since the risks of agglomeration due to the fusion of ashes are important: Their use is favored for thermal applications with a small scale, usually between 5 to 15 MWth (ADEME, FEDEREC, 2019).

1.2.2.2 Fluidized bed gasifiers

In a fluidized bed reactor, the gasification medium and the fuel are mixed in a hot bed of solid material. The gasification agent is blown upwards with a high enough velocity to fluidize the fuel particles and the inert bed material. Drying, pyrolysis and gasification occur in the same zone (in the dense bed), and the intense mixing gives a uniform temperature distribution. With gas residence times from 0 to 10 seconds, secondary gas phase reactions can happen in the freeboard zone. This results in intermediate tar levels and low unconverted carbon (Block et al., 2019). Various types of configurations can be found (Figure 1-9).

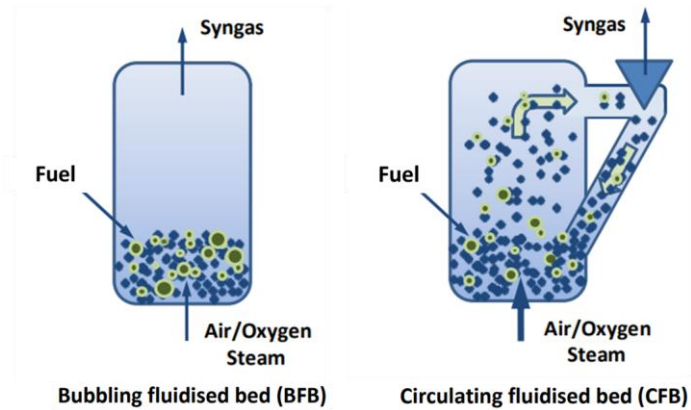


Figure 1-9. Schematic representation of fluidized reactor technologies (E4tech, NNFCC, 2009).

In bubbling fluidizing beds (BFB), the gas velocities are maintained as low as possible to avoid the entrainment of solid particles. In circulating fluidized beds (CFB), the solid particles entrained by the gas are returned to the reactor through a recirculation system. The movement of solids increases the residence time of the carbonaceous residue, thus increasing the conversion efficiency. Fluidized beds represent one of the most popular technologies for gasification, as they are considered to be more robust and flexible than other conventional reactors (Materazzi, 2017), and the most suitable to handle heterogeneous feedstocks like solid waste fuels. To prevent agglomeration and sintering of bed material, bed temperature is maintained below 900 °C.

1.2.2.3 Entrained flow reactors

This type of reactor is heated by a flame, generally coming from the reaction of the solid fuel with O_2 in a specific powder burner (Figure 1-10). Near zero tar content and high carbon conversions are reached thanks to the high reactor temperature (1400 °C). Since the solid residence time in the reactor is very short, the fuel must be prepared into a fine and fluid powder (under 1mm) and must be injected at a constant and controlled rate.

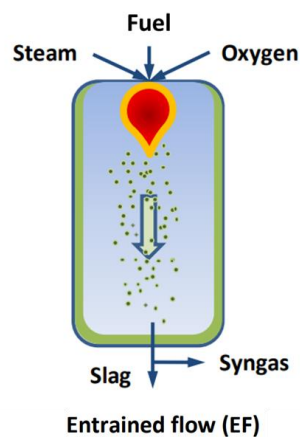


Figure 1-10. Schematic representation of an entrained flow reactor (E4tech, NNFCC, 2009).

This type of technology is not generally applied to SRF for several reasons, which include the need to reduce the particle size of the fuel, and the low energy density of some waste fractions.

1.2.3 Process parameters and performance indicators

Gasifying agent: The oxidant agent chosen for gasification has a direct influence on product gas composition. The most common and affordable option is air, however, the nitrogen present in air dilutes the gas and hence lowers its calorific value (4 – 6 MJ. Nm⁻³). Pure oxygen can be used to avoid this dilution, but its production involves an additional cost. The resulting gas has an energy content of 10-12 MJ. Nm⁻³. (Schuster et al., 2001).

Steam and carbon dioxide can also be used as gasification agents. Their utilization favors the gasification reactions and thus produce more hydrogen and carbon monoxide. In both cases, heat must be supplied by an external heat source because of the endothermic reactions involved. A possible solution is the use of "double" reactors (e.g. dual fluidized beds). One reactor is fed with air (for the combustion of the char and the production of heat), and the other is fed with steam (for the gasification sustained by the heat produced by the first reactor). The lower heating value of the produced gas in steam gasification ranges between 10-20 MJ. Nm⁻³.

Equivalent ratio (ER) is one of the key parameters in air gasification. It is defined as the ratio between the actual O₂ to fuel mass ratio, and the stoichiometric O₂ to fuel mass ratio for complete combustion.

$$ER = \frac{\left(\frac{\dot{m}_{O_2}}{\dot{m}_{fuel}}\right)_{supplied}}{\left(\frac{\dot{m}_{O_2}}{\dot{m}_{fuel}}\right)_{stoech.}} \quad [1.1]$$

This parameter indicates if the reaction conditions are that of pyrolysis (ER=0), gasification (between 0 and 1) or combustion (above 1). The ER value influences product gas distribution, the tar content and the LHV of the produced gas, mainly because oxidation reactions are favored when ER increases.

The gasification performance is usually estimated using the following indicators (Arena & Di Gregorio, 2014a):

- The lower heating value (LHV) of the producer gas, is calculated as the weighted sum of the lower heating value of each gas species i [MJ.Nm³].

$$LHV_{gas} = \sum_i (x_i * LHV_i) \quad [1.2]$$

Where x_i is the molar fraction of the gas species i .

- The gas yield corresponds to the volume of dry gas produced $Q_{v\ gas}$ in [$\text{Nm}^3 \cdot \text{h}^{-1}$] divided by the mass flowrate of feedstock [$\text{kg}_{\text{daf}} \cdot \text{h}^{-1}$]

$$\eta_{gas} = \frac{Q_{v\ gas}}{Q_{fuel}} \quad [1.3]$$

- The Carbon Conversion Efficiency (CCE), is defined as the carbon flow rate converted to gaseous products divided by the one fed to the reactor with the feedstock.

$$CCE = \frac{Q_{v\ gas}}{22.4e-3} M_C \frac{(\sum_i x_i * n_{C,i})}{Q_{fuel} * X_{C,fuel}} * 100 \quad [1.4]$$

Where, M_C the molecular weight of carbon, $n_{C,i}$ is the number of carbon atoms in the molecule i , $X_{C,fuel}$ is the carbon content in the fuel (on daf basis).

- The Cold Gas Efficiency (CGE), is defined as the fraction of the chemical energy of the feedstock (calculated with its LHV) that is transferred to the producer gas.

$$CGE = \frac{\sum_i (Q_i * LHV_i)}{Q_{fuel} * LHV_{fuel}} \quad [1.5]$$

Where Q_i is the volume flowrate of the i species in the gas [$\text{Nm}^3 \cdot \text{h}^{-1}$], and LHV_{fuel} is the lower heating value of the solid fuel [$\text{MJ} \cdot \text{kg}_{\text{daf}}^{-1}$].

1.2.4 Gas applications and cleaning methods

The gas produced through gasification can be used in many applications:

- It can be combusted in a boiler for the production of steam. The latter can be fed to a steam turbine cycle, which can operate in cogeneration.
- It can be used in a thermal engine or gas turbine, for an optimized production of electricity (cogeneration, combined cycle).
- It can be transformed into a wide range of commercial fuels and chemicals by different types of syntheses, such as the Fischer Tropsch one.

Depending on the application, the gas must be cleaned from some pollutants and the generated contaminants must meet environmental requirements. Typical limit values according to type of application are shown in **Table 1-11**.

Contaminant (mg/Nm ³)	Waste gasification	Gas engine	Gas turbine	Methanol synthesis	Fischer Tropsch synthesis	EU emissions standards
Particulates	10 ⁴ -10 ⁵	<50	<5	<0.02	n.d.	10
Tar	0-20000	<100	<10	<0.1	<0.01	n.s.
Sulphur (H ₂ S, COS)	50-100	<20	<1	<1	<0.01	50 (SO _x)
Nitrogen (NH ₃ ,HCN)	200-2000	<55	<50	<0.1	<0.02	200(NO _x)
Alkali metals	0.5-5	n.s.	<0.2	<0.2	<0.01	n.s.
Halides (HCl)	0-300	<1	<1	<0.1	<0.01	10
Heavy metals	0.005-10	n.s.	n.s.	n.s.	<0.001	0.03 (Hg)
Dioxins/furans (ng-TEQ/m ³)	n.s.	n.s.	n.s.	n.s.	n.s.	0.1

n.d. = not detectable, *n.s.* = not specified, * at 11% O₂

Table 1-11. Target levels of pollutants in relation with principal gas applications (Ephraim, 2016a).

In our case, we will focus on bubbling fluidized bed reactors, widely used in the conversion of waste derived fuels for power generation applications. Air is often used as the gasifying agent producing a low-grade syngas with a H₂:CO ratio of approximately 0.25 - 0.5. One of the bottlenecks for SRF gasification is the formation of tar, which results in low conversion of carbon into gaseous products. Moreover, tars can lead to blockages in pipes due to condensation and fouling (You et al., 2018). Tars can be treated by catalytic decomposition, thermal decomposition, or physical separation (Waldheim, 2018). The production of tar as a function of the initial composition of SRF will be of interest in this thesis work.

Other minor contaminants like particulates can be removed with cyclones and filters or by a wet route, using scrubbers or wet electrostatic precipitators. Hot adsorption, and scrubbing, are commonly used methods to remove sulphur and nitrogen compounds (Ephraim, 2016b).

1.3 State of the art on pyrolysis and gasification of solid waste

Since we are interested in the gaseous products and its potential applications, this section focuses on high temperature pyrolysis (above 600 °C) and gasification studies. The reviewed studies are classified according to the scale of the experimental devices used by the authors.

Solid fuels are usually characterized in small-scale laboratory devices. At the analytical scale (under 100mg), substantial work has been done using thermogravimetric analysis (TGA). Main findings in TGA studies of SRF and its materials are presented in section 1.3.1. Other studies have been performed

in laboratory scale reactors (few to several grams of sample), which attempt to reproduce larger-scale reactor conditions. Larger samples are more suitable for a detailed analysis of reaction products. These studies are reviewed in section 1.3.2. At the pilot/industrial scale (starting from a few kg/h), we have focused on studies performed in fluidized bed reactors, since it is the most common and suitable technology for SRF gasification (section 1.3.3). Experimental observations can be transposed to full-scale conditions by modelling. We have especially looked at the models that are intended for the prediction of reaction products (section 1.3.4).

1.3.1 Thermogravimetric analysis for thermal decomposition investigation

Due to its ease of use, TGA has been widely used in research. It gives insight on the degradation behaviour and kinetics of a solid fuel, which are very important for the choice of operating conditions and reactor design. Usually, the sample is heated under a controlled atmosphere at a constant heating rate of 10-20 °C.min⁻¹. The mass of the sample is continuously monitored. The mass loss is usually represented as a function of temperature (called TG curve). The derivate of the mass with respect to temperature (called DTG curve) is also calculated, since it allows identifying the mass loss stages, so as the main degradation temperatures.

1.3.1.1 Thermal decomposition of SRF

The pyrolysis of SRF generally consists of four stages (Goli et al., 2021; Robinson et al., 2016), corresponding to temperature ranges which can be easily identified in the TG curve (Figure 1-11).

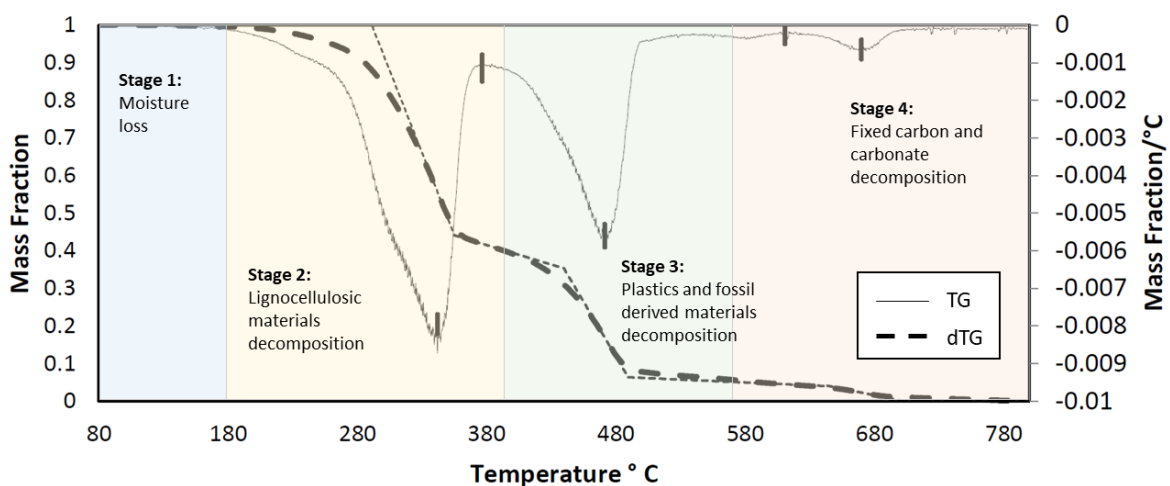


Figure 1-11. TG and DTG curves for an RDF sample. Adapted from (Robinson, 2015).

After the loss of moisture, the first mass loss is attributed to the devolatilization of hemicellulose and cellulose rich materials, with a peak temperature near 330 °C. The second mass loss correspond to the devolatilization of plastic and fossil derived materials, while the latter stage corresponds to decomposition of calcium carbonate and the release of high temperature volatiles, taking place above 700 °C. Based on the above observations, it can be concluded that the biogenic and fossil derived contents of waste derived fuels can be approximately estimated by analyzing their devolatilization profiles (TG and DTG curves).

1.3.1.2 Thermal decomposition of individual materials

Data concerning the thermal behaviour of the main components of biomass (hemicellulose, cellulose, and lignin), and of several biogenic materials are summarized in **Figure 1-12**. This representation makes it possible to identify the temperature ranges in which the mass loss mainly occurs. The maxima of mass loss (which correspond to the peaks of the DTG curve), are indicated with dots. All the listed TGA tests were performed in an inert N₂ atmosphere and with a heating rate of 20 °C.min⁻¹. The amount of solid residue after pyrolysis can be determined by this technique and is also shown in **Figure 1-12**.

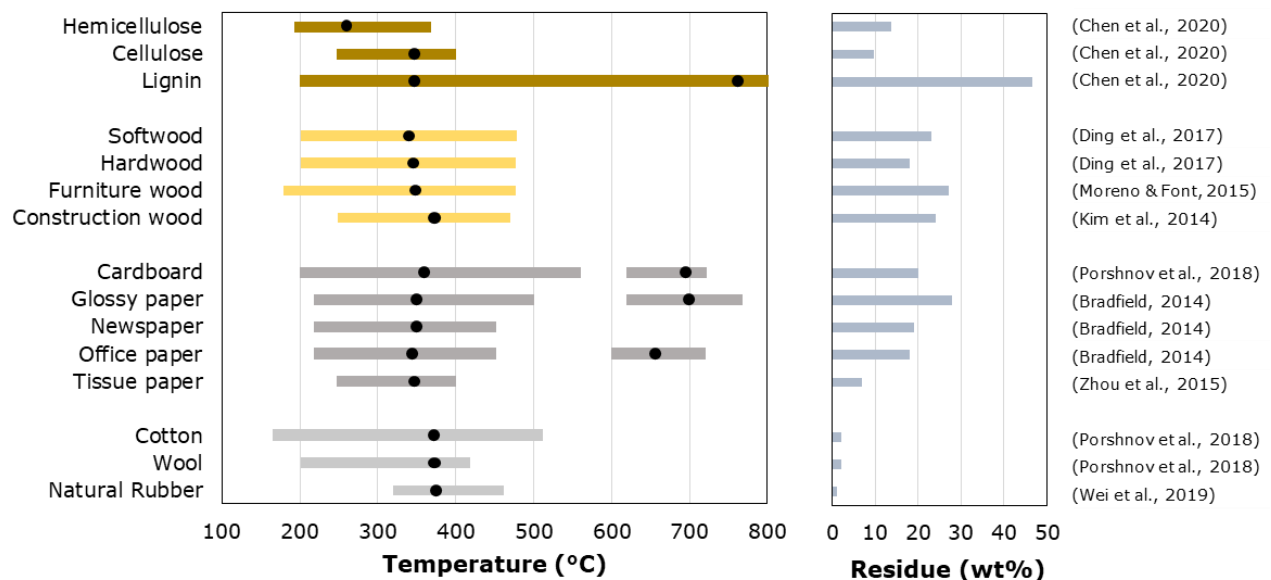


Figure 1-12. Intervals and maxima of thermal decomposition of biomass components and biogenic materials and their char yield after pyrolysis.

Biomass decomposition typically occurs in two stages. The decomposition of hemicellulose occurs between 200 and 350 °C and is followed by cellulose in the 250-400 °C temperature range. Lignin

decomposes in a wide temperature range (200-800 °C). Lignin shows the highest solid residue between the three components (around 40% of its initial mass), which is explained by the aromatic rings with several branches in its structure (W.-H. Chen et al., 2020). Hardwood presents a well-defined shoulder peak between 250 and 300 °C, and a second one near 400 °C. In the case of softwood these two peaks are overlapped (Ding et al., 2017; Grønli et al., 2002a). As expected, the mass fraction of solid residue is lower for the untreated wood in comparison with furniture and construction wood waste, which present a higher ash content.

In the case of paper/cardboard, a second maximum loss is observed near 700 °C, due to the decomposition of inorganic additives (mainly calcium carbonate). The mass fraction of solid residue is the highest for glossy paper, which contains large amounts of clay. Cotton is mainly composed by cellulose, and their decomposition is similar to that of wood or paper, with one single peak near 380 °C. Natural rubber decomposes in one step, and its maximum weight loss is observed near 370 °C.

Experimental TGA results for various fossil derived polymers and materials are shown in **Figure 1-13**. As before, the considered experiments were performed in an inert N₂ atmosphere and a heating rate of 20 °C.min⁻¹.

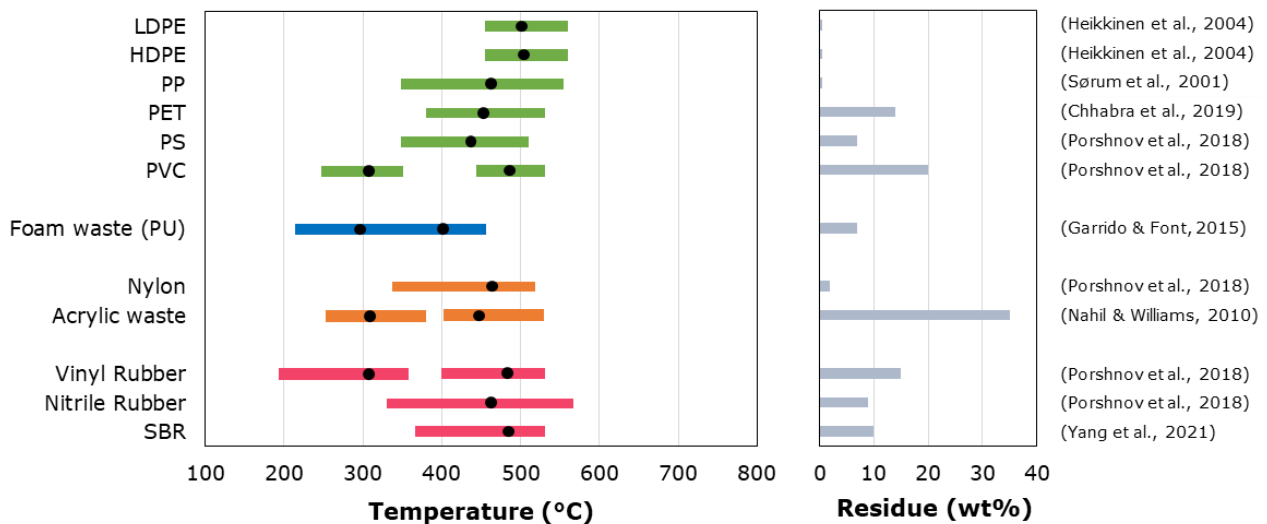


Figure 1-13. Intervals and maximums of thermal decomposition of fossil derived polymers and materials and their char yield after pyrolysis.

HDPE, LDPE, PP and PS decompose in the narrow range of 310 to 480 °C, with rapid weight loss in a single peak. Little or no residue of these plastics remains after pyrolysis. PS has the lowest activation energy, and its decomposition peak temperature is the lowest between all plastics

(Heikkinen et al., 2004). PET is a unique form of plastic because of its C-O bonds and presents a single sharp peak at 440 °C. The residue after pyrolysis represents about 13% of its initial mass.

As already presented before, polyester is the commercial name for the fibers made of PET, so its thermal behavior is very close to that of the initial polymer. Other synthetic fibers like nylon, also show one stage decomposition in the interval from 340 to 510 °C with maximum mass loss at 460 °C. Nitrile rubber, shows a slow decomposition in the range 260 to 560 °C with a maximum around 460 °C.

Contrary to the other thermoplastics, PVC, acrylic waste and vinyl rubber pyrolysis occurs in two stages. The dechlorination stage (250 to 300 °C) accounts for almost 60 % of the initial mass and is followed by a second peak (440 to 470 °C) which corresponds to the degradation of hydrocarbons (Bhaskar et al., 2006). The solid residue for these materials after pyrolysis ranged between 20 and 35% of their initial mass. For the other synthetic rubbers, one decomposition peak is observed at 480 °C for styrene butadiene rubber (SBR) and 450 °C for nitrile rubber. Both showed less solid residue compared to vinyl rubber.

Polyurethane decomposition occurs in two main steps, a first one (200 to 350 °C) being attributed to the breaking of carbonate and urethane bonds, and a narrower second one (350 to 540 °C) related to ester groups (Garrido & Font, 2015). In rigid PU foams, mass loss in the first step is more important since they present more urethane links compared to the semi rigid and soft types (Trovati et al., 2010).

1.3.1.3 Thermal decomposition of mixtures

The mass loss of a mixture of two or more materials can be calculated as the weighted sum of the corresponding mass losses of individual components, under the assumption of negligible interactions between them. A close representation of the mass loss and char yield of a RDF composite can be obtained by the addition of the results obtained for its individual materials (Aluri et al., 2018a). A good agreement can be found when the TG curves are calculated from the pseudo-components of each waste fraction, for example hemicellulose, cellulose, and lignin for lignocellulosic biomass, pectin, starch for food waste, and plastic polymers (PE, PP, PS, PVC, PET) (Long et al., 2017; Meng et al., 2015).

Other authors state that components do not act independently during pyrolysis, mostly because of interaction between them. (Grammelis et al., 2009) observed that a RDF sample decomposed at lower

temperatures than its individual components. The presence of paper accelerated its decomposition. A higher fraction of plastics resulted in a lower char yield and a decrease in reactivity, caused by the high thermal stability of the plastics.

Binary mixtures of biomasses and most binary mixtures of plastic samples do not show significant interactions (Chhabra et al., 2020; J. Zheng et al., 2009). Strongest interactions were found between biomass (wood, paper) and fossil derived materials (PVC; rubber, mixed plastics), causing the pyrolysis of the mixture to start at lower temperature (Zhou et al., 2014b).

As plastic components devolatilize at higher temperatures (300 to 500 °C) than biomass (200 to 400 °C), interactions can occur between char from biomass and volatiles from plastics (Burra & Gupta, 2018b). While the effects on temperatures and degradation curves are known from the results observed in TG devices, few studies have been focused on showing the effect of these interactions on the reaction products.

1.3.1.4 TGA limitations

Conventional thermogravimetric balances present some limitations such as low heating rates (around $1\text{ }^{\circ}\text{C}\cdot\text{s}^{-1}$) and limited gas-solid contact (Saadatkah et al., 2020; Samih & Chaouki, 2015). Sample mass is limited to 10 - 100 mg, which makes it difficult to obtain representative results, especially for mixtures and heterogeneous fuels like SRF (Jagustyn et al., 2017). Scaling these results to commercial-scale units can result in significant errors.

Some authors have tried to investigate thermal decomposition at higher heating rates than in classical TGA (Zheng et al., 2009) studied six typical waste components in a macro-TGA, which was able to handle up to 2g of sample. A maximum heating rate of $865\text{ }^{\circ}\text{C}\cdot\text{min}^{-1}$ was reached. Due to the high heating rates, decomposition peaks of wood and rubber were merged, indicating that several decomposition reactions occurred at the same time. Compared to common TGA curves, main peaks were shifted of 30 – 55 °C towards higher temperatures in macro-TGA results (Fernandez et al., 2019; Meng et al., 2015).

Curie point, pyroprobe, and wire mesh reactors have also proved to be able to achieve higher heating rates ($>10^4\text{ }^{\circ}\text{C}\cdot\text{s}^{-1}$) (Jaradat et al., 1990). As in TGA, the amounts of sample are only a few milligrams. This makes it difficult to perform detailed analysis of the reaction products.

1.3.2 Pyrolysis and gasification studies in laboratory scale fixed bed reactors

Reactors that are able to handle solid fuel samples of a few grams (from 1 to 100 g) seem more suitable than TGA for the study of the products obtained in SRF pyrolysis and gasification. These experimental setups are common because of their easy design and low operation cost. They include tubular, drop-tube and boat furnaces. Usually the feedstock is placed in the reactor before the start of the conversion (batch operation), and the carrier gas or the gasifying agent is injected continuously. Tars are condensed and recovered using cold baths and then analyzed by infrared techniques, mass spectroscopy, etc. Solid and liquid yields are usually obtained experimentally, while gases are calculated by difference or by gas analysis.

As said before, gas, tar and char are the main products from pyrolysis and gasification. Heating rate, temperature and residence time have an influence on the yields of these three types of products in pyrolysis, so as the reactions involved in gasification. Sample particle size, heating technology and the flowrate of the entering gases are factors that can lead to heat transfer limitations.

If the temperature is not uniform inside the sample, the feedstock is decomposed at different temperatures simultaneously (D. Chen et al., 2014). Smaller particles are less prone to heat transfer limitations, which results in a shorter residence time for a complete reaction, in more gaseous products and less char and tar. This effect is more pronounced for materials with high fixed carbon and ash content (Luo et al., 2010).

1.3.2.1 Pyrolysis and gasification studies of SRF/RDF:

Several authors have investigated the pyrolysis or gasification of real SRF. However, less attention is usually paid to the influence of their nature and composition on the experimental results. These usually concern the influence of operating conditions on the product yields and composition, which are common to most carbon-based resources. A few results are presented here on the influence of these parameters.

Above 600 °C, gas yield increases at the expense of the liquid fraction, while the char yield shows little variation with the temperature increase (Buah et al., 2007; Cozzani et al., 1995). Heating rates above 90 °C.min⁻¹ improve the gas yield and its heating value, while char yield do not show significant changes (Efika, 2013), which confirms the observations of the previous studies. The rapid thermal cracking of the primary pyrolysis volatiles, results in a lower tar yield. The tar products obtained from

fast pyrolysis contains mainly aromatic compounds, while the liquid fraction of the slow pyrolysis contains mainly alkanes, alkenes and oxygenated compounds (Singh et al., 2019).

Some gasification studies have been performed using air (Daouk et al., 2018a; Gu et al., 2020) and steam (Hwang et al., 2014; Lee et al., 2016) as gasification agent.

Air gasification and pyrolysis at 800 °C of two SRF real samples were studied by (Daouk et al., 2018a). The samples differed mainly in their carbon (46 and 50 wt.%) and chlorine content (0.3 and 1.1 wt.%). Under inert atmosphere, the product yields for both SRFs were similar, with 50 wt.% of permanent gases, about 20 wt.% of char and 30 wt.% of tar. The produced gas contained mostly CO (~30 vol.%) followed by H₂ (~18 vol.%), CO₂ (~15 vol.%), CH₄ (~14 vol.%) and C₂H₄ (~11 vol.%). Under oxidative atmosphere, the sample with the highest carbon and lowest ash content showed a higher permanent gas yield (95 compared to 89 wt.%). The authors attributed these differences to a possibly higher content of plastics for the second sample, mostly PVC that presents chlorine in its structure. Most of the initial chlorine was measured in the gas phase in the form of HCl. The presence of O₂ accelerates the oxidation of tar and the decomposition of volatiles and increases the fuel gas yield in comparison to pyrolysis. Oxidation reactions are predominant leading to increasing production of CO₂ (Gu et al., 2020).

Compared to pyrolysis results, conversion rates of biomass, refuse derived fuel (RDF) and refuse plastic/paper fuel (RPF) increased in presence of steam above 700 °C (Hwang et al., 2014). The fuels with high plastic content produce a gas with higher LHV, and higher content in methane and hydrocarbons compared to gas produced from biomass and MSW derived RDF.

1.3.2.2 Pyrolysis and gasification studies of individual materials and their mixtures:

Other works in fixed bed reactors have focused on the role of individual materials on the product gas. Common waste fractions (plastics, paper, textile, wood) were tested in air-blown batch gasifiers (Niu et al., 2014; Šuhaj et al., 2020). Paper produced a CO and hydrogen-rich gas with low tar content, while wood results in more CO₂. Biogenic feedstock generated large amounts of primary tars, resulting from the decomposition of cellulose, hemicellulose, and lignin.

Plastics and SRF produced more volatiles and less char than biogenic materials. The decomposition of the plastic polymer chains resulted in the formation of methane and light hydrocarbons, which have relatively high heating values (Honus et al., 2018a). The low oxygen concentration and low fixed

carbon content of the plastics resulted in high tar production. For plastic waste, the formation and evolution of tar depended on the type of plastic. Production of secondary tars was high for PS and PET, with aromatic rings in their structure for both. Polyolefins (PE, PP) degradation gave alkanes and alkenes of varying chain length, which can be easily cracked into light hydrocarbons. PVC generated more polycyclic aromatic hydrocarbons (PAHs) than other components found in waste (Zhou, Wu, et al., 2015).

As in the TGA studies, interaction effects were investigated during the pyrolysis and gasification of mixed feedstock. In the study of (Šuhaj et al., 2020), gasification of RDF showed a lower tar yield when compared to the weighted sum of the yields for the single materials, attributed to synergistic effects between biogenic materials and plastics. Above 900 °C, the thermal cracking of tar became dominant, and the effect of the interactions was less significant. In contrast, higher CO₂ concentrations were observed. A synergistic effect in the methane and hydrogen yields was observed by (Mărculescu et al., 2022) when lignocellulosic, plastic and organic materials were gasified together at 700 °C. However, a strong negative effect on the hydrogen yield was observed with the addition of plastic to the mixture at 800 °C.

Beside the catalytic effect of inorganics like alkali metals and alkaline earth metals (Aluri et al., 2018b), synergy seems to be caused also by interactions among the biomass chars and the polymer devolatilization products, and hydrogen transfer from the polymer to biomass-derived radicals, stabilizing the formed radicals and improving the yield of hydrogen and light hydrocarbons (Burra & Gupta, 2018c; Win et al., 2020).

1.3.3 Pyrolysis and gasification studies in fluidized bed reactors

Fluidized bed (FB) reactors are designed to operate in continuous regime, and present advantages like good mixing, high heat and mass transfer rates and fuel flexibility. Studies in FB reactors mostly focus on the operation conditions and other related topics such as ash agglomeration and tar production.

Most of the studies found in literature used air as gasification agent because of its lower cost. In air gasification, the most important parameters are ER and temperature. These two variables are linked in autothermal reactors, which are the most frequent in pilot and industrial facilities. Using this configuration gases produced from SRF have a LHV between 3.5 and 7 MJ.Nm⁻³ and tar concentrations between 20 to 50 g.Nm⁻³ (Berrueco et al., 2015).

SRF gasification has already been studied in large scale pilot installations (up to 100kg/h) (Arena & Di Gregorio, 2014a). Ash disposal and tar generation are the main technological obstacles in the use of fluidized bed gasifiers for SRF gas production. Depending on the type of minerals contained in the SRF and its ash content, there is a significant risk of agglomeration, which can lead to a defluidization of the bed. This limits the temperature of operation of the reactor, which consequently influences the formation of tars and the carbon conversion to gaseous products. High biomass content in the fuel can lead to agglomeration problems around 900 °C if there is a high presence of Si and P (Hervy et al., 2019). Silicon and aluminium are abundant in the ashes of solid recovered fuels derived from dried sewage sludge and MSW, and can also lead to agglomeration problems during air gasification (Campoy et al., 2014).

One of the proposed strategies to “dilute” the high ash content of the feedstock, is to blend SRF with biomass. In the studies of (Pinto et al., 2014) and (Pio et al., 2020) this resulted in a lower tar content compared to SRF alone, and allowed continuous operation without agglomeration issues. In contrast, in (Robinson et al., 2017), no benefits were observed when the mixture of the two materials was gasified, and agglomeration was observed between 800 and 875 °C. SRF yielded more tar than wood pellets, but the tar produced from wood was more problematic. Several studies on the co-gasification of plastic and biomass were reviewed by (Lopez et al., 2018b). An increase of plastic content in waste fuels improved gas yield and hydrogen production, but also increased tar content (Figure 1-14).

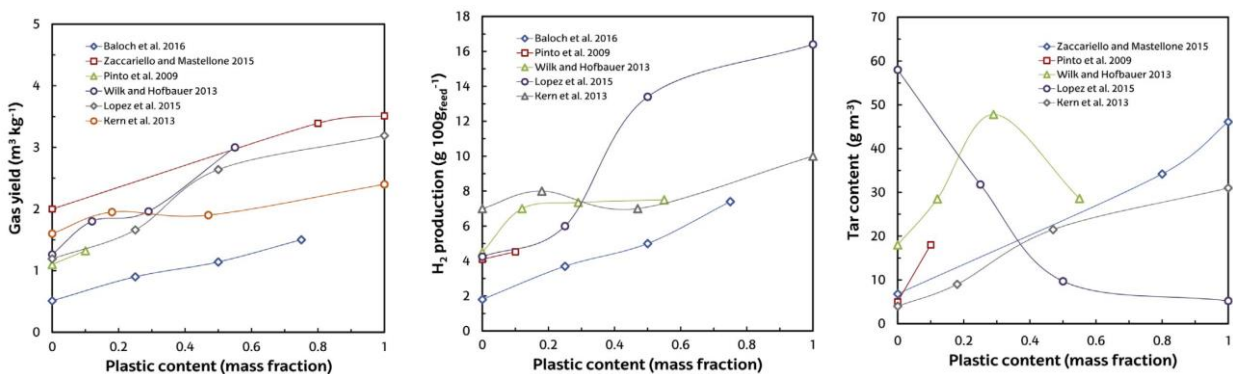


Figure 1-14. Effect of plastic content in the feed on gas yields, hydrogen production and tar content in the co-gasification of plastics with biomass (Lopez et al., 2018b).

Studies on the gasification of pure plastics showed that the use of olivine as bed material improved the overall performance by promoting the cracking reactions, increasing H₂ content and reducing tar content in product gas (Arena & Di Gregorio, 2014b). Dolomite can also be used as bed material, as

it enhances the yield of H₂ and CO, and helped to reduce tar and H₂S contents (Recari et al., 2016). However, the catalytic activity of the bed material was reduced when using mixed plastic waste and SRF with high ash content (Maric et al., 2018).

Feedstocks with high nitrogen content (like ASR which contains large fractions of foams and rubber waste) logically led to a significant formation of NH₃, HCN, NO_x. The nitrogen-containing polymers decomposed towards HCN rather than NH₃, especially under high temperature (W.-S. Yang et al., 2016). It is generally accepted that the reducing atmosphere of the gasification conditions prevents the formation of nitrogen and sulphur species in their oxidized forms (i.e., SO₂, NO_x).

1.3.4 Solid waste pyrolysis and gasification modelling

Different materials or operating conditions can be considered in modelling, saving time and resources compared to systematic experimental investigations. Several models of different complexity have been proposed and reviewed in literature, mainly for biomass materials. In contrast, research on the modelling of pyrolysis and gasification of SRF and its components remains scarce. In the review made by (Ramos et al., 2019) only 8% of the revisited publications involved waste related feedstock.

The models found in literature can be classified in empiric models, thermodynamic equilibrium models, kinetic models, and artificial neural networks. They can be used to represent the whole process or a specific step. For example, some researchers propose models based on the combination of different modules or sub-models (Gómez-Barea & Leckner, 2010; Groleau et al., 2019), where each of the stages involved in gasification (drying, pyrolysis, gas phase reactions, sold-gas reactions) is represented by a dedicated set of assumptions and equations. This is also the methodology used in CFD simulations, which usually include the representation of the reactor in which the process is carried out (thermal and hydrodynamic representation), and the kinetics of the chemical reactions (N. Couto et al., 2015).

Here we are focusing on models that intend to evaluate the variability of the resource and its influence on the products formed. In this manner, it may be possible to identify the materials associated with pollutants, and thus improve the quality and calorific value of the gas. The different model categories are explained below, and the characteristics and findings of the reviewed models are detailed in **Table 1-12**.

-Empiric models: Where experimental data is used to obtain a correlation which represents the experimental results. They can be used for prediction of reaction products (Lopez-Urionabarrenechea et al., 2012). Usually, they need a large quantity of data, and their validity is limited.

-Thermodynamic equilibrium models: They are based on mass and energy balances on the entire reactor, without considering the details of the phenomena occurring inside. For this reason, temperature, gas velocity, or concentration profiles cannot be determined. Two approaches exist, the stoichiometric models based on equilibrium constants and reactions equations (Arafat & Jijakli, 2013), and models based in the minimization of the Gibbs free energy in the system with the use of a larger database of reactions (Barba et al., 2011; Materazzi et al., 2013a; Násner et al., 2017). The main limitation of this approach is the assumption of an equilibrium condition, which is difficult to reach below 1000 °C, as in the case of most fluidized bed reactors (Kalina, 2011). Sometimes, char and tar are not considered. These assumptions make the models over-predict the formation of H₂ and CO and under-predict the CH₄ one. It is also common to use additional modifications or empirical corrections to improve the prediction accuracy of equilibrium models (Aydin et al., 2018; de Priall et al., 2021).

-Kinetic models: They offer a detailed description of the reactions involved in the process. The activation energy and the exponential factors are usually obtained from experimental data obtained in TGA devices. Detailed kinetic mechanisms for the pyrolysis of biomass (Ranzi et al., 2014) and plastics (Marongiu et al., 2007) have been developed by the CRECK modelling group of Politecnico de Milano. These mechanisms involve many reactions and species., which makes them complex and computationally expensive. Some authors have implemented those complex schemes to predict the yields of the gaseous products from RDF pyrolysis (N. Couto et al., 2013).

-Artificial neural network (ANN) models: They use a pure mathematical modelling approach based on deep learning algorithm, which correlates the input and output data to establish a prediction model (Dong, 2016a; Pandey et al., 2016). They do not require a previous knowledge of the phenomena involved in the reactor. However, they need a large quantity of experimental data to train the algorithm, and to validate the model.

Author	Conditions	Model type	Input/Output	Observations
(Lopez-Urionabarrenechea et al., 2012)	Pyrolysis 500 °C	Empiric	<ul style="list-style-type: none"> Input: feedstock material composition Output: liquid/gas/char yields Solver: Excel 	<ul style="list-style-type: none"> Acceptable predictions (up to 10% error) Input requires previous sorting Predicted values are more accurate for mixtures of pure materials than real samples
(Arafat & Jijakli, 2013)	Gasification and combustion 800-1800 °C	Equilibrium (Stoich.)	<ul style="list-style-type: none"> Input: fuel composition, equilibrium constants, process parameters (T) Output: Gas product yields, LHV Solver: Gasify* (MATLAB based tool) 	<ul style="list-style-type: none"> Char and tar are not modelled Less accurate predictions under 900 °C
(Násner et al., 2017)	Gasification 600-800 °C	Equilibrium (Non stoich.)	<ul style="list-style-type: none"> Input: fuel composition and feed rate Output: Gas composition, LHV, CGE Solver: Aspen Plus 	<ul style="list-style-type: none"> Good predictions (under to 2.8% error)
(Barba et al., 2011)	Gasification 700-1100 °C	Equilibrium (Non stoich.)	<ul style="list-style-type: none"> Input: fuel composition and feed rate Output: Gas composition, LHV, CGE Solver: Aspen Plus 	<ul style="list-style-type: none"> Good predictions for LHV Gas yield is overestimated while H₂ is underestimated The model is not able to predict tar content Lack of experimental RDF data for validation
(Materazzi et al., 2013b)	Gasification 700-1100 °C	Equilibrium (Non stoich.)	<ul style="list-style-type: none"> Input: fuel composition steam and oxygen feed rate Output: Gas composition, LHV, CGE Solver: Generalized Reduced Gradient (GRG) method 	<ul style="list-style-type: none"> Single and two stage process (gasification + plasma reforming) Good predictions (error between 3-6%) Underestimation of CH₄, CO and overestimation of H₂ Better predictions for the two stage process
(Sieradzka et al., 2020)	Pyrolysis 700-900 °C	Kinetic	<ul style="list-style-type: none"> Input: Fuel composition, residence time (2-10 s) Output: gas product yields Solver: Ansys CHEMKIN Pro 	<ul style="list-style-type: none"> Not compared with experimental results. H₂ and CH₄ yields are high for plastics, and low for textiles. CO is high for cardboard and wood. H₂, CO₂ yields increase with temperature, while CO and CH₄ decrease. Residence time does not affect gas products.
(N. Couto et al., 2015; N. D. Couto et al., 2016)	Gasification 500-800 °C BFB gasifier	CFD	<ul style="list-style-type: none"> Input: Reactor geometry, MSW composition Output: Product composition Solver: FLUENT 	<ul style="list-style-type: none"> Good predictions for CO₂, H₂, CO and CH₄ contents (under 20% error)
(Dong, 2016b)	Pyrolysis, Air and steam gasification at 650 °C	ANN	<ul style="list-style-type: none"> Input: Experimental yields and MSW composition Output: Gas yield and composition Solver: MATLAB neural network toolbox 	<ul style="list-style-type: none"> Good predictions (Up to 15% error) Tar and char are not taken into account High number of experimental data is used (45 runs)
(Pandey et al., 2016)	Gasification (400-800 °C) ER= 0.2- 0.6 FB gasifier	ANN	<ul style="list-style-type: none"> Input: Ultimate and proximate analysis, temperature, ER Output: Gas yield, LHV Solver: Levenberg–Marquardt (LM) algorithm 	<ul style="list-style-type: none"> Good predictions (R² near 0.98) Gas composition is not predicted Tar and char are not taken into account Large amount of experimental data is used (67 runs) Computational time is between 8 and 190 h

Table 1-12. Summary of the main characteristics of pyrolysis/gasification models for SRF.

1.4 Summary

A broad literature review has been carried out on waste-derived fuels and their thermochemical conversion. The main findings are discussed below and help to define the motivation of this thesis.

Solid waste and its derived fuels are complex and heterogeneous mixtures. In most cases, experimental results remain specific to the studied SRF. The study of the influence of their composition in the products is not systematic. The choice of reference components used in research is sometimes confusing, and not always representative. Categories can be too general (e.g., plastics), although it is well known that this group contains many components with different chemical compositions, structures, and thermal behaviours (PS, PE, PET, etc.). Except for biomass, it is difficult to find studies at the scale in which a single component is studied. This makes it more difficult to identify the effect of each component on the gasification results.

Pyrolysis and gasification studies at lab scale are of interest. Lab scale devices offer a simple and flexible solution, but attention must be paid to heat and mass transfer limitations. A lack of studies at the gram scale with high heating rates has been identified. Moreover, the heating conditions in the reactors are not always reported. In some cases, tar or gas yields are calculated by difference. The gas composition is often well described, while the other fractions are not always studied in detail.

The material content of SRF influences the characteristics and distribution of the main pyrolysis/gasification products. Plastics tend to produce more volatiles and less char compared to biogenic materials. Generally, the increase of plastic content in waste fuels improves gas yield, but also increases the tar content.

Feedstock components can interact during pyrolysis and gasification. Interactive effects can appear during the pyrolysis and gasification of waste materials. Most of these have been observed between biomass and plastics. The consequences of these interactions in the reaction products needs to be studied in depth and validated at the higher scales.

Additional research is needed to develop and validate pyrolysis and gasification models. Highly complex models are not practical for problems involving heterogeneous fuels. It is important that the required properties and parameters can be easily estimated, either by consulting the literature, by measurements or by correlations validated with experimental data. More experimental data can be useful to develop and validate pyrolysis and gasification models.

1.5 Objectives and methodology of the thesis

The current state and the lacks in the research on pyrolysis and gasification of waste derived fuels have been discussed in section 1.4. These findings fix the motivation for the work realized for this thesis.

The principal objective of this thesis is to study the pyrolysis and gasification of solid recovered fuel, in relation with its composition and physicochemical characteristics. We focus on the reaction products, notably the gaseous species, the organic condensable species (tars) and the solid residue. To achieve this goal, the work is divided into 3 main axes:

1. The development of a new experimental setup at laboratory scale, used to investigate pyrolysis and gasification under controlled thermal conditions. This includes the conception and construction of the device, its thermal characterization as well as the development of the experimental protocol.
2. The experimental study of the pyrolysis and gasification of a solid recovered fuel and its model components. Solid recovered fuel is represented by model materials that are studied separately and in binary biomass/plastic mixtures, in inert atmosphere and in presence of air. The yield and distribution of reaction products are determined using analytical methods.
3. The development of a simplified correlation to predict the yield of the pyrolysis products of SRF, based on the experimental results for the single model materials.

2. EXPERIMENTAL SETUP

This chapter is divided in three sections. The first section describes how the induction-heated lab scale reactor used in this thesis work was designed. The second part presents a detailed description of each section of the experimental bench. In the third section a detailed thermal characterization of the reactor is presented.

This part of the work was published in:

O. Sosa Sabogal, S. Valin, S. Thiery, S. Salvador, *Design and thermal characterization of an induction-heated reactor for pyrolysis of solid waste*, Chemical Engineering Research and Design, 173 (2021) 206-214. <https://doi.org/10.1016/j.cherd.2021.07.018>

2.1 Design of the lab scale induction reactor

During gasification, the carbonaceous feedstock is transformed into a synthesis gas, rich in H₂ and CO. The distribution of the main gaseous species depends on the feedstock composition, reactor design and process conditions (temperature, pressure, residence time). Some studies (Díaz & Juliana, 2007; Trninić et al., 2020) have shown that biomass and other carbonaceous feedstock are mainly converted into gas during the pyrolysis, and that the products found at the exit are thus largely those resulting from the devolatilization step, after possible reactions in gas phase.

In order to know the products obtained at the outlet of the gasification reactor, it seems essential to focus initially on the pyrolysis stage and then on the associated gas phase reactions. An analytical device, adapted for the collection and analysis of the resulting products can be used for this purpose. As shown in Chapter 1, most of the studies on pyrolysis and gasification at laboratory scale have been carried out in devices that present limitations in terms of heating rate, handle low amounts of sample, or that focus only into mass loss or reaction kinetics. Test installations must provide operation conditions (like high temperatures, high heating rates, and low volatiles residence times) more similar of those of large scale reactors (Biagini et al., 2004). This motivated us to design and build a specific device for the purpose of this thesis work, this device being based on a previous facility.

Fixed bed reactors have been widely used in pyrolysis research at laboratory scale since they are relatively simple to use and operate. They have been shown to be suitable for experimental studies on pyrolysis and gasification as long as the effect of the secondary reactions can be quantified and controlled (Barr et al., 2019a).

2.1.1 Design objectives

The experimental setup developed for this thesis was designed according to two main criteria:

- I. Have a precise control of the operating conditions (thermal history, residence time of reaction and gaseous atmosphere) to be representative of gasification, with fast pyrolysis as its initial step. These characteristics include:
 - Temperature in the range of 750 to 900 °C.
 - High heating rates. For example, in commercial fluidized bed reactors solid fuels are devolatilized at heating rates between 60 and 1000 °C.s⁻¹ (Nilsson et al., 2012).

- Atmospheric pressure (1bar).
 - Small sample length scale, to reduce the influence of mass transfer limitations.
 - Volatiles residence time between 0.1 and 10 s, long enough to enable secondary reactions. For example, in a fluidized bed these reactions take place at temperatures above 600 °C, before the volatiles exit the reactor's freeboard zone (Barr et al., 2019b).
 - Presence of an inert atmosphere for the pyrolysis tests, and an oxidizing atmosphere (in sub-stoichiometric quantities) for the gasification tests.
 - Ensure a homogeneous temperature distribution throughout the sample.
- II. Ensure an accurate representation of multicomponent feedstock (such as waste-derived fuels), and adequate and reproducible measurements of the amounts of reaction products. The following requirements defined the parameters to be addressed in order to meet the desired criteria:
- Handle samples of a few grams of solid, large enough to be able to perform mass balances and characterization of the reaction products.
 - Have dedicated sections for the sampling and analysis of solid residues, non-condensable volatiles and tars.

2.1.2 Previous works: The PYRATES setup

The reactor developed for this thesis is based on the previous work and experience of (Gauthier G., 2013). In Gauthier's work, an experimental device called *PYRATES* was designed to perform fast pyrolysis of single centimeter-scale wood samples. Thermal limitations inside the large particles (single cylinders of 30 mm height and 20 mm diameter) and quantification of wood pyrolysis products were the main subjects of the previous study. A picture of the device is shown in **Figure 2-1**.

The device consisted in a tubular reactor made from an Inconel tube (90 mm length, 33.5 mm of internal diameter and 0.7 mm thickness). The reactor tube (susceptor) was heated externally using an induction circuit, including a 12kW generator and a coil with 4 turns (inductor). The chosen induction technology and reactor material (Inconel 600) allowed temperatures up to 1050 °C and heating rates up to 500 °C s⁻¹ for the tube. A metallic holder was used to place the sample at the middle of the tube heated zone. Nitrogen at ambient temperature was injected from the bottom to carry the

produced volatiles. The original *PYRATES* setup was designed to minimize the occurrence of secondary reactions, which usually transform the devolatilization products outside the particle. To do so, a second nitrogen flow was injected above the sample to quench the produced volatiles. This allowed to minimize the secondary reactions that could occur in the gas phase, aiming to obtain the primary pyrolysis products.

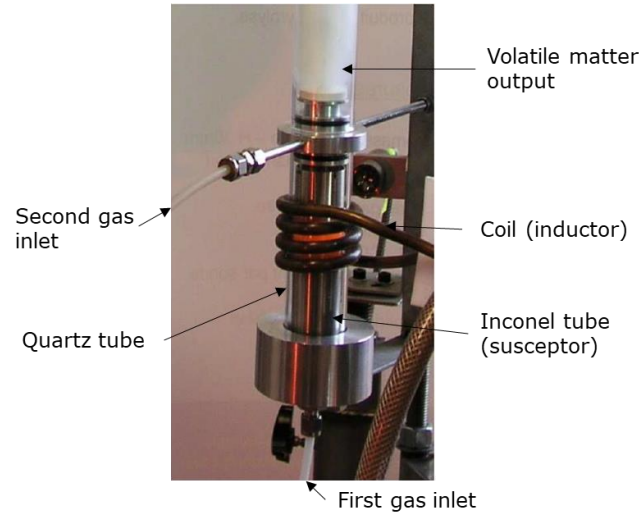


Figure 2-1. Picture of the heated zone of the *PYRATES* device.

The produced volatiles were condensed using an electrostatic precipitator, followed by three cold traps and a cartridge filter. The non-condensable gases were collected and analyzed downstream by micro-GC. As part of the thermal characterization of the reactor, G. Gauthier measured the temperature profile at the external surface of the Inconel tube using a thermal camera.

Figure 2-2 shows the temperature measurements along the tube for a setpoint of 850 °C. The surface temperature was close to the setpoint only in a very limited length.

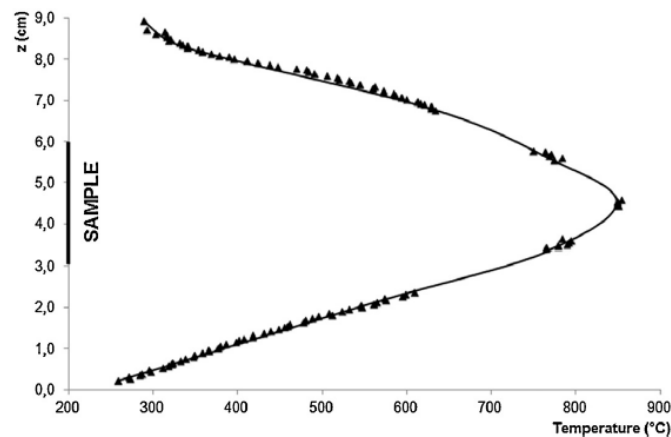


Figure 2-2. Temperature profile along the Inconel pipe (from thermal camera measurements).

Taken from (Gauthier et al., 2013).

Additional tests revealed that the average value of the temperatures measured inside the cylindrical wood samples was 50 °C lower than the tube surface temperature. As indicated by other authors who used this experimental device a few years later (Bellouard et al., 2020), the evaluation of the sample temperature is considered as the main experimental uncertainty of the setup.

2.1.3 Modifications to the PYRATES setup

The original PYRATES setup was not suitable to reach the requirements fixed in this thesis and mentioned in the section 2.1.1. In order to meet the proposed objectives for the new experimental bench, some elements of the original *PYRATES* configuration were retained, and others were added or modified.

Heating technology:

Induction heating proved to be suitable to reach high heating rates in the previous configuration. One of the initial constraints was to use the same power source (generator). A detailed study of the existing power source was commissioned to the ATYS consulting company, specialized in the design of induction heating systems. An initial test performed without the susceptor, allowed measuring the minimal operating frequency (253 kHz) and the maximal power delivered by the induction circuit (8.4 kW).

Subsequently, susceptors of different materials and thicknesses were tested in order to determine the working frequency range of the generator and the delivered power achieved in each case. The results of the ATYS study showed that the existing generator was capable to heat uniformly a length of approximately 200 mm of a stainless-steel tube by using a larger coil with a different geometry. The stainless-steel tube was 500 mm height, had an internal diameter of 31mm and 1 mm thickness.

Reactor size:

In the previous configuration the heated zone was intended to have a limited height, which allowed to minimize secondary reactions. For the new setup, the proposed modification was to increase the height of the heated zone, that is to say, to increase the height of the susceptor and therefore the coil geometry.

The new heated zone was designed with two requirements in mind: first, to be able to heat uniformly a crucible with a capacity of a few grams; second, to maintain the produced volatiles at a temperature

close to the set point in the zone above the solid sample for several seconds. A volatile residence time of a few seconds at a temperature close to 800 °C can allow cracking and reforming reactions in the gas phase as it happens in the freeboard zone in a fluidized bed reactor.

Based on the suggestions of the ATYS study, we designed the reactor tube and the induction coil. A detailed description of both is presented in section 2.2.1.

Reactor tube material:

Susceptors must be made in a ferromagnetic material in order for induction to take place. A compromise must be made between the thermal inertia of a thick susceptor (better mechanical resistance and easier regulation), and the heating rate. The original configuration used a susceptor made of Inconel 600, which is a nickel base chromium alloy steel with good resistance to high temperature oxidation. It has a maximum service temperature of 1175 °C. In our case it was not possible to obtain an Inconel tube with the desired dimensions, so we decided to use stainless steel 316L. This type of steel offers good corrosion and oxidation resistance. However the maximum service temperature is limited to 900 °C to maintain good structural stability.

Exchanger:

As shown in section 2.1.2, the original device presented significant temperature differences between the tube surface and the sample zone for a given setpoint. The cylindrical sample was heated mainly by radiation emitted by the reactor hot wall, but it was affected by convection with the nitrogen flow coming from the bottom of the reactor. The surrounding gas around the sample was at a much lower temperature than the desired setpoint, which had a negative effect on the uniformity of the temperature within the sample.

The main challenge with the redesign of the heated zone was to obtain a controlled and homogeneous temperature for the sample, as close as possible to the desired setpoint. To achieve this, it was essential to preheat the gas coming from the bottom to a temperature as close as possible to the desired reaction temperature. This motivated the addition of a heat exchanger under the sample, designed for this purpose. The exchanger is presented in detail in section 2.2.3.

2.2 Description of the NEW PYRATES setup

A schematic overview of the setup is presented in Figure 2-3, while photos of the installation are shown in Appendix B. Each section is described in detail below.

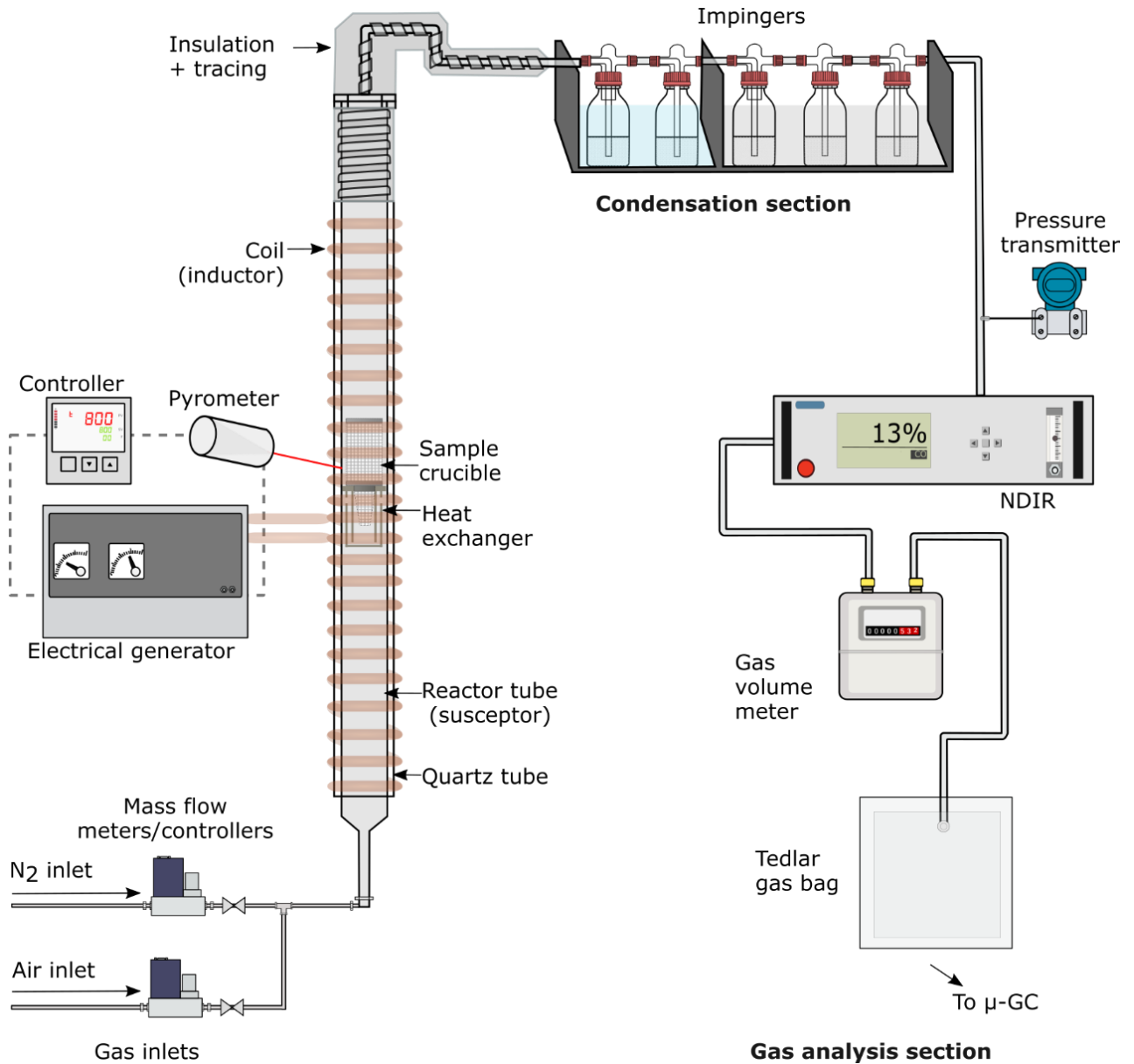


Figure 2-3. Schematic overview of the experimental setup.

2.2.1 Reactor tube

The reactor main body is made up from a stainless-steel tube (316L) of 560 mm in height, 31.75 mm in external diameter and with a thickness of 0.8mm. The first gas inlet is connected to a nitrogen line, used here as carrier gas. A second gas line is installed to introduce air or other gases into the reactor. Flowrates are set using mass flow meters/controllers [Mass flowmeter 5851S, BROOKS Instrument]

controlled by a LabVIEW interface. The maximum working temperature is 900 °C. The empty tube portion above the crucible up to the reactor outlet has a length of 320mm. Most of the tube (310 mm) is located in the area heated by the induction coil. The very last portion of the tube (10mm), is traced with a heating wire, and covered with insulating material on the outside to prevent the temperature from dropping below 300 °C.

2.2.2 Induction system

The reactor is heated externally using an induction set-up very similar to the previous configuration. A generator [HFP 12, EFD induction] supplies an alternating current to the induction coil, which is wrapped around the reactor tube (Figure 2-4). A quartz tube is placed in the 5mm gap between the coil and the reactor tube, in order to avoid an electric arc in case of direct contact between the coil and the susceptor. The maximal power output of the generator (12 kW) is limited to 75% by an internal setting.

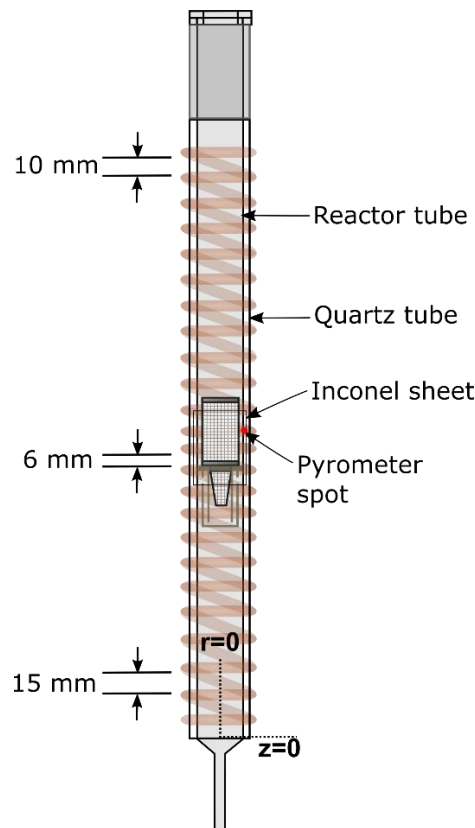


Figure 2-4. Detailed diagram of the induction coil and reactor tube.

The inductor was specifically designed for this set-up. It consists of a water-cooled coil of 24 turns disposed in two parallel sections. The coil was constructed using round copper tubing (8 mm external

diameter, 1mm thickness); its total height is of 420 mm and its outside diameter of 60 mm. An insulating coating was applied to the tubing to minimize the absorption of heat radiated by the reactor tube and to protect it from corrosion. The desired setpoint temperature is regulated by a process controller [GEFRAN 2500 PID], linked to a two-colour optical pyrometer [Impac IGAR 6, range between 100 and 2000 °C, response time 2ms, $\lambda_1 = 1.52 \mu\text{m}$, $\lambda_2 = 1.64 \mu\text{m}$, precision is $\pm(0,4\%.T+1)$]. The pyrometer spot is focused on the tube surface, at the sample crucible height, which is 207 mm from the bottom of the tube (**Figure 2-4**). The reactor tube was coated with a heat-resistant paint to increase the emissivity up to 0.95, and thus improve the precision of the optical temperature measurements.

Position of the coil and working frequency are crucial parameters to attain a desired temperature profile for a specific workpiece (Hadad et al., 2016). The susceptor and the induction heating system underwent various preliminary tests, where the position of the coil and the setpoint spot were changed to reduce the heating time and to improve temperature uniformity along the reactor. Another parameter that was evaluated during these tests was the distance between the turns. It is called “pitch”.

Initially, the induction coil had a pitch of 10mm for all turns. After the preliminary tests, the pitch was changed to 10mm for the top section, 6 mm for the middle section and 15 mm for the bottom section as shown in **Figure 2-4**. This allowed to increase the local magnetic field intensity in the zones where more power density was needed, namely, the middle of the reactor, where the exchanger and the sample crucible were placed. To avoid a temperature overshoot and therefore mechanical instability of the reactor tube, it was necessary to add a thermal screen between the tube and the coil (constituted by an Inconel sheet of 65 mm in height and 1 mm in thickness) placed around the height of the sample.

2.2.3 Heat exchanger

It is expected that the preheating of the entering gas will homogenize the temperature within the sample. (Houzelot & Villermaux, 1984) showed that annular exchangers with small interstitial space performed well in laminar flow. Following these observations, an internal preheating section was added to increase the temperature of the inlet gases before coming into contact with the sample bed. For this purpose, a heat exchanger was constructed using two concentric tubes of 20 mm and 23 mm (i.d.) made from Inconel 600 sheets (50mm height, 0.5 mm thickness). The device is placed just below the

sample crucible. The entering gases are forced to pass through the 2mm spaces between the reactor tube and the cylinders walls, following the flow path illustrated in **Figure 2-5**.

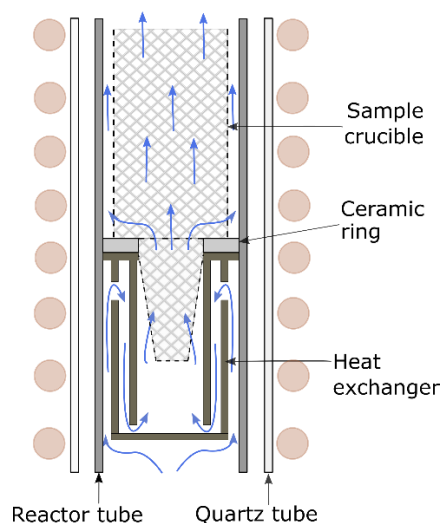


Figure 2-5. Detailed diagram of the middle section of the reactor (sample crucible and heat exchanger).

The efficiency of the exchanger device was tested for different gas flow rates. The results will be discussed in detail with the thermal characterization of the reactor in section 2.3.

2.2.4 Sample crucible

The sample crucible is composed of a steel wire mesh cylinder (550 mm in height and 27 mm in external diameter), in which the sample is placed, with a cone of 35 mm height attached at the bottom (**Figure 2-5**). The meshed material allows inlet gases to flow through the crucible and the sample bed. The conical part was added to improve the homogeneity of distribution of the entering gas at the bottom of the crucible itself. The ensemble is supported by a 5 mm thick ceramic ring placed on top of the heat exchanger, at the middle of the reactor tube. The crucible can contain a few grams of sample.

2.2.5 Condensation section

At the outlet of the reactor tube, an elbow connects the upper part of the reactor with the condensation zone (**Figure 2-3**). They are both traced with a heating cable kept at 250 °C and insulated to prevent early condensation. A silicon gasket and a screwed seal are placed between the tube and the elbow to avoid gas leakage. The carrier gas sweeps the produced volatiles to the condensation section. The

purpose of this assembly is to recover all the condensable species and to clean the gas stream before entering the gas analyzers.

For the sampling of the tars, it was decided to use a condensation method based on the guidelines presented in (Neeft et al., 1999). A train of impingers filled with isopropanol and placed in cold baths is used for the condensation of the tar species. The first two impingers are immersed in a water bath, while the last three are immersed in an isopropanol bath. For the first tests, the first bath was cooled using ice (0 °C) and the second using a mixture of dry ice /isopropanol (around -70 °C).

The cooling conditions were adapted to avoid trapping of CO₂ and hydrocarbons like C₃H₆, which were poorly quantified in solution and could be quantified by μ GC. (Kamp et al., 2006) showed that higher temperatures in the first impingers can also help to dissolve the tars faster. At higher temperatures more isopropanol is evaporated, leading to larger aerosol droplets and then to a more efficient collection of the tars when the gas is cooled in the next impingers. We decided to maintain the first two impingers at ambient temperature. The other three were cooled at -10 °C using an immersion thermostat device, which allowed a better control of the temperature in the second bath.

The impingers are prepared prior to each test, using 500 mL gas washing bottles. Glass wool and glass beads (160 g) are added to increase the liquid-gas contact and therefore the transfer to the solvent. The bottles are then filled with isopropanol to complete a total volume of 300 mL. Glass wool also allows particles to be filtered and prevents their entrainment to gas analyzers. The impingers are connected as shown in Figure 2-6.

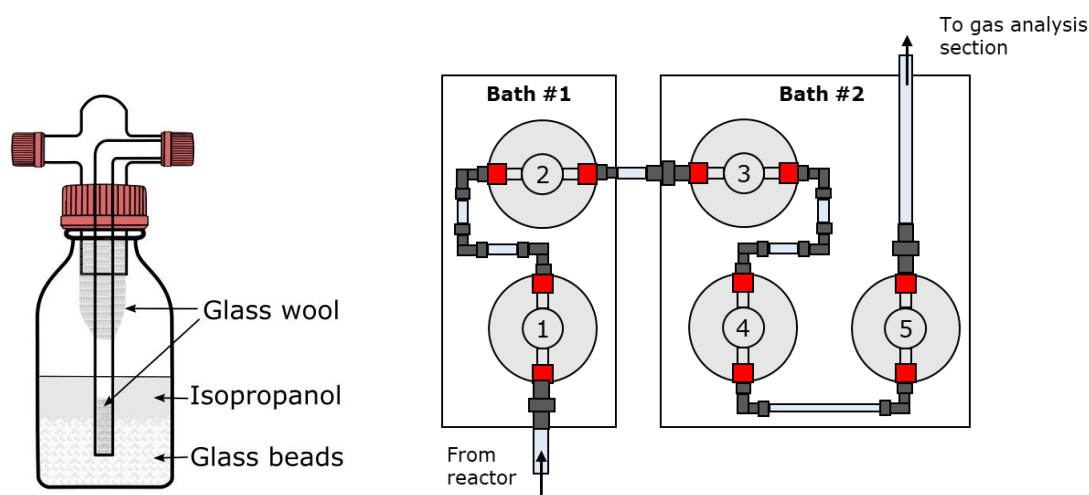


Figure 2-6. Schematic representation of an impinger (left) and layout of the impingers in the condensation zone (right).

At the end of the test, the connections are disassembled and the impingers are taken out of the cooling bath. Each of the five impingers is weighed before and after the experiment, and the mixture tars/solvent is sampled and stored at 5 °C. To gain further insight into the chemical composition of the collected tars, the impinger content is analyzed by GC-FID. Details on the analysis method are presented in Chapter 3.

2.2.6 Gas analysis section

The remaining non-condensable gases flow towards an online NDIR (Non-Dispersive Infra-Red) analyzer, which records the CO, CO₂ and CH₄ concentrations every second (Figure 2-3). The total volumetric flowrate at ambient conditions in cubic meters [m³] is determined using a diaphragm gas volume meter [Gallus, ITRON FR] placed at the outlet of the NDIR analyzer. Moreover, a differential pressure transmitter [1151 Pressure Transmitter, Rosemount], connected at the outlet of the condensation system, is used for the determination of the gas flowrate, following a procedure described in Chapter 3. Finally, the produced gases are collected in a Tedlar sampling bag. The bag content is analyzed after each experiment with a gas-phase micro-chromatograph [Agilent 3000A]. The methods used for the gas analysis are presented in Chapter 3.

2.3 Thermal characterization of the reactor

Knowing the real temperature of the sample is essential when performing pyrolysis and gasification experiments. It is common to assume that reaction temperature is that of the heating source, or that the temperature inside the reactor is uniform, although this can lead to major errors (Lédé, 2013). For high temperature reactions, the sensitivity, response time and location of the temperature measurement elements must be adequate to accurately describe the reaction temperature (Maduskar et al., 2018).

Once the device was built and the induction heating system optimized, a thermal characterization study of the new reactor was carried out. The main objective was to accurately identify the thermal history of the reactor and the sample throughout an experiment. The first implied to observe how the reactor temperature changed as a function of time, while the latter aimed to observe how the sample characteristics (density, heat capacity, conductivity) influenced the sample heating response.

The transient temperature response of the reactor was monitored in various test runs at atmospheric pressure, without and in the presence of an inert sample. The latter consisted of a bed of chemically

inert material (alumina) with similar particle size to the feedstock used in the real experimental runs. The reactor was heated first from ambient temperature to 800 °C (pyrometer temperature), and then held for several minutes to ensure that steady state was reached. Nitrogen (N_2) was used as carrier gas and its flowrate was set at 1 NL.min⁻¹. Temperatures at the external surface of the tube were measured by five K type thermocouples (TW1 to TW5) of 0.5 mm in diameter, distributed on the outer surface at $z = 10, 155, 207, 268, 375$ mm. The position of the sample thermocouples in the reactor surface and the T shaped rod is illustrated in **Figure 2-7**.

The temperature profile inside the sample was measured using a T shaped rod with five K type thermocouples (TS1 to TS5) at different radial ($r = 0, 6, 13$ mm) and axial positions ($z = 185, 210, 235$ mm) within the sample crucible.

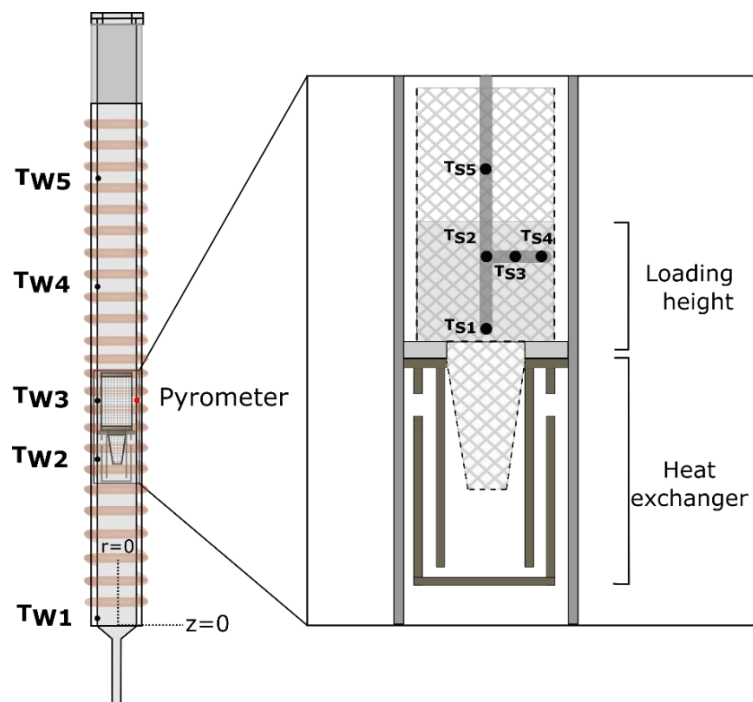


Figure 2-7. Schematic of the reactor tube and middle section outlining the position of the thermocouples.

2.3.1 Transient temperature response of the reactor

The evolution of temperatures at the external reactor tube surface is shown as a function of time in **Figure 2-8**. TW1 is the closest thermocouple to gas entrance and is placed outside the heated area, so its temperature is far below the setpoint. The wall temperature at the sample height (TW3) reaches the setpoint value in 15 s approximately, following a linear behaviour with a steep slope of 80 °C.s⁻¹. At the preheater position (TW2), the thermal response is slower due to the thermal inertia of the

internal elements and to the colder gas flowing faster along the exchanger walls. Temperatures along the empty zone above the sample (TW4, TW5) are very close to the setpoint during the first minute, and then decrease to 750 °C.

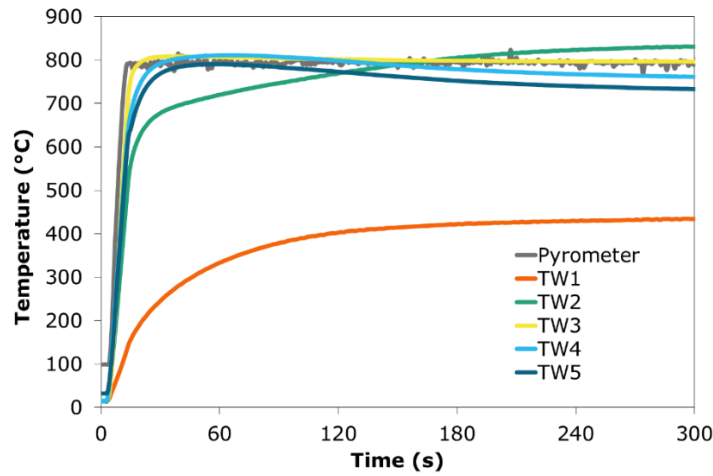


Figure 2-8. Temperature evolution at different locations along the reactor outer wall.

2.3.2 Temperature profile of the sample

The thermal profile inside the crucible was established for two cases and is shown in **Figure 2-9**. In the first case, the crucible was empty, while in the second case it was filled with alumina pieces of irregular shapes and thickness between 1 and 5 mm. The loading height was about 30 mm. A significant temperature difference can be observed between the reactor wall (pyrometer) and the T shaped rod thermocouples for both cases.

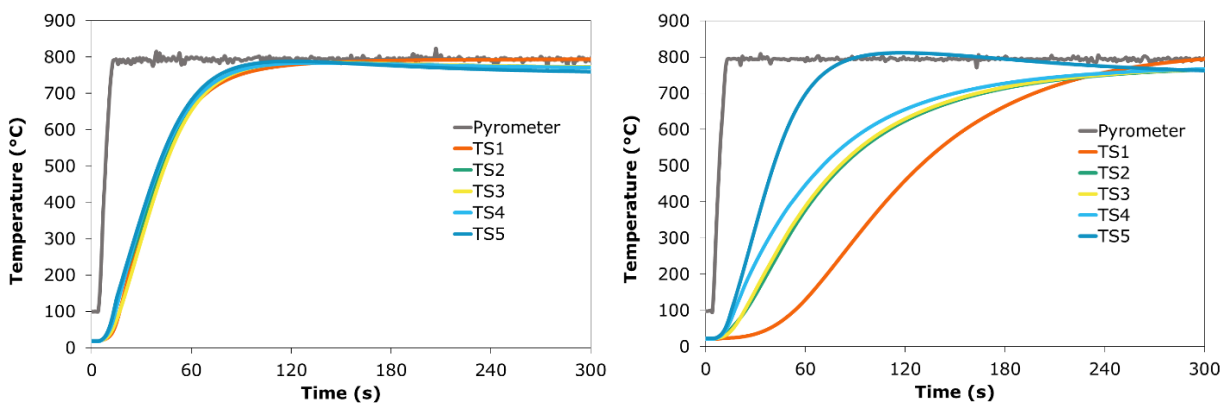


Figure 2-9. Temperature evolution in the empty crucible (left) and in the crucible filled with ceramic material (right).

As expected, the heating rate is higher in the empty crucible than in the crucible filled with the inert sample. It takes about 300 s for the thermocouples inside the sample to reach their final value,

compared to only 100 s for the empty crucible case. Differences between the internal thermocouples (TS1 to TS5) measurements are not significant for the empty case, which suggests a uniform temperature profile in both axial and radial directions. For the second case, the fastest response is recorded above the sample (TS5, $z=235$ mm), where the thermocouple is subjected to radiant heat incident from the reactor wall. This explains why the temperature exceeds the setpoint value before reaching a stable value.

At the middle of the bed ($z=210$ mm) the temperature the nearest to the hot reactor wall (TS4) increases faster than the one at the middle (TS2), which is expected due to the thermal resistance of the bed material. The gradient in the radial direction is very small when compared with the gradient in the axial direction (TS1 compared to TS2). A similar result was observed in previous works of (Fernández et al., 2015) and (Chatterjee et al., 2017) in which negligible radial temperature change was observed on two radio-frequency heated reactors with similar length to diameter ratios. In contrast, temperature differences in the axial direction reached several hundreds of °C. The slowest response was measured at the bottom of the crucible (TS1). At this level, carrier gas coming from the preheater meets the colder solid particles and then must flow through the empty spaces of the bed.

For the conditions of this test, the reactor Reynolds number is equal to 11.75, which indicates a clearly laminar flow regime. The main heat transfer mechanisms involved during the heating of the sample are radiation between the reactor wall and the bed particles, and a smaller contribution of convection with the hot gases flowing through the bed. At 800 °C, the calculated radiative heat transfer coefficient is $344 \text{ W.m}^2.\text{K}^{-1}$, while the convective heat transfer coefficient is only $11 \text{ W.m}^2.\text{K}^{-1}$.

The time needed to reach the setpoint temperature depends on the physical and thermal properties of the fuel, like density (ρ) [kg.m^{-3}], particle size [m], conductivity (k) [$\text{W.m}^{-1}.\text{K}^{-1}$] and heat capacity (C_p) [$\text{J.kg}^{-1}.\text{K}^{-1}$]. The thermal diffusivity (α) [$\text{m}^2.\text{s}^{-1}$ or $\text{mm}^2.\text{s}^{-1}$], characterizes the capacity of a material to transfer heat by conduction and is calculated as follows:

$$\alpha = \frac{k}{\rho * C_p} \quad [2.1]$$

The higher the diffusivity, the higher is the temperature increase inside a material submitted to a temperature change on its boundary. Thermal diffusivity increases with temperature for N_2 , while the opposite behaviour is observed for alumina. At 800 °C, α was equal to $181 \text{ mm}^2.\text{s}^{-1}$ for N_2 and

2.22 mm².s⁻¹ for alumina. This agrees with the quicker temperature increase in gas when submitted to the same temperature step on the reactor wall than alumina (**Figure 2-9**).

The thermal diffusivities of most carbon-based waste materials and of SRF lie between the ones of N₂ and of alumina, which can be considered as extreme cases. Therefore, the temperature evolution of a solid residue is expected to be between that observed in the two experimental test cases. During the first seconds, the heating response will be limited by the thermal inertia of the solid. Then, once its devolatilization is complete, it will behave as in the case of gas.

Nitrogen and ceramic are inert, so the profiles presented in **Figure 2-9** are only controlled by heat transfer. For carbonaceous feedstock, some inflexion points can be expected, because of the physical and chemical changes that can occur during their pyrolysis. Some of them are endothermic and others exothermic. Other tests were performed with the reactor open at the top, which allows a thermocouple to be inserted into a test sample. In this way, it was possible to record the temperature evolution of a biomass and a plastic sample during their pyrolysis. These results will be presented in Chapter 4.

2.3.3 Steady state temperature profiles

A second two-colour optical pyrometer (Impac IGAR 12-LO, 350-1300 °C range) placed on a moving support was used to measure the temperature profile along the reactor external surface in steady state conditions. Both runs (with and without ceramic particle bed) showed the same result, so the mean temperature distribution for the two runs is shown in **Figure 2-10**.

Inside the inert sample bulk (located between 180 and 210 mm), the maximum temperature is 808 °C. Temperature discrepancies are under 10 °C in the bed (TS1 to TS4), which shows that the temperature is uniform and close to the setpoint temperature once the steady state is reached. The highest wall temperature (TW2=825 °C) is measured at 155 mm, where the preheater device is placed. Above the sample zone, a quite isothermal zone of about 200 mm long is maintained at 750 °C. This empty zone is similar to the freeboard zone in a fluidized bed reactor. The tube portion above 400 mm is outside the induction coil, so current density and thus the inducted heat is much lower, which causes the temperature to drop rapidly.

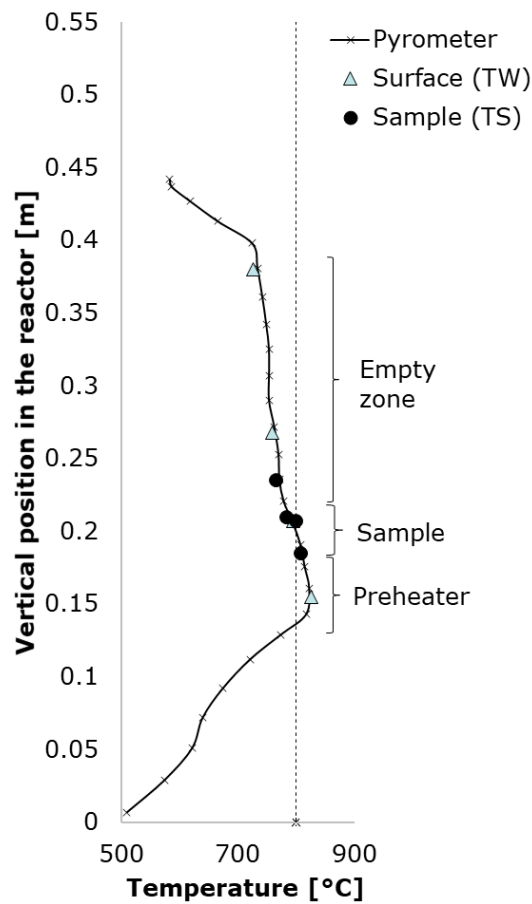


Figure 2-10. Temperature distribution along the reactor wall at steady state for a setpoint of 800 °C.

2.3.4 CFD modeling of the reactor

Measurements performed with the thermocouples introduced in the tubular reactor can be affected by the radiation, especially at high temperatures. A modeling approach combining fluid dynamics and heat transfer was implemented to have a more accurate description of the temperature profile of the gases inside the reactor.

These calculations were also made with the objective of evaluate the efficiency of the heat exchanger device. For this purpose, the carrier gas flowrate was varied, and its influence on the temperature profile of the sample as well as on the residence time of the gases in the free zone was observed. Based on the obtained results, the conditions for the experimental tests were chosen. The commercial software ANSYS FLUENT R19.3 was used to perform these simulations.

Geometry characteristics:

The reactor geometry was discretized using a 2D-axisymmetric approach along the flow direction. Details are given in **Appendix C**. The heat exchanger and sample crucible were included in the description. The mesh contained a total of 71642 nodes.

Materials:

Properties of gas and stainless steel were calculated using the temperature dependent polynomials. The corresponding coefficients were obtained from the Fluent database. The properties of the ceramic material are listed below:

Density	850 kg.m ⁻³
Thermal conductivity	$k(T) = 2.03 \cdot 10^{-8} T^2 + 3.91 \cdot 10^{-5} T + 1.97 \cdot 10^{-1}$ in W.K ⁻¹ .m ⁻¹ (With T in K; from 293 to 1373 K)
Heat capacity	960 J.kg ⁻¹ .K ⁻¹
Emissivity	0.95

Table 2-1. Properties of the ceramic material considered in the CFD calculations.

Model assumptions and boundary conditions:

- The gas phase consists of N₂ only, entering at 25 °C at the bottom of the reactor. The mass flow rate is set as the inlet boundary condition. Carrier gas flowrate values between 0.5 and 4 NL.min⁻¹ are tested. This range corresponds to the values that can be used in the experimental setup.
- Atmospheric pressure (1 atm) is defined as the boundary condition at the reactor outlet.
- The solid bed of ceramic particles is considered by using the porous media zone condition, which is applied to a specific flow domain created for the zone inside the crucible. The porosity of the bed is 0.4.
- A non-reacting scenario is modeled (inert material).
- The experimental profile measured previously at the tube surface (**Figure 2-10**) is implemented to describe the stationary wall temperature boundary condition.
- A no-slip boundary condition for the gas phase is fixed on the reactor wall.

Solution procedure:

Governing equations (mass, energy and momentum balances) are solved numerically by a finite volume method. The PRESTO (PREssure STaggering Option) is used as the pressure interpolation scheme, recommended for problems involving flow through porous media.

We observed that radiation was more important than convection or conduction for heat transfer between the reactor wall and the surface of the sample. In the simulation, radiation is considered and modeled using the surface to surface (S2S) model built in Fluent. The radiation energy balance for each surface is described by the equation 2.2:

$$q_{out,k} = \varepsilon_k \sigma T_k^4 + \rho_k \sum_{j=1}^N F_{kj} q_{out,j} \quad [2.2]$$

Where q_{out} is the energy flux leaving the surface, ε_k is the emissivity, σ is Boltzmann's constant, and F_{kj} is the view factor between surface k and surface j.

This model assumes that gas is transparent to radiation, so only surface to surface radiation is accounted. It is also assumed that all the surfaces behave like gray bodies, which means their properties are independent of radiation wavelength and incident angle.

Nitrogen has a very low absorbance and emissivity, so it behaves like a transparent medium. In reality produced gases during pyrolysis like CO₂ and H₂O can absorb, emit and scatters radiation. This can impact in flow dynamics and the heat transfer within the reactor. Other radiation models like the discret ordinates radiation model, can consider emission, absorption and dispersion phenomena, however they need the specification of many parameters and a higher computational cost.

Once all the boundary conditions were set up the simulation was run. The convergence was verified by monitoring residuals and the mass and energy balances.

Simulation results:

Figure 2-11 shows the temperature distribution of the gas phase inside the reactor at steady state conditions for increasing gas flowrates. The middle zone is presented in more detail in Figure 2-12.

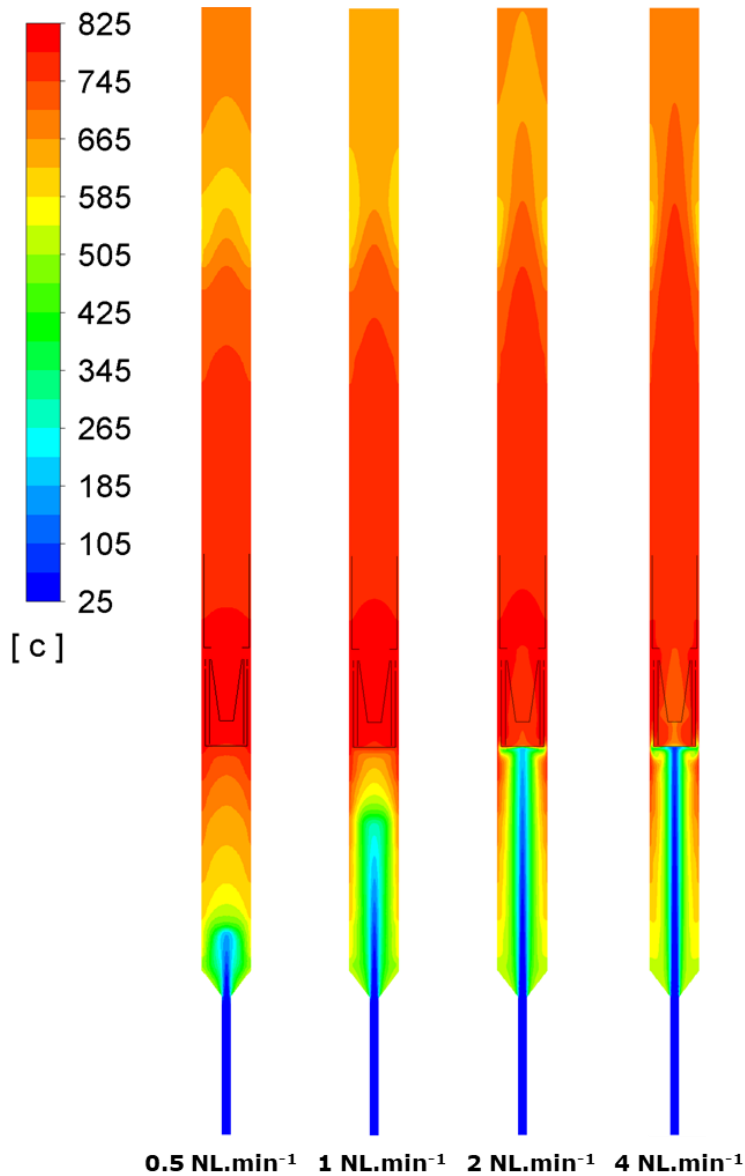


Figure 2-11. Contour plots of temperature distribution in the gas phase for different gas flowrates.

At the lowest flowrate values, inlet gas is properly heated by the heat exchanger, so its temperature remains above 790 °C in the crucible zone with a rather homogeneous profile in both axial and radial directions. As the N₂ flowrate increases, more pronounced temperature gradients are observed in the crucible zone, especially in the radial direction. Because of enhanced convection, the length of the isothermal zone above the crucible increases. N₂ flowrates of 0.5 and 1 NL.min⁻¹ are best suited to achieve a homogeneous temperature profile in the sample as desired. Under these conditions, the estimated residence time of the volatiles in the hot empty zone (temperatures between 750 °C and 800 °C) is between 2 and 4 s.

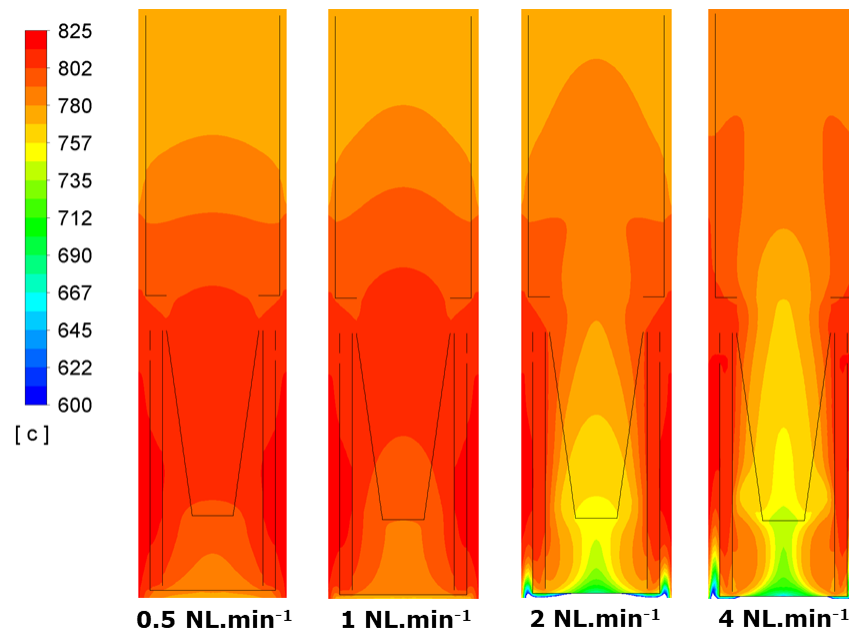


Figure 2-12. Contour plot of temperature at the middle section of the reactor (exchanger and sample crucible).

2.4 Conclusions

An induction heated reactor was designed and built to perform pyrolysis and gasification tests under controlled conditions, starting from a previous installation. Several modifications were proposed, which resulted in the NEW PYRATES setup that was described in detail in section 2.2.

Several experiments were conducted to characterize the heating rate of an inert ceramic sample (alumina) in the new reactor. The time-resolved temperature profile measured at the reactor tube surface showed a heating rate of $80 \text{ }^\circ\text{C}\cdot\text{s}^{-1}$. The transient temperature response for the solid sample indicated a slower heating rate (around $3 \text{ }^\circ\text{C s}^{-1}$) due to the additional thermal inertia imposed by the solid bed sample and the circulating gas. The waste materials which are investigated in the present study are, unlike alumina, subject to various changes during heating (phase changes in the case of plastics, char formation in the case of biomass) which have an influence on their heating rate. Their thermal behavior will be investigated in Chapter 4.

In steady state, the temperature profile was measured along the external surface of the tube. As a result of adjustments of the distance between the coil turns (pitch), the heat exchanger area was maintained at a temperature slightly higher than the set point, which favored the heat transfer between the hot surfaces of the exchanger and the gas entering the reactor. At the height of the sample, the

thermocouple readings inside the sample bulk and on the reactor surface were close to the setpoint temperature, with discrepancies of less than 10 °C. Above the sample crucible, an empty tube section of approximately 200 mm remained at a temperature 50 °C below the setpoint.

The CFD calculations confirmed the effectiveness of the heat exchanger and showed that a uniform temperature (800 ± 10 °C) could be obtained in the sample if the carrier gas flowrate is maintained at moderate values ($0.5 \text{ NL}\cdot\text{min}^{-1}$). Under these conditions, the residence time of the volatiles lies in the desired range of a few seconds.

The developed reactor does not seek to faithfully reproduce the reaction conditions experienced by a particle in a particular industrial reactor, which in reality are difficult to characterize. The reactor and the heating system allow reaching controlled and well-characterized thermal conditions, as well as several of the initially proposed design objectives (temperature level, residence time, uniformity of temperature in the sample). The thermal limitations of the device have been identified and discussed.

3. FEEDSTOCK AND METHODS

In the first part of this chapter, the solid recovered fuel (SRF) sample investigated in the present work is presented. After discussing the selection criteria of model materials representative of SRF, these are presented along with the methods used for their characterization. In the second part of the chapter, the experimental procedure followed for the pyrolysis and gasification tests is presented. Finally, the equipment and methods used for the analysis of reaction products are described.

3.1 Feedstock materials

In section 1.2, we described the typical categories found in solid waste derived fuels. It was observed how the composition and chemical characteristics of SRF are deeply influenced by the source of the waste streams and the presence of certain materials. For the experimental studies of this thesis, a SRF reference sample was selected and is presented in section 3.1.1. In section 3.1.2, the selection criteria for the choice of individual model components representative of this SRF are discussed.

3.1.1 Solid Recovered Fuel

Several tens of kg of SRF fluff were provided by a French solid waste collection and treatment company. The site produces solid waste derived fuels using non-hazardous industrial waste, furniture waste, and bulky waste from disposal centers.

The SRF sample used in this work consisted in pellets of approximately 5 mm in diameter and 15 mm in length produced from a batch of the provided SRF. These pellets were prepared for the needs of one of the projects of the laboratory. Pelletization allows reducing the variability in composition, size and density. For our experiments, pellets were cut to be approximately 5mm in length, as shown in **Figure 3-1**.

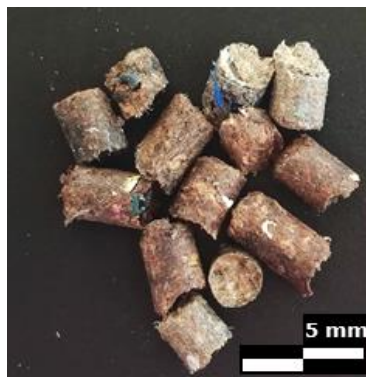


Figure 3-1. SRF pellets used for this study.

A characterization of a batch of the same SRF was previously conducted by Lucas le Martelot, a researcher from our laboratory. It is detailed in **Appendix D**. Starting from a few kilograms of the raw fluff, he carried out a sampling and fractionation procedure according to the quartering method. Then he performed a manual/visual sorting, separating the coarse particles retained on an 850 μm sieve in 9 fractions: hard plastics, soft plastics, textiles, paper/cardboard, wood, foam, expanded polystyrene, elastomers, and inert materials. For the particles under 850 μm , manual sorting was no longer possible,

and they were gathered in the “fines” category. The material composition of the SRF determined from the manual sorting is shown in Figure 3-2.

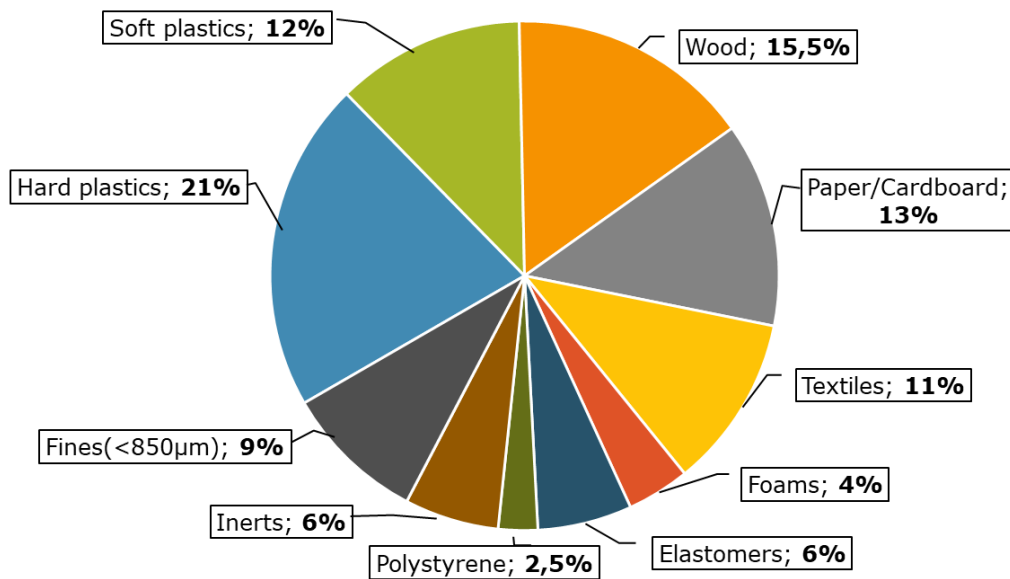


Figure 3-2. Material composition (wt. %) of the SRF fluff.

The fossil derived materials are found in hard and soft plastics, synthetic rubbers, foams, and polystyrene. Expanded polystyrene was sorted in a single category because it was easily identifiable. In total, fossil derived materials account for 45 % of the total mass of the sample. The lignocellulosic materials are wood, cardboard and paper, and represent almost 30 % of the sample mass. The textile fraction is of 11 wt.%. This fraction can contain materials made of natural fibers, synthetic fibers, or a mixture of both. The inert fraction represents 6 wt.%. It contains rubble, plaster, ceramics, and elements containing metal such as electrical cables. The “fines” fraction, with particles under 850 µm accounts for 9 wt.%. It can contain organic matter but also soil and other minerals that usually come from the storage site.

3.1.2 Model materials

Individual model materials were selected to represent the fractions found in SRF. This selection was based on their prevalence. As the studied SRF was produced from industrial and bulky waste, we decided to use materials likely to be found in this type of waste streams. According to literature (Section 1.1.3) these materials are among the most prevalent fractions found in SRFs, and they can represent also other derived fuels. Inert materials were not considered since they are usually removed

during the production of SRF pellets. The fine fraction was also intentionally left out because it seemed difficult to find a single material which could represent accurately such a complex mixture.

Wood: Woody biomass are usually classified into softwood and hardwood. Spruce, used in pallets and construction, is representative of softwood (Grønli et al., 2002b). Beech wood is commonly used for furniture and paper making industry, and it is extensively used in biomass pyrolysis research as a hardwood reference (Wong et al., 2014). In terms of carbon, hydrogen and oxygen, both have a similar composition. It was decided to use beech wood as reference for the wood category, since hardwood is the most common type in France and other western European countries (Karjaleinen et al., 2001).

Paper/cardboard: Corrugated cardboard was chosen to represent the paper/cardboard category. It is essentially composed of cellulose. In TGA presents a first decomposition peak similar to natural textile fibers and natural rubber. Like paper, it contains mineral additives. (Grammelis et al., 2009) evaluated five different paper-based products: magazine, cardboard, newspaper, recycled and copy paper. They found that cardboard had the closest decomposition behavior when compared with real waste samples.

Soft plastics: Most products in the soft plastics category (bags, wrapping films and packaging) are made of polyethylene, so this polymer was chosen to represent this category.

Hard plastics: For the hard plastics, polyethylene (PE), polypropylene (PP) and PET (the only polymer with a significant oxygen content) were selected as representative materials. PVC was not considered as it is usually removed during the production of SRF, to reduce the chlorine content of the fuel and meet the criteria of most common standards. Polystyrene was not considered, since it represented only a small share of the total mass of the SRF.

Textiles: As said before, textile products are manufactured from natural fibers (cotton, wool), synthetic fibers (polyester, nylon), or their combinations under different proportions (Gerassimidou et al., 2020). Since polyester is the most used fiber in textile industry, PET was selected to represent this category.

Due to their low contents in the SRF sample, other minority fractions like elastomers and foams were not considered for the selection. The elastomer fraction can be important in other waste derived fuels like automotive shredder residue (ASR) which contain residues from car recycling, with high contents of waste tires and rubber materials (Vermeulen et al., 2011). The foam fraction, representing only 4 wt.% was also discarded. From its chemical composition (not shown here), it seems to be mainly composed of flexible polyurethane foams, with a high nitrogen content.

The model materials selected to represent the different fractions of the SRF studied in this work are shown in **Figure 3-3**.

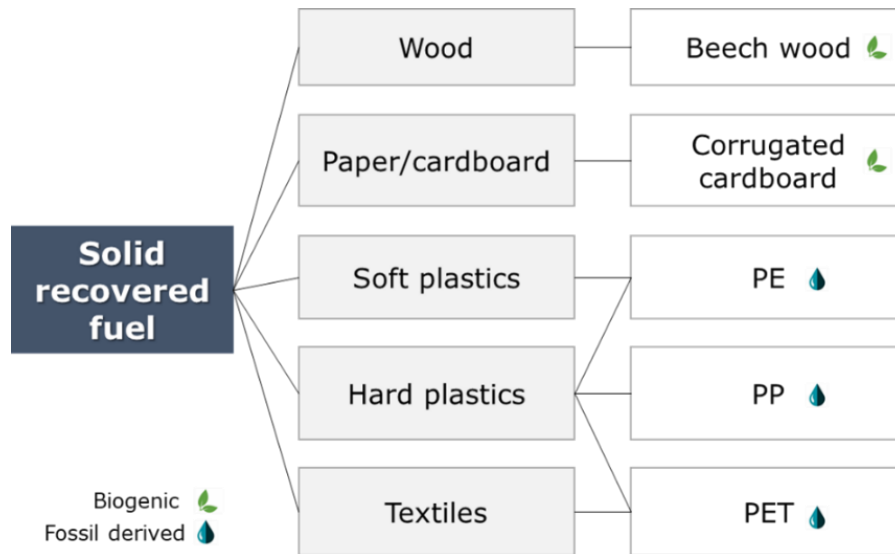


Figure 3-3. Selected model materials.

3.1.2.1 Procurement of model materials

The samples of each model material were taken from commercial products that can be easily found or purchased. This means that, unlike raw waste or the raw SRF fluff produced at a treatment facility, the selected materials were not contaminated by other waste fractions. Pictures of the samples are shown in **Figure 3-4**.

The biogenic category was represented by two materials:

- Beech wood pellets (5 mm diameter and 10 mm length) prepared from chips supplied by a local forestry company. For the experiments, the pellets were cut into particles of approximately 5x5 mm.
- A corrugated cardboard sample procured from discarded packaging boxes, which was cut into 5x5 mm pieces. The presence of ink was noted. No tape or staples were observed.

The non-biogenic category was represented by three fossil-based plastic polymers:

- A low-density polyethylene (LDPE) sample from laboratory bottles (without caps or labels) with a thickness of 1 mm. They were shredded into pieces with a size between 2 to 5 mm. From now on, this material will be addressed as PE.

- A Polypropylene (PP) sample from translucent containers (without caps or labels) of 1 mm thick, commonly used in laboratory work. They were shredded into 2 to 5 mm pieces.
- A Polyethylene terephthalate (PET) sample from water bottles (without caps or labels) of 0.4 mm thick, which were cut into 5x5 mm pieces.

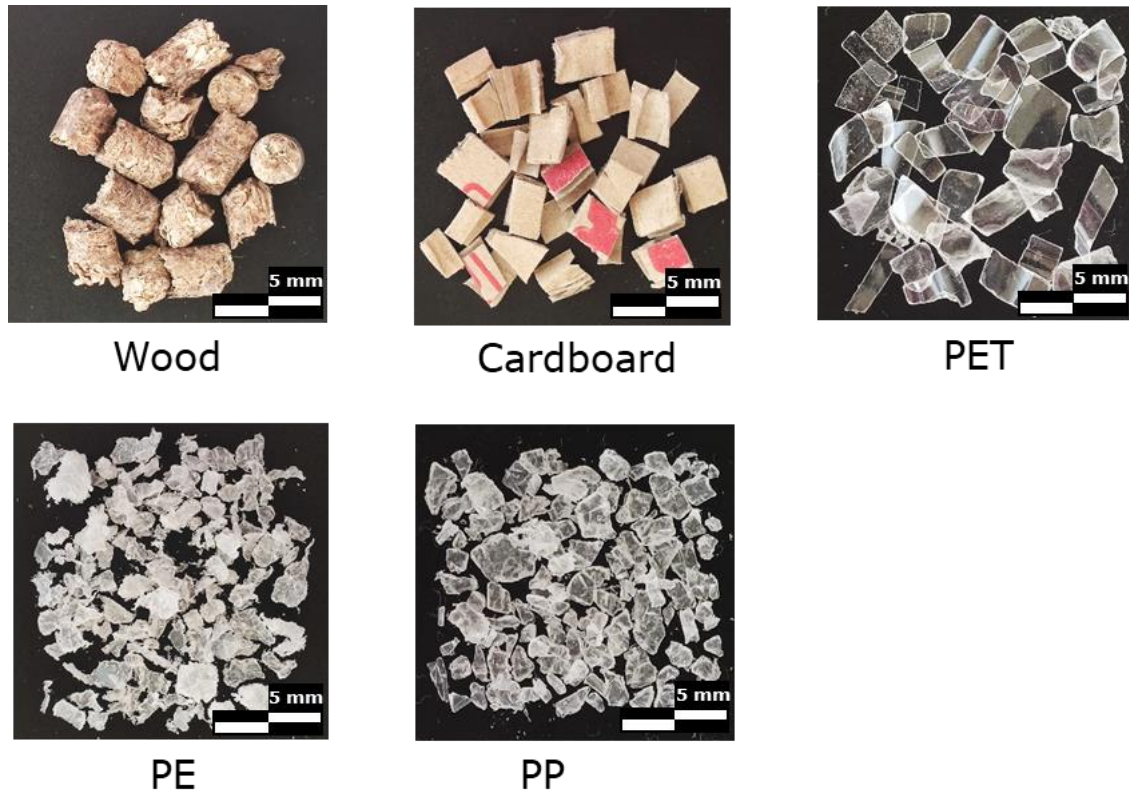


Figure 3-4. Model materials samples used in the experiments.

3.1.2.2 Preparation of model materials mixtures

For the study of the interactions between biogenic and non-biogenic fractions two mixed samples were prepared. The pellet form allows close contact between the materials and can enhance the possible interactive effects (Couhert, 2007; Grieco & Baldi, 2012). First, wood, PE, and PP samples were dried, crushed and screened. The fraction between the 1mm and the 1.2 mm sieve was selected. Then equal parts of wood/PE and wood/PP were weighed and mixed to form mixtures of (1:1) proportion. Finally, the mixture was compacted with a press by applying a compression load of 3 ton for 2 min. The obtained pressed pellets have a diameter of 10 mm, a height of 4 mm, and a weight of 0.8 g. A photograph of the Wood/PE pellets is shown in **Figure 3-5**.



Figure 3-5. Picture of pressed pellets of wood and polyethylene.

3.1.3 Feedstock characterization

The methods used to characterize the feedstock are described below:

- **Moisture content:** the moisture content was quantified by measuring the mass loss after drying the sample at 105 °C during 24h in an oven [Dry-line DL53, VWR], according to the NF EN 14.774 standard. Moisture content was expressed in wt.% (as-received basis), and it was calculated using equation 3.1:

$$\text{Moisture content (\%)} = \frac{m_2 - m_3}{m_2 - m_1} * 100 \quad [3.1]$$

Where:

m_1 : Mass of the empty crucible [g]

m_2 : Mass of the crucible with the sample before drying [g]

m_3 : Mass of the crucible with the sample after drying [g]

- **Ash content:** The ash is the residue obtained after combustion of the sample in air in a muffle furnace [LT 15/11/P330, Nabertherm]. The ash content of biomass samples is usually determined by combustion at 550 °C. However using this procedure can result in a deviation from the ash content observed in process performed at temperatures above 800 °C, such as gasification. Above 600 °C, the loss of volatile inorganic compounds and further oxidation of inorganic compounds can be observed for SRF samples (Aldrian et al., 2020). It is recommended to use a combustion temperature of at least 815 °C, which is closer to the typical temperatures at which our experiments are performed. The temperature profile for determination of the ash content at 815 °C follows the DIN 51719 standard method and is shown in Figure 3-6. The ash content (on dry basis) is calculated using equation 3.2.

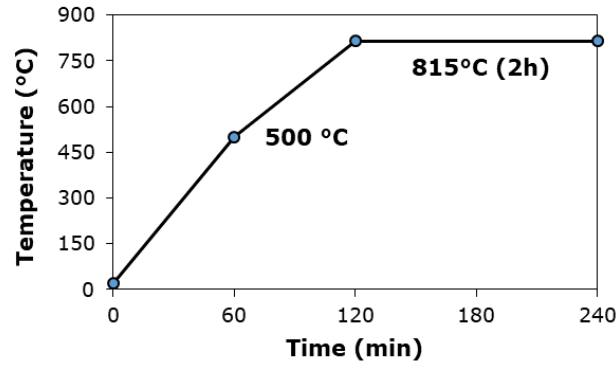


Figure 3-6. Temperature profile for the determination of ash content at 815 °C.

$$\text{Ash content (\%)} = \frac{m_3 - m_1}{m_2 - m_1} * 100 \quad [3.2]$$

Where:

m_1 : Mass of the empty crucible [g]

m_2 : Mass of the crucible with the dried sample before combustion [g]

m_3 : Mass of the crucible with the ash after combustion [g]

- Elementary analyses: The C, H, N and S contents were measured following the ISO 29541 standard which consists in the flash combustion of the sample using an organic elemental analyzer [Vario EL Cube, ELEMENTAR]. The O content was calculated by difference as shown in equation 3.3.

$$\text{Oxygen content (\%)} = 100\% - C\% - H\% - N\% - S\% - Cl\% - \text{Ash content\%} \quad [3.3]$$

The composition of the SRF and of the model materials and mixtures is shown in Table 3-1.

Feedstock	Moisture wt.% ^a	Ash wt.% ^b	C wt.% ^b	H wt.% ^b	N wt.% ^b	S wt.% ^b	O wt.% ^{bc}	Cl wt.% ^b
SRF pellets	5.17	16.38	48.0	6.00	1.33	0.47	26.68	1.14
Wood	7.3	2.53	46.8	6.70	0.2	0.01	43.67	-
Cardboard	6.69	8.80	43.6	6.00	0.30	0.13	41.17	-
PE	0.29	0.00	85.5	13.9	0.02	0.03	0.55	-
PP	0.30	0.00	85.8	13.7	0.01	0.03	0.48	-
PET	0.50	0.00	63.0	5.5	0.02	0.03	31.45	-
Mix Wood/PE	2.42	1.26	64.76	9.95	0.01	0.01	23.85	-
Mix Wood/PP	2.51	1.27	65.95	10.6	0.01	0.03	21.67	-

a. as received. b. dry basis. c. calculated by difference.

Table 3-1. Chemical composition and characteristics of the SRF and of the model materials.

As observed in Table 3-1, biogenic materials present similar compositions, and present an important oxygen content (higher than 40 wt.%) compared to the non-biogenic ones. As expected from their molecular formula, PE and PP plastic polymers present the highest carbon content (about 85 wt.%), no ashes and a very low oxygen content. PET presents an intermediate oxygen content (31.5 wt.%) and lower hydrogen and carbon contents in comparison with the other plastics. The SRF pellets have a carbon content similar to that of wood, and the highest ash content (16.4 wt.%). Lastly, the differences between the measured compositions for both mixtures and the linear sum of the measured composition for the individual components is lower than 5%.

In Figure 3-7, the atomic H/C and O/C ratios of the SRF sample, the model materials and the two mixtures used in this study are represented and compared to those of the biogenic and fossil materials listed in sections 1.2.1 and 1.2.2.

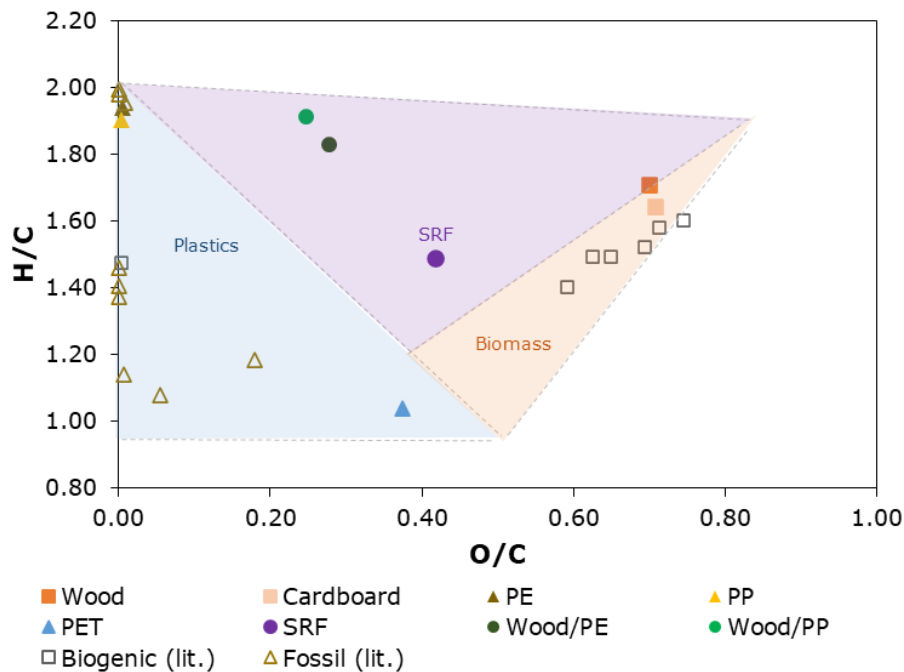


Figure 3-7. Van Krevelen diagram for the different samples used in this study and other common waste materials.

The different families of materials can be grouped in zones in the diagram, as suggested by several authors in literature (Ranzi et al., 2016). Biogenic materials are clustered at the right-hand side due to their higher oxygen content. Most plastic materials are placed on the left part of the diagram, with a null or low oxygen content. PET has the lowest H/C ratio of all materials, and it differs from the other plastics due to its elevated oxygen content. SRF and solid waste fractions have intermediate locations in the diagram and could be represented as combinations of the selected model materials.

3.2 Experimental procedure and conditions of the tests

3.2.1 Pyrolysis tests procedure and conditions

For the pyrolysis tests, the crucible was filled with 1 to 4 g of dried solid feedstock and placed in the reactor. Prior to each test, a pressure drop test was performed to ensure the tightness of the reactor and its connections. A nitrogen flowrate of 0.5 NL.min⁻¹ was used to purge the system before each run and carry the produced volatiles during the test. This value was chosen according to the results of the thermal characterization. The reactor was heated up to 800 °C and then held at this temperature for about 20 min. The estimated residence time for the volatiles was approximately between 4 and 5 s at 750 °C.

Once the heating system was turned off, nitrogen continued to be injected for at least another 20 min in order to flush out all the produced volatiles. They were swept to the condensation section, where the condensable species were collected in the impingers (Figure 2-3 in Chapter 2). The non-condensable gases flowed to the gas analysis section, to be finally collected in the Tedlar sampling bag. The gas volume collected in the bag (in m³) was measured using a diaphragm gas meter. Product gas was analyzed online with the NDIR analyzer, and the bag content was analyzed at the end of the test by Micro GC. After each experiment, the solid remaining in the crucible was collected and weighed. Each test was performed under the same conditions at least twice, with the exception of the Wood/PP mixture. Experimental conditions of pyrolysis tests are listed in Table 3-2.

Test	Feedstock	Mass	Bath 1	Bath 2
1	CSR	2,26 g	0 °C	-70 °C
2	CSR	2,36 g	0 °C	-70 °C
3	Wood	2,39 g	0 °C	-70 °C
4	Wood	2,43 g	0 °C	-70 °C
5	Cardboard	2,43 g	0 °C	-70 °C
6	Cardboard	3,34 g	20 °C	-10 °C
7	PET	1,52 g	0 °C	-70 °C
8	PET	1,55 g	0 °C	-70 °C
9	PE	1,55 g	0 °C	-70 °C
10	PE	2,04 g	20 °C	-10 °C
11	PP	1,57 g	0 °C	-15 °C
12	PP	1,57 g	0 °C	-10 °C
13	Wood/PE	2,44 g	0 °C	-70 °C
14	Wood/PE	2,51 g	0 °C	-15 °C
15	Wood/PP	3,10 g	0 °C	-10 °C

Table 3-2. Experimental conditions of pyrolysis tests.

3.2.2 Procedure and method for the determination of the produced gas flowrate

Some specific pyrolysis tests were performed at 800 °C with wood and PE samples, in order to continuously record the produced gas flowrate during pyrolysis. Another objective was to obtain information on the gas release duration in order to define the conditions of the gasification tests (in particular to adapt the duration of O₂ injection).

Readings in μGC analysis can only be taken at 3 min intervals, so this device was not adequate to follow the evolution of the produced gas species. The NDIR device was able to record the concentration of CO, CO₂, and CH₄ every second. However, it was observed that this device presented a very important delay (around 120 s) in its response time, and the only measurement of these 3 concentrations was not enough to evaluate the total gas flowrate.

To track the flowrate of produced volatiles, a differential pressure transmitter was used. Some tests were performed in order to check if the instrument and data collection system were adequate for our objective. They are described below.

- Calibration:

It is known that the flowrate of a fluid Q is directly proportional to the square root of the differential pressure between two points ΔP . This relation can be expressed as a simplified version of the Bernoulli equation, Eq 3.4 (k being a constant):

$$Q = k \sqrt{\Delta P} \quad [3.4]$$

In our case, one connection of the differential pressure transmitter was located at the outlet of the condensation system, just before the NDIR analyzer, while the other connection was set to atmospheric pressure. The output signal of the transmitter was proportional to the differential pressure. Using an inline resistance of 250 Ω, the output current signal (4-20 mA) was converted to an electric signal (1-5V), compatible with a data logger device [Graphtec GL450]. A measurement was recorded every 200 ms.

To determine the flowrate from the output signal, it was necessary to perform a calibration. The calibration of the device was made by recording the voltage output corresponding to several gas flowrate values fixed with a mass flow controller.

Three calibration runs were realized in steady state, using the same setup as in a regular test (including the five cold impingers used for tar condensation). The details of the calibration runs are explained below, and the results obtained for each test are shown in **Figure 3-8**.

- Test 1: nitrogen gas, reactor at ambient temperature.
- Test 2: nitrogen gas, reactor at 800 °C.
- Test 3: calibration gas bottle (composed of 53% N₂, 10% H₂, 10% CH₄, 10% CO, 15% CO₂, 2% O₂ and 400 ppm of C₂–C₃ hydrocarbons), reactor at ambient temperature.

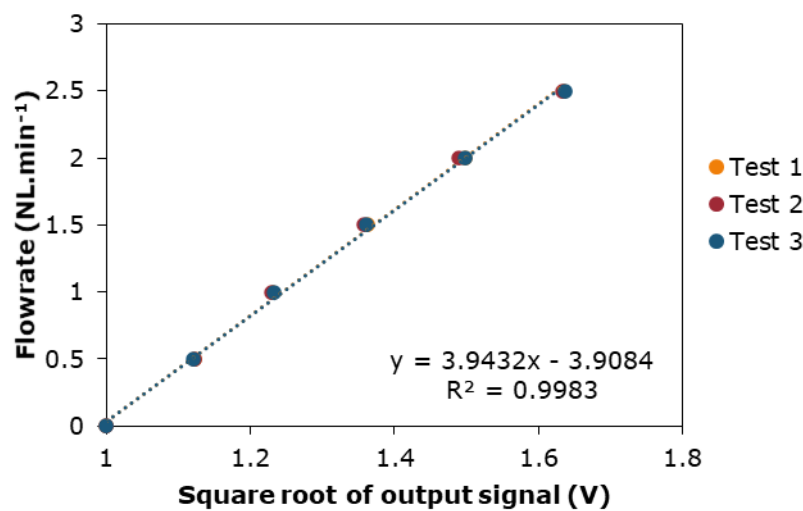


Figure 3-8. Calibration runs for the differential pressure transmitter.

The results obtained in the three cases are similar, which means that the transmitter response is not affected by either the temperature or the nature of the gas. Therefore, the equation shown in **Figure 3-8** was used to calculate the gas flowrate from the pressure transmitter measurement.

- **Determination of the response time:**

Supplementary tests were performed to characterize the response time of the system to a change in the flowrate setpoint. The gas was N₂, and the reactor was at first in steady state at 800 °C. For these tests, the transmitter response to three steps of different magnitudes (from zero to 0.5 NL.min⁻¹ to 1 NL.min⁻¹, and to 2 NL.min⁻¹) was recorded. The time $t = 0$ s corresponds to the time when the flowrate setpoint was increased, and $t = 40$ s the time when it was decreased to 0. The normalized flowrate response, calculated as the ratio of flowrate to its maximum setpoint value, is presented for the three steps in **Figure 3-9**.

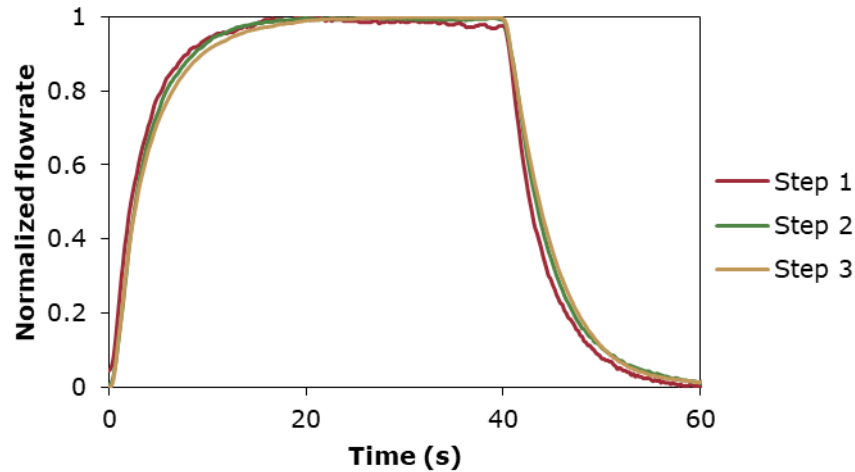


Figure 3-9. Time response of the system at 800 °C.

From **Figure 3-9**, two characteristics of the pressure transmitter response can be observed. First, no initial delay was observed between the change in flowrate setpoint increase and the measurement. Secondly, the response time was independent on the amplitude of the step, as the three tests showed the same behaviour both for the positive and negative steps. From these tests, we can conclude that the measurement device has a fast response time. The 95% of the maximum value is reached in 13 s. This response was not affected by the amplitude of the flow rate change.

- **Response during the transient temperature period:**

In preliminary tests, performed without any sample, a short peak in the flowrate was observed between the time the heating system was turned on and the time needed for the reactor to reach a steady temperature. This pressure peak was attributed to the expansion of the N_2 in the reactor due to the sudden temperature increase.

This N_2 flowrate peak was precisely determined with a blank test performed using a constant flow of nitrogen of $0.5 \text{ NL}\cdot\text{min}^{-1}$, in conditions like those of a pyrolysis test (section 3.2.1). The induction circuit was started ($t=0\text{s}$) and the reactor was heated up to 800 °C. The flowrate and the temperature profile of the reactor surface are displayed in **Figure 3-10**.

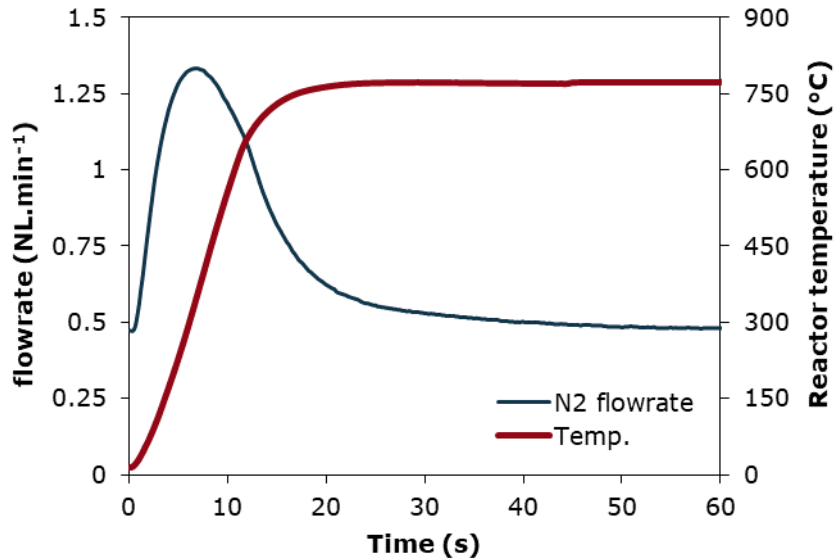


Figure 3-10. Pressure transmitter response in the first seconds after start-up of heating.

The N₂ flowrate peak has a duration of approximately 30 s. A correction was then applied for the flowrate measurements in real tests. It consisted in subtracting this N₂ flowrate response from the flowrate measured with the transmitter, to obtain the actual product gas flowrate coming from sample pyrolysis. The produced gas flowrate evolution during pyrolysis for each of the selected materials will be presented in section 4.1.2.

3.2.3 Gasification tests procedure and conditions

For the gasification tests, a mixture of air and N₂ was used as the oxidizing agent. In the pyrolysis tests, it was observed that the release of volatiles happened only during the first minutes. It was decided to maintain the air injection only for the first 3 min. Indeed, we wanted to avoid the combustion of the formed char after the volatiles were released. The gas products from char combustion would have then been mixed in the sampling bag with the products coming from pyrolysis and volatile matter reforming reactions.

As already presented in Chapter 1, the equivalent ratio (ER), can be defined as the ratio between the actual O₂ to fuel mass ratio and the stoichiometric O₂ to fuel mass ratio for complete combustion. ER is generally calculated for continuous operation, from the supplied air or O₂ flowrate and the feedstock feeding rate. In our case, the feedstock was charged in the reactor at the beginning of the test, while the air/nitrogen mixture was injected continuously into the reactor. For the present work, a time

average or global ER was thus calculated by considering the total mass of sample and of O₂ supplied during the limited injection time, as shown in equation 3.5:

$$ER_{\text{global}} = \frac{Q_{\text{air,sup}} \times t_{\text{inj}}}{m_{\text{air,stoich}}} \quad [3.5]$$

Where:

$Q_{\text{air,sup}}$ is the actual air flowrate [g.min⁻¹], t_{inj} is injection time [min])

$Q_{\text{air,stoich}}$ is the amount of air needed to achieve complete oxidation of the sample. It depends on the C, H, O composition of the feedstock [g].

The flowrate of the carrier gas (in this case air + nitrogen) was kept at 0.5 L.min⁻¹, like in pyrolysis tests. The objective was to keep the same temperature profile in the sample as in pyrolysis tests, as this profile could be influenced by the flowrate at higher values (section 2.3). It was also decided to have a sample mass of at least 2 g in order to be able to carry out the analysis of the products.

Three tests performed with the wood samples were performed initially in order to investigate the influence of the volume fraction of O₂ in carrier gas and of ER (as defined before). The air flowrate and the mass of the samples were adapted to reach three different values of global ER: 0.02, 0.05 and 0.1. On the basis of the results, the conditions for further tests with other materials were chosen. It was decided to keep the volume fraction of O₂ as constant as possible, and a global ER value of 0.05. This value was chosen because it was the only one that could allow meeting the two constraints mentioned before for all materials (gas flowrate of 0.5 L.min⁻¹, and sample with a mass of at least 2 g). The reaction conditions selected for the gasification tests are summarized in **Table 3-3**.

	Feedstock	Temp.	Mass	% O ₂ (v/v)	ER
1	Wood 1	800 °C	4.01	10%	0.02
2	Wood 2	800 °C	2.01	17%	0.1
3	Wood 3	800 °C	4.01	17%	0.05
4	PE	800 °C	2.04	19%	0.05
5	PET	800 °C	3.17	17%	0.05
6	PP	800 °C	2.12	19%	0.05
7	Cardboard	800 °C	5.00	17%	0.05
8	SRF	800 °C	3.48	17%	0.05
9	Wood-PE	800 °C	2.30	17%	0.05

Table 3-3. Experimental conditions for gasification tests.

For the gasification tests, dry air injection from a gas bottle (O₂: 20 vol.% ±2%, rest: N₂) was controlled by a mass flow meter/controller (Brooks Instruments, 0254 series) and injected from the second gas line (Figure 2-3). Nitrogen was injected along with the air in the first line, in order to complete a total gas flowrate of 0.5 NL.min⁻¹. The O₂ concentration in the carrier gas was first checked with the μGC. Once stable, the heating system was turned on. After 3 min, the air was stopped, and nitrogen flowrate was set at 0.5 NL.min⁻¹ to flush the produced volatiles. The gasification tests were performed only once.

3.3 Product collection, quantification and analysis

3.3.1 Quantification and analysis of the solid residue

The mass of the solid residue m_{char} (in grams) was calculated as the difference between the mass of the crucible containing the char after each test, and the mass of the empty crucible. The char yield (g.g_{daf}⁻¹) was calculated in relation to the mass of sample using equation 3.6.

$$y_{char} = \frac{m_{char}}{m_{sample,daf}} = \frac{m_{crucible,2} - m_{crucible,1}}{m_{sample,daf}} \quad [3.6]$$

Where:

$m_{crucible,1}$: Mass of the empty crucible [g]

$m_{crucible,2}$: Mass of the crucible with the solid residue after the test [g]

$m_{sample,daf}$: Mass of the sample on dry ash free basis [g_{daf}]

Elemental C, H, N, S, O composition and the ash content of the solid residue were determined using the methods presented in section 3.1.3.

3.3.2 Quantification and analysis of the permanent gas

A diaphragm gas meter was placed before the Tedlar bag, in which the non-condensable volatiles were sampled. The total gas volume was calculated from the difference between the two readings of the gas meter at the beginning and at the end of the gas sampling time. An uncertainty of ±1% of the measured volume was reported by the manufacturer. The measured volume at ambient conditions, was corrected to standard conditions ($P_N = 1 \text{ bar} = 1013.25 \text{ hPa}$, $T_N = 273.15 \text{ K}$) using Equation 3.7:

$$V_N = V_M * \frac{P}{P_N} * \frac{T_N}{T} \quad [3.7]$$

Where:

V_N is the volume at normal conditions [NL]

V_M is the volume measured at ambient conditions [L]

P is the pressure at metering conditions [hPa]

P_N is the pressure at normal conditions [hPa]

T is the gas temperature at metering conditions [K]

T_N is the temperature at normal conditions [K]

The bag content was analyzed at the end of each test, using a micro- GC, equipped with four columns and a thermal conductivity detector (TCD) for the quantification. The instrument is calibrated to detect and quantify the concentration of CO₂, CO, CH₄, H₂, C₂H₂, C₂H₄, C₂H₆, C₃H_x, C₄H₆, C₆H₆, and C₇H₈. At least 10 analyses were performed for each test, and the average values were considered. The analysis duration for each measurement was 3 min. Details on the device and the columns are presented in **Appendix E**.

The mass yield y_i for each gas i in [g·g_{daf}⁻¹] was calculated using equation 3.8:

$$y_i = \frac{V_N}{m_{sample,daf}} * \frac{M_i}{V_m} * C_{i,\mu GC} \quad [3.8]$$

Where:

$m_{sample,daf}$ is the sample mass on dry ash free basis [g_{daf}]

M_i is the molar mass of the i species in [g·mol⁻¹]

V_m the volume of one mole of gas at normal conditions of T and P (22,4 L)

$C_{i,\mu GC}$ is the volume concentration of the i species in the Tedlar bag, taken from the average of the micro-GC measurements.

3.3.3 Collection, quantification and analysis of the condensable species

Each of the five impingers was weighed at the end of each experiment, and their liquid content was sampled and stored at 5 °C. The difference in weight of the bottles between the beginning and the end of the test was not considered for the determination of the mass of the condensable species, because it was subject to various sources of experimental error, for example the uncertainty on the isopropanol evaporation during the tests.

Condensable species in each impinger were analyzed and their concentration was determined using a gas chromatograph with a flame ionization detector [GC- FID 7890A, Agilent Technologies]. More details of the device are shown in **Appendix E**. The mass of the i tar species (in g) was calculated by equation 3.9:

$$m_{tar,i} = \sum_{j=1}^5 C_{i,j} \times V_j \quad [3.9]$$

Where:

$C_{i,j}$ is the mass concentration of the i species in the impinger j [g.mL⁻¹]

V_j is the volume of solution in the impinger j [mL]

The total mass of condensable gases was calculated as the sum of each of the of the i tar species.

$$m_{cond} = \sum^i m_{tar,i} \quad [3.10]$$

The tar mass yield [g.g_{daf}⁻¹] was calculated in relation to the mass of sample on dry ash free basis using equation 3.11:

$$y_{tar,i} = \frac{m_{tar,i}}{m_{sample,daf}} \quad [3.11]$$

Quantified tar species were categorized into 5 groups according to the classification system proposed by the Energy research Center of the Netherlands (ECN) (Devi et al., 2005). This classification, which is showed in **Table 3-4**, is based on the solubility and condensation properties of the different tar compounds, which will define the downstream treatment conditions.

Trace amounts of C₃H_x, C₄H₆, C₆H₆, and C₇H₈ were detected in the FID analysis of the solvent in the impingers. These amounts were added to the corresponding masses obtained from micro-GC calculations for each of these species. In the ECN classification method, low molecular tar compounds like acids or ketones are not considered. Water is also a condensable product that can be recovered in the bottles. The moisture content in the tar samples can be measured by the Karl Fischer titration method. For our study, it was decided not to perform this quantification due to experimental constraints.

Tar class	Class Name	Properties	Compounds considered in this study
1	GC-undetectable	Very heavy tars, cannot be detected by GC	
2	Heterocyclic	Tars containing heteroatoms; highly water-soluble compounds	Thiofene Pyrrole Benzofurane Aniline Benzonitrile Phenol Benzopyridine Indole
3	Light aromatics	Usually light hydrocarbons with one ring; do not pose a problem regarding condensability and solubility	Ethylbenzene Phenylacetylene Styrene α -Methylstyrene o-Methylstyrene Indene
4	Light polyaromatics	Two and three ring compounds; condense at low temperature even at very low concentration	Naphthalene Naphthalene 2-methyl- Naphthalene 1-methyl- Biphenyl Naphthalene.2-ethenyl- Acenaphthylene Acenaphthene Fluorene Phenanthrene Anthracene
5	Heavy polyaromatics	Larger than three-rings; these components condense at high temperatures at low concentrations	Fluoranthene Pyrene

Table 3-4. Tar classification according to ECN.

4. RESULTS AND DISCUSSION

In this chapter, the experimental results are presented and discussed in five sections:

- Section 4.1 presents the evolution of the sample temperature and of the flowrate of volatile matter produced during pyrolysis at 800 °C, to have a better understanding of the devolatilization of the samples during their conversion in our reactor.
- Section 4.2 presents the distribution of the products generated in the pyrolysis of the SRF and model materials at 800 °C. The analysis of the produced gas, condensable products and solid residue is shown in detail.
- Section 4.3 compare the experimental results for biomass and plastics mixtures with the calculated values assuming an independent reaction of each individual material, to assess their interaction during their co-pyrolysis.
- Section 4.4 investigates the influence of the addition of an oxidant agent (air) during the conversion of the SRF and model materials, as an approach towards gasification conditions. Similarly to the previous sections, the different reaction products are characterized, and the results are compared with those relative to pyrolysis.
- Section 4.5 presents an empirical correlation developed to predict the pyrolysis yields of SRF from its initial elemental composition. First, the methodology is described, and then the predicted results are compared and validated with experimental results obtained in our setup. Finally, the accuracy of the obtained predictions is discussed.

4.1 Evolution of temperature and gas flowrate during pyrolysis

To have a better understanding of the devolatilization of the samples during their conversion, the time evolution of the temperature and the flowrate of produced volatile matter during pyrolysis was monitored. The experiments were performed with a reactor setpoint temperature of 800 °C. This investigation completes the thermal characterization of the reactor and gives an insight into the rate of the devolatilization reactions under the specific conditions of our device.

4.1.1 Time evolution of sample temperature

Specific tests were realized to measure the temperature inside the sample during pyrolysis. To do so, a thermocouple was placed at the middle height of the sample particle bed. The thermocouple was held in this position using a bracket supported on the top cover of the reactor. For this reason, these tests were performed with the top of the reactor open. The tests were performed with one biogenic material (wood), one fossil derived material (PE) and the Wood/PE mixture. The transient temperature evolutions for the three samples are displayed in Figure 4-1. The temperature measured by the pyrometer at the external surface of the reactor and the transient temperatures for the tests with the empty crucible and the inert material (ceramic) from the previous thermal characterization (presented in section 2.3.2) are shown for reference.

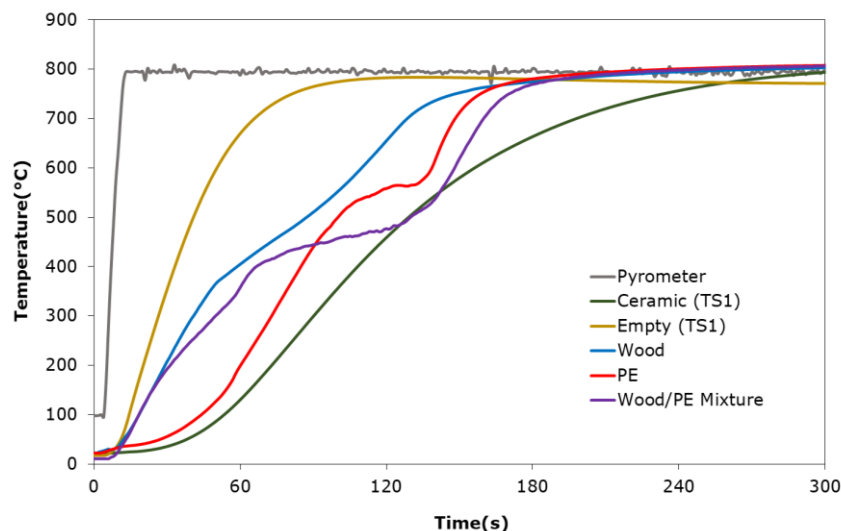


Figure 4-1. Time evolution of temperature during pyrolysis at 800 °C for wood, PE, and the wood/PE mixture.

As was already shown with the thermal characterization of the reactor, thermal gradients occur between the reactor surface and the bulk of the sample. The profiles obtained for the samples are between that

observed in the cases of the empty crucible and of the crucible filled with ceramic. The heating rate of the samples range between 4 and 6 °C.s⁻¹. It depends on the type of solid which undergoes pyrolysis.

The thermal properties depend on the nature of the solid fuel and can be influenced by the changes it is subjected to during its pyrolysis. In the case of lignocellulosic materials like wood, a part of the feedstock is volatilized while the rest remains as char. (Ahonen, 2009) observed that the density and thermal conductivity of pine wood (600 kg.m⁻³, 0.2 W.m⁻¹.K⁻¹) decreased as the sample was pyrolyzed. The measured density and heat conductivity for the char were 200 kg.m⁻³ and 0.1 W.m⁻¹.K⁻¹ respectively. Since the reduction of the density was more significant, the thermal diffusivity was higher for the char than for the initial feedstock. This was also observed by (Redko et al., 2020) who found that the diffusivity at 600 °C of raw wood (0.03 mm².s⁻¹) was significantly lower compared to that of its char (0.5 mm².s⁻¹).

Moreover, the temperature measurements allow identifying some the endothermic/exothermic phenomena during pyrolysis. For the wood, two inflection points are observed. The first one (near 300 °C) is associated with the degradation of cellulose and hemicelluloses which is exothermic, while the second one above 600 °C is related with the formation of char and the secondary reactions of the volatiles, also exothermic.

In the case of PE, under 300 °C, the temperature rise is much slower. Plastics have higher densities (900 - 1400 kg.m⁻³) and heat capacities (2000-2500 J.kg⁻¹.K⁻¹) compared with woody biomasses. When plastic polymers are heated, they are subject to some physical changes. First, the polymer solid state changes to a viscous or rubbery state once it reaches its glass transition temperature. Then, it goes to a liquid phase when the melting temperature is reached, in an endothermic transformation. Gases produced from plastic pyrolysis present diffusivities in the range of 8 to 70 mm²/s at high temperatures depending on the monomer (Honus et al., 2018b).

After 400 °C, we can observe a plateau for PE, followed by an inflection above 600 °C, related also with the secondary reactions of hydrocarbons and tar products. For the Wood/PE, the first part of the curve is like the one from wood, followed by a plateau around 400 °C and then an inflexion in a very similar way to the PE curve.

4.1.2 Time evolution of produced volatiles flowrate

To monitor the progress of pyrolysis volatiles release, the flowrate of produced gas during the pyrolysis of SRF and of the model materials was measured using the pressure transmitter and the procedure described in section 3.2.1. For all tests, a sample of 0.8 g of solid was used, and the flowrate was recorded every 200ms. The obtained curves are shown in **Figure 4-2**. The transient temperature evolution for the test with the empty crucible is presented as an indication.

No gas production is observed during the first seconds, in agreement with the delay for temperature increase. Once the temperature of the sample begins to rise, the decomposition reactions lead to the formation of volatiles. The earliest gas formation is observed for cardboard, reaching its maximum 30s after the start of the test, and finishing in about 75s. In the work of (Dong, 2016b) cardboard samples presented higher reactivity compared to poplar wood, which resulted in an earlier devolatilization and a gas yield two times higher.

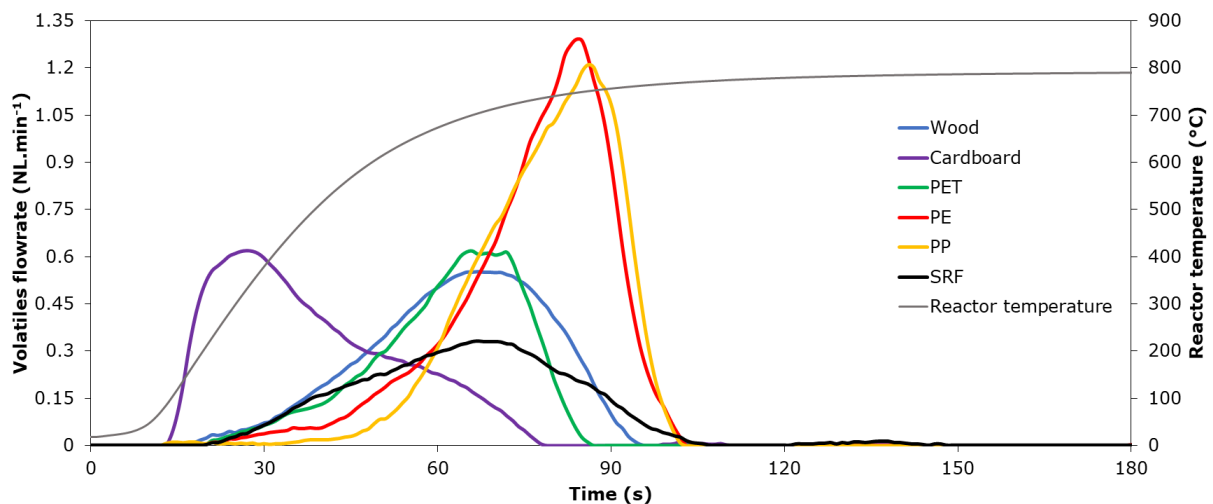


Figure 4-2. Time evolution of the produced gas flowrate during pyrolysis at 800 °C for SRF and model materials.

Volatile matter release for wood, PET and SRF starts a few seconds later. According to (Ojha & Vinu, 2015), CO is one of the first products to be released from holocellulose pyrolysis, usually from the degradation of C-O and C=O functional groups. These reactions are also the first steps in the degradation of PET, the only plastic containing oxygen in its structure. The scission of the ester C=O bonds favours the production of carboxylic acids, which then evolve into aromatic products releasing CO and CO₂. The gas profile for PET shows a progressive increase with a maximum at 70s, followed by a quick decay reaching zero after 90s. The time to reach the maximum rate of produced gas is also

near 70s for the wood sample. However, its pyrolysis ends later than PET. Lignin, present in woody biomass, decomposes over a broad temperature range between 200 to 900 °C (H. Yang et al., 2007). Lignin decomposition products are released at a later stage.

For PE and PP plastics, gas release starts later in comparison to all the other feedstocks. This delay can be linked to the endothermic phase transition already mentioned before (section 4.1.1). The maximum gas release is observed after about 80s for PE and PP. Both materials showed a rapid decay of gas production after 90s.

SRF contains diverse materials, which, as we have seen so far present different decomposition kinetic rates. The maximum gas release coincides with that of PET and wood. The duration of its gas release is the longest (about 110s), similar to that for PE and PP pyrolysis. Overall, these results show that pyrolysis is completed for all materials after 120s.

The devolatilization time (time for a 95% conversion) is function of the pyrolysis kinetics, the heat transfer from the reactor to the sample and of the intra particle heat transfer. In our case, the heat transfer limitations seem to play a major role in the global pyrolysis kinetic rate, as the release rates seem to be correlated to the sample temperature. In comparison, the devolatilization time observed in our reactor is slightly higher than that observed experimentally in a fluidized bed. For example, in the experiments of (Gomez-Barea et al., 2010) the devolatilization time of 6 mm wood pellets in a batch bubbling fluidized bed reactor at 800 °C was about 60s. The heat transfer coefficient is higher in the case of the fluidized bed, due to a good contact and mixing between the gas and the particles. (Santamaria et al., 2021), who studied the evolution of produced gases during the fast pyrolysis of wood and SRF pellets in a batch fluidized bed reactor at 800 °C. In their case, pyrolysis was completed after 150s for wood and 200s for SRF.

4.2 Pyrolysis of solid recovered fuel and its model materials

Pyrolysis tests of the SRF sample and of the five model materials were performed at 800 °C. The yield and composition of the main gas products, of the condensable volatiles and of the solid residue are presented for each sample.

4.2.1 Pyrolysis products distribution

The distribution of the reaction products from the pyrolysis of SRF and the model materials at 800 °C is shown in Figure 4-3. Product yields were calculated as the ratio between the mass of recovered products and the mass of sample (on dry basis). Solid residue contains the produced char and ash. Main gas products comprise all the non-condensable gases by micro-GC (CO_2 , CO , CH_4 , H_2 , C_2H_2 , C_2H_4 , C_2H_6 , C_3H_x , C_4H_6 , C_6H_6 , and C_7H_8), and also trace amounts of C_3H_x , C_4H_6 , C_6H_6 , and C_7H_8 detected in the analysis of the solvent in the impingers. In this work, the term “tar” is used to refer all the organic compounds with a molar mass higher of that of toluene. Their yields were calculated from the GC-FID analysis of the isopropanol content of the impingers. Water can be produced during the pyrolysis of some materials. In our case, the water yield was not determined.

Error bars displayed in the figures of this section, account for the repeatability of the tests which were performed twice for each feedstock.

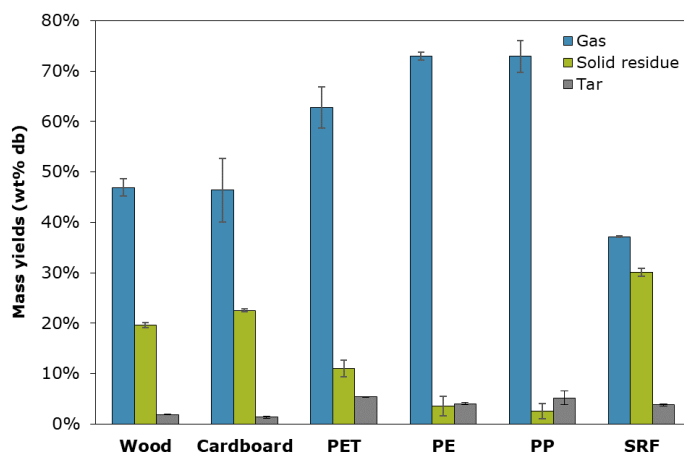


Figure 4-3. Distribution of pyrolysis products at 800 °C for SRF and model materials.

For the model materials and SRF, the initial sample is majorly converted to gas products. Polyolefin plastics (PE, PP) show the highest gas yields above 70 wt.%. PET follows with 62 wt.%. The gas yield is similar for the two biogenic materials (around 45 wt.%), while SRF presents the lowest gas yield (37 wt%).

The yield of solid residue represents 30 wt.% of the initial mass for the SRF sample, due to its high ash content. The solid yield is also high for the biogenic materials (20 wt.%). This can be linked to the fixed carbon content, which reaches 17 wt.% for beech wood (section 1.1.3). For cardboard, the fixed carbon content is lower (6.9 wt.%), however the residue from cardboard contains more ashes than the one from wood, as will be shown in section 4.2.5. PET which has an important oxygen content show a solid yield of 11 wt.%. In the case of PE and PP, the solid residue represents less than 3 wt.% of the initial mass, which is again in agreement with a low fixed carbon content. The tar yield is about 5 wt.% for the PET and PP, followed by SRF and PE (4 wt.%), and biogenic materials (around 2 wt.%).

4.2.2 Distribution of initial C, H and O in pyrolysis products

The overall mass balance (considering only the C, H and O elements) for the pyrolysis tests ranges between 65 and 80 wt.% (on daf basis). Similar balance closures were obtained by other authors (Neves et al., 2017; Win et al., 2020) in fixed and fluidized lab scale reactors. The deviations from a totally closed mass balance can be explained by the uncertainty of the experimental devices used, but also by the species that could not be quantified with these methods. To see how the initial elements are distributed in the products, the elemental C, H and O balances were calculated using the composition of the gas, solid and condensable products, all referred to the initial mass of each element in the raw dried feedstock. The carbon distribution is shown in **Figure 4-4**.

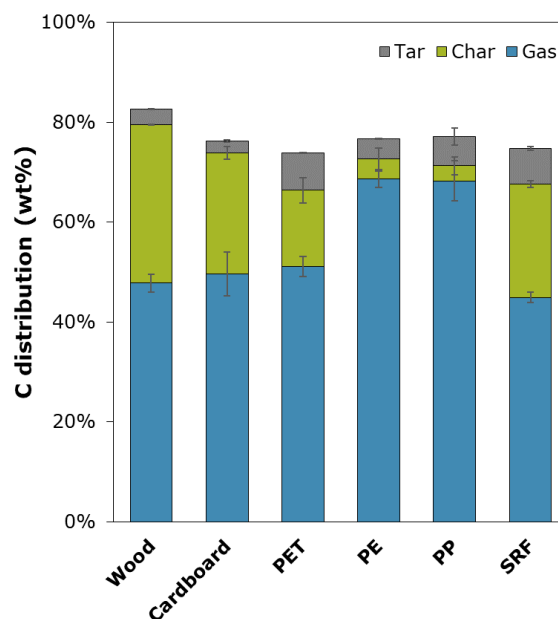


Figure 4-4. Carbon distribution in the pyrolysis products at 800 °C for SRF and model materials.

Carbon balance closure is between 75 and 80%. One explanation for the incomplete balance can come from the undetected species in the gas analysis. These include hydrocarbons between C_3 and C_6 , other than propane (C_3H_8), 1-3 butadiene (C_4H_6), benzene (C_6H_6) and toluene (C_7H_8), which are detected by micro GC. (Honus et al., 2018a) studied the pyrolysis of several plastic polymers in a fixed bed reactor at 700 and 900 °C. In their results, cyclopentadiene (C_5H_{10}) represented up to 4% in volume of the released gases during pyrolysis of PE. Other gases like butane (C_4H_{10}) isoprene (C_5H_8) and pentane (C_5H_{12}) were also detected for PE and PP. However, their amounts did not exceed 1 vol%.

Some C_3 - C_6 hydrocarbons were detected in the GC-MS analysis of the condensed products. However, it is not possible to find calibration standards adapted to GC-FID for some of these compounds. For this reason, it was not possible to quantify them. Deposits of condensable species were observed in the connection between the outlet of the reactor and the condensation section, as shown in **Figure 4-5**. These probably correspond to very heavy aromatic compounds (larger than class 5 tars), which are not detectable by GC columns. According to (Kiel et al., 2004) these compounds can also correspond to primary and secondary tars from lignocellulosic materials, for example lignin/sugar oligomers which were not cracked enough. however, it was not possible to determine their mass. At the end of each test, this surface was cleaned.

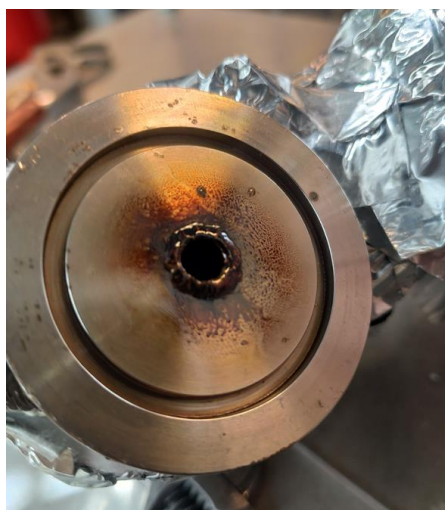


Figure 4-5. Tar deposits found in the connection between the reactor outlet and the condensation section.

The distribution of hydrogen and oxygen in pyrolysis products is shown in **Figure 4-6**. The hydrogen balance is close to 100% for PE and PP, while for the other model materials, it ranges between 60 and

90%. For oxygen, the balance is between 70 and 95%. It was not calculated for PE and PP since their initial oxygen content is negligible.

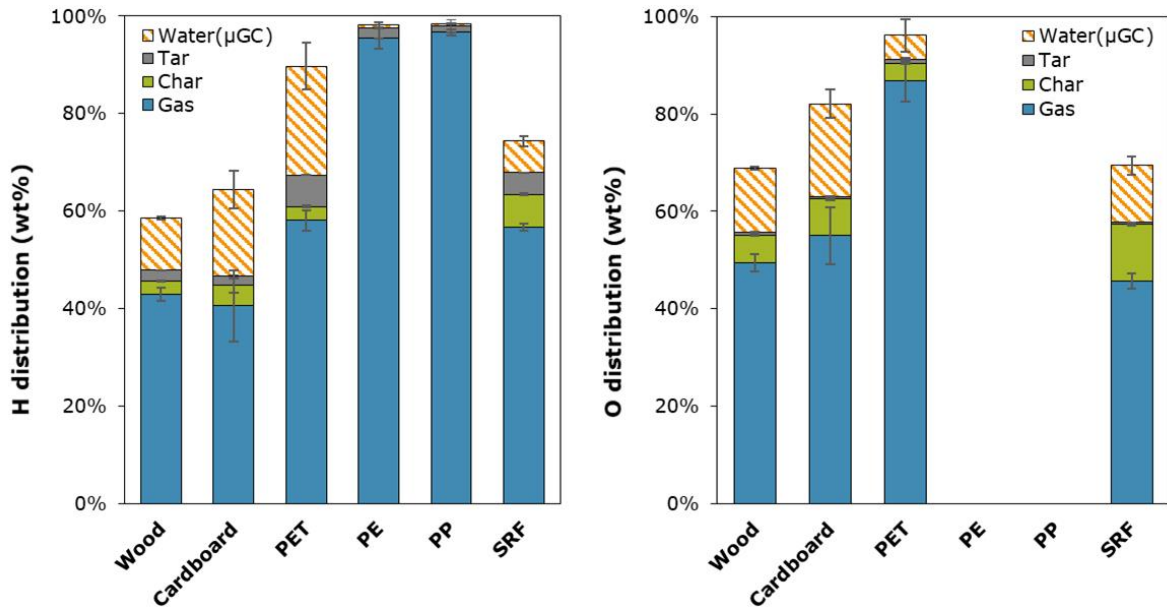


Figure 4-6. Hydrogen and oxygen distribution in the pyrolysis products at 800 °C for SRF and model materials.

Most of the missing fraction in both hydrogen and oxygen balances can be attributed to water. It is known that oxygen containing materials produce water during their pyrolysis. For example, (Tanoh, 2021) measured a pyrolytic water yield of 17% during biomass pyrolysis at 800 °C. In our case, only the water content remaining in the gaseous product was measured with the micro-GC. It represents 6 wt.% (on daf basis) of the wood, 10 wt.% in the case of PET and cardboard and 4 wt.% in the case of SRF.

4.2.3 Pyrolysis gas products yields

The yield of produced gases from the pyrolysis of SRF and of the model materials is shown in Figure 4-7. It is expressed in NL per gram of sample on dry ash free basis. The main species are hydrogen, carbon oxides, and light hydrocarbons like methane and ethylene (C_2H_4). Other hydrocarbons present lower yields. C_3H_x represents propene (C_3H_6) and propane (C_3H_8), which are quantified together with μGC as they have the same retention time in the μGC column. Light aromatics include benzene (C_6H_6) and toluene (C_7H_8), whose masses are calculated from the micro-GC measurements as well as the amounts quantified in the solvent by GC-FID. To explain the differences observed between the

different materials, we refer to their chemical compositions (Table 3.1), the proximate analysis of the initial feedstock, and the chemical structure of the monomers, both presented in section 1.2.

PE shows the highest total gas yield (above $0.8 \text{ NL}\cdot\text{g}_{\text{daf}}^{-1}$). Its long-branched structure follows a random chain scission mechanism during its devolatilization, giving high yields of hydrogen, methane and C2 hydrocarbons (Block et al., 2019). This is also observed for PP, which has a very similar chemical composition. Nevertheless, distribution of the produced hydrocarbons shows some differences. For PE, ethylene is the most abundant hydrocarbon, while PP shows higher yields of methane ($0.24 \text{ NL}\cdot\text{g}_{\text{daf}}^{-1}$).

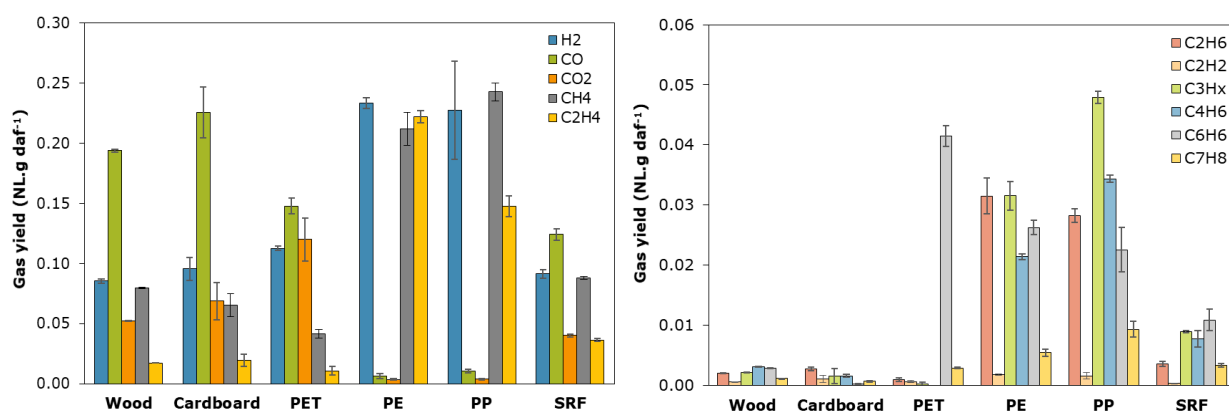


Figure 4-7. Gas yields from the pyrolysis at 800 °C of SRF and of model materials.

It is known that plastics tend to decompose into their monomers during pyrolysis. Around 600 °C, propene (C_3H_6) and butene (C_4H_8) are the main products of PP pyrolysis. At higher temperatures (above 750 °C), these products react to more stable species like methane, ethylene and butadiene (Westerhout et al., 1998). PE and PP do not present oxygen in their structures, however, they show very small quantities of CO and CO₂, probably because of trace amounts of air in the lines.

The presence of oxygen in the PET monomer is responsible for its high CO and CO₂ yields. The yield of light hydrocarbons (C₂-C₄) is much lower when compared to the other plastics, and it represents only 9% of the volume of the produced gases. In contrast, PET shows the highest benzene yield among all the studied materials. Secondary reactions from the intermediate products of PET pyrolysis like benzoic acid, favor the production of benzene at high temperatures (Li, 2019).

Gas yields are very close for the two biogenic materials (wood, cardboard), also present close elemental compositions (Table 3-1). CO is the most abundant component in both cases, followed by hydrogen and methane. CO and CO₂ yields are higher for the cardboard, while methane yield is higher for

wood. Raw materials used in the production of paper and cardboard are submitted to delignification processes, so their cellulose content can go up to 99% (Burra & Gupta, 2018a). (H. Yang et al., 2007) suggest that cracking of carbonyl functional groups of cellulose gives high CO yields, while the degradation of aromatic rings and methoxyl groups from lignin enhances CH₄ production. This would agree with our results of a higher CH₄ yield for wood which contains lignin, and a higher CO yield for cardboard mainly composed of cellulose. For both biogenic materials, the yield of C₂ –C₄ hydrocarbons is low. A small amount of light aromatics is found for wood. Benzene is one of the intermediary products from lignin decomposition at high temperatures (Zhou, Wu, et al., 2015).

Regarding the composition of the gas produced in the pyrolysis of the SRF, CO is the major gas component (0.13 NL. g_{daf}⁻¹), followed by CH₄ and H₂. The same qualitative result was obtained with RDF pyrolysis tests conducted by other researchers in fixed bed reactors 800 °C (Blanco et al., 2012; Daouk et al., 2018b). Gas distribution after SRF pyrolysis is intermediate between the different model materials. Plastics can contribute to the high yields of CH₄ and C₂ hydrocarbons, while lignocellulosic materials would be responsible for the majority of oxygenated compounds. It is known that the sample used here presents small fractions of other fossil derived materials such as PS and rubber, which can also produce methane during their pyrolysis (Zaini et al., 2019).

4.2.4 Tar species yields after pyrolysis

A picture of the tar impingers after a test is shown in **Figure 4-8**, the first one after the reactor being on the left, and the last one on the right-hand side. Small particles are retained in the glass wool of the first two impingers. It can be seen that the solvent in the last impinger is colorless, which indicates that most of the heavy tars and aerosols in the products are captured before the gas analysis section.



Figure 4-8. Picture of the tar impingers after a pyrolysis test.

The solvent with the condensed species in the tar impingers was sampled and analyzed using GC-FID. The tar yield was calculated as the ratio between the mass of quantified tar molecules over the mass of initial dry ash free sample. The quantified species were classified according to the ECN classification, already presented in section 3.3.3 in Figure 4-9.

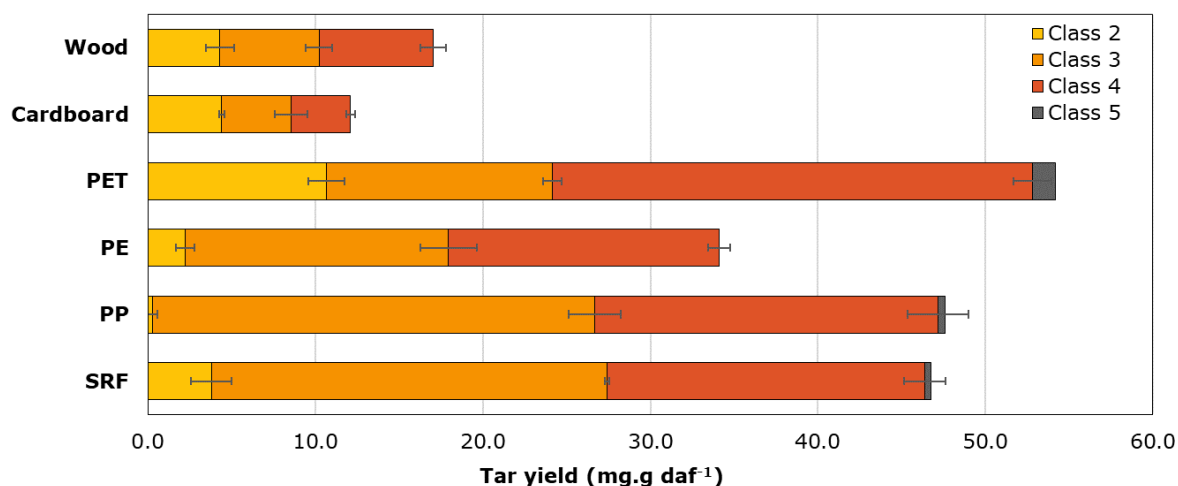


Figure 4-9. Yield of tar species after pyrolysis at 800 °C.

As shown in Figure 4-9, the total tar yield is much higher for plastics than for lignocellulosic materials (more than 33 mg.g_{daf}⁻¹, and less than 18 mg.g_{daf}⁻¹ respectively). When comparing the relative distribution of tar products by group, wood, cardboard and PET show the highest productions of heterocyclic species (class 2), which consist principally in oxygenated compounds. PE and PP tars are mainly composed by one ring aromatics (class 3), followed by two and three ring aromatics (class 4). PET presents the highest presence of heavy PAHs (class 5) among all materials. This could be due to the presence of one aromatic ring in the PET monomer structure, which can induce the formation of these heavy polyaromatic species. SRF also shows a high tar yield (45 mg.g_{daf}⁻¹), similar to the one of PP, with a slight content of class 5 tars.

Class 1 tar includes very heavy tar compounds that cannot be detected through GC, for that reason, they have not been considered for this study. One strategy for a rough estimation of class 1 tars is by gravimetry (Kiel et al., 2004). For a qualitative analysis of these heavy non-polar PAH compounds, High-performance liquid chromatography (HPLC) could be used.

The yields of the quantified tar species produced during the pyrolysis of SRF and of model materials are detailed in Table 4-1. For each sample, the most abundant component is highlighted in red, the second in blue and the third in yellow.

Class	Name	Formula	Wood	Cardboard	PET	PE	PP	SRF
2. Heterocyclics	Thiofene	C ₄ H ₄ S		0.33				
	Pyrrrole	C ₄ H ₅ N	0.72	0.62		2.25		1.33
	Benzofuran	C ₈ H ₆ O	0.98	1.01				0.73
	Aniline	C ₆ H ₇ N		0.85				
	Benzonitrile	C ₇ H ₅ N		0.02				0.51
	Phenol	C ₆ H ₆ O	2.61	1.58	9.83			1.09
	Benzopyridine	C ₉ H ₇ N						0.08
	Indole	C ₈ H ₇ N			0.83		0.29	0.05
<i>Total class 2</i>			4.31	4.41	10.66	2.25	0.29	3.79
3. Light aromatics	Ethylbenzene	C ₈ H ₁₀	0.56	0.72	0.27	0.87	7.61	1.20
	Phenylacetylene	C ₈ H ₆	1.77	0.16	0.94	0.64		0.67
	Styrene	C ₈ H ₈	0.98	2.17	9.80	10.68	10.37	17.15
	a-Methylstyrene	C ₉ H ₁₀		0.10			0.25	0.30
	o-Methylstyrene	C ₉ H ₁₀	0.54	0.39		1.01	2.70	0.61
	Indene	C ₉ H ₈	2.07	0.61	2.46	2.51	5.44	3.70
<i>Total class 3</i>			5.91	4.15	13.47	15.71	26.37	23.63
4. Light PAHs	Naphthalene	C ₁₀ H ₈	2.97	1.80	5.54	10.45	11.83	9.77
	Naphthalene. 2-methyl-	C ₁₁ H ₁₀	0.55	0.32	0.25	0.96	2.27	1.31
	Naphthalene. 1-methyl-	C ₁₁ H ₁₀	0.39	0.27		0.80	1.51	1.06
	Biphenyl	C ₁₂ H ₁₀	0.09		16.60	0.19	0.38	1.06
	Naphthalene.2-ethenyl-	C ₁₂ H ₁₀	0.29			0.40	0.86	0.78
	Acenaphthylene	C ₁₂ H ₈	0.70	0.30	0.73	1.09	1.49	1.30
	Acenaphthene	C ₁₂ H ₁₀			0.24		0.14	
	Fluorene	C ₁₃ H ₁₀	0.32		0.88	0.46	0.50	0.63
	Phenanthrene	C ₁₄ H ₁₀	0.57	0.23	3.55	0.80	1.14	1.90
	Anthracene	C ₁₄ H ₁₀	0.92	0.63	0.89	1.00	0.41	1.16
<i>Total class 4</i>			6.81	3.54	28.67	16.14	20.53	18.96
5. Heavy PAHs	Fluoranthene	C ₁₆ H ₁₀			0.39		0.18	0.20
	Pyrene	C ₁₆ H ₁₀			1.01		0.24	0.15
<i>Total class 5</i>			0.00	0.00	1.40	0.00	0.41	0.35
<i>Total Tars</i>			17.03	12.10	54.20	34.10	47.60	46.74

Table 4-1. Yields of principal tar species (in mg.g_{daf}⁻¹) from pyrolysis at 800 °C of SRF and model materials.

For the lignocellulosic materials, the main tar species formed during pyrolysis depend on their contents of cellulose, hemicellulose, and lignin. Acids, esters, and their derived tars like benzofuran and PAHs, are more abundant for cardboard and paper, both rich in cellulose. Phenols and furans result from lignin and extractives that are more common in wood.

The principal tar species from wood is naphthalene, followed by phenol. A very similar distribution of tar species was observed by (Tsalidis et al., 2018), who studied the tars from fast pyrolysis of wood pellets between 600 and 1000 °C. In their work no phenol was observed above 850 °C since it was converted to benzene and other PAHs. Like wood, cardboard tars contain styrene, naphthalene and phenol with styrene yield higher for cardboard than for wood. Some nitrogen-containing heterocyclic tars (aniline and benzofuran) are only detected for cardboard pyrolysis.

The two principal species in the PE and PP tar products are styrene and naphthalene, with very similar yields. Light aromatics (ethylbenzene, indene) and all the class 3 tars have higher yields for PP pyrolysis. In contrast to PE, the formation of heavy PAHs (fluoranthene, pyrene) is observed for PP.

As said before, these two plastics have similar chemical compositions. Their primary pyrolysis products consist mostly in alkanes and alkenes. They react via Diels-Alder reactions producing single ring tar species like styrene, and 2 to 4 ring aromatics, following the mechanism of **Figure 4-10**. The higher yields of cyclic compounds of more than one ring (naphthalene, acenaphthylene, pyrene) observed for PP, can be a consequence of the additional methyl group in its structure. The combination of several methyl radicals would lead to the formation of additional aromatic rings, as explained in the methyl addition cyclization (MAC) mechanism proposed by (Shukla et al., 2010).

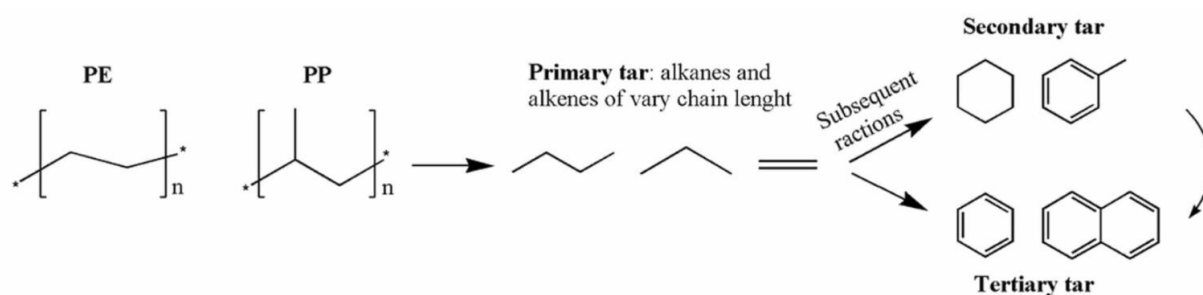


Figure 4-10. Evolution of PE and PP to tar species during pyrolysis (Lopez et al., 2018a).

The tar products of PET pyrolysis include phenol, styrene and biphenyl. A very high production of biphenyl is observed exclusively in the case of PET pyrolysis. The thermal cleavage mechanism during PET pyrolysis proposed by (Brems et al., 2011) is shown in **Figure 4-11**. Carboxylic acids are intermediate products coming from the PET monomer devolatilization. These molecules evolve into more stable compounds through decarboxylation reactions in which CO₂ is released. At high temperatures, benzoic acid reacts to produce benzene and biphenyl. Higher PAHs can grow from cyclation reactions involving biphenyl and phenyl (C₆H₅) radicals (Reizer et al., 2022).

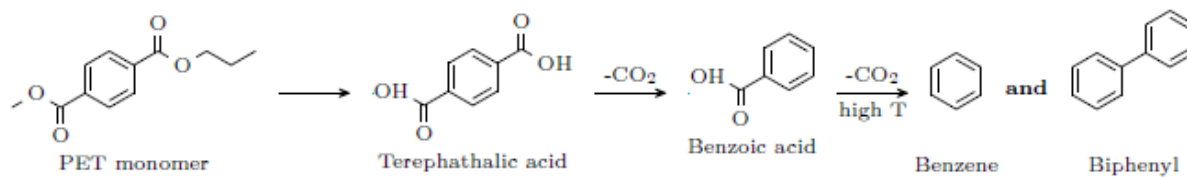


Figure 4-11. A proposed mechanism for PET pyrolysis (Li, 2019).

In the case of SRF, naphthalene and styrene are the main tar species. It has been shown that these molecules can result from pyrolysis of both biomass and plastics. The presence of class 2 tars is a sign of the presence of lignocellulosic compounds. The styrene yield is much higher for SRF than for all model materials. This could be linked to the presence of polystyrene in SRF, which decomposes into styrene monomers during pyrolysis. Styrene also presents an aromatic group in its structure, so it is consistent to observe compounds with 3 or 4 aromatic rings among the SRF tars. Benzene and acetylene are precursors of heavier PAHs compounds. The most common mechanism for PAHs growth is the “hydrogen abstraction and acetylene carbon addition” (HACA), favored by the presence of acetylene, which is a common product in the degradation of long chain hydrocarbons.

4.2.5 Pyrolysis solid residue

The chemical composition of the solid residue after pyrolysis was determined for all materials, except PE and PP which hardly produce any solid residue after pyrolysis. The char yield is determined as only the CHO fraction of the solid residue. The results are presented in Table 4-2.

	C (wt.%)	H (wt.%)	N (wt.%)	S (wt.%)	O (wt.%)	Ash (wt.%)	Char yield ($\text{g}_{\text{daf}} \cdot \text{g}_{\text{daf sample}}^{-1}$)
Wood	75.9	1.0	0.6	0.1	12.5	10.0	0.18
Cardboard	44.5	1.1	0.5	0.1	13.2	40.1	0.15
PET	87.0	1.4	0.2	0.1	9.2	2.0	0.11
SRF	36.0	1.3	1.0	1.0	11.0	49.7	0.18

Table 4-2. Chemical composition of the solid residues after pyrolysis at 800 °C, and char yields.

After the pyrolysis of PE and PP, a very small quantity of soot-like deposit covered the crucible; it was insufficient to perform analyses. Wood pyrolysis residue is mainly composed of carbon, with a small amount of ash (10 wt%). This composition agrees with the one observed for wood char obtained in a drop furnace at 800°C (Chen et al., 2013). For cardboard, 60% of the solid residue is composed of C, H and O, while the rest is the ash that remains in the solid residue. The char yield in relation to the

initial feedstock (in g_{daf}) is 18% for wood and 15% for cardboard. PET feedstock has a fixed carbon content of 6.9 wt.% and does not contain ash. After its pyrolysis, a char yield of 11 % is measured. For SRF, half of the mass of the solid residue is composed of ash, while its carbon content is of only of 36 wt%. Similar compositions with high ash content were observed in char from pyrolysis of RDF in other studies (Bhatt et al., 2021; Buah et al., 2007). The char yield of SRF was the same as that observed for wood.

Solid residues from wood, cardboard and SRF kept the structure of the original feedstock; only a shrinkage of the particles can be observed. On the contrary, the solid residue from PET pyrolysis did not keep the shape of the initial material. Photos of the solid residues are shown in Figure 4-12.

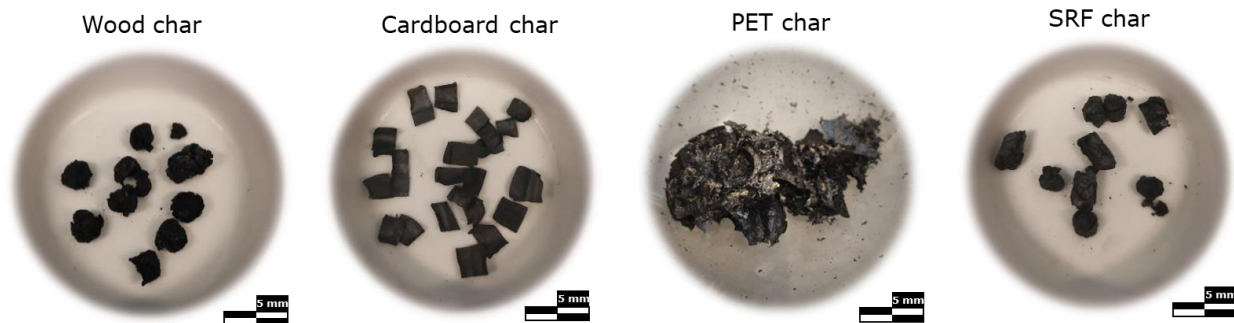


Figure 4-12. Char after pyrolysis at 800 °C.

The elemental compositions of the chars are compared in Figure 4-13 to those of the raw feedstock.

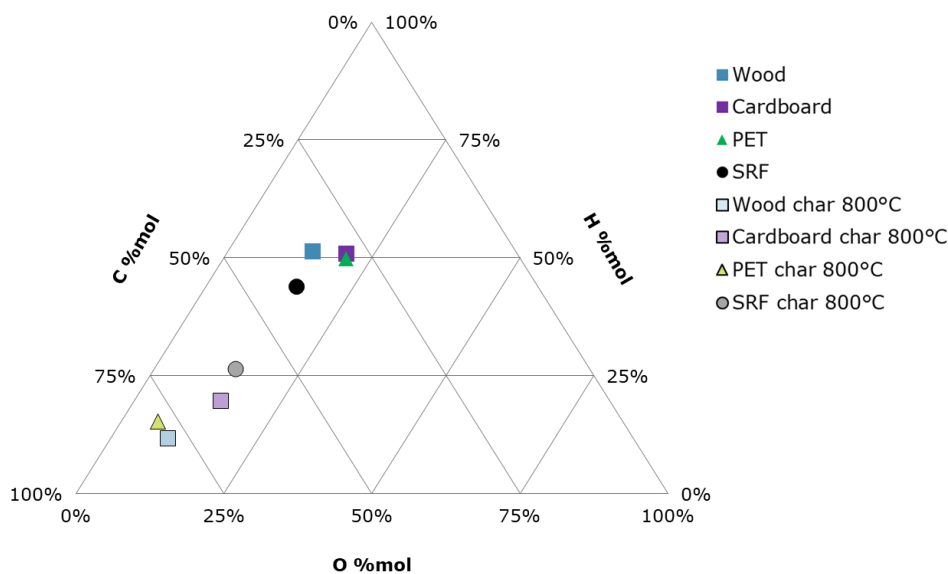


Figure 4-13. Molar composition (without ash) of char after pyrolysis at 800 °C and for the raw feedstock.

With pyrolysis, the oxygen and hydrogen contents of the solid decrease, while the carbon content increases. The evolution is less pronounced for cardboard and SRF, the materials with high ash content. In the case of PET, the presence of oxygen atoms favors the production of char, through carbonization reactions of the aromatic products produced at high temperature.

4.2.6 Distribution of the energy content of the initial feedstock

The energy content (EC) of each feedstock and products is defined here as the energy (in MJ) calculated from the lower heating value. The ratios of the EC in the products (gas, char and tar) to the EC of the initial feedstock are presented in Figure 4-14.

The energy content of the raw feedstock is evaluated from its lower heating value [$\text{MJ}\cdot\text{kg}_{\text{daf}}^{-1}$]. In the case of the char, the available quantity was not sufficient to measure its higher heating value, it was estimated from its chemical composition using the Boie's correlation (Boie, 1953):

$$HHV = 35.2C + 116.2H + 6.3N + 10.5S + 11.1O \quad [4.1]$$

$$LHV = HHV - 2.395 * (MC + 9H) \quad [4.2]$$

In which C, H, N, S and O are the weight fraction of each of these elements expressed in wt.%, and MC is the moisture content of the raw feedstock in wt.%.

For the gas and the tar fraction, the energy content was calculated considering the lower heating value for each of its species. The ratio between the EC of the produced gases and that for the initial feedstock is known as the cold gas efficiency (CGE).

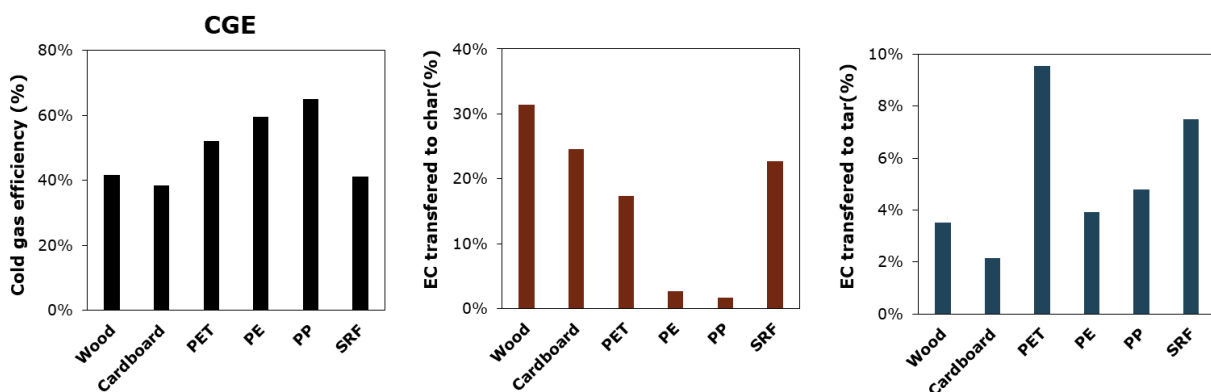


Figure 4-14. Ratios of the EC of the product to the EC of the feedstock after pyrolysis.

The CGE is globally lower for the lignocellulosic materials and the SRF sample. An important part of the initial energy remains in the solid residue, with a high calorific value around $30\text{MJ}/\text{kg}_{\text{daf}}$ for these

three samples. For PE and PP, the CGE value is higher, around 60%. In the case of PET, 17% of the initial energy of the feedstock is transferred to the char product, which presents a lower heating value of 33 MJ/kg daf. A considerable fraction of its feedstock energy remains in the tar fraction (10%). The sum of the total energy transferred from the raw feedstock to the pyrolysis products ranges between 66 and 80%. PET presents the highest value (80%), followed by, wood, SRF, PP, PE, and cardboard.

4.3 Interactions between of biomass and plastic materials during pyrolysis

As discussed in Chapter 1, biomass and plastics are the two main categories in SRF, and they can interact during their co-pyrolysis. Most of the studies in literature have studied these phenomena in TGA reactor devices, focusing more on the kinetics than on the yields of gas, tar, and solid products. Therefore, it is relevant to study the pyrolysis of biomass/plastics mixtures in our experimental device, which offers the advantage of a larger sample mass (few grams) and a higher heating rate than in TGA.

Wood was selected as representative for the biomass and the two olefins (PE, PP) were selected to represent the plastics. Two mixtures were studied: wood/polyethylene and wood/polypropylene. Only mixtures with a 1:1 mass ratio (dry basis) were studied, as according to literature they generally lead to the strongest interaction. As before, error bars account for the repeatability of the tests which were performed twice for the wood/PE mixture. For the wood/PP mixture, only one test was performed.

Calculated yields were determined for the mixtures, assuming no interaction between the two materials. The comparison of these calculated yields with the measured ones is used to put into evidence the interactions, if any. The calculated yields are determined as the weighted sum of the results observed for each of the materials individually, as in equation 4.3:

$$y_{i,calc} = \frac{1}{1 - x_{ash,mixt}} \times 0.5 \times [y_{i,wood} \times (1 - x_{ash,wood}) + y_{i,plastic} \times (1 - x_{ash,plastic})] \quad [4.3]$$

Where:

$y_{i,calc}$ is the calculated yield of the i product ($\text{g}\cdot\text{g}_{\text{daf}}^{-1}$),

$y_{i,wood}$ is the pyrolysis yield of the i product measured for wood ($\text{g}\cdot\text{g}_{\text{daf}}^{-1}$)

$y_{i,plastic}$ is the pyrolysis yield of the i product measured for PE or PP ($\text{g}\cdot\text{g}_{\text{daf}}^{-1}$)

$x_{ash,mixt}$, $x_{ash,wood}$, $x_{ash,plastic}$, is the ash content in the mixture, the wood, and the plastic (PE or PP) respectively (weight fraction).

The uncertainty (σ) for the calculated value is calculated from the uncertainties associated with each experimental value, using equation 4.4:

$$\sigma_{i,calc} = \sqrt{\sigma_{i,wood}^2 + \sigma_{i,plastic}^2} \quad [4.4]$$

4.3.1 Product yields from mixtures pyrolysis

The experimental yields for the mixtures are compared with the calculated values. The difference between the two values, expressed as a percentage, is calculated as the relative difference of the measured value to the calculated one. Figure 4-15 presents the products yields (on daf basis) for the Wood/PE and the Wood/PP mixtures.

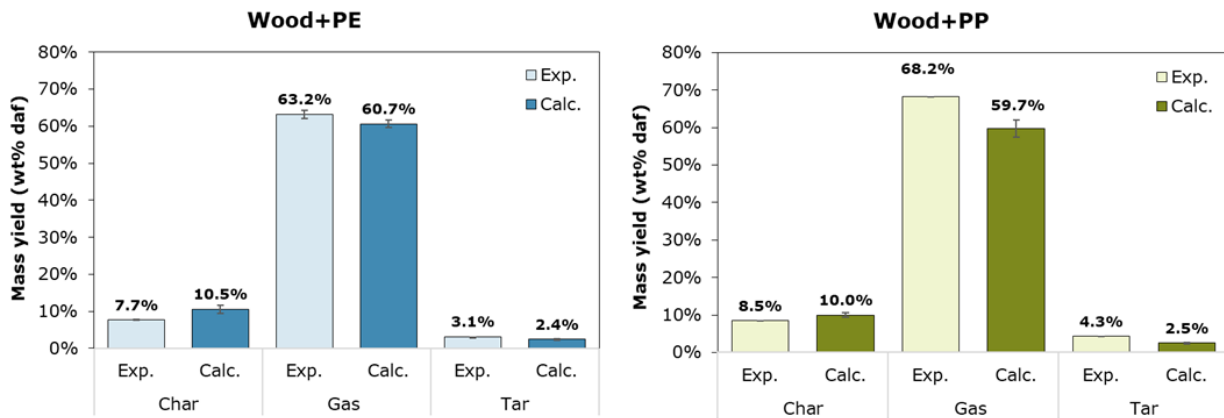


Figure 4-15. Experimental and calculated yields of pyrolysis products for biomass/plastic mixtures at 800 °C.

For both mixtures, the measured gas yield is higher than the calculated value. Differences of 4% and 14% are observed for the wood/PE mixture and the wood/PP mixture respectively. The experimental solid residue yield is smaller than the calculated yield in both cases, while the opposite is observed for tar. A synergistic effect is observed during the pyrolysis of mixtures, as the carbon conversion is favoured to gas products (Figure 4-16). This is in agreement with the findings of several studies (Burra & Gupta, 2018c; Win et al., 2020), in which this same effect was reported.

These differences between measured and calculated yields could be linked to gas phase reactions between the primary volatiles of biomass and the volatiles from plastics. The thermal decomposition of the long hydrocarbon chains from PE or PP, follows a random scission mechanism which results in a wide range of hydrocarbons and hydrogen radicals (Westerhout et al., 1998). Some studies (X. Liu et al., 2020; Ojha & Vinu, 2015) proved that during co-pyrolysis some of these hydrocarbons react

with OH radicals from biomass, yielding alcohols as well as other oxygenated products at moderate temperatures (500–600°C). At higher temperatures, these intermediate products participate in decarboxylation reactions, which result in higher yields of CO, CO₂, and tars.

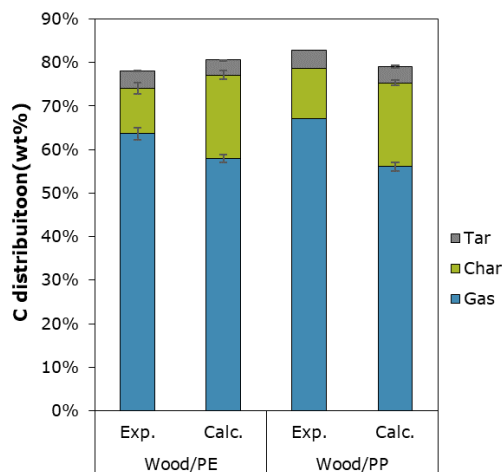


Figure 4-16. Experimental and calculated distributions of initial carbon for the pyrolysis of biomass/plastic mixtures at 800°C.

However, these differences between measured and calculated yields could also come from physical interactions. For example, biomass particles and char can interact with the plastics during the first stages of pyrolysis. In the mixture pellets, wood and plastic particles are in close contact. Once the temperature begins to rise, the wood particles are covered by the melted plastic. (Kasataka et al., 2020) showed that a high content of plastics in the mixture physically inhibits the condensation of wood primary pyrolysis products.

Indeed, during wood pyrolysis, char formation occurs from adhesion and condensation of pyrolysates like levoglucosan and lignin-derived phenolic compounds. In the case of the mixture, these condensation reactions are less likely to happen, as the contact between these compounds is physically inhibited by the melted plastic. Previously we observed that the char obtained after the pyrolysis of the wood kept the original form of the sample (Figure 4-12). In contrast, the solid residue obtained after the pyrolysis of the mixtures consists in small particles dispersed in the crucible (Figure 4-17).

The increased gas yield and the decreased char yield seem to be more pronounced when pyrolysis is performed in devices with high heating rate. In other studies of plastic/biomass mixture pyrolysis performed in tubular reactors at low heating rates (0.1°C.s⁻¹), the char yield remained unchanged, or it was even greater than expected without interaction. The slow temperature rise and a high residence

time of volatiles resulted in condensation and repolymerization reactions of tar species, adsorbed at the surface of char (Grieco & Baldi, 2012).



Figure 4-17. Char of the wood/PE mixture after pyrolysis at 800°C.

4.3.2 Gas products yields from mixtures pyrolysis

The calculated and experimental gas yields are compared in Figure 4-18. For the Wood/PE mixture, the measured hydrogen production is 13% higher than the calculated value. It is also higher for CO and CO₂ yields, but with a smaller relative difference. CH₄ and C₂H₄ yields are lower in the experimental case, while the opposite occurs for C₃-C₄ hydrocarbons. A similar trend was observed by (Grieco & Baldi, 2012) during the pyrolysis of polyethylene mixed with wood or paper. The presence of cellulose in the mixtures favoured the yield of oxygenated gases at the expense of C₂ hydrocarbons. The yields for benzene and toluene show no significant difference.

For the Wood/PP mixture, the relative difference between experimental and calculated yields for CO and CO₂ is higher than for hydrogen. Secondly, C₂ hydrocarbons show higher yields compared to the calculated values, contrary to what is observed for the wood/PE mixture. In the individual pyrolysis of PP, it was observed that high yields of C₃ and C₄ hydrocarbons were obtained. Compared to PE, C-C bonds of the PP backbone structure are broken forming a higher degree of branching structures, due to the lower thermal stability of the tertiary carbon atom (Almeida & Marques, 2016). These less stable species can react with the OH radicals of the biomass volatiles, resulting in oxygenated compounds that give CO and CO₂ at high temperatures.

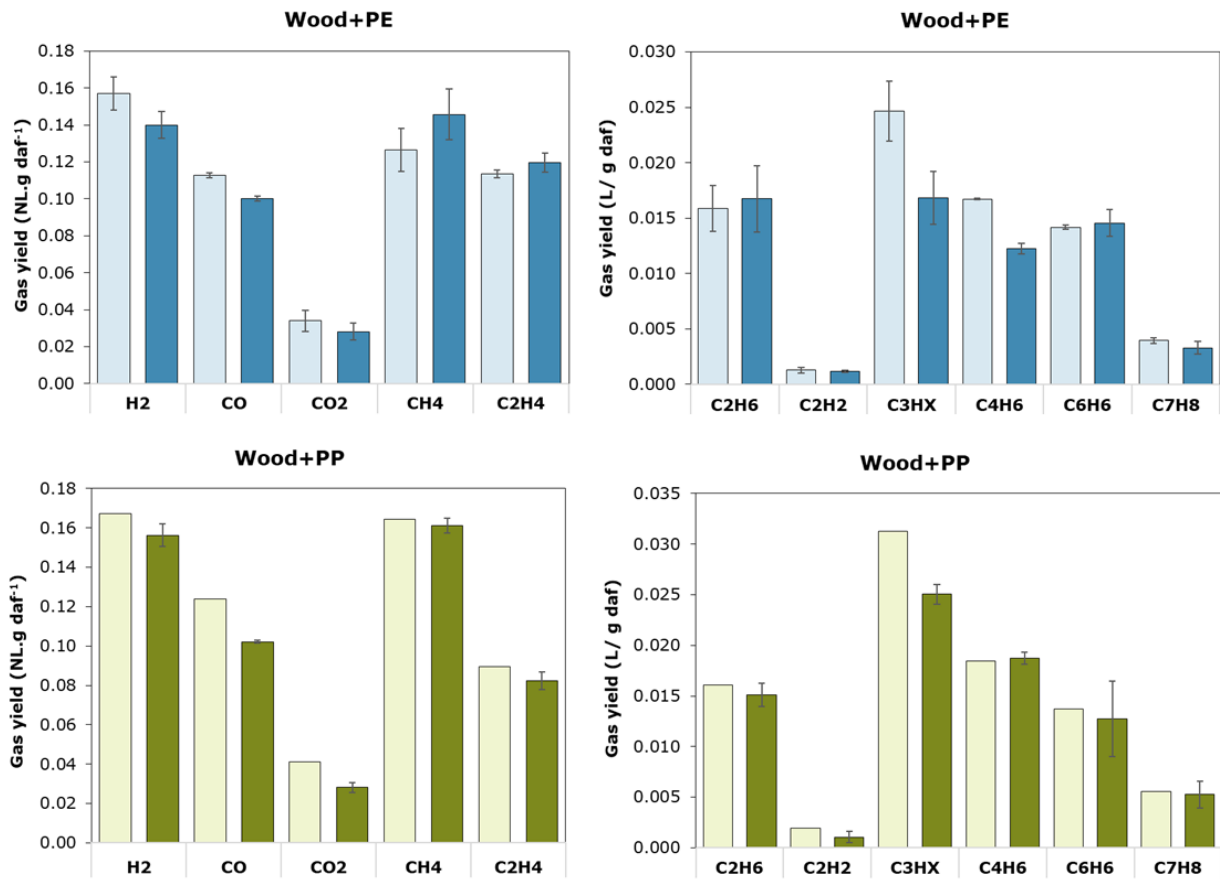


Figure 4-18. Comparison between the calculated and the experimental pyrolysis gas yields of biomass/plastic mixtures at 800 °C.

4.3.3 Tar species yields from mixtures pyrolysis

The yields of main tar species are compared in Table 4-3. As said before, the experimental tar yields are higher than the calculated ones. For the wood/PP mixture, these variations are less significant. In the case of the wood/PE mixture, higher yields of single ring aromatics (styrene, indene) and multi-ring aromatics (naphthalene, phenanthrene) can be observed. A similar result was found in (Y. Zheng et al., 2018) work, where the addition of LDPE during pine wood pyrolysis improved the selectivity towards BTX aromatics and naphthalene.

Class	Name	Formula	Wood/PE		Wood/PP	
			Exp.	Calculated	Exp.	Calculated
2. Heterocyclics	Thiophene	C ₄ H ₄ S				
	Pyrrole	C ₄ H ₅ N	2.90	1.12		
	Benzofuran	C ₈ H ₆ O	0.75	0.26	0.75	0.26
	Aniline	C ₆ H ₇ N			0.08	
	Benzonitrile	C ₇ H ₅ N			0.02	
	Phenol	C ₆ H ₆ O	0.84	0.67	0.87	0.67
	Benzopyridine	C ₉ H ₇ N	0.08		0.04	
	Indole	C ₈ H ₇ N	0.20		0.24	0.14
<i>Total class 2</i>			4.78	2.05	2.01	1.07
3. Light aromatics	Ethylbenzene	C ₈ H ₁₀	0.58	0.68	4.17	4.05
	Phenylacetylene	C ₈ H ₆	0.06	1.19	0.15	0.88
	Styrene	C ₈ H ₈	7.24	5.34	5.76	5.19
	a-Methylstyrene	C ₉ H ₁₀	0.08		0.14	0.13
	o-Methylstyrene	C ₉ H ₁₀	1.31	0.64	1.64	1.49
	Indene	C ₉ H ₈	3.77	1.81	3.65	3.27
<i>Total class 3</i>			13.04	9.66	15.52	14.99
4. Light PAHs	Naphthalene	C ₁₀ H ₈	7.91	6.04	6.62	6.73
	Naphthalene, 2-methyl-	C ₁₁ H ₁₀	1.20	0.64	1.43	1.29
	Naphthalene, 1-methyl-	C ₁₁ H ₁₀	0.83	0.51	0.94	0.87
	Biphenyl	C ₁₂ H ₁₀	0.35	0.14	0.31	0.24
	Naphthalene, 2-ethenyl-	C ₁₂ H ₁₀	0.63	0.28	0.58	0.52
	Acenaphthylene	C ₁₂ H ₈	1.01	0.73	1.09	0.93
	Acenaphthene	C ₁₂ H ₁₀	0.17		0.12	0.07
	Fluorene	C ₁₃ H ₁₀	0.51	0.32	0.51	0.34
	Phenanthrene	C ₁₄ H ₁₀	1.11	0.57	0.78	0.74
	Anthracene	C ₁₄ H ₁₀	0.61	0.87	0.43	0.58
<i>Total class 4</i>			14.34	10.10	12.81	12.30
5. Heavy PAHs	Fluoranthene	C ₁₆ H ₁₀	0.20		0.13	0.09
	Pyrene	C ₁₆ H ₁₀	0.12		0.18	0.12
<i>Total class 5</i>			0.32	0.00	0.31	0.21
<i>Total Tars</i>			32.48	21.82	30.65	28.57

Table 4-3. Comparison between the calculated and the experimental pyrolysis tar species yields of biomass/plastic mixtures at 800 °C.

4.4 Influence of oxygen addition on SRF conversion: towards gasification

To approach the reaction conditions of gasification, the presence of an oxidizing agent is necessary. In our case we used air, common in autothermal gasification in fluidized bed reactors. First, different gasification conditions were tested using wood samples. Then, a single condition was used to compare the gasification of SRF, of the model materials and of the wood/PE mixture. The choice of these conditions was explained in section 3.2.3. The results are compared with those obtained under pyrolysis conditions (ER=0).

4.4.1 Influence of ER on beech wood gasification at 800 °C

Some preliminary tests were performed using beech wood pellets, with different O₂/wood mass ratios. The sample mass and air flowrate were varied to obtain different values for the global equivalent ratio ER (ER = 0.02, 0.05 and 0.1). We have shown in section 4.1.2 that volatiles from pyrolysis are released in 2 min. For these tests, the duration of the air injection was of 3 min. Consequently, it is expected that the injected air mostly reacts with the produced volatiles.

The mass yields of gas, char (without the ash content) and tar products (on daf basis) and the distribution of the initial carbon on the reaction products are presented in Figure 4-19. They are compared with the results from pyrolysis (ER=0).

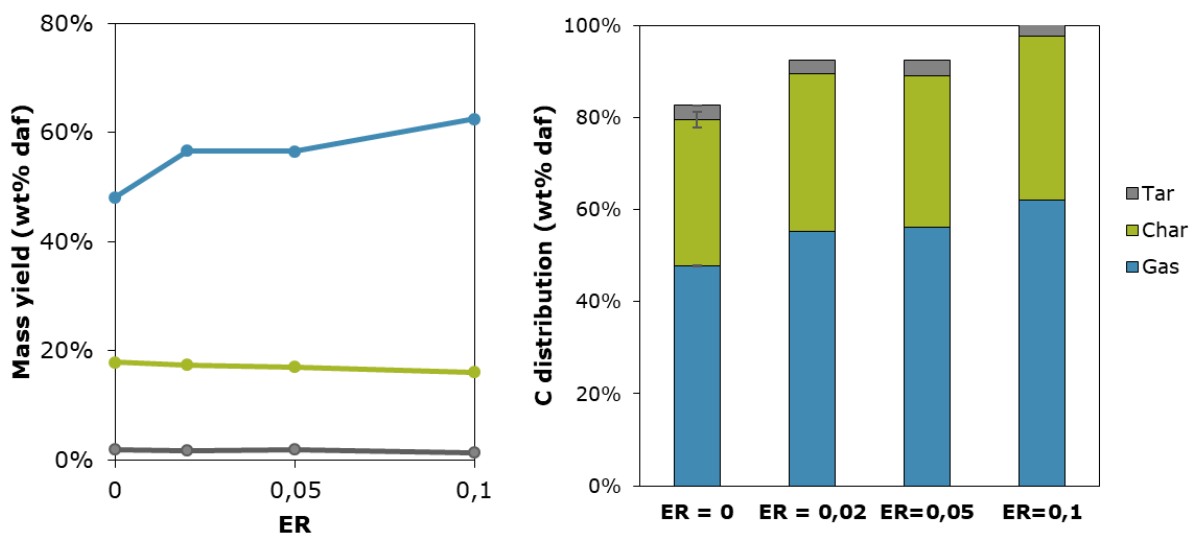


Figure 4-19. Mass yields of gas, char and tar products and carbon distribution for the pyrolysis and gasification tests with beech wood at 800 °C.

The carbon conversion to gas increases with ER, reaching 62 wt.% for ER=0.1. In the pyrolysis test, the char yield represents 18 wt.% of the initial sample (on daf basis). For the gasification tests, the char yield shows little variation, with only a slight tendency to decrease with increasing ER. This confirms that injected air mostly reacts with the volatile products, since the heterogeneous reactions between the char and the oxidant agent are slower compared to gas phase reactions.

In all cases, more than 30% of the initial carbon is recovered in char. No significant change is observed with the addition of oxygen. The carbon fraction in tar decreases as ER increases, except for the ER=0.05 case, which matches the tar yield of the pyrolysis case. However, this difference can be explained by the uncertainty of the measurements and the quantification of the condensed species. The test with the higher addition of air (ER=0.1) shows a fully closed carbon balance. This is an indication that some of the products that cannot be measured in pyrolysis tests, or their precursors (such as hydrocarbons with low vapour pressure) react with oxygen producing quantifiable gas species.

The effect of the addition of O₂ on gas species yields is detailed in **Figure 4-20**.

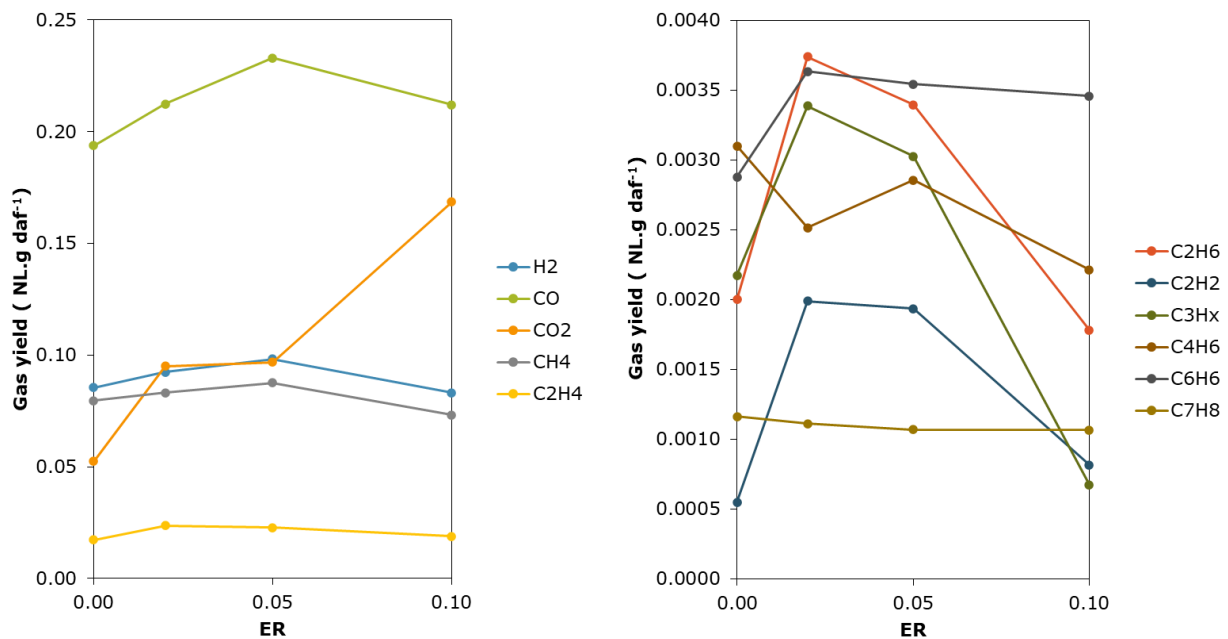


Figure 4-20. Effect of ER on gas species yields for wood at 800 °C.

In all cases, CO is the major gas species. The CO yield first increases with ER, reaching a maximum value of 0.23 NL.g_{daf}⁻¹, at ER=0.05, and then decreases to 0.21 NL.g_{daf}⁻¹ at ER=0.1. Hydrogen and methane follow the same trend. Compared to pyrolysis, higher gas yields of hydrocarbons are observed at ER=0.02 except for butadiene and toluene. As ER increases between 0.02 and 0.1, all the hydrocarbons yields tend to decrease. It is possible that reforming reactions involving hydrocarbons

and H₂O or CO₂ led to the increase in yield observed for CO, H₂, and CH₄ for ER between 0 and 0.05. However, at a higher oxygen concentration (ER=0.1) the observed yield for hydrogen and methane is lower than that observed during pyrolysis. Between ER=0.05 and 0.1, more CO₂ is formed at the expense of CO. More available oxygen from air can enable partial oxidation reactions of organic volatiles, producing CO and subsequently CO₂.

The total gas yield and the cold gas efficiency for these tests are shown in **Figure 4-21**. The total gas yield increases with ER, from 0.45 NL.g_{daf}⁻¹ in pyrolysis, to 0.68 NL.g_{daf}⁻¹ for ER=0.1. The cold gas efficiency for the gasification tests is slightly higher than that for pyrolysis, which is linked to the higher gas yield despite a lower LHV of the gas.

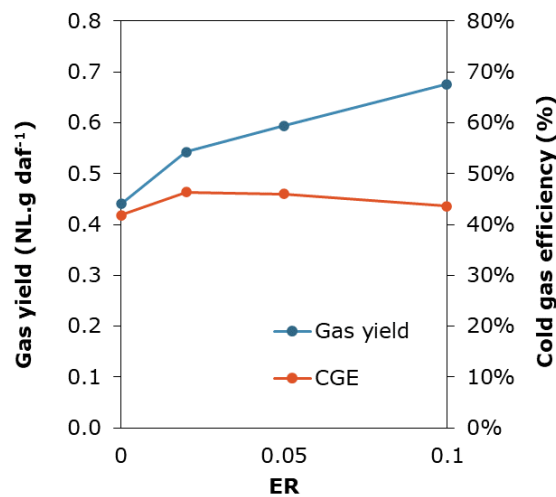


Figure 4-21. Effect of ER on gas yield and on cold gas efficiency for wood at 800 °C.

The influence of the addition of oxygen on the produced tar species yields is shown in **Table 4-4**. With the increase of ER, the total tar yield decreases, being 15 mg.g_{daf}⁻¹ for pyrolysis and 11 mg.g_{daf}⁻¹ for the ER=0.1 condition. This represents a decrease of 27% of the tar yield.

In the tar obtained during pyrolysis, around 50% of the quantified species are PAHs of two and three rings like naphthalene and acenaphthylene (Class 4 tars). The presence of oxygen induces the decrease of some of these species yields, that are no longer quantified at ER=0.1. In contrast, more class 3 tars are produced in the presence of air. For example, in all gasification tests, styrene yields are twice that observed in pyrolysis. A different trend was observed in the work of (Font Palma, 2013) who studied the influence of ER in the distribution of tar products during beech wood gasification in a fluidized bed at 800 °C. In their results, the increase of ER from 0.25 to 0.26 showed a high reduction of tar species of classes 2 and 3.

Class	Name	Formula	ER=0	ER=0.02	ER=0.05	ER=0.1
2. Heterocyclics	Thiophene	C ₄ H ₄ S				
	Pyrrole	C ₄ H ₅ N				
	Benzofuran	C ₈ H ₆ O	0.98	0.88	1.20	0.95
	Aniline	C ₆ H ₇ N				
	Benzonitrile	C ₇ H ₅ N				
	Phenol	C ₆ H ₆ O	2.61	2.39	2.86	2.10
	Benzopyridine	C ₉ H ₇ N		0.01	0.06	
Indole		C ₈ H ₇ N				
<i>Total class 2</i>			3.59	3.28	4.12	3.05
3. Light aromatics	Ethylbenzene	C ₈ H ₁₀	0.56	0.72	0.27	0.87
	Phenylacetylene	C ₈ H ₆				
	Styrene	C ₈ H ₈	0.98	1.79	1.89	1.72
	α-Methylstyrene	C ₉ H ₁₀				
	o-Methylstyrene	C ₉ H ₁₀				
	Indene	C ₉ H ₈	2.07	1.78	1.81	1.62
<i>Total class 3</i>			3.61	4.47	4.60	4.17
4. Light PAHs	Naphthalene	C ₁₀ H ₈	2.97	2.69	2.68	2.38
	Naphthalene, 2-methyl-	C ₁₁ H ₁₀	0.55	0.54	0.61	0.40
	Naphthalene, 1-methyl-	C ₁₁ H ₁₀	0.39	0.43	0.44	0.31
	Biphenyl	C ₁₂ H ₁₀	0.09	0.09	0.13	
	Naphthalene,2-ethenyl-	C ₁₂ H ₁₀	0.29	0.21	0.32	
	Acenaphthylene	C ₁₂ H ₈	0.70	0.60	0.64	0.49
	Acenaphthene	C ₁₂ H ₁₀			0.11	
	Fluorene	C ₁₃ H ₁₀	0.32	0.22	0.26	
	Phenanthrene	C ₁₄ H ₁₀	0.57	0.30	0.37	0.35
	Anthracene	C ₁₄ H ₁₀	0.92		0.23	
<i>Total class 4</i>			6.81	5.07	6.00	3.93
5.Heavy PAHs	Fluoranthene	C ₁₆ H ₁₀				
	Pyrene	C ₁₆ H ₁₀				0.09
<i>Total class 5</i>			0.00	0.00	0.00	0.09
<i>Total Tars</i>			14.01	12.82	14.80	11.15

Table 4-4. Effect of ER on tar species yields(in mg.g_{daf}⁻¹) for wood at 800 °C.

4.4.2 Influence of oxygen addition on the conversion of SRF and of model materials

We showed that the addition of oxygen modifies the yield and composition of the reaction products in the case of wood, depending on the ER value. Then, it was of interest to compare the effects of the oxygen addition for the other studied feedstock. Gasification tests were performed for the SRF sample, the five model materials and the Wood/PE mixture. The mass of sample and the air flowrate were adjusted so that the ER value was equal to 0.05 for all tests, while the temperature was maintained at 800 °C.

4.4.2.1 Influence of O₂ addition on product distribution

The distribution of initial carbon into gas, condensable and solid products is shown in Figure 4-22. The mass yields for gas, char, and tar products for gasification tests (ER=0.05) are compared in Table 4-5. The results obtained during pyrolysis (ER=0) are used as reference.

For both pyrolysis (ER=0) and gasification (ER=0.05), the initial carbon is mostly converted into gas. In general, the presence of O₂ favors this conversion, being 5% higher for all the model materials with the exception of polypropylene, for which the variation is minimal. In the case of SRF, the carbon conversion to gas increases by 10%, while for the wood/PE mixture a 13% increase is observed.

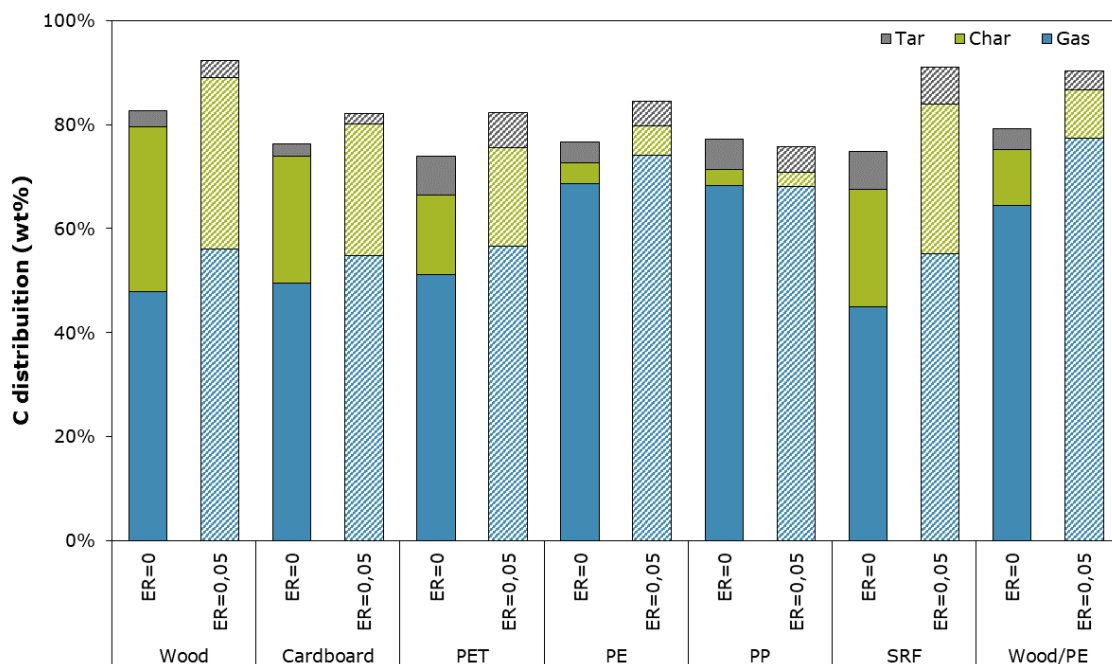


Figure 4-22. Conversion of the initial carbon to different products in pyrolysis and gasification of SRF, of model materials and of the wood/PE mixture at 800 °C.

ER	Wood		Cardboard		PET		PE		PP		SRF		Wood/PE	
	0	0.05	0	0.05	0	0.05	0	0.05	0	0.05	0	0.05	0	0.05
Gas yield (wt% daf)	48.1%	56.6%	48.1%	57.3%	62.7%	68.8%	73.2%	77.8%	71.3%	73.1%	44.4%	60.0%	63.2%	80.6%
Char yield (wt% daf)	17.9%	17.1%	15.0%	13.5%	10.9%	11.8%	3.1%	4.0%	1.9%	2.1%	18.3%	16.4%	7.7%	6.2%
Tar yield (wt% daf)	1.9%	1.9%	1.5%	1.3%	5.4%	4.4%	2.9%	4.2%	3.1%	4.1%	4.2%	4.4%	3.1%	2.7%

Table 4-5. Mass yields for pyrolysis and gasification tests at 800 °C, for SRF, for the five model materials and for the Wood/PE mixture.

The char yield in relation to the total sample mass (on daf basis) decreases for the lignocellulosic materials, while the opposite is observed for the plastics (Table 4-5). In the case of SRF, the char yield is 10% lower in gasification compared to pyrolysis. For the wood/PE mixture the char yield is 19% lower, a higher difference than that observed for wood or PE alone. This was seen also by (Ahmed et al., 2011) during gasification of PE and pinewood chips in a tubular semi-batch reactor a 900 °C. For PE and PET, the increase in char yield with O₂ addition is inferior to 10%.

The tar yield shows no significant variation in the case of wood and SRF. In the case of PE and PP, it showed a considerable increase, of 45% and 30% for PE and PP respectively. A more detailed discussion on the influence of air addition on tar products will be presented in section 4.2.2.3.

The carbon balance closure is better for gasification than for pyrolysis for all materials (except for PP which remains the same), and ranges between 80 and 95%. As discussed for the preliminary tests with wood in the previous section, this is probably due to the conversion into gas of some hydrocarbons and tar species that were not quantified in the pyrolysis tests or their precursors, which react with the O₂.

4.4.2.2 Influence of O₂ addition on gas species yields

The influence of the addition of O₂ on the main gas species yields is illustrated in Figure 4-23. To explain the observed trends, we will refer to the gasification reactions presented before in Table 1-9.

For PE and PP hydrogen is the principal component, and its yield shows a 10% decrease in the presence of oxygen. The reduction is less important for PET, SRF and cardboard, while wood and the Wood/PE mixture show the opposite trend with 15 and 5% increase respectively. The formation of water during wood devolatilization can favor the water gas shift reaction (R7) to the right side, giving higher yields of H₂ and carbon dioxide.

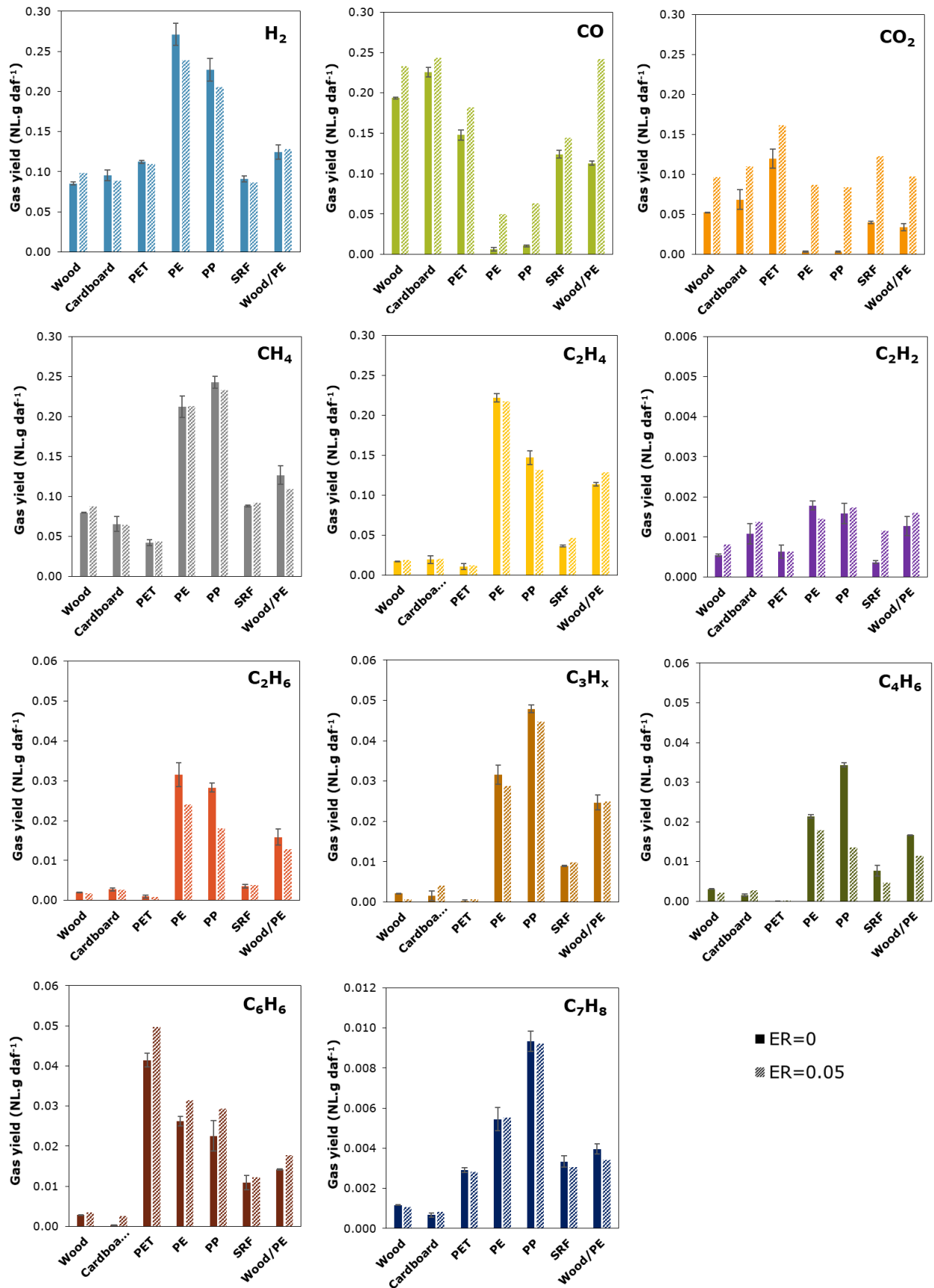


Figure 4-23. Yields of gas species obtained from pyrolysis and gasification of SRF, from model materials and from the Wood/PE mixture at 800 °C.

An increased production of carbon oxides is observed for all materials in gasification. With some O₂ available, reactions like the partial oxidation of hydrocarbons (R5), and the reforming of heavy tar species (R13) can be promoted, both resulting in higher yields of carbon monoxide. CO is the main component of the produced gas from the lignocellulosic materials, PET and RDF.

The highest increase in CO yield in presence of O₂ is observed for the Wood/PE mixture (from 0.11 NL.g daf⁻¹ in pyrolysis to 0.24 NL.g daf⁻¹). The CO yield with O₂ addition is far above the weighted average of the individual yields of its components (0.14 NL.g daf⁻¹). As discussed earlier, two synergistic effects are observed during the co-pyrolysis of wood/plastic mixtures: the interactions between volatiles and the inhibition of char forming reactions. This results in more carbon converted into gas products, notably CO. As more oxygen is available, the production of CO₂ is favoured. OH radicals can result from CO₂ conversion ($\text{CO}_2 + \text{H} = \text{CO} + \text{OH}$) (Hervy et al., 2021). Further oxidation reactions of hydrocarbons and tar products can subsequently increase the production of CO and CO₂ from their decarboxylation reactions.

An important reduction in the yield of light hydrocarbons is observed for the gasification of plastics. For example, the yield of C₃/C₄ hydrocarbons decreased by 16% for PE and by 60% for PP. Previous works have shown that propene and butene, both characteristic products of the pyrolysis of PP, are much sensitive to thermal degradation compared to the main pyrolysis products of PE (Westerhout et al., 1998). For the other materials, C₂-C₄ hydrocarbons yields are very close in pyrolysis and in gasification.

The yield of benzene and toluene is higher with O₂ addition than in pyrolysis for all samples, and the difference is more significant for the three plastic materials. During PE and PP gasification, some hydrogen seems to be converted, contrary to the other materials. This is in agreement with the results of (Win et al., 2019), who investigated the air gasification of plastic rich SRF and wood pellets in a fluidized bed reactor. With the increase of ER, the decrease of hydrogen yield was more pronounced for the feedstock with a high plastic content.

In the case of PET, the reduction in the hydrogen yield is less important, however, higher yields of benzene are observed. Intermediate species during the devolatilization of PET are unstable at high temperatures (see **Figure 4-11**). The presence of oxygen favours the conversion of these species, which can produce benzene, and CO₂.

For higher ER values, it could be expected that more hydrocarbons are converted, further reducing the calorific value of the gas produced. These trends have been observed in literature and are also in agreement with what we observed in preliminary tests with wood varying ER from 0 to 0.1. Results obtained by (Ouiminga et al., 2012) in a tubular reactor, similar to our device, showed that almost all hydrocarbons detected in the pyrolysis of a biomass waste at 800 °C, were converted to CO and CO₂ when the carrier gas was changed to an atmosphere containing 10% and 21% of oxygen. The residence time of volatiles was about 2 s for both conditions.

An air injection longer than 3 min would have favoured heterogeneous reactions between the char and the oxidizing agent, towards a complete combustion of solid char (R1 and R3) after the depletion of volatile hydrocarbons.

4.4.2.3 Influence of O₂ addition on tar yields

The distribution of quantified tar species is shown for each of the studied samples in **Figure 4-24**, and they are listed in detail in **Table 4-6**. The general trend is a reduction of tar yields with the addition of oxygen, except for polyethylene. In the case of PE, an increase of 16% on the tar yield is observed. This increase is especially linked to a higher naphthalene yield and also to the quantification of nitrogen based heterocyclic tar species, like aniline (C₆H₇N), that were not observed in pyrolysis.

Heavy PAHs observed during PP pyrolysis are not observed for the gasification test. It is possible that some of the intermediate pyrolysis products, which are precursors of PAH formation, react with the available oxygen. Less class 5 tars are also observed for PET and SRF samples. Biphenyl, which is one of the most abundant tar species from PET degradation, shows a 10% decrease in its yield with the addition of oxygen. This reduction is consistent with the results mentioned by (Choi et al., 2021), who studied the air gasification of PET in a two stage gasifier.

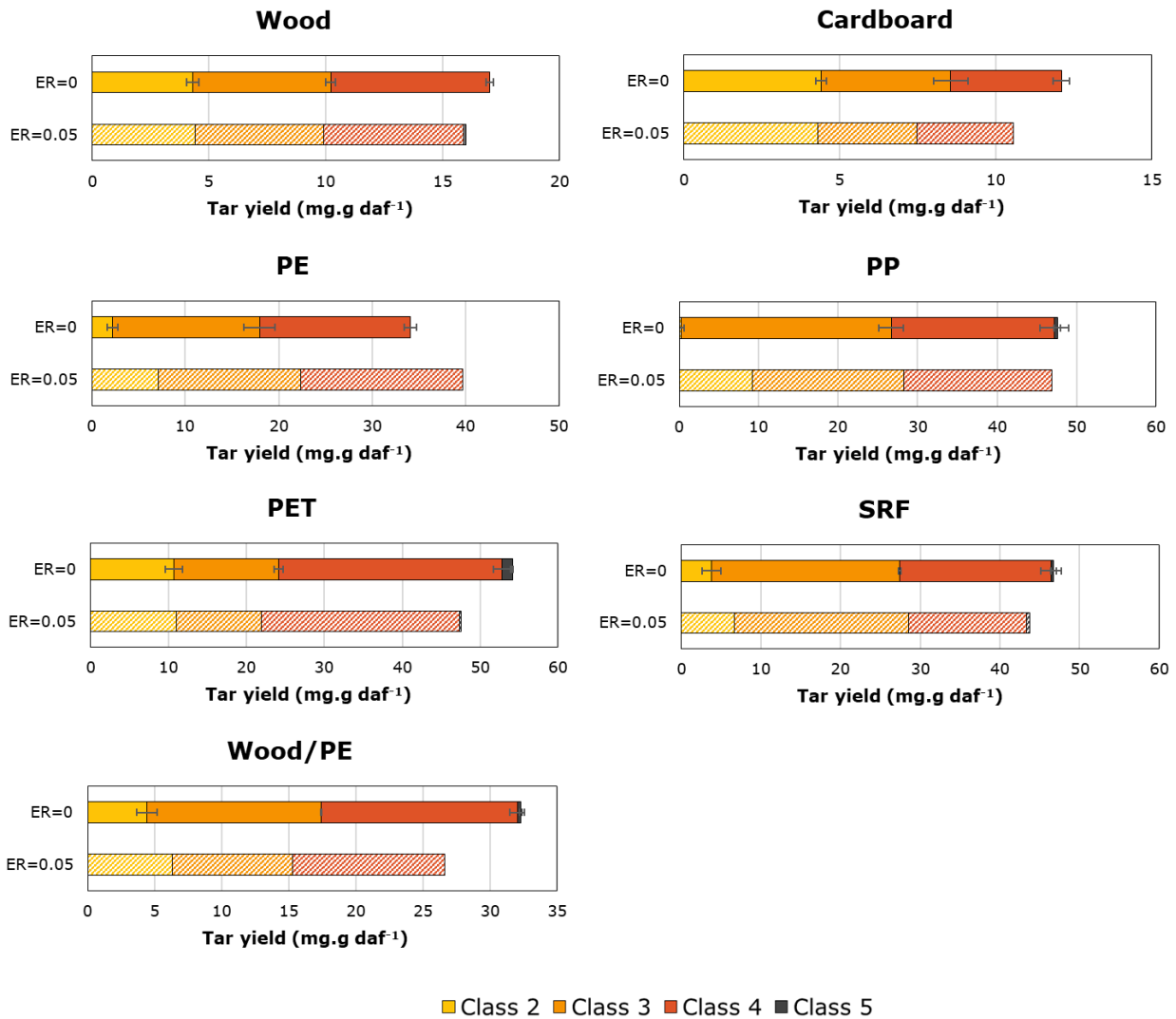


Figure 4-24. Tar yields from the pyrolysis and gasification for SRF, model materials and the Wood/PE mixture at 800 °C.

The variation in tar yield is for wood is a decrease of 6%, and it mainly concerns class 3 and class 4 tars. In the case of cardboard, a 13% decrease is observed. It is known that tar species from lignin are more stable than the ones derived from cellulose (Yu et al., 2014). In addition, calcium additives used in cardboard and paper production can promote tar decomposition (Šuhaj et al., 2020). Difference in class 2 tars, higher in the case of cardboard, consisted in nitrogen containing tars like aniline and benzonitrile.

Class	Name	Formula	Wood	Cardboard	PET	PE	PP	SRF	Wood /PE
2. Heterocyclics	Thiophene	C ₄ H ₄ S		0.33					
	Pyrrrole	C ₄ H ₅ N		0.57	0.61	1.20	2.12	0.79	1.10
	Benzofurane	C ₈ H ₆ O	1.20	0.74	0.84			0.84	0.60
	Aniline	C ₆ H ₇ N		1.21	2.56	5.58	6.33	3.84	3.71
	Benzonitrile	C ₇ H ₅ N						0.43	
	Phenol	C ₆ H ₆ O	2.86	1.61	5.65			0.30	0.55
	Benzopyridine	C ₉ H ₇ N	0.06						
	Indole	C ₈ H ₇ N	0.28	0.14	0.52	0.38	0.42	0.37	0.36
<i>Total class 2</i>			4.40	4.28	10.99	7.16	9.22	6.64	6.32
3. Light aromatics	Ethylbenzene	C ₈ H ₁₀	0.90	0.36	0.18	1.11	4.72	0.89	0.81
	Phenylethyne	C ₈ H ₆	0.30	0.30	0.78	1.34	3.05	0.69	0.94
	Styrene	C ₈ H ₈	1.89	2.10	9.75	12.04	10.25	18.97	6.70
	a-Methylstyrene	C ₉ H ₁₀		0.07		0.08	0.24	0.54	0.07
	o-Methylstyrene	C ₉ H ₁₀	0.62	0.36	0.21	0.62	0.81	0.83	0.42
	Indene	C ₉ H ₈	1.81						
<i>Total class 3</i>			5.51	3.19	10.92	15.19	19.07	21.92	8.93
4. Light PAHs	Naphtalène	C ₁₀ H ₈	2.89	1.83	6.27	11.81	10.89	8.37	7.19
	Naphtalene. 2-methyl-	C ₁₁ H ₁₀	0.60	0.32	0.27	1.06	1.97	1.03	0.74
	Naphtalene. 1-methyl-	C ₁₁ H ₁₀	0.44	0.24	0.21	0.88	1.33	0.86	0.60
	Biphenyl	C ₁₂ H ₁₀	0.13	0.09	14.75	0.31	0.42	0.87	0.22
	Naphtalene.2-ethenyl-	C ₁₂ H ₁₀	0.32	0.13	0.16	0.50	0.63	0.64	0.41
	Acenaphthylene	C ₁₂ H ₈	0.64	0.00	0.32	1.18			
	Acenaphthene	C ₁₂ H ₁₀	0.11	0.25	0.41		1.44	0.98	0.89
	Fluorene	C ₁₃ H ₁₀	0.26		0.56	0.46	0.55	0.51	0.36
	Phenanthrene	C ₁₄ H ₁₀	0.37	0.23	2.16	0.83	0.89	1.05	0.61
	Anthracene	C ₁₄ H ₁₀	0.23		0.37	0.33	0.51	0.48	0.36
<i>Total class 4</i>			5.99	3.10	25.48	17.35	18.63	14.80	11.40
5. Heavy PAHs	Fluoranthene	C ₁₆ H ₁₀			0.18			0.22	
	Pyrene	C ₁₆ H ₁₀						0.09	
<i>Total class 5</i>			0.00	0.00	0.18	0.00	0.00	0.31	0.00
<i>Total Tars</i>			15.90	10.57	47.57	39.70	46.92	43.67	26.65

Table 4-6. Tar yields from the gasification of SRF, of model materials and of the Wood/PE mixture at 800 °C (in mg.g daf¹).

The highest decrease in the tar yield between pyrolysis and gasification is observed for the wood/PE mixture, with 18%. Tar species like indene or pyrene, observed during the pyrolysis of the mixture, are not observed in the tests with oxygen, and the yields for the other class 3 and class 4 species are lower in gasification. Their interactions during pyrolysis and the available oxygen can facilitate the conversion of the intermediate devolatilization species.

4.4.2.4 Influence of O₂ addition on solid residue composition

With the addition of O₂ in the reaction atmosphere, oxidation reactions are enhanced. Due to the limited duration of the air injection, the reactions are significant for the released volatiles, while reactions involving char are less important. Chemical composition for the solid residues after the gasification tests is shown in Table 4-7.

Sample	%C ^a	%H ^a	%N ^a	%S ^a	%O ^b	%Ash ^a
Wood	83.4	1.0	1.0	0.2	5.7	8.7
Cardboard	47.1	1.2	0.4	0.3	7.0	43.7
PET	92.1	1.6	0.3	0.0	5.9	0.0
SRF	44.8	1.2	0.9	1.4	1.3	50.4
Wood/PE	83.4	1.5	0.5	0.2	8.9	5.5

a) % on dry basis. b) By difference.

Table 4-7. Chemical composition of the solid residues after gasification at 800 °C.

The chemical composition of the chars obtained in the gasification tests show a higher carbon content than the chars obtained from pyrolysis. The comparison of the molar compositions in the ternary diagram shown in Figure 4-25, shows that the C molar content tends to increase, while the O molar content tends to decrease with O₂ addition.

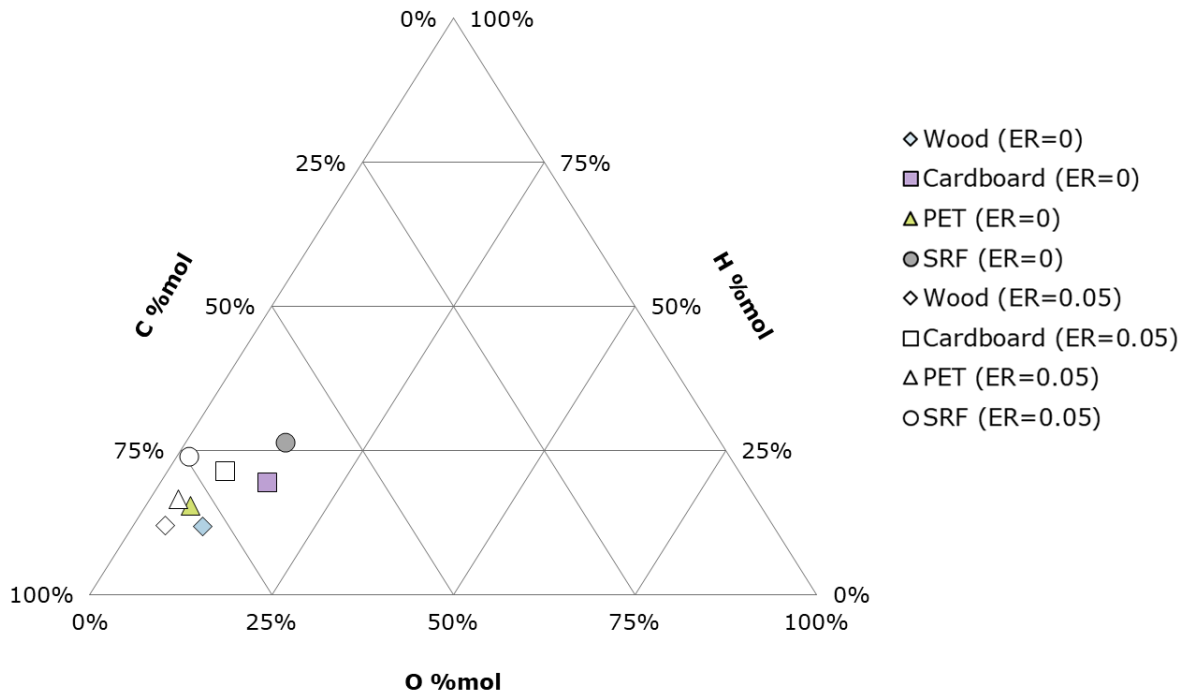


Figure 4-25. Molar composition (without ash) of the char produced in pyrolysis and gasification at 800 °C.

4.4.2.5 Influence of O₂ addition on the distribution of the energy content of the feedstock

The ratios of the EC in the products (gas, char and tar) to the EC of the initial feedstock was calculated for the gasification tests, and they are compared with that from pyrolysis in Figure 4-26.

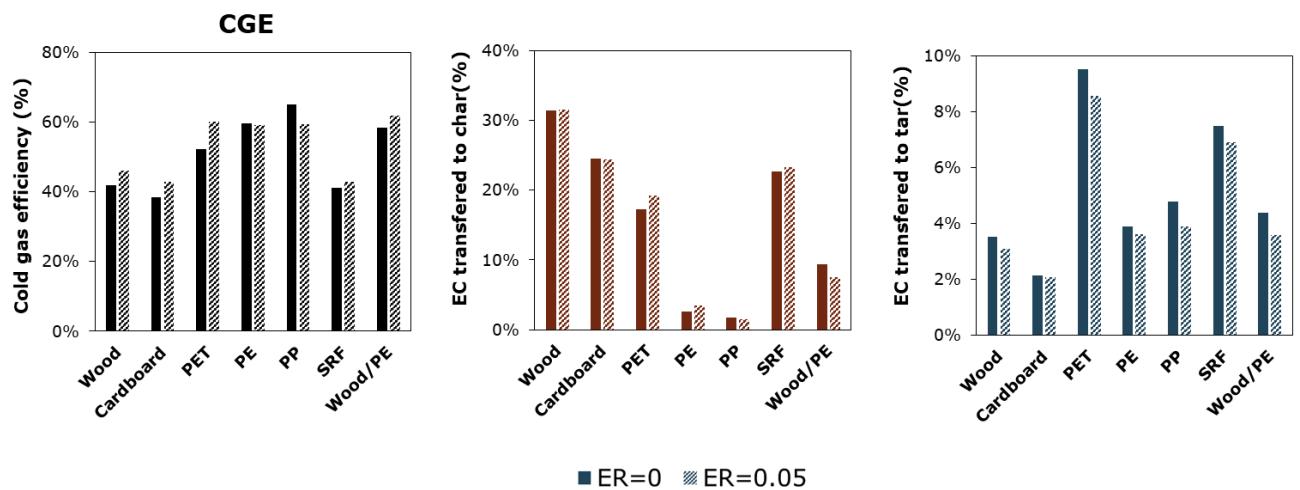


Figure 4-26. Ratios of the EC of the product to the EC of the feedstock after pyrolysis and gasification.

Most of the initial EC is transferred in the produced gas. The CGE value is higher under gasification conditions in most cases, with the exception of PE and PP. This is linked to the decrease in the hydrogen yield, which is significant for these two materials.

For the biogenic samples, the energy content transferred to the char do not show significant variations between pyrolysis and gasification. In some cases, for example for the PET, PE and SRF samples, the value is higher under gasification conditions. This is unexpected, and which can come from the use of the Boie's correlation with a higher uncertainty than a direct HHV measurement, due to the correlation itself and to the uncertainty of elemental content measurement.

The initial energy content transferred to the tar fraction is lower for all the tests in presence of oxygen, showing that some tars species or their precursors are oxidized. This agrees with the higher carbon balance closure observed for the gasification tests. The decrease is more important for the plastic materials (10 to 20%) compared to the lignocellulosic ones (around 5%). The SRF was 8% lower compared to the value obtained during its pyrolysis, while for the Wood/PE mixture, the difference was of 18% . The sum of the three fractions was slightly higher for all cases, which indicates that the gasification conditions used allow a more efficient conversion of the initial products.

4.5 Development of a correlation for the prediction of pyrolysis yields

Based on the experimental results of the pyrolysis of the model materials, an empirical correlation was developed for predicting the yield of the main pyrolysis products. It consists in a set of equation which aims to predict the distribution of char, gas and tar as well as the composition of the produced gas, by only using the characterization data of the initial feedstock (chemical composition, ash content). The underlying assumptions are discussed first, and then the methodology is presented. Finally, the suggested correlation is tested with experimental data obtained in our experimental device. The accuracy and validity of this correlation is discussed at the end of the section.

4.5.1 Feedstock representation

The elemental mass composition of the feedstock from the ultimate analysis is normalized to the carbon, hydrogen and oxygen content, expressed on dry, ash, S, and N-free basis. The mass fractions x_C , x_H and x_O are related by equation 4.5, which means that only two of these three variables are independent.

$$x_C + x_H + x_O = 1 \quad [4.5]$$

Nitrogen and sulfur represent only a small fraction of the studied feedstock, and their transformation into products during pyrolysis is not considered. The feedstock is represented by a molecule expressed by the chemical formula $C H_y O_z$, where y , and z represent the H/C and O/C molar ratios respectively. They are calculated from the normalized CHO composition of the material, using the following expressions:

$$y = \frac{x_H * M_C}{x_C * M_H} \quad [4.6]$$

$$z = \frac{x_O * M_C}{x_C * M_O} \quad [4.7]$$

M_C , M_H , and M_O are the molecular weights of carbon, hydrogen and oxygen respectively. The molecular weight of the model molecule is determined from the following formula:

$$M_{C H_y O_z} = M_C + y * M_H + z * M_O \quad [4.8]$$

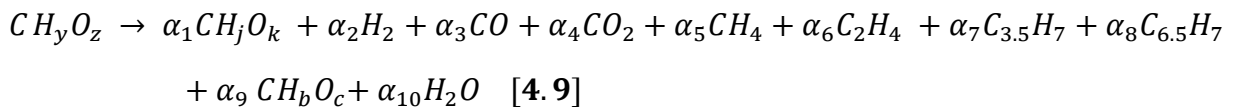
The normalized composition of the five model materials is presented in Table 4-8, along with their respective molecular formulas, elemental mass composition and molecular weights.

	Feedstock composition			Feedstock formula		Molecular weight (g/mol)
	x_C	x_H	x_O	y	z	
Wood	48.2%	6.9%	44.9%	1.706	0.701	24.94
Cardboard	48.0%	6.6%	45.4%	1.639	0.709	25.05
PET	63.0%	5.5%	31.5%	1.040	0.375	19.06
PE	85.5%	13.9%	0.6%	1.937	0.005	14.04
PP	85.8%	13.7%	0.5%	1.903	0.004	13.99

Table 4-8. Normalized CHO mass composition, molecular formula, and weight of the five model materials.

4.5.2 Pyrolysis products representation

The pyrolysis of the carbonaceous feedstock is expressed as a single step reaction, where the feedstock is decomposed into char, gaseous species, tar species and H_2O , as follows:



The considered permanent gases are hydrogen (H_2), carbon monoxide (CO), carbon dioxide (CO_2), methane (CH_4), and water (H_2O). Ethylene (C_2H_4), acetylene (C_2H_2) and ethane (C_2H_6) are lumped in a single “C2” molecule, whose formula is assumed to be that from ethylene, since in our experiments it represents the largest part (80-90 wt.%) of total C2 hydrocarbons.

Propene/propane (C_3H_x) and butadiene (C_4H_6) are lumped in the “C3/C4” component. The formula is assumed to be $C_{3.5}H_7$, as the average mass repartition between these two species in the pyrolysis results of the model materials is close to 1:1.

Monoaromatic gas species (benzene B, toluene T, and xylene X) are represented by a single lumped component with the formula $C_{6.5}H_7$, which corresponds to a mass ratio for BTX of 6:3:1, which is determined from the experimental results. The same distribution has also been proposed for the lumped component of single ring aromatics in pyrolysis models by (Ranzi et al., 2016).

Char is represented with the molecular formula CH_jO_k . The subscripts j and k are calculated for each feedstock using equations 4.6 and 4.7, using the C, H, O mass composition of the solid residue determined after pyrolysis. The composition, formula and molecular weight of the pyrolysis char are shown in Table 4-9. The solid residue in the case of PE and PP is assumed to be composed of carbon only.

	Char composition			Char Formula		Molecular weight (g/mol)
	x_C	x_H	x_O	j	k	
Wood	85.0%	1.1%	14%	0.149	0.012	12.36
Cardboard	74.8%	1.8%	23.5%	0.279	0.236	16.07
PET	88.2%	1.4%	10.4%	0.193	0.009	12.35
PE	100%	0.0%	0.0%	0	0	12.01
PP	100%	0.0%	0.0%	0	0	12.01

Table 4-9. CHO normalized composition, molecular formula and weight of the char produced by pyrolysis at 800 °C for the five model materials.

Tar is represented by a mean molecule with the formula CH_bO_c . The ratios b and c are determined from the elemental composition of the measured tar species, using equations 4.6 and 4.7. The composition, molecular formula and weight of the tar produced during the pyrolysis of the model materials are shown in Table 4-10.

	Tar composition			Tar Formula		Molecular weight (g/mol)
	x_C	x_H	x_O	b	c	
Wood	75.7%	8.0%	16.3%	1.252	0.162	15.86
Cardboard	72.3%	8.3%	17.5%	1.372	0.182	16.30
PET	88.5%	6.7%	4.8%	0.895	0.041	13.57
PE	85.3%	7.4%	6.2%	1.032	0.054	13.92
PP	84.1%	10.3%	5.6%	1.454	0.050	14.28

Table 4-10. CHO normalized composition, molecular formula and weight of the tar produced by pyrolysis at 800 °C for the five model materials.

The elemental mass balances for carbon, hydrogen and oxygen are shown in equations 4.10, 4.11 and 4.12 respectively.

$$\alpha_1 + \alpha_3 + \alpha_4 + \alpha_5 + \alpha_6 * 2 + \alpha_7 * 3.5 + \alpha_8 * 6.5 + \alpha_9 - 1 = 0 \quad [4.10]$$

$$\alpha_1 * j + \alpha_2 * 2 + \alpha_5 * 4 + \alpha_6 * 4 + \alpha_7 * 7 + \alpha_8 * 7 + \alpha_9 * b + \alpha_{10} * 2 - y = 0 \quad [4.11]$$

$$\alpha_1 * k + \alpha_3 + \alpha_4 * 2 + \alpha_9 * c + \alpha_{10} - z = 0 \quad [4.12]$$

4.5.3 Methodology

As shown in equation 4.9, a total of 10 products are considered. The term α_i represent the stoichiometric coefficients of each of these species, which are unknown. Additionally, b , c , j , and k need to be determined, which gives a total of 14 unknown parameters to be calculated. In order to have a defined system, it is necessary to have the same number of equations.

Equations for the stoichiometric coefficients for char and gas products ($\alpha_1 - \alpha_8$) and the parameters c , j , and k are obtained from the regression of the experimental results from the pyrolysis of the five model materials at 800 °C. These were fitted using a multi linear regression method (MLR), available in the statistical software Minitab. This resulted in a set of 11 linear equations in function of the two independent variables x_C and x_H , shown below:

$$Y_i = \beta_0 + \beta_1 * x_C + \beta_2 * x_H \quad [4.9]$$

Where Y_i is the predicted response, and β_0 , β_1 , β_2 are the coefficients of the linear equations obtained from the MLR.

Since the experimental mass balance closure of the pyrolysis tests do not reach 100%, some assumptions are made to ensure the conservation of mass in equation 4.9. Previously, it was observed

that only a part of the tar species is collected in the impingers. In section 4.1.5, we showed that a tar deposit remains in the connections at the reactor outlet. A strong assumption is proposed, which consists in attributing most part of the missing mass to the lumped species “tar”. According to this hypothesis, the stoichiometric coefficient of tar (α_9) is calculated from the difference of the carbon balance, and the b parameter is deduced from the hydrogen balance. . Nevertheless, this assumption can considerably increase the predicted yield of tars.

On the other hand, the stoichiometric coefficient for water (α_{10}), which was not experimentally quantified, is calculated by difference from the oxygen balance

An analysis of variance (ANOVA) was performed to test the accuracy of the regressions obtained by the MLR, and to estimate how each of the independent variables contributed to the result. The performance of the correlation was evaluated with the coefficient of determination (R^2) and the F-value.

The R^2 value determines the amount of variance that can be explained by the independent variables. The higher the R^2 value (maximum value is 1), the better the fit of the correlation with the experimental data. The F-test is used to determine if there is a relationship between the response and at least one of the predictor variables in the MLR, that is to say, to reject the null hypothesis (the case in which all the coefficients are zero and there is no correlation between the data and the variables). To do so, the F-value is calculated as shown below:

$$F = \frac{\frac{TSS - RSS}{p}}{\frac{RSS}{n - p - 1}} \quad [4.10]$$

Where:

- TSS is the total sum of squares (calculated as the variation between the observed data Y and the mean value \bar{Y}): $TSS = (Y - \bar{Y})^2$
- RSS is the residual sum of squares (calculated as the variation in the error between the observed data and the predicted value \hat{Y}): $RSS = (Y - \hat{Y})^2$
- n is the number of observations (10 sets of experimental results in our case)
- p is the number of parameters (2 parameters x_C and x_H in our case)

For the overall correlation to be significant, the F value must be higher than a critical value. In our case, for two parameters ($p=2$) and 10 observations ($n=10$), the critical value of F is of 3.25 for a confidence interval of 10%.

The P-value was calculated for each of the terms of the equation. A term is significant for the regression if its P-value is lower than a threshold of significance. For instance, when the P-value is lower than 0.05, the variations on the experimental data can be explained by the variable, with a maximum 5% risk. The coefficients for the linear equations obtained from the MLR are shown in Table 4-11, with the results from the statistical analysis.

	β_0	β_1	β_2	R^2	F	P-value for β_0	P-value for β_1	P-value for β_2
α_1 (Char)	0.604	-0.780	0.691	0.92	42.5	1.14E-05	1.80E-03	3.77E-01
α_2 (H ₂)	0.042	0.022	0.679	0.7	19	2.67E-02	8.19E-01	2.40E-03
α_3 (CO)	0.524	-0.665	0.372	0.99	1077	2.41E-10	7.80E-08	2.68E-02
α_4 (CO ₂)	0.113	0.112	-1.496	0.95	78.0	1.00E-04	3.25E-02	1.00E-04
α_5 (CH ₄)	0.038	-0.154	1.705	0.93	49.5	2.35E-02	2.81E-02	3.00E-04
α_6 (C2)	-0.085	0.023	1.455	0.93	50.4	1.43E-02	7.74E-01	4.40E-03
α_7 (C3-C4)	-0.069	0.237	-0.539	0.96	82.0	9.46E-05	3.10E-05	2.30E-03
α_8 (BTX)	-0.031	0.17	-0.692	0.97	135	4.72E-05	7.50E-07	1.70E-06
j	0.448	-0.245	-1.728	0.74	11.8	2.60E-03	4.19E-01	1.20E-03
k	0.417	-0.547	0.373	0.83	16.8	3.00E-04	2.21E-02	6.76E-01
c	0.369	-0.696	2.03	0.9	32.1	1.42E-05	2.00E-04	3.20E-03

Table 4-11. Coefficients for the linear equations obtained by MLR, and results of the ANOVA analysis.

The equations obtained with the MLR method globally show a good fit with the experimental results. The best fit is observed in the case of CO (highest R^2 and F values), and a good correspondence is also observed for char, CO₂, C2, C3-C4, BTX, and the c parameter, all with R^2 values above 0.9. An acceptable fit ($R^2=0.70$ to 0.80) is observed for H₂ and the j , k parameters.

In some cases, only one of the variables show a strong correlation with the data. For example, char yield and the ratio k , show a strong correlation with the carbon content only (P-value under 0.05

for β_1 , and higher than 0.3 for β_2), while H₂ and C₂ yields, and the j parameter show strong correlations with the hydrogen content only. In those cases, we decided to remove the terms with $P > 0.05$ (marked in red in Table 4-11). The regression was made a second time, only using the relevant variables. The equations used for the calculation of the unknown parameters are shown in Table 4-12.

Parameter	Equation
α_1 (Char)	$0.578 - 0.644 * x_C$
α_2 (H ₂)	$0.042 + 0.679 * x_H$
α_3 (CO)	$0.524 - 0.665 * x_C + 0.372 * x_H$
α_4 (CO ₂)	$0.113 + 0.112 * x_C - 1.496 * x_H$
α_5 (CH ₄)	$0.038 - 0.154 * x_C + 1.705 * x_H$
α_6 (C ₂)	$-0.079 + 1.549 * x_H$
α_7 (C ₃ -C ₄)	$-0.069 + 0.237 * x_C - 0.539 * x_H$
α_8 (BTX)	$-0.031 + 0.170 * x_C - 0.692 * x_H$
α_9 (Tar)	$1 - (\alpha_1 + \alpha_3 + \alpha_4 + \alpha_5 + \alpha_6 * 2 + \alpha_7 * 3.5 + \alpha_8 * 6.5)$
α_{10} (H ₂ O)	$z - (\alpha_1 * k + \alpha_3 + \alpha_4 * 2 + \alpha_9 * c)$
j	$0.380 - 2.735 * x_H$
k	$0.403 - 0.474 * x_C$
b	$y - (\alpha_1 * j + \alpha_2 * 2 + \alpha_5 * 4 + \alpha_6 * 4 + \alpha_7 * 7 + \alpha_8 * 7 + \alpha_{10} * 2) / \alpha_9$
c	$0.369 - 0.696 * x_C + 2.030 * x_H$

Table 4-12. Equations for the calculation of the unknown parameters.

4.5.4 Results

4.5.4.1 Test of the correlation for model materials

Parity plots of the mass yields predicted with the correlation, versus the experimental yields from the pyrolysis of the five model materials are provided in Figure 4-27. The closer the results are to the diagonal line, the better the correlation predicts the experimental results. The other two lines correspond to intervals of $\pm 10\%$.

The correlation globally shows a good accuracy in the predictions, with R² values ranging between 0.86 and 0.99. In the case of CO, CH₄ and BTX, all experimental results are within the confidence intervals of $\pm 10\%$. The simplified expressions for char, C₂ and C₃-C₄ coefficients lead to rather

good predictions, with R^2 values that are only slightly lower than that of Table 4-7 for C2 and C3-C4 coefficients. The R^2 value relative to char mass yield in Figure 4-27, depends on the α_1 coefficient, but also on j and k . The char yield is predicted with a rather good accuracy ($R^2=0.89$), even if some experimental values for the plastics show high residuals (notably for PE). The estimations are less accurate for H_2 , as two data points show large residuals and are not well fitted by the equation. As shown in Figure 4-27, the repeatability error associated with the experimental H_2 yields for PE and PP is high. However, if we consider the average of the two experimental results for each material, the relative difference with the prediction is reduced to 3 %.

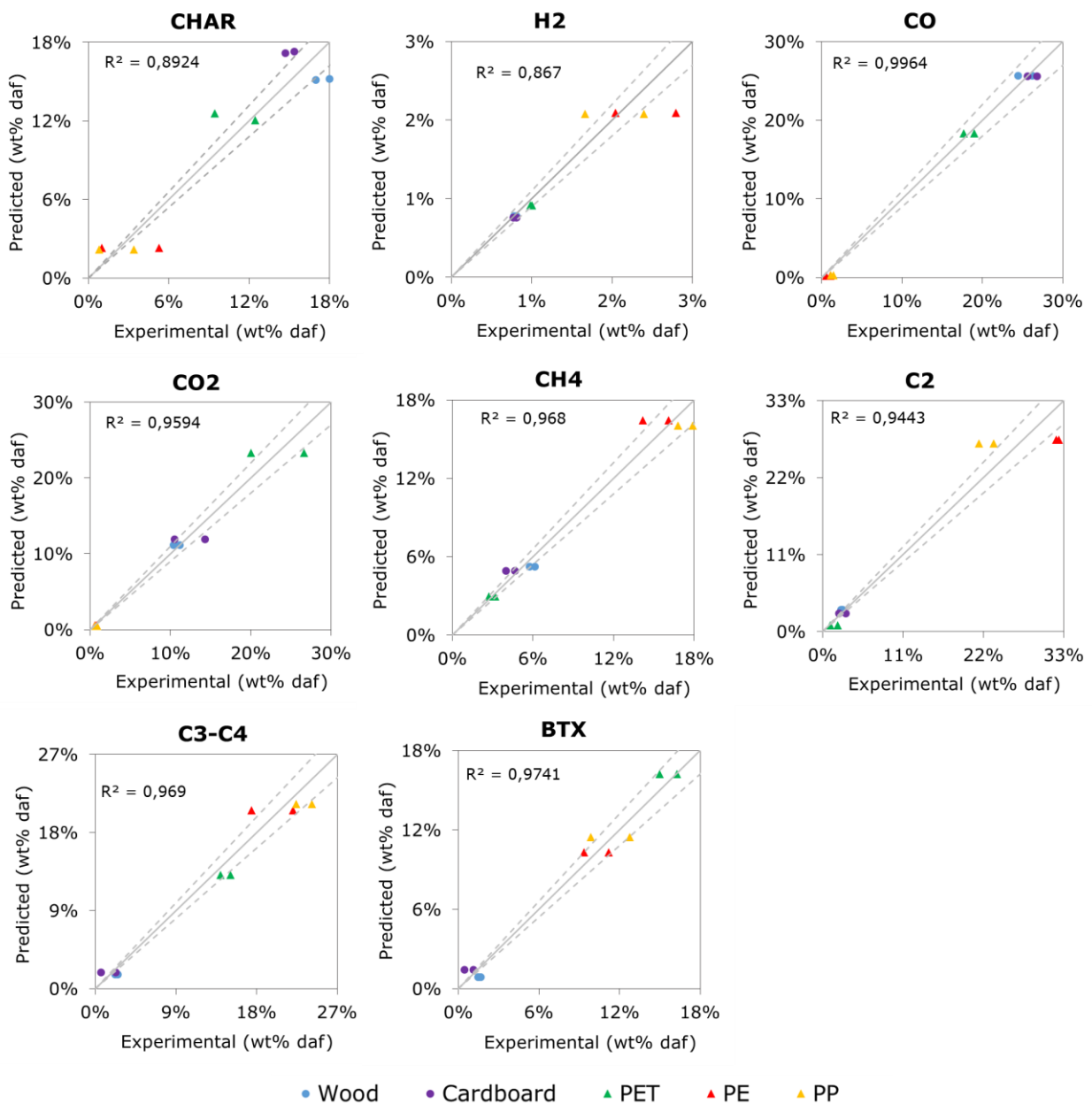


Figure 4-27. Predicted versus experimental pyrolysis mass yields for the five model materials.

The fit of the correlations for the hydrocarbons is globally good ($R^2=0.94$ for C2 and $R^2=0.96$ for C3- C4). However, the prediction shows some differences with the experiments notably for PE and PP. As their chemical compositions are very close, the predicted values for the hydrocarbon yields are the same. However, we observed experimentally that their different chemical structures have an effect on the composition of the produced gas. These effects cannot be represented by the correlation, and the C2 yield is underestimated by 15% in the case of PE, and overestimated by 15% in the case of PP. The opposite is observed for the CH₄ yield, with a 10% difference. When the sum of both is compared, the difference is only of 5%.

The results of the prediction could be further improved by using the average values of the two experimental points relative to the same material, or by removing the unusual values. However, if the number of data points is too low, a higher attention must be paid to R^2 and P-values, because they will become more sensitive to errors. To obtain more accurate predictions, unusual experimental values must be confirmed with additional tests.

4.5.4.2 Validation with experimental data obtained for SRF and mixtures

For the development of the correlation only the data for the model materials was used, while the experimental results from the tests of heterogeneous feedstock like SRF or the two wood/plastic mixtures were used to validate the accuracy of the predictions. This decision was made in order to see if the proposed method, developed on the basis of experimental results obtained with model materials, also allows to represent the behavior of mixtures of materials, and thus to consider the interaction effects between the materials.

The C, H, O composition of these samples and their corresponding molecular formula are shown in Table 4-13, together with those of the chars and tar obtained after their pyrolysis.

Feedstock composition			Feedstock formula		Molecular weight (g/mol)	
x_C	x_H	x_O	y	z		
SRF	59.5%	7.4%	33.1%	1.49	0.42	20.19
Wood/PE	65.7%	10.1%	24.2%	1.83	0.28	18.28
Wood/PP	67.1%	10.8%	22.1%	1.91	0.25	17.89
Char composition			Char Formula		Molecular weight (g/mol)	
x_C	x_H	x_O	j	k		
SRF	75.6%	2.8%	21.6%	0.44	0.21	15.89
Wood/PE	91.2%	1.4%	7.4%	0.18	0.06	13.17
Wood/PP	94.4%	1.1%	4.5%	0.14	0.04	12.72
Tar composition			Tar Formula		Molecular weight (g/mol)	
x_C	x_H	x_O	b	c		
SRF	90.9%	7.1%	2.0%	0.92	0.01	13.21
Wood/PE	86.2%	7.4%	6.4%	1.02	0.05	13.93
Wood/PP	79.2%	7.7%	13.1%	1.16	0.12	15.17

Table 4-13. CHO normalized composition, molecular formula and weight for the feedstock, char and tar products of SRF and the two mixtures.

The predicted and experimental values for each product mass yield are compared in **Figure 4-28** (left), with the relative error of the predicted value relatively to the experimental one (right).

In the case of SRF, the calculated yields for char, methane, C₂ and C₃/C₄ hydrocarbons are well predicted, with relative errors lower than 10%. For all the other products, the yields are overestimated, with differences particularly high for CO₂ and CO. As it was explained before, neither ash, moisture content nor other minor elements are involved in the calculations. Feedstock composition is recalculated to be only in terms of C, H, and O. SRF presents a high ash content (16.4 wt% on dry basis), so the averaged values show a 20% variation compared to the original composition on dry basis (58.7% vs. 48% for %C) and (7.33% vs. 6% for %H). As this composition is rather close to the PET one, the prediction results for SRF are close to the pyrolysis results of this plastic material (such as a relatively high CO₂ mass yield). However, SRF and PET pyrolysis yields show significant differences, especially concerning the CO₂ yield, which cannot be represented by the present correlation.

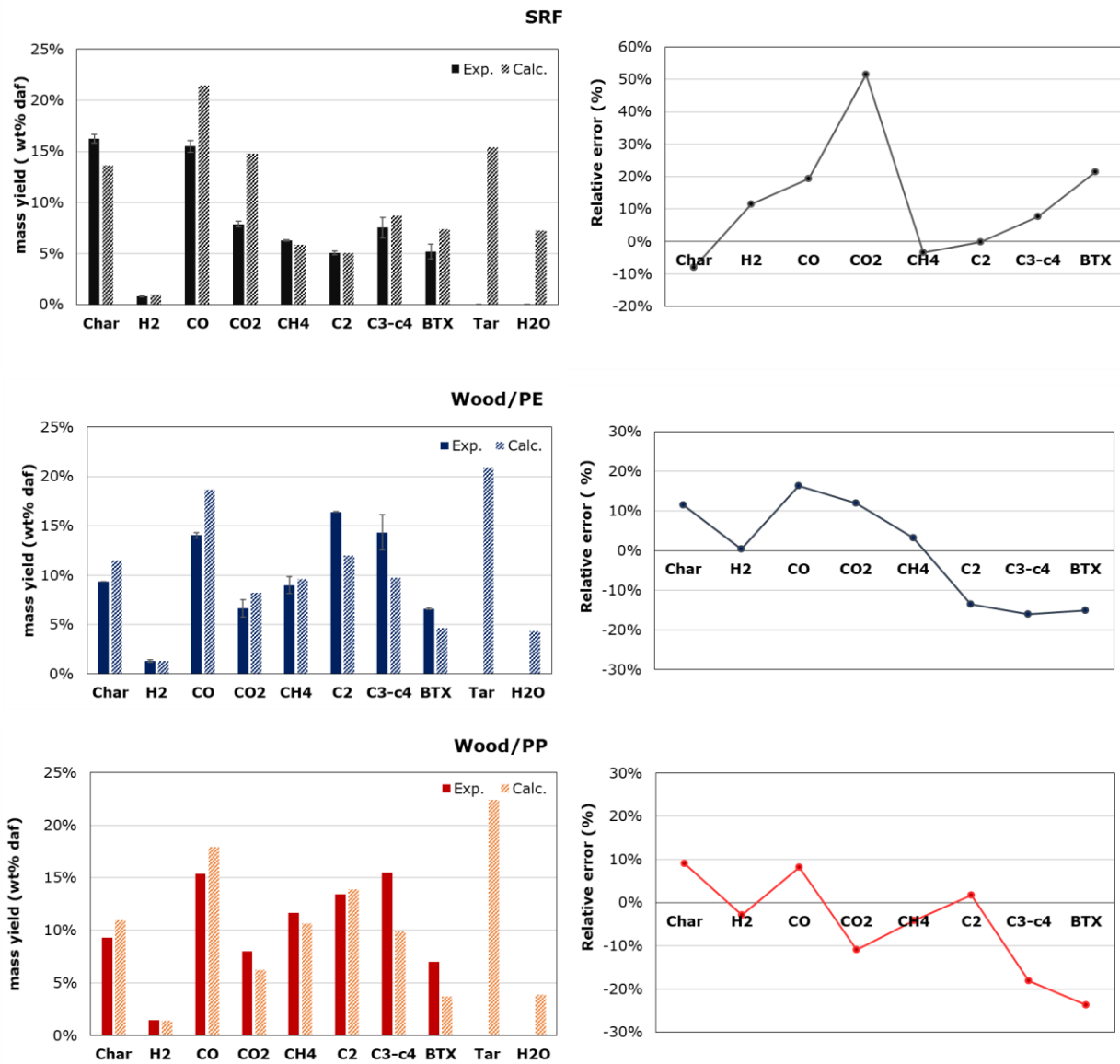


Figure 4-28. Experimental and predicted pyrolysis mass yields for SRF, the Wood/PE mixture and the Wood/PP mixture, with their corresponding relative error values.

Chemical compositions of both plastics (PE and PP) are very similar, and so are the composition of the PE/Wood and PP/Wood mixtures. As expected, the predicted values for the product mass yields are thus very close for the two mixtures. For the wood/PP mixture, rather good predictions are observed for most of the gas yields (H₂, CO, CO₂, CH₄, C₂), with a relative error under 10 %. For the wood/PE mixture, the predictions are globally less accurate than for the wood/PP one. The char yield is calculated with a 10% error in both cases.

When making predictions for heterogeneous resources, the correlation shows less effective results than those observed for individual materials. This was expected since the data for these materials were used for setting the correlation. The overall trend and distribution of the products agrees with the

experimental results, with acceptable predictions for char, hydrogen, and methane ($\pm 10\%$). However, quite important differences are observed notably for CO_2 (up to 50% for SRF) and BTX (up to 25%). These differences show that the methodology is probably too simplified to reach an acceptable prediction for all product yields, only relying on the C, H and O contents, and as a one-step simplified reaction.

Other characteristics of the initial material besides the C, H, O content should be used as parameters. In our case, some of the selected model materials with similar chemical compositions (PE and PP) show different experimental behaviors. It is then necessary to find variables that allow differentiating components with unique behaviors or tendencies. However, if more independent variables are considered, it is necessary to have a higher number of observations. Some rules of thumb suggest a minimum of 5 or 10 observations for each independent variable, however, the minimum number of experiments to be considered depends on the level of precision to be achieved (Knofczynski & Mundfrom, 2008). Another option is to adjust the experimental results using non-linear relations, but in that case also a large number of experimental observations is needed, since the results are more sensitive to small changes in the variables.

One final suggestion would be to divide the reaction scheme in two steps. Initially the char yield would be determined as above, and then the regressions would be performed again but only considering the amounts of C, H and O in the volatiles.

4.5.5 Conclusions

The time evolution of the temperature was measured during the pyrolysis of wood and PE samples, for tests carried out at 800 °C. The heating rate ranges between 4 and 6 °C.s⁻¹. The observed profiles show the different processes that occur during conversion, for example, char generation in the case of biomass and melting in the case of plastics.

The production of volatile matter was monitored versus time. For cardboard, with a high content in cellulose (which decomposes between 300 and 400 °C) the devolatilization is the fastest. On the other hand, wood, with a higher lignin content, is pyrolyzed on a larger temperature range. For PE and PP, the release of volatiles starts after about 40 s, since they are first subjected to an endothermic melting phase, which induces a delay in their heating compared to the other materials. In all cases, the devolatilization is ended after 120s.

The gas products, condensable species and solid residue obtained in the pyrolysis of SRF and of model materials at 800 °C were analyzed and quantified. For all cases, the carbon conversion into gas is higher than 45%. The char yield is higher for lignocellulosic materials and PET, all with oxygen in their structure. Even if the elemental composition of some materials is very similar, such as for PE and PP, or wood and cardboard, differences are observed in their gaseous and condensable product yields, which shows that macromolecular composition and chemical structure influence the final product distribution. Plastics contribute to the high yields of CH₄ and C₂ hydrocarbons, while lignocellulosic materials are responsible for the majority of oxygenated compounds. The pyrolysis of plastic materials results in high tar yields (35 to 55 mg.g_{daf}⁻¹) being naphthalene and styrene the most prevalent species. In the case of biogenic materials, phenol and other heterocyclics tar species are formed. PET, with aromatic groups in its structure, results in an elevated concentration of PAHs.

Pyrolysis yields for the Wood/PE and wood/PP mixtures were compared to the weighted sum of the results for the individual components. The co-pyrolysis of biomass and plastic results in a higher conversion of carbon to volatile products than expected from the calculation. This is correlated to a reduction of the char yield of 30% for the Wood/PE and of 15% for the Wood/PP mixture. In both cases, the yields of H₂, CO and CO₂ are higher than the calculated results. Differences between tar species are significant for the Wood/PE mixture with an improved selectivity toward aromatic species.

The influence of the oxygen addition on the reaction products was studied in three different conditions (ER = 0.02, 0.05 and 0.1) with a beech wood sample, and in one condition (ER=0.05) for the SRF and for the rest of the model materials. Air was injected along with the carrier gas during the first 3 min. For wood, the carbon conversion to gas increases with ER, resulting in higher yields of CO and CO₂. The char yield shows little variation. This confirms that the inlet O₂ mostly reacts with the volatile products. The yields of benzene and toluene are higher with O₂ addition than in pyrolysis for all samples, and the difference is more significant for the three plastic materials. Moreover, the available oxygen seems to react with intermediate devolatilization species, which affects the distribution of tar species.

An empirical correlation was developed to estimate the pyrolysis yields of waste derived fuels, by only using the C, H and O contents of the resource. It provides a global insight on how the reaction products are affected by the initial composition of the feedstock. Good predictions (± 10%) are

obtained for char, H₂, CH₄ and C₂ gas yields, while the predictions for the yields of some species like CO₂ and BTX are entailed by a significant error compared to experimental values.

CONCLUSION AND PERSPECTIVES

The principal objective of this thesis was to study the pyrolysis and gasification of solid recovered fuel, and in particular to make the link between the pyrolysis and gasification products and the initial characteristics of the feedstock. To attain this goal, this work was divided into three main parts:

- In the first one, a novel experimental setup at laboratory scale was developed to perform tests under controlled reaction conditions.
- The second part of the work consisted in an experimental study of the pyrolysis and gasification of solid recovered fuel represented by model materials. These materials were studied individually and in mixtures to assess their interaction during pyrolysis. The influence of the addition of air in the product yields was studied, just as in gasification conditions.
- In the third part of the work, a straightforward correlation was developed, intended to predict pyrolysis products by using the feedstock elementary composition.

The experimental setup consists in a reactor made of a stainless-steel tube heated by an induction system. The system can handle samples of a few grams, which are placed in a wire mesh crucible. A heat exchanger was included inside the reactor to preheat the carrier gases. Thermal characterization tests were performed to evaluate the thermal history of the reactor and the sample, in conditions typical of the experimental tests. The reactor surface presents a heating rate of about $80\text{ }^{\circ}\text{C}\cdot\text{s}^{-1}$, while the heating rate for wood and plastic samples is found to be comprised between 4 and $6\text{ }^{\circ}\text{C}\cdot\text{s}^{-1}$.

CFD calculations confirmed that the heat exchanger was suitable for preheating the gases fed to the reactor. A uniform temperature ($800 \pm 10\text{ }^{\circ}\text{C}$) could be reached in the sample for a moderate carrier gas flowrate ($0.5\text{ NL}\cdot\text{min}^{-1}$). The geometry of the designed reactor with an empty heated volume above the sample, allows gas phase reactions to take place. A heated section about 20 cm long is maintained between 750 and $800\text{ }^{\circ}\text{C}$, resulting in a volatiles residence time between 2 to 4 s. In addition, the setup has dedicated sections for the collection and analysis of gases and condensable products.

The reactor and its heating system allow to achieve controlled and well-characterized thermal conditions, as well as to reach several of the initially defined goals (temperature level, gas residence time, temperature uniformity in the sample). The thermal limitations of the device have been identified.

A solid recovered fuel (SRF) and five model materials (wood, cardboard, polyethylene terephthalate, polyethylene, and polypropylene), were studied separately, in inert atmosphere and in the presence of air as an oxidizing agent at $800\text{ }^{\circ}\text{C}$. Measurement of the flowrate of produced volatiles during pyrolysis

showed different devolatilization rates among the studied materials. Cardboard was the first to release gases, followed by PET, Wood, PP, PE and the SRF sample. This agreed with the differences in the temperature history observed between biomass and plastic materials, which were subjected to several endothermic/exothermic changes during pyrolysis. In all cases, devolatilization was completed after 120s.

Char, gas, and tar were collected and analyzed separately. The carbon balance closure ranged between 75 and 80% for the pyrolysis tests. The missing fraction is attributed to heavy tars deposits observed at the reactor outlet and to hydrocarbons that could not be identified or quantified in subsequent analyses. The distribution and composition of products is found to vary significantly among model materials. Polyolefins (PE and PP) give high yields of hydrogen and hydrocarbons, while PET and lignocellulosic materials mostly produce CO and CO₂. The highest tar yields (35 to 55 mg.g_{daf}⁻¹) are observed for SRF and plastic materials, notably for PET with a high yield of PAHs (30 mg.g_{daf}⁻¹). The predominant tar species are styrene and naphthalene.

To study the possible interaction between biomass and plastics during pyrolysis, experimental results for wood/PE and wood/PP mixtures were compared to the weighted sum of the results for the individual components. For both mixtures, the carbon conversion to gas products was higher than expected without interaction. The observed synergistic effects could be attributed to reactions in gas phase between the oxygen containing radicals from wood pyrolysis and hydrogen donor species from plastic pyrolysis, which enhance the production of oxygenated compounds such as CO and CO₂. Another possible explanation is the inhibition of condensation and aggregation reactions of wood volatiles which resulted in a reduction of 15% to 30% in the char yield compared to the calculated value. The co-pyrolysis of biomass and plastics results in lower concentration of tars than that observed for plastics individually. However, because of the observed interactions, the tars concentration obtained experimentally for the mixtures was higher than expected. This was seen especially in the wood/PE case, with a higher concentration of aromatic tar species.

In order to approach the conditions of gasification, the influence of O₂ addition in the atmosphere was studied. Air was injected along with N₂ during the first 3 min of heating, maintaining a total flow rate of 0.5 NL/min. The oxygen concentration of the gas was between 17 and 19 vol %. Char yield and composition showed little variation between gasification and pyrolysis. As expected, since the air injection was carried out for a limited time, the oxygen mainly reacts with the volatile products. The

addition of oxygen favor the carbon conversion to gas, notably producing CO, CO₂, and benzene. Tar species were slightly reduced for lignocellulosic materials, while the opposite was observed for PE and PP. Lower amounts of PAH were obtained with the addition of oxygen, which suggested that some pyrolysis intermediates that are PAH precursors react with the available oxygen, thus limiting their formation.

We tried to represent as closely as possible the gasification conditions in our batch reactor paying a special attention to the mean ER value with a limited O₂ injection (flowrate and duration) compared to the mass of sample. However, the comparison of these results with those obtained in a continuously fed gasification reactor should be performed very carefully.

A simplified correlation using the experimental data from the pyrolysis of the model materials was developed with the aim to link the initial composition of the feedstock and its reaction products. The developed correlation attempted to predict the yields of the main pyrolysis products of SRF and the mixtures using only the C, H and O contents of the feedstock. Yields of char, H₂, CO and CH₄ are predicted with acceptable accuracy, while the predictions for the yields of CO₂ and BTX present a high difference with the experimental values.

Several perspectives have been identified for future work in the experimental axis:

- Identification of unmeasured fractions should be improved to obtain a more accurate description of the reaction products. This implies to analyze and quantify the tars deposited at the outlet of the reactor by other methods like HPLC. The recovery of the tars in the impingers could be improved by alternating the temperature of the baths between 40 °C and -20 °C as in the Tar protocol method suggested by (Neeft et al., 1999). The water content in the condensed products could be determined through Karl-Fischer titrations.
- The experimental setup and procedures could be adapted to perform pyrolysis kinetic studies. It would then be necessary to implement techniques that allow an online analysis of the concentration of the generated gases with an appropriate time resolution. It must be ensured that the methods are not affected by the configuration of the experimental system (transfer time between the reactor and the detector, analysis time, etc.), or corrected by the determination of the residence time distribution of the system.

- We measured and analyzed the tars produced during the pyrolysis of the different materials found in the SRFs. However, attention should be paid to other process pollutants like nitrogen, chlorine, and sulfur-containing compounds, as well as heavy metals.
- The results for the co-pyrolysis of biomass and plastic showed an improved conversion to gases, and a reduced char yield, but also a slight increase of the yields of some aromatic species. It is preferable for these species to be converted into simpler molecules that do not represent problems for the gas (for example benzene, toluene) and not into complex aromatic species such as PAHs. This makes it necessary to further investigate the interaction effects and their impact on the formation of tars to reduce their concentration in the produced gas. For example, other experiments should be performed to isolate the interactions occurring in the gas phase and the interactions occurring between the plastic melt and the wood particles. Additional tests should be also conducted at different biomass/plastic ratios and temperatures to better identify the impact of these interactions on the tar yields and thus select operating conditions that minimize them.

In relation to the modeling axis, some alternatives for improvement and some perspectives are proposed:

- The first proposition would be to continue using a simple, empirical approach that does not require many input characteristics. It would then be necessary to include a much larger number of experiments. These can be performed on other materials or their mixtures. Another option would be to reduce the number of output variables, for example in our case it was found that the sum of CH_4 and C_2 was better predicted by the correlation. This is close to the methodology of ANN type models seen in the literature.
- Another approach consists in increasing the complexity of the model by adding details to better describe the assumptions. For example, separating char and volatiles, or detailing more precisely the distribution of tars or lumped species. However, this implies the inclusion of additional parameters in the model, which must then be accompanied by new measurements and results to ensure its validity.
- Such kinds of empiric pyrolysis correlations could be implemented in the construction of more complex models, which consider other process parameters such as temperature or the kinetics of the involved reactions. For example, some gasification equilibrium models (Gómez-Barea

& Leckner, 2010; Groleau et al., 2019) describe the process as a sequence of steps (drying, pyrolysis, oxidation, reduction). The pyrolysis step description could then be coupled with other sub-models, for instance describing gas phase reactions or char gasification.

REFERENCES

- ADEME. (2021). *Transition(s) 2050. Choisir maintenant. Agir pour le climat*. <https://librairie.ademe.fr/recherche-et-innovation/5072-prospective-transitions-2050-rapport.html>
- ADEME, FEDEREC. (2019). *Technologies innovantes de valorisation des CSR (Combustibles Solides de Récupération)*. La librairie ADEME. https://librairie.ademe.fr/dechets-economie-circulaire/4641-technologies-innovantes-de-valorisation-des-csr-combustibles-solides-de-recuperation.html?search_query=lettre+ademe+international&results=3673
- Ahmed, I. I., Nipattummakul, N., & Gupta, A. K. (2011). Characteristics of syngas from co-gasification of polyethylene and woodchips. *Applied Energy*, 88(1), 165–174. <https://doi.org/10.1016/j.apenergy.2010.07.007>
- Ahonen, T. (2009). *ON THERMAL PROPERTIES OF A PYROLYSING WOOD PARTICLE*. <https://www.semanticscholar.org/paper/ON-THERMAL-PROPERTIES-OF-A-PYROLYSING-WOOD-PARTICLE-Ahonen/d97bfd998f4bb0b2b4b90ae6b389cbe2c54698c9>
- AIDA. (2016). *ICPE Rubrique 2971. Installation de production de chaleur ou d'électricité à partir de déchets non dangereux préparés sous forme de combustibles solides de récupération dans une installation prévue à cet effet, associés ou non à un autre combustible* | https://aida.ineris.fr/consultation_document/37556
- Aldrian, A., Viczek, S. A., Pomberger, R., & Sarc, R. (2020). Methods for identifying the material-recyclable share of SRF during co-processing in the cement industry. *MethodsX*, 7, 100837. <https://doi.org/10.1016/j.mex.2020.100837>
- Almeida, D., & Marques, M. de F. (2016). Thermal and catalytic pyrolysis of plastic waste. *Polímeros*, 26, 44–51. <https://doi.org/10.1590/0104-1428.2100>
- Al-Salem, S. M., Antelava, A., Constantinou, A., Manos, G., & Dutta, A. (2017). A review on thermal and catalytic pyrolysis of plastic solid waste (PSW). *Journal of Environmental Management*, 197, 177–198. <https://doi.org/10.1016/j.jenvman.2017.03.084>
- Aluri, S., Syed, A., Flick, D. W., Muzzy, J. D., Sievers, C., & Agrawal, P. K. (2018a). Pyrolysis and gasification studies of model refuse derived fuel (RDF) using thermogravimetric analysis. *Fuel Processing Technology*, 179, 154–166. <https://doi.org/10.1016/j.fuproc.2018.06.010>
- AMEC. (2013). *Research into SRF and RDF Exports to Other EU Countries*. AMEC Environment & Infrastructure UK Limited.
- ANCRE. (2018). *Les Combustibles Solides de Recupération (CSR): Les verrous techniques, réglementaires, économiques et sociétaux de la filière CSR en France*. ANCRE.
- Arafat, H. A., & Jijakli, K. (2013). Modeling and comparative assessment of municipal solid waste gasification for energy production. *Waste Management*, 33(8), 1704–1713. <https://doi.org/10.1016/j.wasman.2013.04.008>

- Arena, U. (2012). Process and technological aspects of municipal solid waste gasification. A review. *Waste Management*, 32(4), 625–639. <https://doi.org/10.1016/j.wasman.2011.09.025>
- Arena, U., & Di Gregorio, F. (2014a). Gasification of a solid recovered fuel in a pilot scale fluidized bed reactor. *Fuel*, 117, 528–536. <https://doi.org/10.1016/j.fuel.2013.09.044>
- Arena, U., & Di Gregorio, F. (2014b). Energy generation by air gasification of two industrial plastic wastes in a pilot scale fluidized bed reactor. *Energy*, 68, 735–743. <https://doi.org/10.1016/j.energy.2014.01.084>
- Aydin, E. S., Yucel, O., & Sadikoglu, H. (2018). Numerical and experimental investigation of hydrogen-rich syngas production via biomass gasification. *International Journal of Hydrogen Energy*, 43(2), 1105–1115. <https://doi.org/10.1016/j.ijhydene.2017.11.013>
- Barba, D., Prisciandaro, M., Salladini, A., & Mazziotti di Celso, G. (2011). The Gibbs Free Energy Gradient Method for RDF gasification modelling. *Fuel*, 90(4), 1402–1407. <https://doi.org/10.1016/j.fuel.2010.12.022>
- Barr, M. R., Volpe, R., & Kandiyoti, R. (2019a). Influence of Reactor Design on Product Distributions from Biomass Pyrolysis. *ACS Sustainable Chemistry & Engineering*, 7(16), 13734–13745. <https://doi.org/10.1021/acssuschemeng.9b01368>
- Barr, M. R., Volpe, R., & Kandiyoti, R. (2019b). Influence of Reactor Design on Product Distributions from Biomass Pyrolysis. *ACS Sustainable Chemistry & Engineering*, 7(16), 13734–13745. <https://doi.org/10.1021/acssuschemeng.9b01368>
- Bellouard, Q., Rodat, S., Grateau, M., & Abanades, S. (2020). Solar Biomass Gasification Combined With Iron Oxide Reduction for Syngas Production and Green Iron Metallurgy. *Frontiers in Energy Research*, 8, 66. <https://doi.org/10.3389/fenrg.2020.00066>
- Berruenco, C., Recari, J., Abelló, S., Farriol, X., & Montané, D. (2015). Experimental Investigation of Solid Recovered Fuel (SRF) Gasification: Effect of Temperature and Equivalence Ratio on Process Performance and Release of Minor Contaminants. *Energy & Fuels*, 29(11), 7419–7427. <https://doi.org/10.1021/acs.energyfuels.5b02032>
- Bhaskar, T., Negoro, R., Muto, A., & Sakata, Y. (2006). Prevention of chlorinated hydrocarbons formation during pyrolysis of PVC or PVDC mixed plastics. *Green Chemistry*, 8(8), 697–700. <https://doi.org/10.1039/B603037H>
- Bhatt, M., Wagh, S., Chakinala, A. G., Pant, K. K., Sharma, T., Joshi, J. B., Shah, K., & Sharma, A. (2021). Conversion of refuse derived fuel from municipal solid waste into valuable chemicals using advanced thermo-chemical process. *Journal of Cleaner Production*, 329, 129653. <https://doi.org/10.1016/j.jclepro.2021.129653>
- Biagini, E., Fantozzi, C., & Tognotti, L. (2004). CHARACTERIZATION OF DEVOLATILIZATION OF SECONDARY FUELS IN DIFFERENT CONDITIONS. *Combustion Science and Technology*, 176(5–6), 685–703. <https://doi.org/10.1080/00102200490428008>
- Blanco, P. H., Wu, C., Onwudili, J. A., & Williams, P. T. (2012). Characterization of Tar from the Pyrolysis/Gasification of Refuse Derived Fuel: Influence of Process Parameters and Catalysis. *Energy & Fuels*, 26(4), 2107–2115. <https://doi.org/10.1021/ef300031j>

- Block, C., Ephraim, A., Weiss-Hortala, E., Minh, D. P., Nzihou, A., & Vandecasteele, C. (2019). Co-pyrogasification of Plastics and Biomass, a Review. *Waste and Biomass Valorization*, 10(3), 483–509. <https://doi.org/10.1007/s12649-018-0219-8>
- Boie, W. (1953). Fuel technology calculations. *Energietechnik*, 3, 309–316.
- Brems, A., Baeyens, J., Beerlandt, J., & Dewil, R. (2011). Thermogravimetric pyrolysis of waste polyethylene-terephthalate and polystyrene: A critical assessment of kinetics modelling. *Resources, Conservation and Recycling*, 55(8), 772–781. <https://doi.org/10.1016/j.resconrec.2011.03.003>
- Bridgwater, A. V. (2003). Renewable fuels and chemicals by thermal processing of biomass. *Chemical Engineering Journal*, 91(2), 87–102. [https://doi.org/10.1016/S1385-8947\(02\)00142-0](https://doi.org/10.1016/S1385-8947(02)00142-0)
- Buah, W. K., Cunliffe, A. M., & Williams, P. T. (2007). Characterization of Products from the Pyrolysis of Municipal Solid Waste. *Process Safety and Environmental Protection*, 85(5), 450–457. <https://doi.org/10.1205/psep07024>
- Burra, K. G., & Gupta, A. K. (2018a). Thermochemical Reforming of Wastes to Renewable Fuels. In A. K. Runchal, A. K. Gupta, A. Kushari, A. De, & S. K. Aggarwal (Eds.), *Energy for Propulsion* (pp. 395–428). Springer Singapore. https://doi.org/10.1007/978-981-10-7473-8_17
- Burra, K. G., & Gupta, A. K. (2018b). Kinetics of synergistic effects in co-pyrolysis of biomass with plastic wastes. *Applied Energy*, 220, 408–418. <https://doi.org/10.1016/j.apenergy.2018.03.117>
- C. Clifford. (2020). 5.1 Biomass Pyrolysis | EGEE 439: Alternative Fuels from Biomass Sources. <https://www.education.psu.edu/egee439/node/537>
- Campoy, M., Gómez-Barea, A., Ollero, P., & Nilsson, S. (2014). Gasification of wastes in a pilot fluidized bed gasifier. *Fuel Processing Technology*, 121, 63–69. <https://doi.org/10.1016/j.fuproc.2013.12.019>
- Chatterjee, S., Houlding, T. K., Doluda, V. Yu., Molchanov, V. P., Matveeva, V. G., & Rebrov, E. V. (2017). Thermal Behavior of a Catalytic Packed-Bed Milli-reactor Operated under Radio Frequency Heating. *Industrial & Engineering Chemistry Research*, 56(45), 13273–13280. <https://doi.org/10.1021/acs.iecr.7b01723>
- Chen, L., Dupont, C., Salvador, S., Grateau, M., Boissonnet, G., & Schweich, D. (2013). Experimental study on fast pyrolysis of free-falling millimetric biomass particles between 800°C and 1000°C. *Fuel*, 106, 61–66. <https://doi.org/10.1016/j.fuel.2012.11.058>
- Chen, D., Yin, L., Wang, H., & He, P. (2014). Pyrolysis technologies for municipal solid waste: A review. *Waste Management*, 34(12), 2466–2486. <https://doi.org/10.1016/j.wasman.2014.08.004>
- Chen, W.-H., Eng, C. F., Lin, Y.-Y., & Bach, Q.-V. (2020). Independent parallel pyrolysis kinetics of cellulose, hemicelluloses and lignin at various heating rates analyzed by evolutionary computation. *Energy Conversion and Management*, 221, 113165. <https://doi.org/10.1016/j.enconman.2020.113165>
- Chhabra, V., Bambery, K., Bhattacharya, S., & Shastri, Y. (2020). Thermal and in situ infrared analysis to characterise the slow pyrolysis of mixed municipal solid waste (MSW) and its components. *Renewable Energy*, 148, 388–401. <https://doi.org/10.1016/j.renene.2019.10.045>

- Choi, M.-J., Jeong, Y.-S., & Kim, J.-S. (2021). Air gasification of polyethylene terephthalate using a two-stage gasifier with active carbon for the production of H₂ and CO. *Energy*, *223*, 120122. <https://doi.org/10.1016/j.energy.2021.120122>
- Couhert, C. (2007). *Pyrolyse flash à haute température de la biomasse ligno-cellulosique et de ses composés: Production de gaz de synthèse* [These de doctorat, Paris, ENMP]. <https://www.theses.fr/2007ENMP1531>
- Couto, N. D., Silva, V. B., & Rouboa, A. (2016). Thermodynamic Evaluation of Portuguese municipal solid waste gasification. *Journal of Cleaner Production*, *139*, 622–635. <https://doi.org/10.1016/j.jclepro.2016.08.082>
- Couto, N., Rouboa, A., Silva, V., Monteiro, E., & Bouziane, K. (2013). Influence of the Biomass Gasification Processes on the Final Composition of Syngas. *Energy Procedia*, *36*, 596–606. <https://doi.org/10.1016/j.egypro.2013.07.068>
- Couto, N., Silva, V., Monteiro, E., Teixeira, S., Chacartegui, R., Bouziane, K., Brito, P. S. D., & Rouboa, A. (2015). Numerical and experimental analysis of municipal solid wastes gasification process. *Applied Thermal Engineering*, *78*, 185–195. <https://doi.org/10.1016/j.applthermaleng.2014.12.036>
- Cozzani, V., Nicoletta, C., Petarca, L., Rovatti, M., & Tognotti, L. (1995). A Fundamental Study on Conventional Pyrolysis of a Refuse-Derived Fuel. *Industrial & Engineering Chemistry Research*, *34*(6), 2006–2020. <https://doi.org/10.1021/ie00045a010>
- Czajczyńska, D., Anguilano, L., Ghazal, H., Krzyżyńska, R., Reynolds, A. J., Spencer, N., & Jouhara, H. (2017). Potential of pyrolysis processes in the waste management sector. *Thermal Science and Engineering Progress*, *3*, 171–197. <https://doi.org/10.1016/j.tsep.2017.06.003>
- Daouk, E., Sani, R., Pham Minh, D., & Nzihou, A. (2018a). Thermo-conversion of Solid Recovered Fuels under inert and oxidative atmospheres: Gas composition and chlorine distribution. *Fuel*, *225*, 54–61. <https://doi.org/10.1016/j.fuel.2018.03.136>
- de Priall, O., Gogulancea, V., Brandoni, C., Hewitt, N., Johnston, C., Onofrei, G., & Huang, Y. (2021). Modelling and experimental investigation of small-scale gasification CHP units for enhancing the use of local biowaste. *Waste Management*, *136*, 174–183. <https://doi.org/10.1016/j.wasman.2021.10.012>
- Demirbas, A. (2004). Combustion characteristics of different biomass fuels. *Progress in Energy and Combustion Science*, *30*(2), 219–230. <https://doi.org/10.1016/j.pecs.2003.10.004>
- Devi, L., Ptasiński, K. J., Janssen, F. J. J. G., van Paasen, S. V. B., Bergman, P. C. A., & Kiel, J. H. A. (2005). Catalytic decomposition of biomass tars: Use of dolomite and untreated olivine. *Renewable Energy*, *30*(4), 565–587. <https://doi.org/10.1016/j.renene.2004.07.014>
- Deglise, X., Donnot, A., 2004. Bois énergie. Techniques de l'ingénieur BE85.
- Díaz, G., & Juliana, C. (2007). *Understanding Biomass Pyrolysis Kinetics: Improved Modeling -based on -comprehensive -thermokinetic Analysis*. Universitat Politècnica de Catalunya. <https://upcommons.upc.edu/handle/2117/93764>
- Ding, Y., Ezekoye, O. A., Lu, S., Wang, C., & Zhou, R. (2017). Comparative pyrolysis behaviors and reaction mechanisms of hardwood and softwood. *Energy Conversion and Management*, *132*, 102–109. <https://doi.org/10.1016/j.enconman.2016.11.016>

- Directive 2008/98/EC of the European Parliament and of the Council of 19 November 2008 on waste and repealing certain Directives (Text with EEA relevance), EP, CONSIL, 312 OJ L (2008). <http://data.europa.eu/eli/dir/2008/98/oj/eng>
- Dong, J. (2016a). *MSWs Gasification with emphasis on energy, environment and life cycle assesment*.
- E4tech, NNFCC. (2009). *Review of Technologies for Gasification of Biomass and Wastes*. E4tech. <https://www.e4tech.com/resources/95-review-of-technologies-for-gasification-of-biomass-and-wastes.php?filter=year%3A2009>
- Efika, E. C. (2013). *Hydrogen rich syngas from the pyrolysis and gasification of solid waste and biomass* [Phd, University of Leeds]. <https://etheses.whiterose.ac.uk/4943/>
- Ephraim, A. (2016a). *Valorization of wood and plastic waste by pyro-gasification and syngas cleaning* [Ecole des Mines d'Albi-Carmaux]. <https://tel.archives-ouvertes.fr/tel-01562225>
- FEDEREC, COMPTE-R. (2015). *Combustibles solides de récupération (CSR)—Caractérisation et évaluation de leurs performances en combustion* (p. 95). ADEME.
- Fernandez, A., Soria, J., Rodriguez, R., Baeyens, J., & Mazza, G. (2019). Macro-TGA steam-assisted gasification of lignocellulosic wastes. *Journal of Environmental Management*, 233, 626–635. <https://doi.org/10.1016/j.jenvman.2018.12.087>
- Fernández, J., Chatterjee, S., Degirmenci, V., & Rebrov, E. V. (2015). Scale-up of an RF heated micro trickle bed reactor to a kg/day production scale. *Green Processing and Synthesis*, 4(5), 343–353. <https://doi.org/10.1515/gps-2015-0035>
- Font Palma, C. (2013). Model for Biomass Gasification Including Tar Formation and Evolution. *Energy & Fuels*, 27(5), 2693–2702. <https://doi.org/10.1021/ef4004297>
- Garrido, M. A., & Font, R. (2015). Pyrolysis and combustion study of flexible polyurethane foam. *Journal of Analytical and Applied Pyrolysis*, 113, 202–215. <https://doi.org/10.1016/j.jaap.2014.12.017>
- Gauthier, G. (2013). *Synthèse de biocarburants de deuxième génération: Étude de la pyrolyse à haute température de particules de bois centimétriques*. [PhD Thesis]. <http://www.theses.fr/2013EMAC0004/document>
- Gauthier, G., Melkior, T., Grateau, M., Thierry, S., & Salvador, S. (2013). Pyrolysis of centimetre-scale wood particles: New experimental developments and results. *Journal of Analytical and Applied Pyrolysis*, 104, 521–530. <https://doi.org/10.1016/j.jaap.2013.05.017>
- Gerassimidou, S., Velis, C. A., Williams, P. T., & Komilis, D. (2020). Characterisation and composition identification of waste-derived fuels obtained from municipal solid waste using thermogravimetry: A review: *Waste Management & Research*. <https://doi.org/10.1177/0734242X20941085>
- Goli, V. S. N. S., Singh, D. N., & Baser, T. (2021). A critical review on thermal treatment technologies of combustible fractions from mechanical biological treatment plants. *Journal of Environmental Chemical Engineering*, 9(4), 105643. <https://doi.org/10.1016/j.jece.2021.105643>
- Gómez-Barea, A., & Leckner, B. (2010). Modeling of biomass gasification in fluidized bed. *Progress in Energy and Combustion Science*, 36(4), 444–509. <https://doi.org/10.1016/j.pecs.2009.12.002>
- Gomez-Barea, A., Nilsson, S., Vidal Barrero, F., & Campoy, M. (2010). Devolatilization of wood and wastes in fluidized bed. *Fuel Processing Technology*, 91(11), 1624–1633. <https://doi.org/10.1016/j.fuproc.2010.06.011>

- Götze, R., Pivnenko, K., Boldrin, A., Scheutz, C., & Astrup, T. F. (2016). Physico-chemical characterisation of material fractions in residual and source-segregated household waste in Denmark. *Waste Management*, *54*, 13–26. <https://doi.org/10.1016/j.wasman.2016.05.009>
- Grammelis, P., Basinas, P., Malliopoulou, A., & Sakellariopoulos, G. (2009). Pyrolysis kinetics and combustion characteristics of waste recovered fuels. *Fuel*, *88*(1), 195–205. <https://doi.org/10.1016/j.fuel.2008.02.002>
- Grieco, E. M., & Baldi, G. (2012). Pyrolysis of polyethylene mixed with paper and wood: Interaction effects on tar, char and gas yields. *Waste Management*, *32*(5), 833–839. <https://doi.org/10.1016/j.wasman.2011.12.014>
- Groleau, G., Tanguay-Rioux, F., Spreutels, L., Heroux, M., & Legros, R. (2019). Development of a msw gasification model for flexible integration into a MFA-LCA framework. *Detritus*, *7*. <https://doi.org/10.31025/2611-4135/2019.13850>
- Grønli, M. G., Várhegyi, G., & Di Blasi, C. (2002a). Thermogravimetric Analysis and Devolatilization Kinetics of Wood. *Industrial & Engineering Chemistry Research*, *41*(17), 4201–4208. <https://doi.org/10.1021/ie0201157>
- Grønli, M. G., Várhegyi, G., & Di Blasi, C. (2002b). Thermogravimetric Analysis and Devolatilization Kinetics of Wood. *Industrial & Engineering Chemistry Research*, *41*(17), 4201–4208. <https://doi.org/10.1021/ie0201157>
- Gu, Q., Wu, W., Jin, B., & Zhou, Z. (2020). Analyses for Synthesis Gas from Municipal Solid Waste Gasification under Medium Temperatures. *Processes*, *8*(1), 84. <https://doi.org/10.3390/pr8010084>
- Hadad, Y., Kochavi, E., & Levy, A. (2016). Inductive heating with a stepped diameter crucible. *Applied Thermal Engineering*, *102*, 149–157. <https://doi.org/10.1016/j.applthermaleng.2016.03.151>
- Heikkinen, J. M., Hordijk, J. C., de Jong, W., & Spliethoff, H. (2004). Thermogravimetry as a tool to classify waste components to be used for energy generation. *Journal of Analytical and Applied Pyrolysis*, *71*(2), 883–900. <https://doi.org/10.1016/j.jaap.2003.12.001>
- Hervy, M., Remy, D., Dufour, A., & Mauviel, G. (2019). Air-blown gasification of Solid Recovered Fuels (SRFs) in lab-scale bubbling fluidized-bed: Influence of the operating conditions and of the SRF composition. *Energy Conversion and Management*, *181*, 584–592. <https://doi.org/10.1016/j.enconman.2018.12.052>
- Hervy, M., Remy, D., Dufour, A., & Mauviel, G. (2021). Gasification of Low-Grade SRF in Air-Blown Fluidized Bed: Permanent and Inorganic Gases Characterization. *Waste and Biomass Valorization*, *12*(11), 6231–6244. <https://doi.org/10.1007/s12649-021-01434-w>
- Honus, S., Kumagai, S., Fedorko, G., Molnár, V., & Yoshioka, T. (2018a). Pyrolysis gases produced from individual and mixed PE, PP, PS, PVC, and PET—Part I: Production and physical properties. *Fuel*, *221*, 346–360. <https://doi.org/10.1016/j.fuel.2018.02.074>
- Houzelot, J. L., & Villermaux, J. (1984). A novel device for quenching: The cylindrical annular exchanger in laminar flow. *Chemical Engineering Science*, *39*(9), 1409–1413. [https://doi.org/10.1016/0009-2509\(84\)80074-3](https://doi.org/10.1016/0009-2509(84)80074-3)

- Hwang, I.-H., Kobayashi, J., & Kawamoto, K. (2014). Characterization of products obtained from pyrolysis and steam gasification of wood waste, RDF, and RPF. *Waste Management*, 34(2), 402–410. <https://doi.org/10.1016/j.wasman.2013.10.009>
- Iacovidou, E., Hahladakis, J., Deans, I., Velis, C., & Purnell, P. (2018). Technical properties of biomass and solid recovered fuel (SRF) co-fired with coal: Impact on multi-dimensional resource recovery value. *Waste Management*, 73, 535–545. <https://doi.org/10.1016/j.wasman.2017.07.001>
- ISO/TC 300—Solid recovered materials, including solid recovered fuels. (n.d.). ISO. Retrieved January 25, 2022, from <https://www.iso.org/cms/render/live/en/sites/isoorg/contents/data/committee/59/60/5960430.html>
- Jagustyn, B., Plis, A., Mastalerz, M., Hrabak, J., & Ściażko, M. (2017). Investigation of homogeneity and stability of items for proficiency testing of solid recovered fuels (SRF) analysis. *Accreditation and Quality Assurance*, 22, 1–6. <https://doi.org/10.1007/s00769-017-1283-7>
- Jaradat, Q. M., Saleh, F. Y., Lewis, R. V., Daugherty, K. E., & Rice, J. A. (1990). Characterization of refuse-derived fuel by pyrolysis-gas chromatography and gas chromatography/mass spectrometry. *Journal of Analytical and Applied Pyrolysis*, 17(2), 169–180. [https://doi.org/10.1016/0165-2370\(90\)85030-Q](https://doi.org/10.1016/0165-2370(90)85030-Q)
- Kalina, J. (2011). Modelling of fluidized bed biomass gasification in the quasi-equilibrium regime for preliminary performance studies of energy conversion plants. *Chemical and Process Engineering*, 32(2). <https://doi.org/10.2478/v10176-011-0007-5>
- Kamp, W. V. D., Wild, P., Knoef, H., & Kiel, J. (2006). Tar measurement in biomass gasification, standardisation and supporting R&D. *Undefined*. <https://www.semanticscholar.org/paper/Tar-measurement-in-biomass-gasification%2C-and-R%26D-Kamp-Wild/8b2ee8f68ba439120043a781e6bcbfbbd77d1485>
- Karjalainen, T., Bernhard Zimmer, & Staffan Berg. (2001). *Energy, carbon and other material flows in the life cycle assessment of forestry and forest products: Achievements of the Working Group 1 of the COST action E* (T. Karjalainen, Ed.). European Forest Institute.
- Kasataka, K., Kumagai, S., Kameda, T., Saito, Y., & Yoshioka, T. (2020). Enhancement of gasification and liquefaction during fast co-pyrolysis of cedar wood and polyethylene through control of synergistic interactions. *Bioresource Technology Reports*, 11, 100431. <https://doi.org/10.1016/j.biteb.2020.100431>
- Kaza, S., Yao, L., Bhada-Tata, P., & Van Woerden, F. (2018). *What a Waste 2.0: A Global Snapshot of Solid Waste Management to 2050*. The World Bank. <https://doi.org/10.1596/978-1-4648-1329-0>
- Kiel, J. H. A., Van Paasen, S. V. B., Neeft, J. P. A., Devi, L., Ptasiński, K. J., Janssen, F., Meijer, R., Berends, R. H., Temmink, H. M. G., & Brem, G. (2004). Primary measures to reduce tar formation in fluidised-bed biomass gasifiers. *ECN, ECN-C-04-014*.
- Kim, J. W., Lee, H. W., Lee, I.-G., Jeon, J.-K., Ryu, C., Park, S. H., Jung, S.-C., & Park, Y.-K. (2014). Influence of reaction conditions on bio-oil production from pyrolysis of construction waste wood. *Renewable Energy*, 65, 41–48. <https://doi.org/10.1016/j.renene.2013.07.009>
- King, S., Hutchinson, SA and Boxal, & NJ. (2021). *Advanced recycling technologies to address Australia's plastic waste*. CSIRO.

- Knofczynski, G. T., & Mundfrom, D. (2008). Sample Sizes When Using Multiple Linear Regression for Prediction. *Educational and Psychological Measurement*, 68(3), 431–442. <https://doi.org/10.1177/0013164407310131>
- Kwon, D., Yi, S., Jung, S., & Kwon, E. E. (2021). Valorization of synthetic textile waste using CO₂ as a raw material in the catalytic pyrolysis process. *Environmental Pollution*, 268, 115916. <https://doi.org/10.1016/j.envpol.2020.115916>
- Lédé, J. (2013). Biomass Fast Pyrolysis Reactors: A Review of a Few Scientific Challenges and of Related Recommended Research Topics. *Oil & Gas Science and Technology – Revue d'IFP Energies Nouvelles*, 68(5), 801–814. <https://doi.org/10.2516/ogst/2013108>
- Lee, U., Dong, J., & Chung, J. N. (2016). Production of useful energy from solid waste materials by steam gasification. *International Journal of Energy Research*, 40(11), 1474–1488. <https://doi.org/10.1002/er.3529>
- Li, S. (2019). *PET recycling via gasification—Influence of operating conditions on product distribution*. <https://aaltodoc.aalto.fi/443/handle/123456789/39818>
- Liu, S., Yu, J., Bikane, K., Chen, T., Ma, C., Wang, B., & Sun, L. (2018). Rubber pyrolysis: Kinetic modeling and vulcanization effects. *Energy*, 155, 215–225. <https://doi.org/10.1016/j.energy.2018.04.146>
- Liu, X., Burra, K. G., Wang, Z., Li, J., Che, D., & Gupta, A. K. (2020). On deconvolution for understanding synergistic effects in co-pyrolysis of pinewood and polypropylene. *Applied Energy*, 279, 115811. <https://doi.org/10.1016/j.apenergy.2020.115811>
- Long, Y., Meng, A., Chen, S., Zhou, H., Zhang, Y., & Li, Q. (2017). Pyrolysis and Combustion of Typical Wastes in a Newly Designed Macro Thermogravimetric Analyzer: Characteristics and Simulation by Model Components. *Energy & Fuels*, 31(7), 7582–7590. <https://doi.org/10.1021/acs.energyfuels.7b00796>
- Lopez, G., Artetxe, M., Amutio, M., Alvarez, J., Bilbao, J., & Olazar, M. (2018a). Recent advances in the gasification of waste plastics. A critical overview. *Renewable and Sustainable Energy Reviews*, 82, 576–596. <https://doi.org/10.1016/j.rser.2017.09.032>
- Lopez-Uribebarrenechea, A., de Marco, I., Caballero, B. M., Adrados, A., & Laresgoiti, M. F. (2012). Empiric model for the prediction of packaging waste pyrolysis yields. *Applied Energy*, 98, 524–532. <https://doi.org/10.1016/j.apenergy.2012.04.021>
- Luo, S., Xiao, B., Hu, Z., & Liu, S. (2010). Effect of particle size on pyrolysis of single-component municipal solid waste in fixed bed reactor. *International Journal of Hydrogen Energy*, 35(1), 93–97. <https://doi.org/10.1016/j.ijhydene.2009.10.048>
- Luque, R., & Speight, J. G. (Eds.). (2015). *Gasification for synthetic fuel production: Fundamentals, processes, and applications*. Elsevier/WP, Woodhead Publ.
- Maduskar, S., Facas, G. G., Papageorgiou, C., Williams, C. L., & Dauenhauer, P. J. (2018). Five Rules for Measuring Biomass Pyrolysis Rates: Pulse-Heated Analysis of Solid Reaction Kinetics of Lignocellulosic Biomass. *ACS Sustainable Chemistry & Engineering*, 6(1), 1387–1399. <https://doi.org/10.1021/acssuschemeng.7b03785>

- Mărculescu, C., Tîrțea, R. N., Khachatryan, L., & Boldor, D. (2022). Investigation of gasification kinetics of multi-component waste mixtures in a novel thermogravimetric flow reactor via gas analysis. *Bioresource Technology*, *343*, 126044. <https://doi.org/10.1016/j.biortech.2021.126044>
- Maric, J., Berdugo Vilches, T., Thunman, H., Gyllenhammar, M., & Seemann, M. (2018). Valorization of Automobile Shredder Residue Using Indirect Gasification. *Energy & Fuels*, *32*(12), 12795–12804. <https://doi.org/10.1021/acs.energyfuels.8b02526>
- Marongiu, A., Faravelli, T., & Ranzi, E. (2007). Detailed kinetic modeling of the thermal degradation of vinyl polymers. *Journal of Analytical and Applied Pyrolysis*, *78*(2), 343–362. <https://doi.org/10.1016/j.jaap.2006.09.008>
- Materazzi, M. (2017). *Clean Energy from Waste: Fundamental Investigations on Ashes and Tar Behaviours in a Two Stage Fluid Bed-Plasma Process for Waste Gasification*. Springer International Publishing. <http://www.springer.com/kr/book/9783319468693>
- Materazzi, M., Lettieri, P., Mazzei, L., Taylor, R., & Chapman, C. (2013a). Thermodynamic modelling and evaluation of a two-stage thermal process for waste gasification. *Fuel*, *108*, 356–369. <https://doi.org/10.1016/j.fuel.2013.02.037>
- Materazzi, M., Lettieri, P., Mazzei, L., Taylor, R., & Chapman, C. (2013b). Thermodynamic modelling and evaluation of a two-stage thermal process for waste gasification. *Fuel*, *108*, 356–369. <https://doi.org/10.1016/j.fuel.2013.02.037>
- Meng, A., Chen, S., Long, Y., Zhou, H., Zhang, Y., & Li, Q. (2015). Pyrolysis and gasification of typical components in wastes with macro-TGA. *Waste Management*, *46*, 247–256. <https://doi.org/10.1016/j.wasman.2015.08.025>
- Moreno, A. I., & Font, R. (2015). Pyrolysis of furniture wood waste: Decomposition and gases evolved. *Journal of Analytical and Applied Pyrolysis*, *113*, 464–473. <https://doi.org/10.1016/j.jaap.2015.03.008>
- Nahil, M. A., & Williams, P. T. (2010). Activated carbons from acrylic textile waste. *Journal of Analytical and Applied Pyrolysis*, *89*(1), 51–59. <https://doi.org/10.1016/j.jaap.2010.05.005>
- Násner, A. M. L., Lora, E. E. S., Palacio, J. C. E., Rocha, M. H., Restrepo, J. C., Venturini, O. J., & Ratner, A. (2017). Refuse Derived Fuel (RDF) production and gasification in a pilot plant integrated with an Otto cycle ICE through Aspen plus™ modelling: Thermodynamic and economic viability. *Waste Management*, *69*, 187–201. <https://doi.org/10.1016/j.wasman.2017.08.006>
- Nasrullah, M., Hurme, M., Oinas, P., Hannula, J., & Vainikka, P. (2017). Influence of input waste feedstock on solid recovered fuel production in a mechanical treatment plant. *Fuel Processing Technology*, *163*, 35–44. <https://doi.org/10.1016/j.fuproc.2017.03.034>
- Neef, J. P. A., Knoef, H. A. M., Zielke, U., Sjöström, K., Hasler, P., Simell, P. A., Dorrington, M. A., Thomas, L., Abatzoglou, N., & Deutch, S. (1999). Guideline for sampling and analysis of tar and particles in biomass producer gases. *Energy Project ERK6-Ct199-2002 Www. Tarweb. Net*.
- Neves, D., Matos, A., Tarelho, L., Thunman, H., Larsson, A., & Seemann, M. (2017). Volatile gases from biomass pyrolysis under conditions relevant for fluidized bed gasifiers. *Journal of Analytical and Applied Pyrolysis*, *127*, 57–67. <https://doi.org/10.1016/j.jaap.2017.09.002>

- Nilsson, S., Gómez-Barea, A., & Cano, D. F. (2012). Gasification reactivity of char from dried sewage sludge in a fluidized bed. *Fuel*, *92*(1), 346–353. <https://doi.org/10.1016/j.fuel.2011.07.031>
- Niu, M., Huang, Y., Jin, B., & Wang, X. (2014). Oxygen Gasification of Municipal Solid Waste in a Fixed-bed Gasifier. *Chinese Journal of Chemical Engineering*, *22*(9), 1021–1026. <https://doi.org/10.1016/j.cjche.2014.06.026>
- Ojha, D. K., & Vinu, R. (2015). Fast co-pyrolysis of cellulose and polypropylene using Py-GC/MS and Py-FT-IR. *RSC Advances*, *5*(82), 66861–66870. <https://doi.org/10.1039/C5RA10820A>
- Ouiminga, S. K., Rogaume, T., Daho, T., Richard, F., & Koulidiati, J. (2012). Thermal Degradation of Polyethylene Bags and Millet Stalks: Influence of the Temperature and the Local Concentration of Oxygen on the Conversion Rate of Carbon. *Advances in Chemical Engineering and Science*, *02*(01), 155–165. <https://doi.org/10.4236/aces.2012.21019>
- Pandey, D. S., Das, S., Pan, I., Leahy, J. J., & Kwapinski, W. (2016). Artificial neural network-based modelling approach for municipal solid waste gasification in a fluidized bed reactor. *Waste Management*, *58*, 202–213. <https://doi.org/10.1016/j.wasman.2016.08.023>
- Pinto, F., André, R. N., Carolino, C., Miranda, M., Abelha, P., Direito, D., Perdikaris, N., & Boukis, I. (2014). Gasification improvement of a poor quality solid recovered fuel (SRF). Effect of using natural minerals and biomass wastes blends. *Fuel*, *117*, 1034–1044. <https://doi.org/10.1016/j.fuel.2013.10.015>
- Pio, D. T., Tarelho, L. A. C., Tavares, A. M. A., Matos, M. A. A., & Silva, V. (2020). Co-gasification of refused derived fuel and biomass in a pilot-scale bubbling fluidized bed reactor. *Energy Conversion and Management*, *206*, 112476. <https://doi.org/10.1016/j.enconman.2020.112476>
- Porshnov, D. (2022). Evolution of pyrolysis and gasification as waste to energy tools for low carbon economy. *WIREs Energy and Environment*, *11*(1), e421. <https://doi.org/10.1002/wene.421>
- Ramos, A., Monteiro, E., & Rouboa, A. (2019). Numerical approaches and comprehensive models for gasification process: A review. *Renewable and Sustainable Energy Reviews*, *110*, 188–206. <https://doi.org/10.1016/j.rser.2019.04.048>
- Ramos, A., Monteiro, E., Silva, V., & Rouboa, A. (2018). Co-gasification and recent developments on waste-to-energy conversion: A review. *Renewable and Sustainable Energy Reviews*, *81*, 380–398. <https://doi.org/10.1016/j.rser.2017.07.025>
- Ramos Casado, R., Arenales Rivera, J., Borjabad García, E., Escalada Cuadrado, R., Fernández Llorente, M., Bados Sevillano, R., & Pascual Delgado, A. (2016). Classification and characterisation of SRF produced from different flows of processed MSW in the Navarra region and its co-combustion performance with olive tree pruning residues. *Waste Management*, *47*, 206–216. <https://doi.org/10.1016/j.wasman.2015.05.018>
- Ranzi, E., Corbetta, M., Manenti, F., & Pierucci, S. (2014). Kinetic modeling of the thermal degradation and combustion of biomass. *Chemical Engineering Science*, *110*, 2–12. <https://doi.org/10.1016/j.ces.2013.08.014>
- Ranzi, E., Faravelli, T., & Manenti, F. (2016). Pyrolysis, Gasification, and Combustion of Solid Fuels. In *Advances in Chemical Engineering* (Vol. 49, pp. 1–94). Elsevier. <https://doi.org/10.1016/bs.ache.2016.09.001>

- Recari, J., Berruoco, C., Abelló, S., Montané, D., & Farriol, X. (2016). Gasification of two solid recovered fuels (SRFs) in a lab-scale fluidized bed reactor: Influence of experimental conditions on process performance and release of HCl, H₂S, HCN and NH₃. *Fuel Processing Technology*, *142*, 107–114. <https://doi.org/10.1016/j.fuproc.2015.10.006>
- RECORD. (2018). *Utilisation des CSR et des RDF en Europe. Synthèse bibliographique et situations administratives rencontrées sur le terrain* (p. 393p). n°16-0250/1A.
- Redko, T., Volford, A., Marek, E. J., Scott, S. A., & Hayhurst, A. N. (2020). Measurement of the times for pyrolysis and the thermal diffusivity of a pyrolysing particle of wood and also of the resulting char. *Combustion and Flame*, *212*, 510–518. <https://doi.org/10.1016/j.combustflame.2019.10.024>
- Reizer, E., Viskolcz, B., & Fiser, B. (2022). Formation and growth mechanisms of polycyclic aromatic hydrocarbons: A mini-review. *Chemosphere*, *291*, 132793. <https://doi.org/10.1016/j.chemosphere.2021.132793>
- Ribeiro, A., Vilarinho, C., Araújo, J., & Carvalho, J. (2017). Refuse Derived Fuel (RDF) Gasification Using Different Gasifying Agents. *Volume 6: Energy*, V006T08A057. <https://doi.org/10.1115/IMECE2017-71268>
- Robinson, T. (2015). *Bubbling Fluidized Bed Gasification of Biomass and Refuse Derived Fuel* [Thesis, Université d'Ottawa / University of Ottawa]. <https://doi.org/10.20381/ruor-4078>
- Robinson, T., Bronson, B., Gogolek, P., & Mehrani, P. (2016). Sample preparation for thermo-gravimetric determination and thermo-gravimetric characterization of refuse derived fuel. *Waste Management*, *48*, 265–274. <https://doi.org/10.1016/j.wasman.2015.11.018>
- Robinson, T., Bronson, B., Gogolek, P., & Mehrani, P. (2017). Air-blown bubbling fluidized bed co-gasification of woody biomass and refuse derived fuel. *Canadian Journal of Chemical Engineering*, *95*(1), 55–61. Scopus. <https://doi.org/10.1002/cjce.22641>
- Runchal, A. K., Gupta, A. K., Kushari, A., De, A., & Aggarwal, S. K. (2018). *Energy for Propulsion A Sustainable Technologies Approach*. Springer Singapore : Imprint: Springer. <https://link.springer.com/10.1007/978-981-10-7473-8>
- Saadatkah, N., Garcia, A. C., Ackermann, S., Leclerc, P., Latifi, M., Samih, S., Patience, G. S., & Chaouki, J. (2020). Experimental methods in chemical engineering: Thermogravimetric analysis—TGA. *The Canadian Journal of Chemical Engineering*, *98*(1), 34–43. <https://doi.org/10.1002/cjce.23673>
- Saghir, M., Rehan, M., & Nizami, A.-S. (2018). Recent Trends in Gasification Based Waste-to-Energy. In Y. Yun (Ed.), *Gasification for Low-grade Feedstock*. InTech. <https://doi.org/10.5772/intechopen.74487>
- Samih, S., & Chaouki, J. (2015). Development of a fluidized bed thermogravimetric analyzer. *AIChE Journal*, *61*(1), 84–89. <https://doi.org/10.1002/aic.14637>
- Santamaria, L., Beirow, M., Mangold, F., Lopez, G., Olazar, M., Schmid, M., Li, Z., & Scheffknecht, G. (2021). Influence of temperature on products from fluidized bed pyrolysis of wood and solid recovered fuel. *Fuel*, *283*, 118922. <https://doi.org/10.1016/j.fuel.2020.118922>
- Shukla, B., Miyoshi, A., & Koshi, M. (2010). Role of Methyl Radicals in the Growth of PAHs. *Journal of the American Society for Mass Spectrometry*, *21*(4), 534–544. <https://doi.org/10.1016/j.jasms.2009.12.019>

- Siedlecki, M., De Jong, W., & Verkooyen, A. H. M. (2011). Fluidized Bed Gasification as a Mature And Reliable Technology for the Production of Bio-Syngas and Applied in the Production of Liquid Transportation Fuels—A Review. *Energies*, 4(3), 389–434. <https://doi.org/10.3390/en4030389>
- Sieradzka, M., Rajca, P., Zajemska, M., Mlonka-Mędrala, A., & Magdziarz, A. (2020). Prediction of gaseous products from refuse derived fuel pyrolysis using chemical modelling software—Ansys Chemkin-Pro. *Journal of Cleaner Production*, 248, 119277. <https://doi.org/10.1016/j.jclepro.2019.119277>
- Singh, R. K., Ruj, B., Sadhukhan, A. K., & Gupta, P. (2019). Impact of fast and slow pyrolysis on the degradation of mixed plastic waste: Product yield analysis and their characterization. *Journal of the Energy Institute*. <https://doi.org/10.1016/j.joei.2019.01.009>
- Solid Recovered Fuels: Specification and Classes: CEN/TS 15359 Technical Specification : English Version*. (2006). European Committee for Standardization.
- Sørum, L., Grønli, M. G., & Hustad, J. E. (2001). Pyrolysis characteristics and kinetics of municipal solid wastes. *Fuel*, 80(9), 1217–1227. [https://doi.org/10.1016/S0016-2361\(00\)00218-0](https://doi.org/10.1016/S0016-2361(00)00218-0)
- Souza-Santos, M. L. de. (2010). *Solid Fuels Combustion and Gasification: Modeling, Simulation, and Equipment Operations Second Edition*. CRC Press.
- Stančin, H., Růžičková, J., Mikulčić, H., Raclavská, H., Kucbel, M., Wang, X., & Duić, N. (2019). Experimental analysis of waste polyurethane from household appliances and its utilization possibilities. *Journal of Environmental Management*, 243, 105–115. <https://doi.org/10.1016/j.jenvman.2019.04.112>
- Šuhaj, P., Husár, J., & Haydary, J. (2020). Gasification of RDF and Its Components with Tire Pyrolysis Char as Tar-Cracking Catalyst. *Sustainability*, 12(16), 6647. <https://doi.org/10.3390/su12166647>
- Tanoh, T. S. (2021). *Production d'un syngaz par pyrogazéification de biomasse en vue d'une biométhanation* [These de doctorat, Ecole nationale des Mines d'Albi-Carmaux]. <http://www.theses.fr/2021EMAC0002>
- Trninić, M., Stojiljković, D., Manić, N., Skreiberg, Ø., Wang, L., & Jovović, A. (2020). A mathematical model of biomass downdraft gasification with an integrated pyrolysis model. *Fuel*, 265, 116867. <https://doi.org/10.1016/j.fuel.2019.116867>
- Trovati, G., Sanches, E. A., Neto, S. C., Mascarenhas, Y. P., & Chierice, G. O. (2010). Characterization of polyurethane resins by FTIR, TGA, and XRD. *Journal of Applied Polymer Science*, 115(1), 263–268. <https://doi.org/10.1002/app.31096>
- Tsalidis, G. A., Tsekos, C., Anastasakis, K., & de Jong, W. (2018). The impact of dry torrefaction on the fast pyrolysis behavior of ash wood and commercial Dutch mixed wood in a pyroprobe. *Fuel Processing Technology*, 177, 255–265. <https://doi.org/10.1016/j.fuproc.2018.04.026>
- US EPA, O. (2017, October 2). *National Overview: Facts and Figures on Materials, Wastes and Recycling* [Overviews and Factsheets]. <https://www.epa.gov/facts-and-figures-about-materials-waste-and-recycling/national-overview-facts-and-figures-materials>
- Velis, C. A., Wagland, S., Longhurst, P., Robson, B., Sinfield, K., Wise, S., & Pollard, S. (2013). Solid Recovered Fuel: Materials Flow Analysis and Fuel Property Development during the Mechanical Processing of Biodried Waste. *Environmental Science & Technology*, 47(6), 2957–2965. <https://doi.org/10.1021/es3021815>

- Vermeulen, I., Van Caneghem, J., Block, C., Baeyens, J., & Vandecasteele, C. (2011). Automotive shredder residue (ASR): Reviewing its production from end-of-life vehicles (ELVs) and its recycling, energy or chemicals' valorisation. *Journal of Hazardous Materials*, *190*(1), 8–27. <https://doi.org/10.1016/j.jhazmat.2011.02.088>
- Waldheim, L. (2018). *Gasification of waste for energy carriers: A review*. <http://edepot.wur.nl/471047>
- Wei, X., Zhong, H., Yang, Q., Yao, E., Zhang, Y., & Zou, H. (2019). Studying the mechanisms of natural rubber pyrolysis gas generation using RMD simulations and TG-FTIR experiments. *Energy Conversion and Management*, *189*, 143–152. <https://doi.org/10.1016/j.enconman.2019.03.069>
- Westerhout, R. W. J., Kuipers, J. A. M., & van Swaaij, W. P. M. (1998). Experimental Determination of the Yield of Pyrolysis Products of Polyethylene and Polypropene. Influence of Reaction Conditions. *Industrial & Engineering Chemistry Research*, *37*(3), 841–847. <https://doi.org/10.1021/ie970384a>
- Wilk, V., & Hofbauer, H. (2013). Conversion of mixed plastic wastes in a dual fluidized bed steam gasifier. *Fuel*, *107*, 787–799. <https://doi.org/10.1016/j.fuel.2013.01.068>
- Win, M. M., Asari, M., Hayakawa, R., Hosoda, H., Yano, J., & Sakai, S. (2019). Characteristics of gas from the fluidized bed gasification of refuse paper and plastic fuel (RPF) and wood biomass. *Waste Management*, *87*, 173–182. <https://doi.org/10.1016/j.wasman.2019.02.002>
- Win, M. M., Asari, M., Hayakawa, R., Hosoda, H., Yano, J., & Sakai, S.-I. (2020). Gas and tar generation behavior during flash pyrolysis of wood pellet and plastic. *Journal of Material Cycles and Waste Management*, *22*(2), 547–555. <https://doi.org/10.1007/s10163-019-00949-8>
- Wong, K. K., Gamage, N., Setunge, S., & Pannirselvam, M. (2014). Thermal Behaviour of Hardwood and Softwood Composites. *Advanced Materials Research*, *905*, 220–225. <https://doi.org/10.4028/www.scientific.net/AMR.905.220>
- Yang, H., Yan, R., Chen, H., Lee, D. H., & Zheng, C. (2007). Characteristics of hemicellulose, cellulose and lignin pyrolysis. *Fuel*, *86*(12), 1781–1788. <https://doi.org/10.1016/j.fuel.2006.12.013>
- Yang, Q., Yu, S., Zhong, H., Liu, T., Yao, E., Zhang, Y., Zou, H., & Du, W. (2021). Gas products generation mechanism during co-pyrolysis of styrene-butadiene rubber and natural rubber. *Journal of Hazardous Materials*, *401*, 123302. <https://doi.org/10.1016/j.jhazmat.2020.123302>
- Yang, W.-S., Lee, J.-S., Park, S.-W., Kang, J.-J., Alam, T., & Seo, Y.-C. (2016). Gasification applicability study of polyurethane solid refuse fuel fabricated from electric waste by measuring syngas and nitrogenous pollutant gases. *Journal of Material Cycles and Waste Management*, *18*(3), 509–516. <https://doi.org/10.1007/s10163-016-0512-1>
- You, S., Ok, Y. S., Tsang, D. C. W., Kwon, E. E., & Wang, C.-H. (2018). Towards practical application of gasification: A critical review from syngas and biochar perspectives. *Critical Reviews in Environmental Science and Technology*, *48*(22–24), 1165–1213. <https://doi.org/10.1080/10643389.2018.1518860>
- Yu, H., Zhang, Z., Li, Z., & Chen, D. (2014). Characteristics of tar formation during cellulose, hemicellulose and lignin gasification. *Fuel*, *118*, 250–256. <https://doi.org/10.1016/j.fuel.2013.10.080>
- Zaini, I. N., García López, C., Pretz, T., Yang, W., & Jönsson, P. G. (2019). Characterization of pyrolysis products of high-ash excavated-waste and its char gasification reactivity and kinetics under a steam atmosphere. *Waste Management*, *97*, 149–163. <https://doi.org/10.1016/j.wasman.2019.08.001>

- Zheng, J., Jin, Y., Chi, Y., Wen, J., Jiang, X., & Ni, M. (2009). Pyrolysis characteristics of organic components of municipal solid waste at high heating rates. *Waste Management*, *29*(3), 1089–1094. <https://doi.org/10.1016/j.wasman.2008.06.034>
- Zheng, Y., Tao, L., Yang, X., Huang, Y., Liu, C., & Zheng, Z. (2018). Study of the thermal behavior, kinetics, and product characterization of biomass and low-density polyethylene co-pyrolysis by thermogravimetric analysis and pyrolysis-GC/MS. *Journal of Analytical and Applied Pyrolysis*, *133*, 185–197. <https://doi.org/10.1016/j.jaap.2018.04.001>
- Zhou, H. (2017). *Combustible Solid Waste Thermochemical Conversion*. Springer Singapore. <https://doi.org/10.1007/978-981-10-3827-3>
- Zhou, H., Long, Y., Meng, A., Li, Q., & Zhang, Y. (2015). Classification of municipal solid waste components for thermal conversion in waste-to-energy research. *Fuel*, *145*, 151–157. <https://doi.org/10.1016/j.fuel.2014.12.015>
- Zhou, H., Meng, A., Long, Y., Li, Q., & Zhang, Y. (2014a). Classification and comparison of municipal solid waste based on thermochemical characteristics. *Journal of the Air & Waste Management Association*, *64*(5), 597–616. <https://doi.org/10.1080/10962247.2013.873094>
- Zhou, H., Meng, A., Long, Y., Li, Q., & Zhang, Y. (2014b). Interactions of municipal solid waste components during pyrolysis: A TG-FTIR study. *Journal of Analytical and Applied Pyrolysis*, *108*, 19–25. <https://doi.org/10.1016/j.jaap.2014.05.024>
- Zhou, H., Wu, C., Onwudili, J. A., Meng, A., Zhang, Y., & Williams, P. T. (2015). Polycyclic aromatic hydrocarbons (PAH) formation from the pyrolysis of different municipal solid waste fractions. *Waste Management*, *36*, 136–146. <https://doi.org/10.1016/j.wasman.2014.09.014>

APPENDICES

A.	APPENDIX A. SRF CLASSIFICATION BY THE EN15359 STANDARD.....	162
B.	APPENDIX B. THE NEW PYRATES SETUP.....	163
C.	APPENDIX C. GEOMETRY OF THE CFD MODEL OF THE NEW PYRATES REACTOR.....	164
D.	APPENDIX D. CHARACTERIZATION OF THE SRF SAMPLE.....	166
E.	APPENDIX E. CONDENSABLE AND GAS ANALYSIS INSTRUMENTS.....	168
	RESUME ETENDU EN FRANÇAIS.....	172

Appendix A. SRF Classification by the EN15359 standard

The EN 15359 standard proposed a quality classification system based on three parameters: The lower heating value (LHV) (economic criterion), the chlorine content (technical criterion, as it conditions the post processing techniques) and the mercury content (environmental criterion). This classification system is presented in Table A-1. Each parameter is be assigned into five classes, where Class 1 represents the most desirable attribute. More detailed classifications have been proposed (FEDEREC, COMPTE-R, 2015), taking into account other parameters (like ash content, density and size distribution) but they are not widely implemented.

Criteria	Statistical parameter	Unit	Classes				
			1	2	3	4	5
Lower heating value (LHV)	Mean	MJ.kg ⁻¹ (ar)	≥25	≥20	≥15	≥10	≥3
Chlorine (Cl)	Mean	% (db)	≤0.2	≤0.6	≤1.0	≤1.5	≤3
Mercury (Hg)	Median	mg.kg ⁻¹ (ar)	≤0.02	≤0.03	≤0.08	≤0.15	≤0.50
	80th percentile	mg.kg ⁻¹ (ar)	≤0.04	≤0.06	≤0.16	≤0.30	≤1.00

a (ar): as received, (db): dry basis.

Table A-1. SRF Classification system according to EN15359 (Solid Recovered Fuels, 2006).

Appendix B. The NEW PYRATES setup

A photo of the experimental device is showed in **Figure B-1**. This photo shows the reactor main body, the induction coil, the gas outlet and the first two impingers, which are immersed in a cold bath.



Figure B-1. Photo of the experimental setup.

Appendix C. Geometry of the CFD model of the NEW PYRATES reactor

Figure C-1 and Figure C-2 illustrate the model geometry used in the CFD calculations, which was discretized using a 2D-axisymmetric approach. The exchanger and sample crucible were also considered. The mesh contains a total of 71642 nodes.

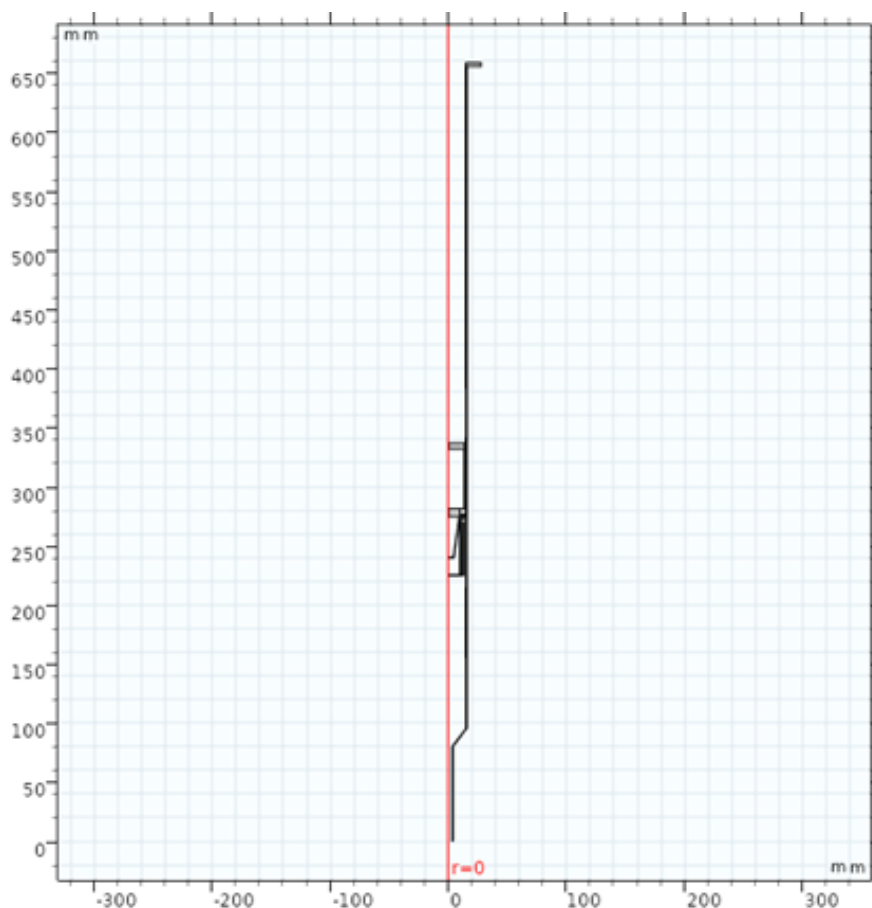


Figure C-1. Simulated system geometry.

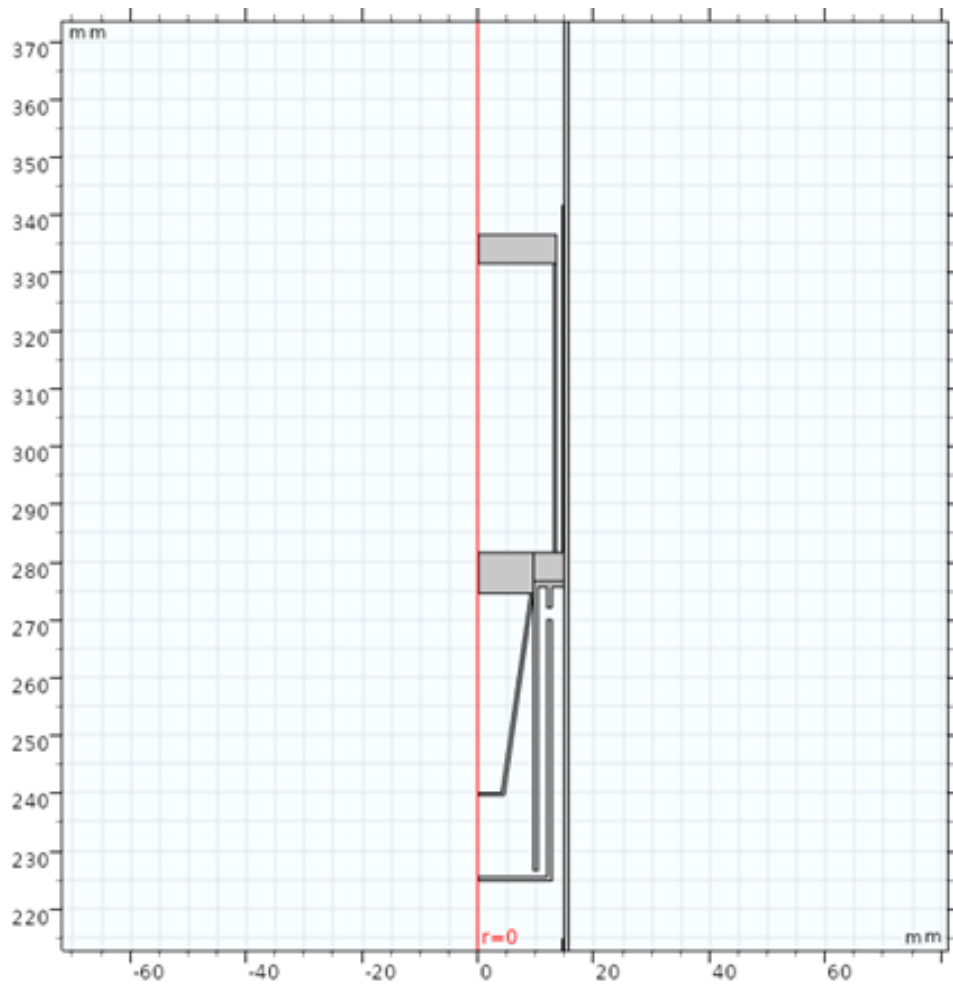


Figure C-2. Close up of the exchanger and sample crucible.

Appendix D. Characterization of the SRF sample

A characterization of a batch of the SRF fluff was previously conducted by Lucas le Martelot, a researcher from our laboratory. A picture of the raw SRF is shown in **Figure D-1**. The measured lower heating value was of 18.8 MJ.kg^{-1} .



Figure D-1. Photograph of the supplied SRF fluff.

The size distribution of the raw fluff was very heterogeneous. It contained large particles of several centimeters as well as fines of less than 1 mm. A sample of 5.76 kg was taken from the provided big-bags and then reduced to a 1.24 kg sample following the quartering and sampling protocol of NF EN 14778. The particles with a size superior to 1cm were manually sorted into 9 unique fractions:

- Dense plastics
- light plastics
- textiles
- paper/cardboard
- wood
- foam
- expanded polystyrene
- elastomers
- and inert materials (e.g. rubble, plaster, ceramics, and elements containing metal such as electrical cables).

Photos of the sorted fractions are presented in **Figure D-2**.



Figure D-2. Manually sorted fractions from the SRF fluff sample.

The undersize fraction (fines) was divided into two categories 500–850 μm , and below 500 μm . Then, each one of the separated fractions was weighted which resulted in the fractional composition of the sample presented in Table D-1.

Fraction	wt %
Dense plastics	21%
Light plastics	12%
Wood	15,5%
Paper/Cardboard	13%
Textiles	11%
Foams	4%
Elastomers	6%
Polystyrene	2,5%
Inerts	6%
Fines(<850 μm)	9%

Table D-1. Fractional composition (wt %) of the SRF fluff.

Appendix E. Condensable and gas analysis instruments

- Analysis of condensable species:

For the analysis of condensable species a gas chromatograph with a flame ionization detector [GC-FID 7890A, Agilent Technologies] was used. In this device, a flame breaks down the species within the sample into ions and free electrons, producing a specific current flow. The electric current generated is reported in a chromatogram, where each species is represented by a peak at a given retention time. Concentration was calculated from the peak area. More details of the device are shown in Table E-1.


Flame ionization detector gas chromatograph (GC-FID)		
	Model	7890A, Agilent Technologies
	Capillary column	Elite 1701 Column PerkinElmer 60m length, 0.25 mm internal diameter, 0.25 μm film thickness -20 $^{\circ}\text{C}$ to 280 $^{\circ}\text{C}$
	Carrier gas	Helium (He), 1.0 mL/min
	Oven temperature program	Ramp 1: 45 $^{\circ}\text{C}/\text{min}$ to 40 $^{\circ}\text{C}$, hold for 5 min. Ramp 2: 6 $^{\circ}\text{C}/\text{min}$ to 230 $^{\circ}\text{C}$, hold for 23 min.
	Relative uncertainty (%)	1-10%

Table E-1. Gas chromatograph used for the analysis of non-condensable species.

A total of 38 organic compounds can be detected, however, only 30 had calibration standards. The quantification of the remaining 8 compounds was realized by assuming a response factor equal to unity, as recommended in the ECN tar protocol sampling guidelines. The detected and calibrated species (highlighted in green) are listed in Table E-2.

Class	Name	Formula	Molecular weight (g/mol)	Boiling point (°C)
Other	Propene	C ₃ H ₆	42	-47.7
Other	1,3 Butadiene	C ₄ H ₆	54	-4.4
Other	Methanol	CH ₄ O	32	64.7
Other	1,3 cyclopentadiene	C ₅ H ₆	66	40.8
Other	Formaldehyde	CH ₂ O	30	-19
Acid/Ketones	Acid acetic methylester	C ₃ H ₆ O ₂	74	141,7
Tar species				
Heterocyclics	Thiofene	C ₄ H ₄ S	84	84
Heterocyclics	Pyridine	C ₅ H ₅ N	79	116
Heterocyclics	Pyrrole	C ₄ H ₅ N	67	130,5
Heterocyclics	Benzofuran	C ₈ H ₆ O	118	174
Heterocyclics	Aniline	C ₆ H ₇ N	93	184
Heterocyclics	Benzonitrile	C ₇ H ₅ N	103	191
Heterocyclics	Phenol	C ₆ H ₆ O	94	181,7
Heterocyclics	Benzopyridine	C ₉ H ₇ N	129	238
Heterocyclics	Indole	C ₈ H ₇ N	117	254
Heterocyclics	Dibenzofuran	C ₁₂ H ₈ O	168	287
Light Aromatics	Benzene	C ₆ H ₆	78	80
Light Aromatics	Toluene	C ₇ H ₈	92	110,6
Light Aromatics	Ethylbenzene	C ₈ H ₁₀	106	136
Light Aromatics	p-Xylene	C ₈ H ₁₀	106	138
Light Aromatics	o-Xylene	C ₈ H ₁₀	106	144
Light Aromatics	Phenylacetylene	C ₈ H ₆	102	142
Light Aromatics	Styrene	C ₈ H ₈	104	145
Light Aromatics	a-Methyl styrene	C ₉ H ₁₀	118	166
Light Aromatics	o-Methylstyrene	C ₉ H ₁₀	118	166
Light Aromatics	Indene	C ₉ H ₈	116	182
Light PAHs	Naphthalene	C ₁₀ H ₈	128	218
Light PAHs	Naphthalene, 2-methyl-	C ₁₁ H ₁₀	142	239,9
Light PAHs	Naphthalene, 1-methyl-	C ₁₁ H ₁₀	142	241
Light PAHs	Biphenyl	C ₁₂ H ₁₀	154	255
Light PAHs	Naphtalene,2-ethenyl-	C ₁₂ H ₁₀	154	270,9
Light PAHs	Acenaphthylene	C ₁₂ H ₈	152	280
Light PAHs	Acenaphthene	C ₁₂ H ₁₀	154	279
Light PAHs	Fluorene	C ₁₃ H ₁₀	166	295
Light PAHs	Phenanthrene	C ₁₄ H ₁₀	178	336
Light PAHs	Anthracene	C ₁₄ H ₁₀	178	340
Heavy PAH	Fluoranthene	C ₁₆ H ₁₀	202	375
Heavy PAH	Pyrene	C ₁₆ H ₁₀	202	404

Table E-2. Detected and calibrated species in the GC-FID analysis.

- **Analysis of permanent gases:**

Online analysis by NDIR

Produced gases were analyzed online using a Non-Dispersive Infrared Gas Analyzer (NDIR) [Model 30, California Analytical Instruments, Inc.]. This device measures the concentration of CO, CO₂, and CH₄, based on the principle that each component shows a unique absorption line spectrum in the infrared region. Details of the device are shown in Table E-3.


Non-Dispersive Infrared Gas Analyzer (NDIR)		
	Model	Model 30, California Analytical Instruments, Inc.
	Recommended flow rate	0.5 to 2 NL.min ⁻¹
	Maximum working temperature	50 °C
	Maximum concentration	50% for CO, 30% for CO ₂ , and 15% for CH ₄ .
	Relative uncertainty (%)	5%

Table E-3. Gas detector used for the online analysis of permanent gases.

Offline analysis by gas chromatography:

Non-condensable gases were analyzed using a micro-gas chromatograph [micro-GC-3000A analyzer, Agilent Technologies]. In the micro-GC, components in the sampled gas are separated inside four different columns. The component peak for a given retention time is compared with the previously calibrated standard to determine its concentration. The quantification is made with a thermal conductivity detector (TCD). Details of the device and the columns are presented in Table E-4. The relative uncertainty of the measurements was calculated from occasional calibration runs performed with standard gas mixtures.


Micro-gas chromatograph (μ GC)						
	Model		3000A, Agilent Technologies			
	Carrier gases		Argon (Ar): Column A Helium (He): Columns B,C,D			
	Relative uncertainty (%)		10%			
Column details:						
Name	Length (m)	Injection temp. ($^{\circ}$ C)	Column temp. ($^{\circ}$ C)	Column pressure (psi)	Injection time (ms)	Calibrated species
A. VAR Molsieve 5 Å	10	90	90	28	50	Helium (He), Hydrogen (H ₂), Oxygen (O ₂), Nitrogen (N ₂), Methane (CH ₄) Carbon monoxide (CO)
B. VAR Molsieve 5 Å	10	90	90	28	50	Argon + Oxygen (O ₂ +Ar), Nitrogen (N ₂) Methane (CH ₄), Carbon monoxide (CO)
C.VAR PPU	8	80	70	24	30	Carbon dioxide (CO ₂), Acetylene (C ₂ H ₂), Ethylene (C ₂ H ₄), Ethane (C ₂ H ₆) Propane (C ₃ H ₈), Butadiene (C ₄ H ₆), Water (H ₂ O)
D. Stabilwax	10	70	50	28	180	2-propanol(C ₃ H ₈ O), Benzene(C ₆ H ₆) Toluene(C ₇ H ₈), Water (H ₂ O)

Table E-4. Characteristics of the micro-GC chromatograph and its columns.

Résumé étendu en français

La consommation d'énergie et de biens a considérablement augmenté depuis le début du vingtième siècle, entraînant une surconsommation des ressources fossiles, et par conséquent une augmentation importante des émissions de gaz à effet de serre. Ceci est couplé à une production accrue de déchets, issus des activités humaines quotidiennes. Dans ce contexte, un des objectifs de la loi de transition énergétique pour la croissance verte (LTECV) est la réduction de 50% de la quantité de déchets non dangereux dans les décharges d'ici à 2025.

Les combustibles solides de récupération (CSR) sont produits à partir de matériaux à haut pouvoir calorifique (papier, carton, plastiques, textiles, bois, élastomères entre autres), provenant de gisements de déchets non dangereux industriels ou ménagers. En France, l'Agence de l'environnement et de la maîtrise de l'énergie (ADEME) estime que les objectifs réglementaires conduiront à la production d'environ 5 MT/an de CSR dans le pays d'ici 2050 (ADEME, 2021), dont environ 30% seront consommés par l'industrie du ciment. Par conséquent, il reste une grande place pour l'utilisation des CSR dans des unités de production d'énergie dédiées, autres que l'industrie cimentière.

Les procédés thermochimiques comme la pyrolyse et la gazéification sont des alternatives intéressantes à la combustion pour la valorisation énergétique. Parmi les technologies de réacteur utilisées dans la gazéification, la technologie du lit fluidisé présente un intérêt particulier, car c'est l'une des plus matures, et aussi la plus adaptée aux ressources hétérogènes telles que les CSR. Cependant, des problèmes techniques, économiques et environnementaux doivent encore être surmontés pour une application industrielle à grande échelle de la gazéification des CSR. La plupart de ces défis sont liés à l'hétérogénéité et à la variabilité de la composition du combustible, qui influencent le rendement et la qualité du gaz produit.

L'objectif principal de cette thèse est d'étudier la pyrolyse et la gazéification des combustibles solides de récupération, et en particulier de faire le lien entre les produits de pyrolyse et de gazéification et les caractéristiques initiales de la ressource. Pour atteindre cet objectif, ce travail est divisé en trois parties principales :

- Dans la première, un nouveau dispositif expérimental à l'échelle du laboratoire est développé pour effectuer des tests dans des conditions de réaction contrôlées. Le développement du réacteur est complété par une caractérisation thermique pendant le chauffage et en régime permanent.

- La deuxième partie du travail consiste en une étude expérimentale de la pyrolyse et de la gazéification de combustible solide de récupération représenté par des matériaux modèles. Ces matériaux ont été étudiés individuellement et en mélange pour évaluer leur interaction au cours de la pyrolyse. L'influence de l'ajout d'air sur les quantités et compositions des produits, est étudiée.

- Dans la troisième partie du travail, une corrélation est développée, destinée à prédire les produits de pyrolyse en utilisant la composition élémentaire de la matière première. La corrélation est ensuite validée avec des résultats expérimentaux pour le CSR et les mélanges

Ce manuscrit est organisé en 4 chapitres, complétés par l'introduction et la conclusion :

Le chapitre 1 présente une revue de la littérature pour comprendre les sujets abordés dans cette thèse.

Le chapitre 2 décrit le dispositif expérimental, ainsi que sa caractérisation thermique.

Le chapitre 3 présente les échantillons utilisés dans l'étude, les procédures expérimentales et les méthodes utilisées pour quantifier et caractériser les produits de la réaction.

Le chapitre 4 présente et discute les résultats expérimentaux obtenus dans le dispositif expérimental, ainsi que le développement et la validation de la corrélation.

Chapitre 1 : Revue Bibliographique

Les déchets solides peuvent provenir des nombreuses sources, résumés dans le **Table 1-1**. Dans ce travail, nous nous intéressons aux déchets solides combustibles à haut pouvoir calorifique ($>10\text{MJ.kg}^{-1}$), qui sont généralement utilisés dans la production de combustibles dérivés de déchets. Ces combustibles ont reçu de nombreuses dénominations, généralement confuses et mal utilisées dans la littérature. Les Combustibles Solides de Récupération (CSR) correspondent à des matériaux combustibles dérivés de déchets qui respectent les spécifications et les exigences de qualité en France (ICPE 2971. AIDA). Ils sont en partie composés de matériaux d'origine fossile, et d'origine biogénique (50 à 70 % du total) (ADEME, FEDEREC, 2019). Les caractéristiques physiques et chimiques des CSR peuvent varier significativement en fonction de leur origine (**Figure 1-3**). Dans la section 1.1.3., des données sur la composition et le pouvoir calorifique des matériaux les plus courants dans chacune des fractions typiques des CSR sont présentées. Les **Tableaux 1-2 à 1-5** montrent l'analyse proximale (qui comprend la teneur en humidité, les matières volatiles et le carbone fixe), et l'analyse finale (qui comprend le carbone, l'hydrogène, l'oxygène, le soufre et le chlore).

Les principaux procédés thermochimiques pour la valorisation énergétique des CSR sont la torrefaction, la combustion, la pyrolyse et la gazéification (Table 1-7). Les procédés hydrothermaux sont aussi des voies de valorisation énergétique, qui fonctionnent à haute pression et conviennent mieux aux combustibles à forte teneur en humidité. La gazéification et la pyrolyse, qui font l'objet de cette étude, présentent divers avantages par rapport à la combustion (permettant par exemple une plus large gamme d'applications pour le gaz produit), mais elle doit surmonter plusieurs problèmes technologiques pour être mise en œuvre à grande échelle dans l'industrie. Des constatations générales, concernant l'influence des matériaux constitutifs sur les propriétés des CSR et leur impact sur la conversion thermochimique, sont rassemblées dans le Table 1-8.

Une description phénoménologique et technique du processus de gazéification est réalisée dans la section 1.2.1. Dans la gazéification, les ressources carbonées sont transformées en un gaz de synthèse (principalement H_2 , CO , CO_2 , CH_4), une fraction organique condensable (goudrons) et, dans certains cas, un résidu solide (char). La répartition des produits dépend de la composition de la ressource, de la conception du réacteur et des conditions du procédé (température, pression, temps de séjour). À l'échelle industrielle, on peut distinguer trois grands types de réacteurs : les réacteurs à lit fixe (à courant ascendant et descendant), les réacteurs à lit fluidisé et les réacteurs à flux entraîné. Leurs caractéristiques sont décrites dans la section 1.2.2. Dans notre cas, nous nous concentrerons sur les réacteurs à lit fluidisé bouillonnant, largement utilisés dans la conversion des combustibles pour les applications de production d'énergie. Ils sont considérés comme plus robustes et plus flexibles que les autres réacteurs conventionnels, et les plus adaptés pour traiter des matières premières hétérogènes comme les déchets solides.

L'état de la recherche actuelle sur la pyrolyse/gazéification des CSR et de leurs composants est discuté dans la section 1.3. Tout d'abord, les études réalisées sur les balances thermogravimétriques sont évoquées. Ensuite, nous nous concentrons sur d'autres études à l'échelle de quelques grammes, généralement réalisées dans des réacteurs tubulaires. Enfin, quelques études sur les réacteurs à lit fluidisé à l'échelle pilote sont discutées.

Les déchets solides et leurs combustibles dérivés sont des mélanges complexes et hétérogènes. L'étude de l'influence de leur composition sur les produits formés n'est pas systématique. Les dispositifs à l'échelle du laboratoire offrent une solution simple et flexible, mais les limitations en termes de transferts de chaleur et de masse doivent être prises en compte. Un manque d'études sur des

échantillons de quelques grammes à dizaines de grammes, avec des vitesses de chauffage élevées, a été identifié.

La teneur en matériaux des CSR influence les caractéristiques et la distribution des principaux produits de pyrolyse/gazéification. Des effets d'interaction entre les matériaux peuvent apparaître pendant la pyrolyse et la gazéification des déchets. La plupart d'entre eux ont été observés entre la biomasse et les matières plastiques. Les conséquences de ces interactions sur les produits de réaction doivent être étudiées en profondeur, et validées à des échelles plus élevées.

Enfin, une brève évaluation des approches de modélisation pour la prédiction des produits de réaction et de leurs rendements est présenté dans le **Table 1-12**. Plusieurs modèles de complexité différente ont été proposés et examinés dans la littérature. Les modèles très complexes ne sont pas appropriés pour des situations impliquant des combustibles hétérogènes, car ils nécessitent la définition et l'évaluation de nombreuses propriétés et paramètres qui ne peuvent pas être facilement estimés.

Chapitre 2 : Installation Expérimentale

Le dispositif expérimental développé pour cette thèse a été conçu en fonction de deux critères principaux :

- I. Avoir un contrôle précis des conditions opératoires (température, temps de séjour de la réaction et atmosphère gazeuse), afin d'être représentatif de la gazéification.
- II. Permettre d'étudier des solides très hétérogènes (tels que les CSR), et obtenir des mesures adéquates et reproductibles des quantités de produits de réaction.

Le réacteur est chauffé par induction électromagnétique. Un générateur fournit un courant alternatif à une spirale située autour du tube qui constitue le corps principal du réacteur. Cette technologie permet d'atteindre des taux de chauffage très rapides par rapport aux technologies conventionnelles. Un schéma de l'installation est présenté sur la **Figure 2-3**, tandis que des photos de l'installation sont présentées dans l'**Annexe B**. Le système se compose des éléments suivants : le tube principal (réacteur), la bobine d'induction, un système de piégeage des goudrons et les modules d'analyse des gaz produits, chacun de ces éléments étant décrit en détail dans la section 2.2.

Le système est capable de traiter des échantillons de quelques grammes, qui sont placés dans un creuset fait avec une maille métallique. Un échangeur de chaleur est inclus à l'intérieur du réacteur pour préchauffer les gaz porteurs.

Une caractérisation thermique du nouveau réacteur a été réalisée. L'objectif principal était d'identifier avec précision le comportement thermique du réacteur et de l'échantillon tout au long d'une expérience. Dans un premier temps, nous avons suivi l'évolution de la température de la surface du réacteur en fonction du temps, pour une consigne de 800 °C (**Figure 2-8**). La température de la surface du réacteur atteint la valeur de consigne en environ 15 s, avec une vitesse de chauffe de 80 °C. s⁻¹. Ensuite, nous avons mesuré la température à l'intérieur du creuset lors de divers essais, avec le creuset vide puis en présence d'un échantillon inerte (alumine). L'évolution de la température à l'intérieur du réacteur en utilisant un lit de céramique inerte entraîne une vitesse de chauffage d'environ 4 °C. s⁻¹.

Le profil de température le long de la surface extérieure du réacteur a été mesuré une fois le régime permanent atteint. Il est montré dans la **Figure 2-10**. À l'intérieur du lit de particules de l'échantillon en céramique, la température maximale est de 808 °C. Les écarts de température sont inférieurs à 10 °C dans le lit (TS1 à TS4), ce qui montre que la température est uniforme et proche de la température de consigne.

Finalement, des calculs CFD (menés avec ANSYS FLUENT 19.3) ont été réalisés afin de compléter la caractérisation thermique du réacteur et d'évaluer l'influence du débit de gaz porteur sur le profil de température à l'intérieur du réacteur.

Certaines hypothèses ont été formulées pour simplifier les calculs. La géométrie du réacteur a été représentée en utilisant une approche 2D-axysymétrique le long de la direction du flux. Le gaz mis en œuvre était du diazote, entrant à 25 °C avec un débit compris entre 0.5 et 4 NL.min⁻¹. Le lit de particules de céramique a été aussi représenté. Le rayonnement a été pris en compte, en utilisant le module Surface to Surface inclus dans Fluent. Une représentation graphique des contours de la distribution de la température dans la phase gazeuse est montrée pour différents débits de gaz dans la **Figure 2-11**.

Si le débit du gaz porteur est maintenu à des valeurs modérées (0,5 NL.min⁻¹), le profil de température dans la zone de l'échantillon reste uniforme. A des valeurs de débit plus élevées, l'échangeur de chaleur n'est pas suffisant et les gradients de température au dans l'échantillon sont plus prononcés. Une section de réacteur tubulaire d'environ 20 cm au-dessus de l'échantillon est maintenue entre 750 et 800 °C, ce qui permet d'obtenir un temps de séjour des espèces volatiles compris entre 2 et 4 s.

La configuration du réacteur et le système de chauffage se sont avérés appropriés pour les essais dans des conditions contrôlées. Grâce aux mesures effectuées, les limitations thermiques ont été identifiées.

Chapitre 3 : Ressources et Méthodes

L'échantillon de combustible solide de récupération (CSR) sélectionné pour ce travail est utilisé sous forme de granulés, produits à partir de déchets industriels non dangereux, de déchets d'ameublement et d'encombrants provenant de déchetteries (**Figure 3-1**). Une caractérisation d'un lot du même CSR est détaillée dans l'**Annexe D**. Des matériaux modèles ont été sélectionnés pour représenter les fractions trouvées dans les CSR. Cette sélection était basée sur leur abondance et leurs caractéristiques chimiques. Les polymères les plus courants dans les déchets (PE, PP et PET) ont servi de matériaux modèles pour la fraction plastique, tandis que le bois de hêtre et le carton représentent la fraction biogénique. Ils sont présentés dans la **Figure 3-4**.

Afin d'étudier les interactions entre les fractions biogéniques et dérivés des fossiles, deux mélanges ont été préparés. Les mélanges bois/PE et bois PP, après broyage fin, ont été mis sous forme de pastilles afin d'assurer un contact étroit entre les deux matériaux et de renforcer leurs interactions (**Figure 3-5**). La composition chimique et les caractéristiques du CSR, des matériaux modèles et des mélanges sont présentées dans le **Table 3-1**.

Les procédures expérimentales et les conditions de fonctionnement utilisées pour les essais de pyrolyse sont détaillées dans la section 3.2.1. Les essais ont été réalisés à 800 °C avec un débit de gaz porteur constant égal à 0.5 NL.min⁻¹. Le réacteur reste à la température de consigne pendant 20 min. A la fin de l'essai, les produits solides sont collectés dans le creuset, les produits condensables sont récupérés dans des flacons laveurs avec de l'isopropanol, et les gaz permanents sont collectés dans un sac Tedlar. Pour les essais de gazéification les conditions sont décrites dans la section 3.2.2. Un ajout d'air en quantités contrôlées est réalisé pendant les premières 3 min de l'essai. Un facteur d'air global a été calculé à partir de la durée de l'injection d'air et de la masse totale de l'échantillon.

Les méthodes d'analyse et les calculs pour la détermination des rendements des différents produits de réaction sont décrits à la fin de ce chapitre, dans la section 3.3. Un diaphragme a été installé pour mesurer le débit de production gazeuse. Un micro-GC est utilisé pour analyser les gaz. L'instrument est calibré pour détecter et quantifier la concentration du CO₂, CO, CH₄, H₂, C₂H₂, C₂H₄, C₂H₆, C₃H_x, C₄H₆, C₆H₆, and C₇H₈. Les espèces condensables sont analysés via GC-FID. Les espèces de goudron quantifiées ont été classées en 5 groupes selon le système de classification proposé par l'ECN comme indiqué dans le **Table 3-4**. Des détails additionnels sur les dispositifs utilisés pour les analyses de gaz et des condensables ainsi que les espèces quantifiées figurent dans l'**Annexe E**.

Chapitre 4 : Résultats et discussion

Ce chapitre présente et discute les résultats expérimentaux obtenus dans le dispositif expérimental. Il est divisé en cinq parties.

Tout d'abord, dans la section 4.1, l'évolution temporelle de la température (**Figure 4-1**) et du débit des espèces volatiles produites pendant la pyrolyse (**Figure 4-2**) a été suivie. Les résultats montrent que dans le réacteur, la pyrolyse est terminée après 120 s dans tous les cas. Pour les matériaux à haute teneur en hémicellulose et en cellulose comme le carton, la pyrolyse se produit plus rapidement (dès qu'une température de 300 °C environ est atteinte), tandis que le bois, avec une teneur plus forte en lignine, se pyrolyse sur une durée plus longue et une gamme de températures plus large. Pour les plastiques comme le PE et le PP, la libération de matière volatile commence à des températures plus élevées, car ils sont soumis à une étape de changement de phase endothermique. La vitesse de chauffage des échantillons est comprise entre 4 et 6 °C. s⁻¹.

Des tests de pyrolyse de l'échantillon de CSR et des cinq matériaux modèles ont été réalisés à 800 °C. Le rendement et la composition des principaux produits gazeux, des espèces volatiles condensables et du résidu solide sont présentés pour chacun des échantillons sélectionnés dans la section 4.2.

Chaque ressource est convertie majoritairement en produits gazeux (**Figure 4-3**). Le bilan massique global des produits de la pyrolyse se situe entre 65 et 80 % de l'échantillon initial. Une discussion sur ce sujet est conduite dans la section 4.2.2, avec les bilans élémentaires pour le carbone, l'hydrogène et l'oxygène. Les rendements en gaz produits par la pyrolyse des CSR et des matériaux modèles sont présentés sur la **Figure 4-7**. Les plastiques polyoléfinés (PE, PP) présentent les rendements totaux en gaz les plus élevés, avec des rendements importants en hydrogène et en hydrocarbures. Le PET, le bois et le carton donnent principalement du monoxyde de carbone et du dioxyde de carbone. En ce qui concerne le gaz produit lors de la pyrolyse du CSR, le CO est le principal composant gazeux (0,13 L. g daf⁻¹), suivi par CH₄ et H₂.

Les espèces des goudrons quantifiées ont été classées selon la classification ECN, et sont détaillées dans le **Table 4-1**. Des rendements élevés en goudrons totaux (35- 55 mg. g daf⁻¹) sont mesurés pour les CSR et les matériaux plastiques. La répartition relative des goudrons par groupe, montre que le bois, le carton et le PET présentent les productions les plus élevées d'espèces hétérocycliques (classe 2), qui consistent principalement en composés oxygénés. Les goudrons issus de PE et de PP sont principalement des composés aromatiques à un cycle (classe 3), suivis de goudrons à 2 ou 3 cycles

benzéniques (classe 4). Le PET présente le rendement en goudrons de classe 5 (HAP) le plus élevé parmi tous les matériaux.

La composition chimique du char évolue par rapport à celle de la ressource brute (**Figure 4-13**). Avec la pyrolyse, les teneurs en oxygène et en hydrogène du solide diminuent, tandis que la teneur en carbone tend vers 100%. Cette évolution est moins prononcée pour le carton et les CSR, peut-être en lien avec leur teneur en cendres élevée.

Les résultats expérimentaux pour les mélanges bois/PE et bois/PP ont été comparés à la somme pondérée des résultats pour les composants individuels dans la section 4.3, suivant une hypothèse de non-interaction entre chaque. Un effet synergique est observé lors de la pyrolyse des mélanges, car la conversion du carbone est favorisée vers les produits gazeux (**Figure 4-16**). Ceci peut être expliqué par des réactions en phase gazeuse entre les espèces volatiles primaires de la pyrolyse des deux matériaux, ainsi qu'à des interactions physiques entre le char du bois et le plastique fondu pendant les premières secondes de la pyrolyse.

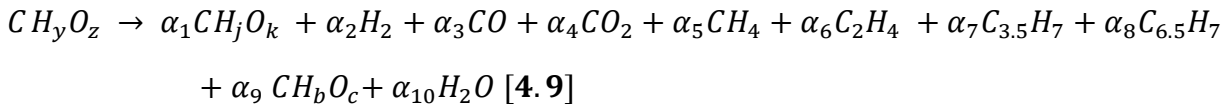
Une réduction du rendement en char de 30 % est observé pour le mélange bois/PE et de 15 % pour le mélange bois/PP par rapport au cas sans interaction. Pour les deux mélanges, les rendements expérimentaux en H₂, CO et CO₂ sont plus élevés que les rendements calculés (**Figure 4-18**). Les rendements totaux en goudrons pour les expériences avec les mélanges sont supérieurs aux valeurs calculées (**Table 4-3**). Ces différences sont plus marquées pour le mélange Bois/PE, avec une sélectivité vers les espèces aromatiques.

Pour se rapprocher des conditions de gazéification, l'influence de l'ajout d'oxygène sur les produits de la réaction a été étudiée dans trois conditions différentes (ER = 0.02, 0.05 et 0.1) avec un échantillon de bois de hêtre, et dans une seule condition (ER=0.05) pour le CSR et pour le reste des matériaux modèles. Les résultats sont comparés à ceux obtenus dans des conditions de pyrolyse dans la section 4.4.

L'ajout d'oxygène a favorisé la conversion du carbone en gaz (**Figure 4-22**). Les réactions d'oxydation partielle de H₂, d'hydrocarbures et d'espèces volatiles organiques ont donné lieu à des rendements gazeux plus élevés, notamment en CO, CO₂ et benzène (**Figure 4-23**). La fraction de C identifiée a augmenté par rapport aux essais en pyrolyse. Les rendements en goudrons ont été légèrement réduits pour les matériaux lignocellulosiques, tandis que l'inverse a été observé pour le PE et le PP (**Table 4-6**). Des quantités plus faibles de HAP ont été obtenues avec l'ajout d'oxygène, ce qui suggère que

certaines intermédiaires de pyrolyse qui sont des précurseurs de HAP réagissent avec l'oxygène disponible, limitant ainsi leur formation.

Enfin, dans la section 4.5 une corrélation a été développée à partir des résultats obtenus avec les matériaux modèles, en utilisant uniquement la composition chimique comme donnée initiale. La pyrolyse est exprimée comme une réaction en une seule étape [Eq. 4.9], et un total de 10 produits est pris en compte.



Les expressions des coefficients stœchiométriques ($\alpha_1 - \alpha_8$) et des paramètres c , j et k en fonction de la composition élémentaire des ressources, sont obtenues à partir de la régression des résultats expérimentaux de pyrolyse des cinq matériaux modèles à 800 °C. Ils ont été ajustés à l'aide d'une méthode de régression multi linéaire (MLR), disponible dans le logiciel statistique Minitab. Le coefficient stœchiométrique des goudrons (α_9), le paramètre b , et le coefficient stœchiométrique de l'eau (α_{10}), ont été calculés par différence à partir des bilans carbone, hydrogène et oxygène respectivement. Ces expressions sont résumées dans le **Table 4-12**.

Les diagrammes de parité des rendements massiques prédits avec la corrélation, par rapport aux rendements expérimentaux de la pyrolyse des cinq matériaux modèles, sont fournis dans la **Figure 4-27**. En général, les prédictions sont satisfaisantes. La corrélation a été confrontée aux résultats obtenus avec les ressources hétérogènes (CSR et les deux mélanges bois/plastique). Les valeurs prédites et expérimentales pour le rendement massique de chaque produit sont comparées dans la **Figure 4-28**. De bonnes prédictions ($\pm 10\%$) ont été obtenues pour les rendements en gaz, char, H_2 , CH_4 et C_2 , tandis que les prédictions pour certaines espèces comme le CO_2 et le BTX sont entachées d'une erreur significative par rapport aux valeurs expérimentales.

Conclusions et perspectives

Le réacteur et le système de chauffage permettent d'atteindre des conditions thermiques contrôlées et bien caractérisées, ainsi que plusieurs des objectifs de conception initialement proposés (niveau de température, temps de séjour des gaz, uniformité de la température dans l'échantillon). Les limitations thermiques du dispositif ont été identifiées et discutées.

La distribution et la composition des produits varient de manière significative entre les matériaux modèles, ce qui montre que les compositions élémentaire, macromoléculaire et la structure chimique influencent la distribution du produit final. Des profils de dévolatilisation différents ont été observés pour chacun des matériaux. Ceux-ci sont aussi en accord avec les différences de montée en température observées entre la biomasse et les matériaux plastiques.

Pour les deux mélanges, la conversion du carbone en produits gazeux est plus élevée que prévue sans interaction. Les effets synergiques observés pourraient être attribués aux réactions en phase gazeuse entre les radicaux provenant de la pyrolyse, et aussi à l'inhibition des réactions de condensation et d'agrégation des espèces volatiles, qui a entraîné une réduction de 15 à 30 % du rendement en char par rapport à la valeur calculée sans interaction.

Les expériences en présence d'oxygène, ont montré une conversion du carbone en produits gazeux favorisée par rapport à la pyrolyse. Comparé à la pyrolyse, des rendements en gaz plus élevés ont été observés, notamment en CO, CO₂ et benzène. Des quantités plus faibles de HAP ont été obtenues avec l'ajout d'oxygène, ce qui suggère que certains intermédiaires de pyrolyse qui sont des précurseurs de HAP réagissent avec l'oxygène disponible, limitant ainsi leur formation. La comparaison de ces résultats avec ceux obtenus dans un réacteur de gazéification à alimentation continue doit encore être effectuée très soigneusement.

La corrélation développée a tenté de prédire les rendements des principaux produits de pyrolyse de CSR et des mélanges en utilisant uniquement les teneurs en C, H et O de la charge d'alimentation. Les différences observées montrent que la méthodologie est probablement trop simplifiée pour pouvoir atteindre une prédiction acceptable pour tous les rendements en produits, en se basant uniquement sur les teneurs en C, H et O, et sur une réaction en une seule étape.

Des perspectives sont suggérées pour la suite. Du côté expérimental, l'identification des produits non mesurés doit être améliorée. Pour progresser dans la compréhension des effets d'interaction sur les produits formés, d'autres expériences avec différentes proportions massiques dans le mélange, et à plusieurs températures, pourraient être réalisées. Ceci pourrait permettre de sélectionner les conditions de fonctionnement qui favorisent les produits d'intérêt.

En ce qui concerne l'axe de modélisation, quelques perspectives sont proposées. Dans un premier temps, il semble intéressant de continuer à utiliser une approche simple et empirique qui nécessite peu de paramètres d'entrée. Il serait alors nécessaire d'inclure un nombre beaucoup plus important

d'expériences. Par ailleurs, une autre approche consiste à augmenter la complexité du modèle en considérant des paramètres supplémentaires. Les corrélations empiriques de la pyrolyse pourraient ensuite être couplées à d'autres sous-modèles, décrivant par exemple les réactions en phase gazeuse ou la gazéification des chars.

Pyrolysis and gasification of a solid recovered fuel (SRF) and its model materials

Abstract

Solid waste materials that cannot be reused or recycled are increasingly used to produce Solid Recovered Fuels (SRF). They can be transformed by thermochemical processes such as gasification, thus producing a synthesis gas that can be used in cogeneration (heat and electricity) or for the synthesis of liquid or gaseous fuels. SRF constitute a raw material of interest that has been largely less studied than biomass in gasification. The objective of the thesis is to investigate the pyrolysis and gasification of SRF, in relation with their physical and chemical characteristics, under controlled operating conditions. For this purpose, a new laboratory-scale experimental device was developed. An experimental characterization and CFD calculations provided a complete description of the temperature profiles for the sample and the gas inside the reactor. Several model materials (wood, cardboard, polyethylene terephthalate, polyethylene, and polypropylene), often found in SRF, were studied separately, in an inert atmosphere and in the presence of air as an oxidizing agent. The yield and distribution of reaction products (char, gas species, and tar) were determined. Pyrolysis of wood/plastic mixtures showed an increased conversion of carbon to gaseous products in comparison with what would be expected with no interaction. Based on the experimental pyrolysis results for the individual model materials, a correlation was developed to predict the product yields as a function of the feedstock C, H and O contents.

Keywords : SRF, Pyrolysis, Gasification, Solid waste, Energy valorisation.

Pyrolyse et gazéification d'un combustible solide de récupération (CSR) et de ses matériaux modèles

Résumé

Certains déchets solides qui ne peuvent être ni réutilisés ni recyclés sont de plus en plus utilisés dans la production de Combustibles Solides de Récupération (CSR). Ils peuvent être valorisés par des procédés thermochimiques comme la gazéification, produisant ainsi un gaz de synthèse utilisable en cogénération (chaleur et électricité) ou pour la synthèse de carburants liquides ou gazeux. Les CSR constituent une matière première d'intérêt, qui a cependant été largement moins étudiée que la biomasse en gazéification. L'objectif de la thèse est d'étudier la pyrolyse et la gazéification de CSR, en lien avec leurs caractéristiques physiques et chimiques, dans des conditions opératoires contrôlées. Pour cela, un nouveau dispositif expérimental à l'échelle du laboratoire a été développé. Une caractérisation expérimentale et des calculs CFD ont fourni une description complète des profils de température pour l'échantillon et le gaz à l'intérieur du réacteur. Plusieurs matériaux modèles (bois, carton, polyéthylène téréphtalate, polyéthylène et polypropylène), souvent présents dans les CSR, ont été étudiés séparément, en atmosphère inerte et en présence d'air en tant qu'agent oxydant. Le rendement et la distribution des produits de réaction (résidu carboné, espèces gazeuses, goudrons) ont été déterminés. La pyrolyse des mélanges bois/plastique a montré une conversion accrue du carbone en produits gazeux en comparaison à ce qui aurait été attendu sans interaction. En se basant sur les résultats expérimentaux de pyrolyse pour les matériaux modèles, une corrélation a été développée dans le but de prévoir les rendements de pyrolyse à partir des fractions massiques en C, H et O des ressources.

Mots clés : CSR, Pyrolyse, Gazéification, Déchets solides, Valorisation Énergétique